Exploiting Stable Isotope Imaging with High Resolution Secondary Ion Mass Spectrometry for Applications in Biology

Haibo Jiang

St. Anne's College

A thesis submitted for the degree of Doctor of Philosophy in the University of Oxford

Supervised by Professor C. R. M. Grovenor

Hilary Term 2014

ABSTRACT

Exploiting Stable Isotope Imaging with High Resolution Secondary Ion Mass Spectrometry for Applications in Biology

Haibo Jiang
St. Anne's College

A thesis submitted for the degree of Doctor of Philosophy in the University of Oxford
Hilary Term 2014

This thesis presents applications of high resolution secondary ion mass spectrometry (NanoSIMS) analysis for stable isotope imaging in biological samples. These projects were designed to explore the potential applications of NanoSIMS analysis, and to develop protocols and novel methodologies to visualize and quantify biological processes. Working with collaborators in the UK and USA, I have applied NanoSIMS analysis to study 3 research areas, including molecule interactions, single cell metabolisms and lipid imaging in tissues. Antimicrobial peptides (AMPs) play important role in the immune system, and understanding how AMPs interact with cell membranes can provide useful information to design new therapies to control infection. The pore structures and dynamics of the interaction of AMPs with membranes has been visualized for the first time and confirmed with combined AFM and NanoSIMS analysis. A correlative backscattered electron (BSE) imaging and NanoSIMS analysis methodology has been developed to study glutamine metabolism in single cancer cells. This method enables us to measure the chemical information in specific organelles in these cells and can be widely applied to study metabolisms and to trace the uptake of labelled molecules in biological matrices. Quantitative analysis on the effects of hypoxic conditions and the PYGL gene were studied. Applying correlative BSE and NanoSIMS analysis, I also studied lipid uptake mechanisms in various mouse tissues, including brown adipose tissue, heart, intestines, liver and skeletal muscle, mainly focused on a recently discovered protein, GPIHBP1, and its function in the lipid uptake process. TRL margination was proved to depend on the GPIBP1-LPL complex, and 3 stages of lipid transport from capillary lumen to lipid droplets was also visualized by combined BSE and NanoSIMS analysis.

ACKNOWLEDGEMENTS

During my DPhil study, I have received a lot of help and assistance from many people. I would like to take this opportunity to thank them.

Firstly, I would like to thank Prof. Chris Grovenor, my supervisor, who provided me the opportunity to study on this interesting project at Oxford, and gave me invaluable training to be a researcher and fully supported me all the time through my DPhil.

I would like to thank all my collaborators support and help on my projects. It would not be possible to finish my DPhil without them. My collaborators, Prof. Adrian Taylor, Prof. David Ferguson, Dr. Elena Favaro provided me the first samples for NanoSIMS analysis, and started my idea on developing new correlative EM and NanoSIMS methods for biological Materials. I am grateful for the help from Dr. Max Ryadnov, Paulina Rakowska and Dr. Santanu Ray at the National Physical Laboratory. They have provided me the opportunity to study the exciting project on interaction between antimicrobial peptides and lipid bilayers, and helped me on sample preparation and data interpretation. I would like to thank Prof. Stephen Young, Prof. Loren Fong and Dr. Chris Goulbourne at UCLA and their guidance on the lipid metabolism project, and also thank Dr. Jean-Nicolas Audinot and Patrick Grysan for their help on correlative AFM and NanoSIMS analysis.

There are many other people who had helped me during my DPhil, even though the work I have done with them is not discussed in this thesis. I would like thank Prof. Peter Cook for his useful discussions on my projects; Dr. Errin Johnson, Dr. Mike Shaw, Dr. Louise Hughes for their help my sample preparations; Dr. Sabyasachi Baboo, Bhaskar Bhushan for their help on investigating protein synthesis and turnover.

I appreciate many help from my colleagues at Materials Department of Oxford University. I would like to thank Dr. Katie Moore and Clive Downing for their help on NanoSIMS training, in particularly, Dr. Katie Moore's very useful suggestions on NanoSIMS experiments. The help from Dr. Sverre Myhra, Dr. Alison Crossley, Gabriella Chapman, Dr. Gareth Hughes, and Chris Salter is much appreciated. I would like to thank Carol Spruce, Lorraine Laird for arranging meetings with Chris.

I would like to thank all my friends and officemates. I really enjoyed my life at Oxford around them.

Thank Nanobeams PhD School, St. Anne's College, Biophysical Society and Institute of Physics for generous travel grants supported me to attend several courses and conferences.

Finally, I would like thank my mother, father, grandmother, aunt, Mengzhi and all other family members for their full support and encouragement on my DPhil studies.

PREFACE

The work reported in this thesis was undertaken by the author in the Department of Materials, University of Oxford between October 2010 and March 2014, under the supervision of Prof. Chris R. M. Grovenor. No part of this work has been submitted for a degree at this or any other university. All references are listed at the end of this thesis.

Some of the work described in this thesis has been published in the following journals and has been presented at conferences listed below:

Peer-review articles:

Nanoscale imaging reveals laterally expanding antimicrobial pores in lipid bilayers. P. D. Rakowska, H. Jiang, S. Ray, A. Pyne, B. Lamarre, M. Carr, P. J. Judge, J. Ravi, U. I. Gerling, and B. Koksch, Proceedings of the National Academy of Sciences, 2013. 110(22): p. 8918-8923.

Stable isotope imaging of biological samples with high resolution secondary ion mass spectrometry and complementary techniques. H. Jiang, E. Favaro, C. Goulbourne, P. Rakowska, G. Hughes, M. Ryadnov, L. Fong, S. Young, D. Ferguson, and A. Harris, Methods, 2014. 68(2): p. 317-324.

The GPIHBP1–LPL complex is responsible for the margination of triglyceride-rich lipoproteins in capillaries. C. N. Goulbourne, P. Gin, A. Tatar, C. Nobumori, A. Hoenger, H. Jiang, C. R. M. Grovenor, J. D. Esko, I. J. Goldberg, K. Reue, P. Tontonoz, A. Bensadoun, A. P. Beigneux, S. G. Young, and L. G. Fong, Cell metabolism, 2014. 19(5): p. 849-860..

Human proteins are made in both the nucleus and cytoplasm, and most are degraded within a minute, S. Baboo, B. Bhushan, H. Jiang, C. R. M. Grovenor, P. Pierre, B. G. Davis, and P. R. Cook, PloS one, 2014. 9.6: e99346.

Presentations:

58th Biophysics Society Annual Meeting, San Francisco, USA, Feb. 2014.

International NanoSIMS Workshop, Luxembourg, Oct. 2013.

New Ideas in Bioanalysis and Analytical Toxicology, London, UK, May 2013.

AnalytiX-2013, Suzhou, China, Mar. 2013.

The Analysis of Complex Biological Systems, a meeting to celebrate the contribution of Alice Warley to Analytical Electron Microscopy, London, UK, Apr. 2013.

Nano-Molecular Analysis for Emerging Technologies V, Teddington, UK, Nov. 2012

Annual Oxford Biomedical imaging Festival, Oxford, UK, Oct. 2012.

European Microscopy Congress, Manchester, Sep. 2012.

This thesis is approximately 30,000 words.

CONTENTS

1 Introduction

As early as 1935 Schoenheimer *et al.* [1] started using stable isotopes to study biological processes – what they described as *intermediary metabolism* - and they are still widely used in biomedical studies after almost 80 years. By contrast, the NanoSIMS is the newest of a long line of developments in the technique of secondary ion mass spectrometry (SIMS). This instrument was first invented in the late 1990s, and is starting to be recognized by biological community as a powerful tool to study some of their most complex and challenging problems. This thesis will present new results on the combination of this technique with more traditional experimental methods to study three important biological processes. These interdisciplinary projects were developed with collaborators in the UK and USA, and my role was to design experimental protocols to take advantage of the special capabilities of the NanoSIMS and to explore which complementary analysis technique could add useful information on each particular kind of sample. Each of these sample types required the development of different analysis protocols, and results from Atomic Force Microscopy (AFM), Fluorescence Microscopy and Backscattered Electron (BSE) imaging will also be presented in this thesis.

Chapter 2 and Chapter 3 will give a detailed description of NanoSIMS analysis, including instrumental basics, sample preparation and high resolution imaging, in particular for biological materials. They will also review the recent literature on NanoSIMS studies on biological materials, emphasizing the use by other groups of correlative methods. A brief introduction to the techniques and instruments used for my three projects will be also included in Chapter 3.

Chapter 4 will present my work on molecular imaging, concentrating on antimicrobial peptides and lipids. Antimicrobial peptides play important roles in the innate immune system thanks to their ability to kill bacteria, viruses, protozoa and fungi. Understanding these interaction mechanisms will help the development of anti-infective therapeutics, and could help overcome the growing problem

of resistance to conventional antibiotics. Collaborating with Dr. Max Ryadnov, Paulina Rakowska and Dr. Santanu Ray from the National Physical Laboratory, I have worked on imaging directly the location of isotopically labelled molecules, and will discuss the combination of NanoSIMS and AFM for direct imaging of the interactions between antimicrobial peptides and lipid bilayers.

Chapter 5 will demonstrate the NanoSIMS ability in single cell analysis. I will present results from a project I carried out with Prof. Adrian Harris, Prof. David Ferguson, and Dr. Elena Favaro from Oxford University. The project is about NanoSIMS analysis of the glutamine metabolism in single cancer cells. Glutamine is regarded as a critical molecule in cancer metabolism, and developing a better understanding of how this metabolism functions would help to develop novel targeted cancer therapies. My work on subcellular analysis with a combination of NanoSIMS and backscattered electron imaging will be discussed in this chapter.

Chapter 6 will show results from applying the NanoSIMS to tracking stable isotope labelled molecules in tissue samples. The recent discovery by Prof Stephen Young's team in UCLA of a GPI-anchored protein (GPIHBP1) solved the mystery of the transport of lipoprotein lipase to the action site. Working with them, I have designed and carried out a project to improve our understanding of lipid transport. The difficulty of direct visualization of the location of fatty acid lipids can be overcome by high resolution, quantitative stable isotope imaging in the NanoSIMS. Correlative BSE and NanoSIMS imaging was used intensively in the results presented in this chapter to visualize the transport states of fatty acids in various tissues.

Finally, Chapter 7 will give overall conclusions to the work in this thesis, also gives some suggestions for the future work, both on biological projects and technical development of high resolution SIMS analysis.

2 Literature Review

Secondary Ion Mass Spectrometry (SIMS) is a technique which can be used to obtain chemical distributions from both the surfaces and 3D volumes of a large number of different types of sample. It has been widely and successfully used in physical science studies since the 1980s [2]. New developments of the SIMS technique, including cluster sources and time of flight mass analysers, have made it increasingly powerful for biological research in the last decade [3], and an increasing number of interesting biological studies have been conducted with different SIMS techniques [4-7]. The stable isotope labelling method has also been widely used in biological research since 1935 [1], in fields such as proteomics [8] and microbiological ecology [9]. This thesis explores applications combining NanoSIMS analysis and stable isotope labelling on biological materials. The instrumental basics of the SIMS technique will be discussed in this chapter, and current applications of stable isotope labelling will be reviewed with the emphasis on recent studies carried out with NanoSIMS analysis on samples labelled with stable isotopes. I will also give a short review of recent publications on the use of complementary analysis techniques with high resolution SIMS as a background for the results on correlative methods which will be presented in the following chapters.

2.1 Stable Isotope Labelling

It has been almost 80 years since the first use of stable isotopes as probes to study metabolisms [1, 10]. Compared with the use of radiolabelled molecules, one of the most important advantages of the stable isotope labelling method is that these molecules have the same biochemical properties as the natural molecules and so they can be expected to behave in precisely the same way in the biological environment. The non-toxicity of stable isotopes also enables organisms to stay healthy for long experimental periods, whereas radiotracer may cause tissue damage from the radioactive emissions [11, 12].

The applications of stable isotope labelling keep growing with new developments of analytical techniques, in particular mass spectrometry [13-16] and nuclear magnetic resonance [17, 18] methods. The most successful applications of this kind of labelling are in the field of proteomics, with methods such as Stable Isotope Labelling by Amino acids in Cell cultures, SILAC [8, 19-21]. This methodology allows the simultaneous identification and quantification of complex protein mixtures, and enables the accurate analysis of changes in protein expression in different biological processes [8]. Stable isotope labelling has also been successfully used in several other areas, including microbiology and environmental science studies with labelled nucleic acids [9, 14] and food web studies with labelled fatty acids [22]. Naturally occurring stable isotopes have also been used as the analyte in experiments in fields as diverse as geochemistry [23], historical diets [24] and migration [25, 26]. However, this thesis is going to focus on methods by which the addition of stable isotopes to the environment allows us to study how biological samples interact with that environment.

As a natural and stable state of a molecule, stable isotope labelling has been extensively used to generate metabolic tracers that can be seamlessly incorporated into organisms. Chemically modified or radiotracer labelled molecules can have some safety issues [27], and so the number of human studies carried with stable isotopes has grown substantially in the last few decades, as reviewed by Steinhauser (Figure 2.1) [28]. ^{2}H, ^{13}C, ^{15}N, ^{18}O and other heavy isotopes have been used in these research projects.

In the last few decades most of these studies have been carried out on bulk or fluid samples [29], without trying to analyse the local distributions of the labelled molecules. For example, Figure 2.2 shows the analysis of Arabidopsis cell cultures to quantitatively measure the incorporation of ^{13}C-Arginine in DTDILAAFR peptide [30]. However, for many kinds of experiments, it would be useful to know where these molecules are in cells and tissues to understand the details of complex biological processes and mechanisms [31]. Due to the development of improved mass spectrometry

techniques, in particularly SIMS techniques, this high resolution chemical imaging is now possible. The instrumental details and applications of SIMS techniques will be discussed in the next section.

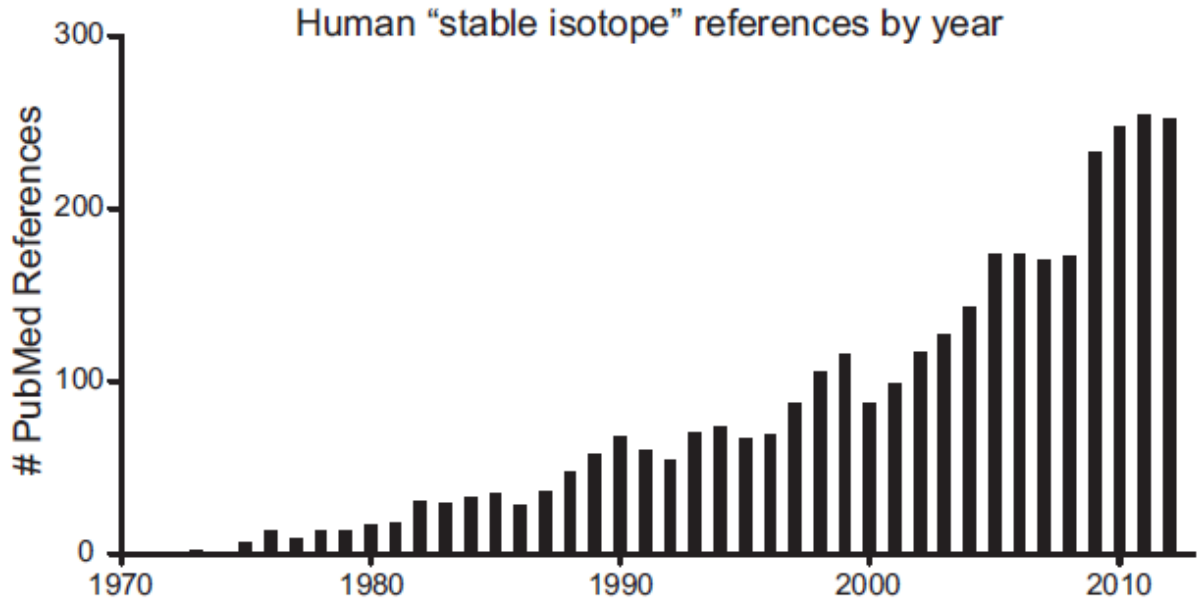

Figure 2.1: References published since 1970 on stable isotope applications on human studies. From reference [28].

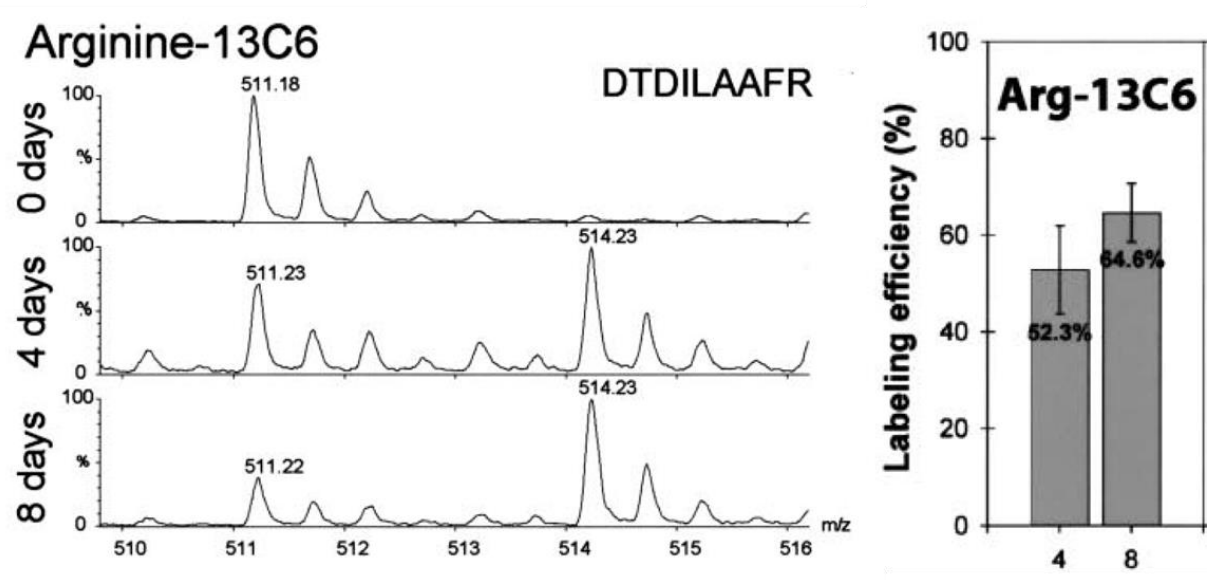

Figure 2.2: Measurement of Arginine incorporation into Arabidopsis cell culture with stable isotope labelling and mass spectrometry analysis. Modified from reference [30].

2.2 Secondary Ion Mass Spectrometry

SIMS is the mass spectrometry of ionised secondary particles emitted from a sample surface during bombardment by primary particles [32] (Figure 2.3). Due to collisions between primary projectiles and samples, electrons, molecules, atomic or cluster ions can be emitted from the surface of the sample. Most of the emitted particles from the bombardment are neutral, and in most SIMS instruments only the secondary ions can be analysed unless special measures are taken to achieve post ionisation [33].

A significant step in the invention of mass spectrometry was when J. J. Thomson measured the mass-to-charge ratio of an electron using magnetic and electrical deflection. Not long afterwards, he constructed the first mass spectrometer [34], and used it to obtain mass spectra of O_2, N_2, CO, CO_2 and $COCl_2$. In 1913, he used the mass spectrometer to discover the two isotopes of neon (^{20}Ne and ^{22}Ne), which was the first time the isotopes of stable elements were identified.

Figure 2.3 has been removed due to copy right restrictions. The original image can be found in the reference.

Figure 2.3: A schematic of collision process of the primary ion on the sample [32].

The concepts of SIMS as an analytical tool were developed in the 1960s, and in the last 50 years these basic concepts have remained mostly unchanged. However, SIMS instruments have been significantly improved because of the need for chemical analysis with high sensitivity, high spatial resolution and high precision, both in industry and academia. Depending on the primary beam current (ion dose) used in the instrument, SIMS is generally divided to two types, dynamic and static SIMS. Dynamic SIMS employs a relatively high dose primary ion beam (usually higher than 10^{17} ions/cm^2) for analysis. Due to the high dose and resulting high sensitivity for trace elements, the main use for dynamic SIMS is depth profiling and measuring the chemical distribution of dopants in semiconductors and related devices [35]. There are whole book chapters on SIMS for semiconductors [36-38]. Current dynamic SIMS instruments can offer parts per billion sensitivity, tens of nanometres lateral resolution and sub-nanometre depth resolution.

Static SIMS usually employs low primary ion doses (less than 10^{13} ions/cm^2). This technique is widely used to investigate the chemistry of surfaces [39]. As the interactions between the primary ion beam and sample are limited almost to the top monolayer of the surface and signals originate from previously undisturbed areas, the surface is said to be static, i.e. it is not removed or substantially modified during analysis [40]. Static SIMS is usually used to determine the composition of surface contaminants or molecular information. Current developments in static SIMS instrumentation include the use of cluster ions such as Au_n^+, Bi_n^+, SF_5^+, C_{60}^+ and argon clusters instead of the atomic primary ions (Ar^+, Ga^+, Cs^+ etc.) [41, 42]. Compared with atomic primary ions, cluster primary ions can usually give a much higher secondary ion sputtering yield [43] and cause less damage to the sample surface. These important developments have in the past 10 years given the technique of static SIMS a higher surface selectivity, higher spatial resolution and improved sensitivity [43].

To fully understand what is happening to the sample during SIMS experiments, it is necessary to understand several concepts including; yield, ionisation efficiency, different kinds of resolution (lateral resolution, mass resolution and depth resolution), sensitivity, steady state, and relative

sensitivity factors etc. All of these concepts have been nicely discussed in references [32, 44, 45] and are briefly outlined below.

2.2.1 Basics of SIMS

Sputter Yield and Preferential Sputtering

The sputter yield is defined as the average number of particles ejected from the target per incident ion. It is affected by the beam energy, angle of incidence and the surface binding energy of atoms. The variation in the sputter yield between elements results in a composition change at the surface of multi-element sample, which is called preferential sputtering [41] and causes the surface to become enriched in the element with the lower yield.

Mass Resolution

SIMS techniques separate secondary ion signals by a difference in mass-to-charge ratio. The ability to separate two elements is called mass resolving power. Mass resolution indicates the ability to distinguish between two peaks with almost the same mass-to-charge ratio and is given by Equation 2.1 [46]:

$$R = \frac{m}{\Delta m} = \frac{\frac{m}{z}}{\frac{\Delta m}{z}} \qquad \text{(Equation 2.1)}$$

Mass resolution is one of the most important characteristics of a SIMS instrument. The higher mass resolution the closer the peaks which can be separated, which means the instrument can correctly detect the correct signal without interferences.

Lateral Resolution

Lateral resolution describes the ability of a SIMS instrument to differentiate between two features close together on the surface of the sample. The lateral resolution of a SIMS instrument depends most strongly on the size of the primary ion beam and sensitivity.

Depth Resolution

The depth resolution is determined by the thickness of the sampling depth from which the secondary ions originate in a single measurement [47], and it can be defined using full width at half maximum definition or by the distance over which the signal changes by a factor of x. It is especially important in dynamic SIMS which is often used for depth profiling. The depth resolution depends on (1) impact energy, (2) impact angle, and (3) primary ion type [40].

Sensitivity

The sensitivity of SIMS depends on the ionization efficiency of the analyte ion, the dark counts on the electron multiplier and any background signal generated elsewhere in the electronics or from overlapping peaks not fully separated. The sensitivity also depends on the transmission of the instrument, which only varies with the configuration and type of mass analyser used [40]. Vickerman claimed that the sensitivity of static SIMS can achieve sub-attomole range [42], and CAMECA that dynamic SIMS can reach part per billion for high yield elements [41].

Steady State

The primary ion dose implanted in the rastered area increases as the primary ion beam sputters away the surface. The ionization probability is also affected by the work function of the surface, and the implanted primary ions can significantly change it, e.g. Cs^+ implantation lowers the surface work function leading to an increase of negative ion formation. As a result, the secondary ion signals change at the start of the analysis due to the implanted dose of the primary ions, and signals will reach steady state after the transient state at the beginning. Reliable quantification can only be done in the steady state.

Relative Sensitivity Factor (RSF)

Relative sensitivity factors are used to quantify SIMS data. As the secondary ion yields vary from element to element, signal intensities are not directly related to surface composition. RSF values are conversion factors from secondary ion intensity to atom density [48], and they have been measured

on standard samples, mainly in a silicon matrix, for each element (Figure 2.4). They can be used through equation 2.2 to get the real concentration of the element in an unknown sample [44]. RSF values vary by more than 10^5, which makes it very difficult to achieve reliable quantification in SIMS.

$$C_E = RSF \cdot \frac{I_E}{I_M} \qquad \text{(Equation 2.2)}$$

Figure 2.4 has been removed due to copy right restrictions. The original image can be found in the reference.

Figure 2.4: RSF of negative secondary and positive ions under caesium and oxygen primary beam. From reference [48].

2.2.2 Artefacts in SIMS

There are also three important artefacts that will affect ion signals significantly; including matrix effects, surface topography and sample charging.

The Matrix Effect

The matrix effect is the combined effect of the local chemistry and bonding on secondary ion yield of an element in an environment compared with those signals from a pure element [49], and it makes it more difficult for quantification.

Surface topography

Sample topography can change the secondary ion signals significantly in SIMS experiments because ions can be more easily sputtered from edges. A flat surface is good for secondary ion transmission and reliable analysis [50]. During the bombardment of the primary ion beams, any initial surface topography can result in increasing roughness with depth due to differential sputtering on different areas of the composition, or local changes in mechanical properties.

Sample Charging

During the bombardment, primary ions, secondary ions and secondary electrons are involved, which can produce a net electric charge on the sample surface. Conductive samples can disperse the charge, but in insulating samples charge will build up and result in potential sample surface charging. Charged samples divert the primary ion beam from the analytical area, and significantly decrease the secondary ion signals by reducing secondary ion transmission and detection through the optical system in the instrument due to the change of the secondary ion energy distribution. In charged samples, mobile ions can migrate to disperse charges, and this migration may modify the chemical information of interest [44]. Solutions to this problem involve either coating with metals (dynamic SIMS) or using an electron flood gun (dynamic SIMS and static SIMS).

2.2.3 SIMS Instrumentation

Figure 2.5 shows the basic components of all SIMS instruments. Primary ion beams are produced by an ion source and focused onto the sample in the primary ion column generating secondary ions in the manner shown in Figure 2.3. These secondary ions will be collected by extraction optics and

separated according to their mass-to-charge ratio in the energy analyser and mass analyser. Finally the signals are collected by ion detectors. These signals are processed depending on the working mode chosen (i.e. depth profile, image, or line scan) and give the experimental information required. Most SIMS instruments have a setup of this kind, although there are significant variations especially between dynamic and static SIMS instruments. I will concentrate in this thesis on the layout of the NanoSIMS instrument I have used for all my experiments.

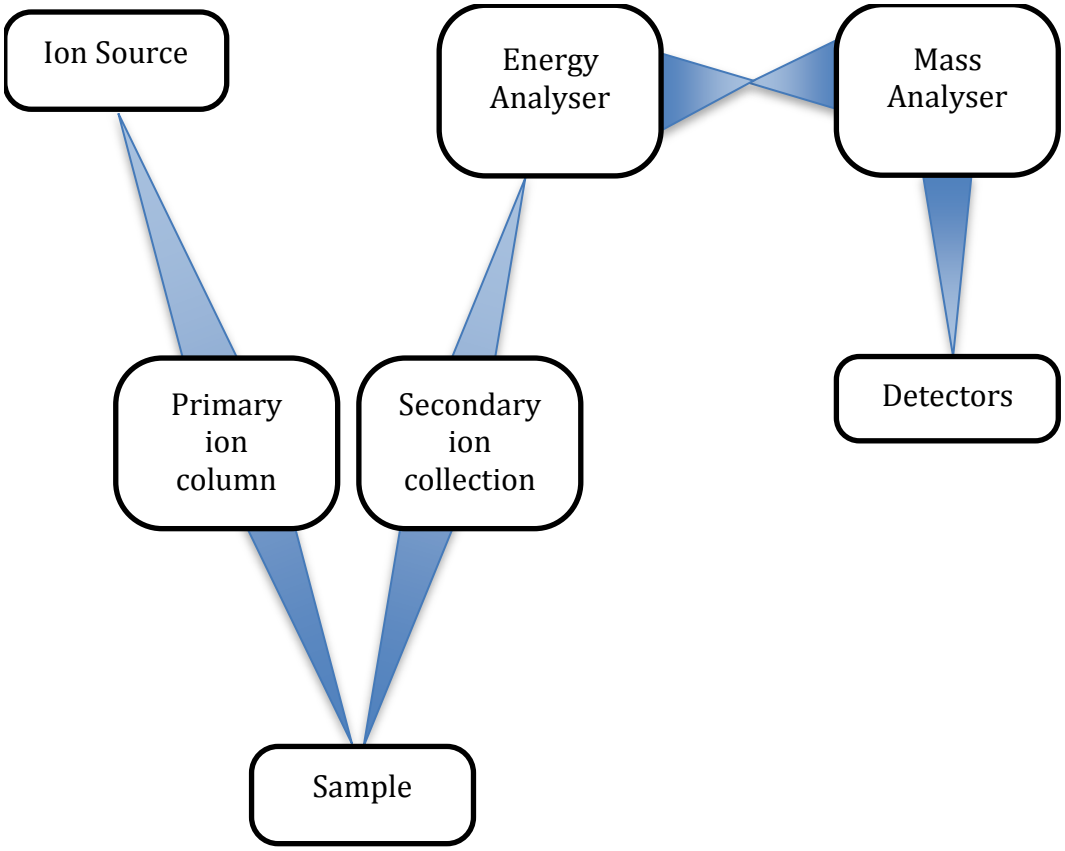

Figure 2.5: Schematic outlining the basic components of a SIMS instrument, drawn based on [44].

2.2.4 Overview of Applications of SIMS

Generally, there are four types of analysis can be done in a SIMS instrument: (1) acquiring a mass spectrum, (2) ion imaging, (3) depth profiling and (4) isotopic ratio measurements. I will consider each one of these in turn.

2.2.4.1 Mass Spectrum

A mass spectrum is a plot of detected intensity vs. m/z and gives chemical information about a sample surface which is an important and basic application of SIMS. From a mass spectrum it is possible to isolate both elemental and molecular peaks. A mass spectrum not only provides information regarding which elements are present but also the possible compounds, especially organic compounds. Figure 2.6 shows a spectrum of phenylalanyglycine on silver surface, which is a typical ToF-SIMS experiment [51]. This type of analysis is often applied to organic chemistry related research, such as organic contamination on surface, or in medical areas, including drug discovery [52].

Figure 2.6 has been removed due to copy right restrictions. The original image can be found in the reference.

Figure 2.6: Positive and negative ion spectra from SIMS of phenylalanyglycine on silver. From reference [51].

2.2.4.2 Ion Imaging

Imaging is another important characteristic of SIMS, giving information on the spatial distribution of the element or molecule of interest. There are two different modes for ion imaging, microscope mode and microprobe mode [53]. The microscope mode is a fast, real time method of ion imaging, where signals from the targeted area are collected at the same time, and one type of secondary ion is used to form the whole image. This only takes a few seconds for secondary ion signals with high intensity, and only a few minutes for trace elements that produce low intensity secondary ion signals [54]. Figure 2.7 shows ^{24}Mg and ^{39}K images of frozen freeze-dried kidney tissue, which took 60s and 0.4s to collect respectively [54].

Figure 2.7 has been removed due to copy right restrictions. The original image can be found in the reference.

Figure 2.7: SIMS imaging in microscope mode with $^{24}Mg^{+}$ and $^{39}K^{+}$ signal on frozen freeze-dried kidney tissue [54].

In microprobe mode, a focused ion beam is scanned across the sample bombarding only a very small part of the targeted surface at any one time. Signals from each part of the sample are collected by electron multipliers, and built up to form the whole image from the scanned area. The microprobe mode overcomes the main limitation of microscope mode, poor lateral resolution, and can reach 50 nm spatial resolution in instruments like the CAMECA NanoSIMS. However, the method of picking up signals pixel by pixel makes it very time consuming, especially for trace elements where the counting time needs to be long since the signal intensity is low. The choice between these two

modes depends on the aims and requirements of the user and on sample restrictions. Many examples of microprobe images will be shown in the experimental chapters of this thesis.

2.2.4.3 Depth Profile

Depth profiles can provide information on chemical distributions at different depths through the sample. The key parameter for depth profiling is depth resolution. To interpret a depth profile properly, we need to consider preferential sputtering mechanisms which roughen the sample surface, crater edge effects and atomic mixing. To obtain a reliable depth profile, it is common to only use the data from the central region of a larger crater when doing a depth profile [48, 55]. RSFs and standards are used to quantify depth profile data, which can reach precisions of 1% in concentration and 4% in depth in modern instruments [41]. Depth profiling is still a very common method in the semiconductor industry to determine the elemental distribution in products [35]. Figure 2.8 shows an example of SIMS depth profile in semiconductor research. It is very easy to do depth profiling with dynamic SIMS since the primary beam dose is high enough to sputter the sample surface and get a depth profile as material is removed. In static SIMS, another ion gun is usually required to sputter the sample between data acquisitions as the analytical primary beam has a low dose [41]. The recent development of cluster primary ions such as C_{60}, Bi_n^+, SF_5^+ also provide higher depth resolution than atomic primary ion beams [56].

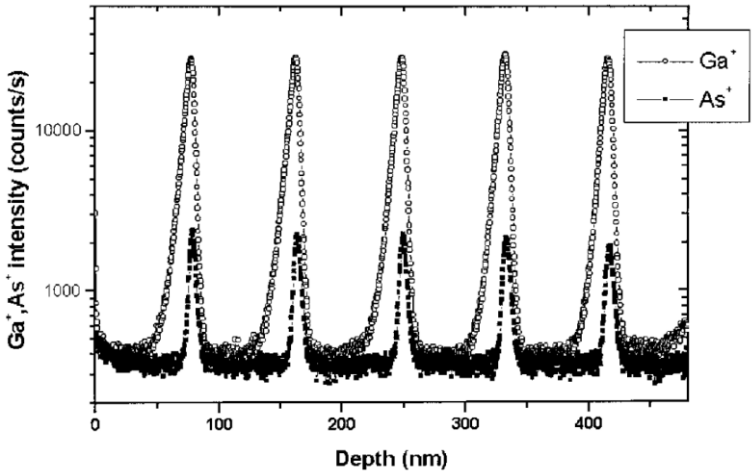

Figure 2.8: Depth profile of GaAs delta-doped layers in silicon. From reference [57].

2.2.4.4 Isotopic Ratio Measurement

Mass spectrometry techniques like SIMS have the unique ability to be able to distinguish between different isotopes of the same element. Isotopic ratio measurements have been used in many areas, including cosmochemistry and geology [58-61]. One example used ^{15}N, ^{13}C and ^{2}H abundance for identification of molecular-cloud material in interplanetary dust particles [62]. In the last two decades, the use of stable isotopes in biological samples as markers or trackers of the way the molecules interact with cells or tissue samples has increased [63-66]. This will be the main focus of the work reported in the experimental chapters in this thesis, and previous work in this field will be described in a separate section below.

2.3 NanoSIMS

Recent developments of SIMS instruments have focussed mainly on increasing sputtering yield, ionization efficiency, the precision of the mass spectrometer and spatial resolution [42, 43]. The NanoSIMS 50 instrument (CAMECA, France) is a state-of-the-art high-resolution secondary ion mass spectrometry instrument developed in the 1990s, designed to improve spatial resolution without losing the sensitivity for dilute or trace analytes. The NanoSIMS uses the same ion matter interaction mechanisms as other SIMS instruments, but with normal incidence. Figure 2.9 shows the schematic of a NanoSIMS. There are 2 types of ion sources for the NanoSIMS, O^- and Cs^+ primary beams, which are able to increase the yield of secondary positive and negative ions respectively, and the secondary ion signals are 100 - 1000× more than those from Ga^+ sources [67]. The sources provided in current NanoSIMS instrument can achieve spatial resolutions of 50 nm for a 0.3 pA Cs^+ primary ion beam and 200 nm pA for a 0.3 pA O^- primary ion beam [67].

2.3.1 Ion Optics

The NanoSIMS uses a co-axial design of ion optics (Figure 2.10), so that the same lens assembly focusses the primary ion beam and extracts the secondary ions. This design has a very short working distance, allowing a small probe size and improved ion transmission to be achieved as well as

minimising shadowing effects [68]. However, the co-axial design of the optics also means that it only can collect secondary ions of the opposite polarity and equal energy to the primary ions. This is a fact that always need to borne in mind when designing NanoSIMS experiments. The Cs^+ source is used for detection of negative secondary ions and the O^- source is used for detection of positive secondary ions.

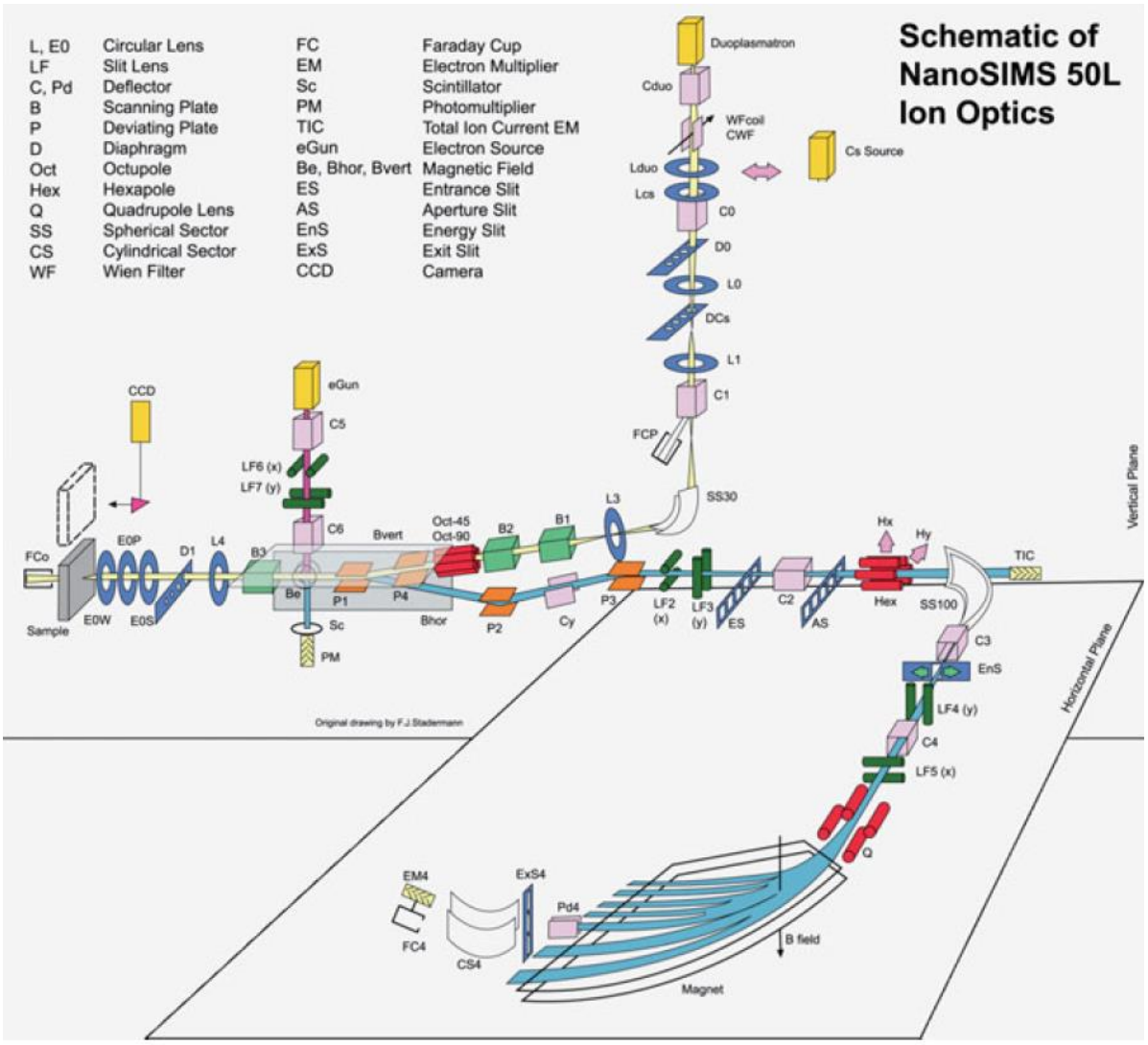

Figure 2.9: Schematic of the NanoSIMS. From reference [68].

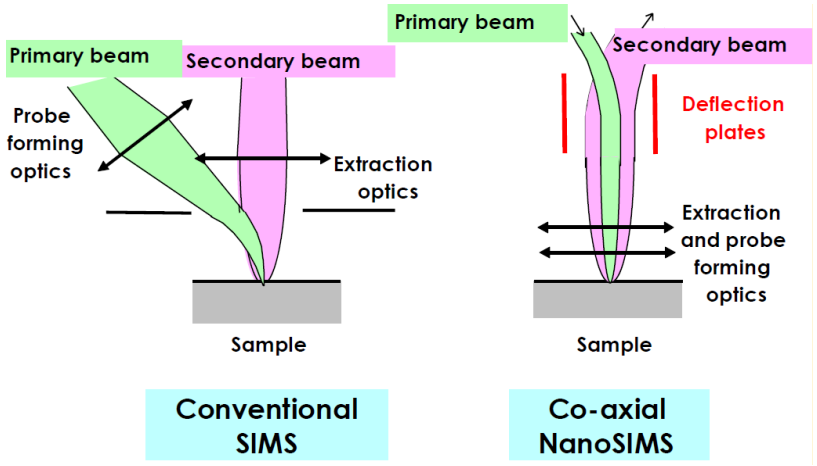

Figure 2.10: Comparison between ion optics in conventional SIMS and co-axial design in the NanoSIMS, from reference[67].

2.3.2 Analyser and Detector

Another important design feature of the NanoSIMS is the mass analyser in a Mauttach-Herzog configuration with a 90° spherical electrostatic section and asymmetric magnet (Figure 2.11). This mass analyser allows the NanoSIMS to achieve both high ion transmission (for sensitivity) and high mass resolution (for precise selection of the correct ion) combined with high lateral resolution [32]. The electrostatic sector is used to compensate for the energy spread, which is present when the ions leave the surface, before they enter the magnetic field.

Figure 2.11 has been removed due to copy right restrictions. The original image can be found in the reference.

Figure 2.11: Schematic diagram of a double focusing mass spectrometer. From reference [32].

2.3.3 NanoSIMS Characteristics

Due to the design features described above, the NanoSIMS has an unusual combination of high lateral resolution, high mass resolution and high sensitivity [32], which has made it a valuable new analytical tool in the study of a wide range of materials.

High lateral resolution

The NanoSIMS has a lateral resolution down to 50 nm for the Cs^+ beam and 200 nm for the O^- beam [69] while still maintaining a high primary beam current and high transmission efficiency in the secondary ion optics. Very recently a new O^- source has been tested and reported to achieve a similar lateral resolution as the Cs^+ source. It is this high lateral resolution which is probably the biggest advantage of the instrument when compared to other dynamic SIMS instruments.

High Sensitivity

Due to the short working distance of the co-axial optics and improved transmission, the NanoSIMS has high sensitivity, down to parts per million concentrations for the correct combination of target ion and matrix, which makes it possible to detect trace elements [70, 71] and low levels of isotope spiking [72].

High mass resolution

High mass resolution is another key feature of the NanoSIMS, reaching $\Delta m/m$ values of 4500 with 80% transmission [73]. By using the appropriate combination of aperture and energy selecting slits, it is relatively easy to completely separate two peaks with very similar masses. Figure 2.12 shows that similar masses can easily be distinguished even if they are not fully resolved. For example, $^{13}C^-$ and $^{12}C^1H^-$ around mass 13, $^{12}C^{14}N^-$ and $^1H^{12}C^{13}C^-$ around mass 26, and $^{12}C^{15}N^-$, and $^{13}C^{14}N^-$ around mass 27. The mass resolutions ($\Delta m/m$) required to separate these three sets of ions are listed in Table 2.1.

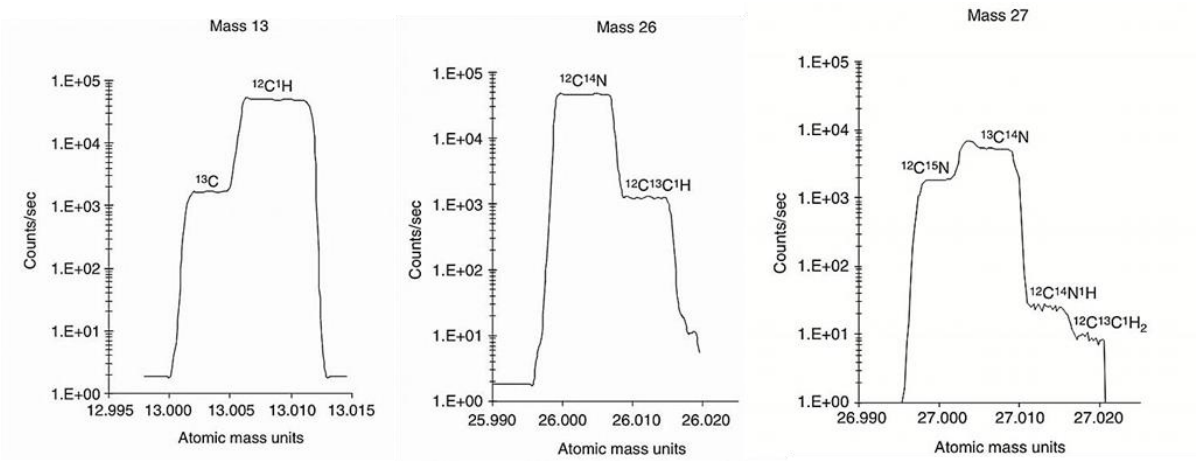

Figure 2.12: High mass resolution scans for ions around masses 13, 26 and 27. From reference [74].

Ions	Mass, u	M/ΔM
^{13}C	13.004	2956
$^{12}C^{1}H$	13.0078	
$^{12}C^{14}N$	26.0031	7224
$[^{13}C]_2$	26.0067	
$^{12}C^{15}N$	27.0001	4287
$^{13}C^{14}N$	27.0064	
$^{12}C^{14}N^{1}H$	27.0109	7504
$[^{13}C]_2{}^{1}H$	27.0145	

Table 2.1: The masses of some common ions analysed from biological samples and the mass resolution required to separate the isobaric ion pairs shown in Figure 2.12 [74].

Ability to detect light elements and isotopes

The NanoSIMS, and SIMS instruments in general, can detect elements from H to U, almost the whole range of elements in the periodic table [75]. As SIMS is a mass separation technique, isotopes can also be distinguished.

Collect up to 7 ions simultaneously

The multicollection ability of the NanoSIMS means that 5 or 7 (for the 50L model) ions can be collected simultaneously. This ability allows the user to determine reliable isotope ratios and

compare the relative locations of different ion signals which originate from exactly the same sputtered volume [76].

2.3.4 Comparison with Other Techniques

Combining SIMS with other techniques has become more and more important to obtain the most complete analysis of any particular sample. Correlations between the data available from different instruments can give us more information to explore challenging analytical questions. Figure 2.13 compares analytical spot size and detection limits of a range of common techniques in physical science studies. There are techniques which have extremely high lateral resolution (< 1 nm), such as transmission electron microscopy (TEM) and scanning tunnelling microscopy, and some techniques which can detect local chemical distributions such as energy-dispersive X-ray spectroscopy, X-ray photoelectron spectroscopy and X-ray fluorescence techniques. There are also techniques which can be used to obtain molecular information, like ToF-SIMS and Raman spectroscopy. All of these have been commonly used in a wide range of scientific fields due to the impressive analytical capabilities that they offer.

The NanoSIMS has a relatively small spot size compared with other SIMS instruments and has the advantage of being able to detect much lower concentrations of trace elements and molecules compared with techniques such as EDX or EELS in a TEM.

2.3.5 Biological NanoSIMS

The first 'NanoSIMS' like instrument was built in late 1990s in the United States, and was designed for geochemistry and cosmochemistry studies which require very high lateral resolution isotope analysis on small grains [77]. Since then, the NanoSIMS has been very successfully used by geologists for studies like presolar silicate identification [77, 78] and extraterrestrial organics studies [79, 80]. The CAMECA NanoSIMS 'prototype' was installed at the Harvard Medical School and started a 15 year intense investigation of its application to biological studies.

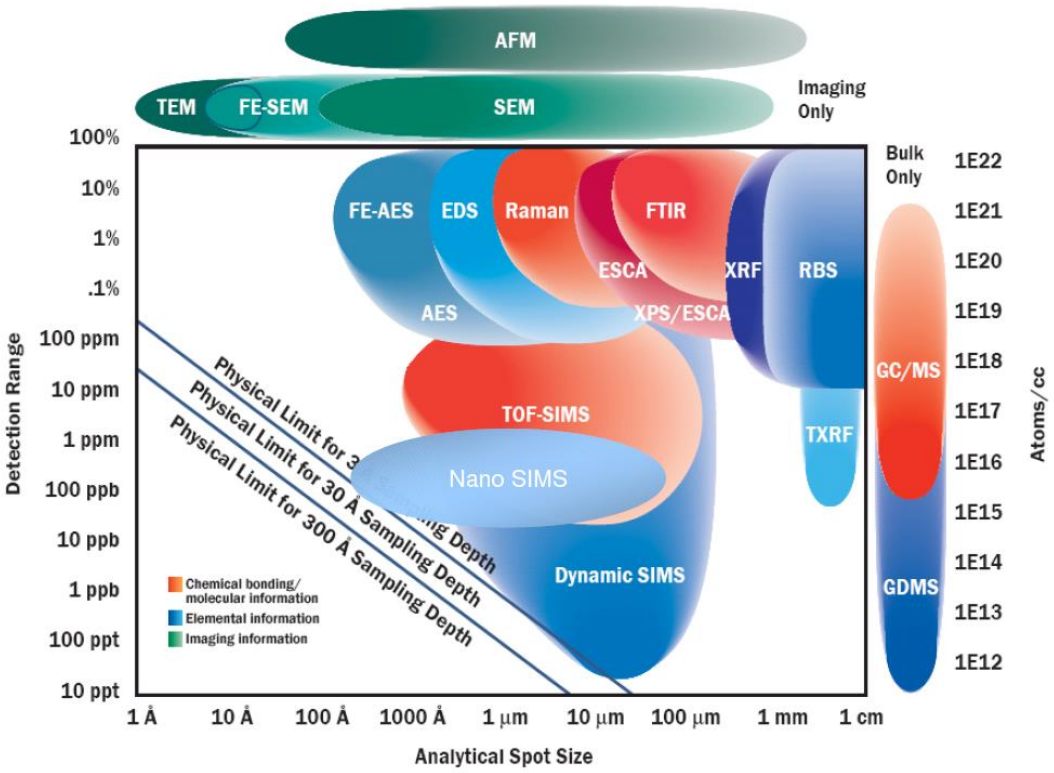

Figure 2.13: Comparison of the spatial resolution and detection limit of different common analytical techniques. Graph from [81] and altered using information from lecture notes from the Luxembourg PhD School.

2.3.5.1 Biological Sample Preparation

One of the challenges of NanoSIMS analysis on biological samples is sample preparation, and is often the most critical step of the whole experiment. The aim of sample preparation for biological samples is to maintain the interesting biological information in as close to the original state as possible while still achieving reliable and reproducible analysis. Unlike physical or some geochemical applications, samples cannot be put directly into the NanoSIMS for analysis. Complex, hydrated biological systems are difficult to prepare for NanoSIMS analysis, since they must be stable in the ultra-high vacuum in the analysis chamber. A number of different sample preparation techniques have been designed to retain the *in vivo* chemical distribution and morphology in biological samples to study different kinds of analysis techniques, especially by TEM, and each NanoSIMS project needs specific designed sample preparation protocols depending on the required information and sample type [4, 82]. In

general, sample preparation for NanoSIMS analysis can be divided to two types; chemical procedures and cyro-procedures. Both of them have fixation and dehydration steps, and some samples require further processes such as staining, resin embedding and microtomy into thin sections.

Chemical procedures are used to preserve the location of non-diffusible molecules or ions bonded to big molecules. This is also the conventional method for preparing biological TEM samples for morphological studies [83]. In previous NanoSIMS studies of biological materials, samples were mostly fixed using various concentrations of glutaraldehyde [84-86], and then dehydrated with increasing concentrations of ethanol. This kind of relatively simple process has shown success on the preservation of the distributions of large molecule, like nucleic acids [87] and proteins [88].

Cryo-procedures, on the other hand, are generally used to prepare samples where the analyte of interest is a diffusible molecule or ion. It has been reported to be a better method for preserving ultra-structures and to immobilize all the cellular components [54, 89] but is much more complex than simple chemical fixation. There are two main methods for cryofixation, plunge-freezing and high pressure freezing [90]. Both of them can rapidly freeze the sample and maintain the local distribution even of small, diffusible molecules, importantly without the creation of ice crystals which can damage the structure of biological samples. Plunge-freezing is more often used for thin samples, like molecular bilayers or single cells, and is usually followed by a slow drying procedure at low temperature [90, 91]. High pressure freezing requires more complex instrumentation, which is widely available but are still much more expensive than those needed for plunge-freezing. High pressure suppresses the formation of ice crystallisation and growth therefore minimising ice crystal damage, and it can be applied to preserve much thicker initial specimens, like tissue sections [91, 92]. Unless the samples are going to be analysed in the frozen-hydrated state, a freeze substitution procedure, which slowly replaces water with dry acetone at very low temperature, is then usually used to dehydrate high pressure frozen samples to allow resin embedding.

Both chemical fixation and cryo-procedures are now commonly used in NanoSIMS studies, and the work in following chapters will use both methods for sample preparation.

2.3.5.2 Biological Applications of NanoSIMS analysis

The NanoSIMS has been successfully applied to analyse several types of biological sample, particularly in environmental biology, plant science and cell biology. In environmental biology, it is reported as an very important technique for the future of environmental microbiology due to its ability to analyse individual cells [93], and interesting studies have been carried out in microorganism identification and nitrogen fixation [94]. Lechene *et al.* [85] imaged the nitrogen fixation of bacterial symbionts within the marine bivalve L. pedicellatus by using $^{15}N_2$ as a tracer, and they demonstrated that the host also uses fixed nitrogen from bacterium (Figure 2.14). Cyanobacteria which can fix both nitrogen and carbon dioxide also have been imaged by Clode et al using ^{13}C and ^{15}N [95].

In plant science studies, the NanoSIMS has been extensively used to study nutrient uptake from soil and transport through plant tissues. Clode *et al.* [96] used NanoSIMS analysis to visualize the pathways of ^{15}N from soil to plant root cells, and the interactions of the soil-microbe-plant (Figure 2.15). Nickel distributions in a hyperaccumulator plant (Alyssum lesbiacum) were investigated by Smart et al. [97]. Moore et al. have reported a series of studies on trace element distributions in plant tissues, including arsenic and selenium in cereal grain [98], arsenic and silicon in rice roots [99] and rice grain, iron in wheat grain [100], and copper and zinc in rice nodes [101]. It has been suggested that this kind of analysis can also be used in studies of plant responses to abiotic stress, signal exchange, nutrient flow and plant-microbial interactions [102].

Figure 2.14 has been removed due to copy right restrictions. The original image can be found in the reference.

Figure 2.14: Hue saturation intensity (HSI) images of the $^{15}N/^{14}N$ ratio in L. pedicellatus. Size of each image: 100 × 100 µm and 256 × 256 pixels. The HSI scales show the measured $^{15}N/^{14}N$ ratio divided by the natural abundance ratio [85].

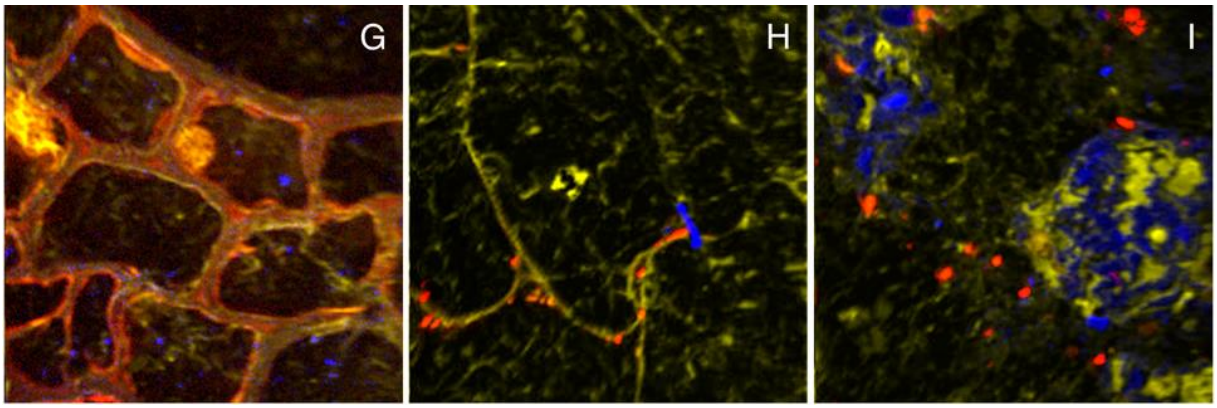

Figure 2.15: NanoSIMS overlay images of plant root cells (left), rhizosphere (middle), and soil matrix (right). Images are from overlay of $^{12}C^{14}N$ (yellow), ^{28}Si (blue) and $^{15}N/^{14}N$ (red) images. From reference [96].

The NanoSIMS has also enabled some important studies on cell biology. The areas of quantitative analysis of metabolisms, regenerative medicine, cell membrane chemical compositions and subcellular distributions of drugs have all been recently investigated. Lechene et al. have extensively used the NanoSIMS on cell biology studies, particularly for quantitative measurements on metabolisms and regenerative medicine projects. The Harvard group has reported quantitative analysis of stem cell division [87], mammalian heart renewal [86] and proven the potential of the NanoSIMS for regenerative medicine studies. The rate of the protein turnover in hair-cell stereocilia was also measured by Zhang et al. [88] at the Harvard Medical School.

Kraft et al. focused on exploiting the excellent depth resolution of the NanoSIMS for membrane imaging [103-106]. Figure 2.16 shows a montage of ^{15}N-enrichment images that are direct evidence for the formation of microdomains of sphingolipid in the plasma membranes of fibroblast cells. The high resolution ion imaging characteristic of the instrument has also enabled cell biologists and pharmacologists to image the subcellular distributions of drugs [107-109].

The NanoSIMS also has been applied in several other interesting areas, such as virology [110] and biomineralisation [111]. The characteristics and special design of the NanoSIMS have made all of these important studies possible in the last decade, and is thus attracting growing attention from the biological community.

Figure 2.16 has been removed due to copy right restrictions. The original image can be found in the reference.

Figure 2.16: ^{15}N-enrichment images of Clone 15 fibroblast cell membranes showing ^{15}N-sphingolipid distribution. From reference [105].

2.3.5.3 Stable Isotope Imaging

Several of the examples above have taken advantage of the ability of the NanoSIMS to provide high lateral resolution information of the distribution of stable isotopes that can distinguish exogenous from endogenous molecules without chemical modifications that might alter their biological behaviour. ^{1}H and ^{2}H, ^{12}C and ^{13}C, ^{16}O and ^{18}O, ^{14}N and ^{15}N are the common stable isotopes used in biological studies, and they all have been analysed or imaged by the NanoSIMS (Figure 2.17) [88, 112-114]. ^{13}C is usually used to label lipids and sugars, and has been used to study lipid phase separation [112], lipid metabolisms [87], carbon fixation [115, 116] and glucose incorporation [117]. On the other hand, ^{15}N is used to label amino acids and nucleic acids. For example, the protein turnover rate in hair-cells with ^{15}N labelled leucine [88] and stem cell division with ^{15}N labelled thymidine [87]. Since all organic molecules can be labelled with ^{13}C and ^{15}N by chemists, and they are also now commonly available products from stable isotope labelled molecule suppliers. Most research concentrates on these two stable isotopes, which have natural abundances of 1.1% and 0.37% respectively. ^{2}H and ^{18}O are also used for their special analytical characteristics. ^{2}H has an extremely low natural background (0.015%), which can produce high signal to noise images, especially useful for visualizing low concentrations of labelled molecules. The other advantage of ^{2}H labelling is that it is perfectly safe in humans, which is extremely useful to clinical researches [114].

In terms of the specific technical differences between NanoSIMS instruments, the NanoSIMS 50 and NanoSIMS 50L can simultaneously detect two and three sets of stable isotopes respectively. It is thus possible to use three of the four sets of stable isotopes mentioned above to label 3 different types of molecules, and investigate the locations of these labelled molecules independently in the NanoSIMS 50L. The NanoSIMS 50L also allows automatic magnetic peak switching, which can be used to image all four sets of stable isotope images in three consecutive images.

Figure 2.17 has been removed due to copy right restrictions. The original image can be found in the reference.

Figure 2.17: Examples of stable isotope ion/ratio images taken from a variety of types of biological samples: ^{2}H [113]: quantification of cell division with D_2O; ^{13}C [112]: lipid phase separation; ^{15}N [88]: protein turnover in hair-cell; and ^{18}O [118]: protein turnover in cultured hippocampal neurons. Images have been modified from references.

2.3.5.4 Correlative Analysis with NanoSIMS and Complementary Techniques

The powerful abilities of NanoSIMS have been discussed in the previous sections. However, the limitations of NanoSIMS are also obvious: (1) the highest resolution is only about 30 nm; (2) lack of molecular information; (3) slow analysis, especially when imaging low concentration elements or molecules. To overcome these limitations, NanoSIMS groups have developed several types of correlative analysis methods to obtain additional information from the same areas of the same samples. The other factor that also encourages development of correlative analysis methods is the

complexity of biological systems where as many different kinds of information as possible are required to understand specific processes or mechanisms.

Even though the NanoSIMS is the highest lateral resolution mass spectrometry technique at the moment, the 30 – 50 nm lateral resolution limit is still too big for the analysis of vital processes in some biological samples. Electron microscopy techniques, including transmission electron microscopy and scanning electron microscopy, are very commonly used to obtain morphological information from biological samples to support NanoSIMS analysis. Clode et al. [96] conducted correlative analysis with TEM and NanoSIMS on root-soil samples, and confirmed the microorganisms are adjacent to the root surface and that some of them are enriched with ^{15}N (Figure 2.18). Moore et al. used correlative NanoSIMS and TEM analysis to image the distributions of iron and silicon in rice roots [99]. Kraft et al. used low voltage SEM and NanoSIMS to image the same cell surfaces to obtain morphology and chemical distribution changes from the same surface [105].

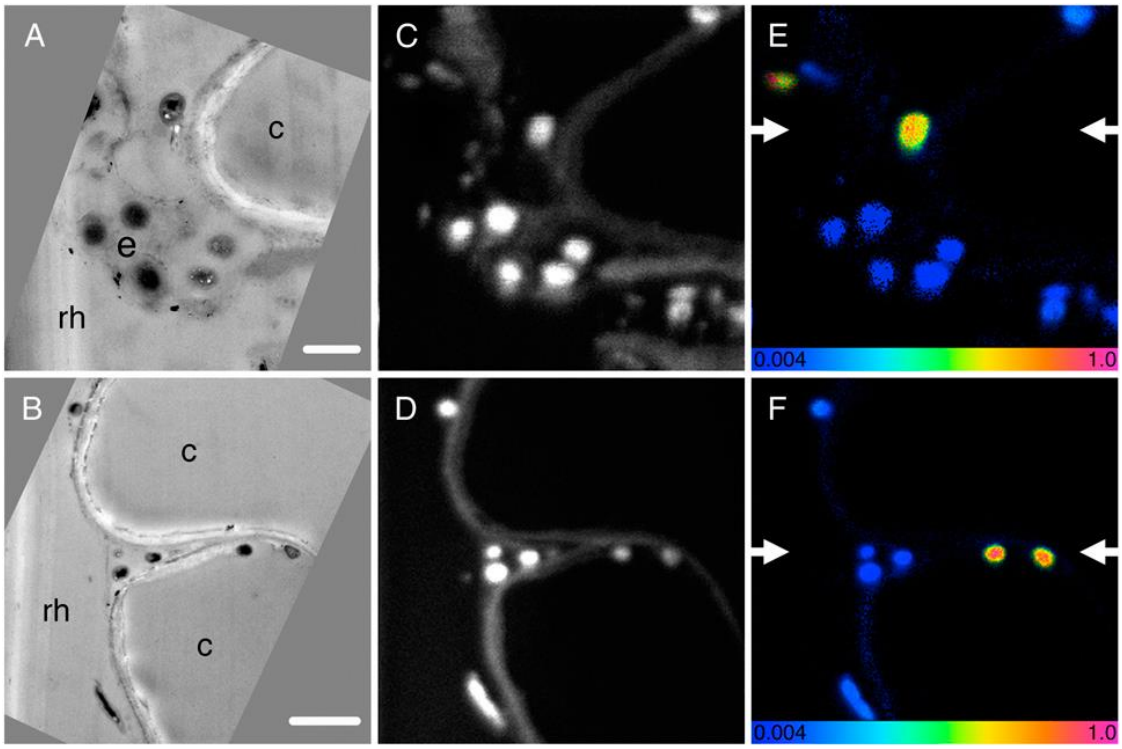

Figure 2.18: Correlative TEM (A, B) and NanoSIMS (C – F) show the ^{15}N enriched microorganisms in the rhizosphere and extracellular mulicage matrix adjacent to the root cells, From reference [96].

Due to the high energy primary ion beam, the NanoSIMS can only detect secondary ions or small cluster ions. This makes the identification of the location of specific molecules difficult unless one can be confident that the ion analysed could only originate from one specific molecule [109]. This has been major limitation for NanoSIMS applications in biology. The development of improvements in other imaging mass spectrometry techniques, including ToF-SIMS and MALDI-MS, have allowed us to visualize the distribution of specific molecules in cells and tissues, which has made them very useful in the medical sciences [31, 119-121]. The comparison of NanoSIMS, ToF-SIMS and MALDI-MS has been reviewed in [122] (Figure 2.19). In this order, MALDI-MS, ToF-SIMS and NanoSIMS have improving lateral resolutions, and can detect lower mass ion signals. Combining these three technique would allow chemical imaging from the whole body level to subcellular level [123]. The other technique which is worthy of mention for molecule detection is fluorescence microscopy. This has been used to provide additional information for understanding biological mechanisms in combination with the NanoSIMS [88, 124]. It is an extremely sensitive technique, which also can detect specific molecules if there are selective proper labels. The recent ground-breaking developments in optics, imaging methods and image processing have broken the barrier of diffraction limits and achieved tens of nanometre lateral resolution in optical techniques [125-127]. This high resolution, molecular-specific imaging technique would be another good complement to NanoSIMS analysis.

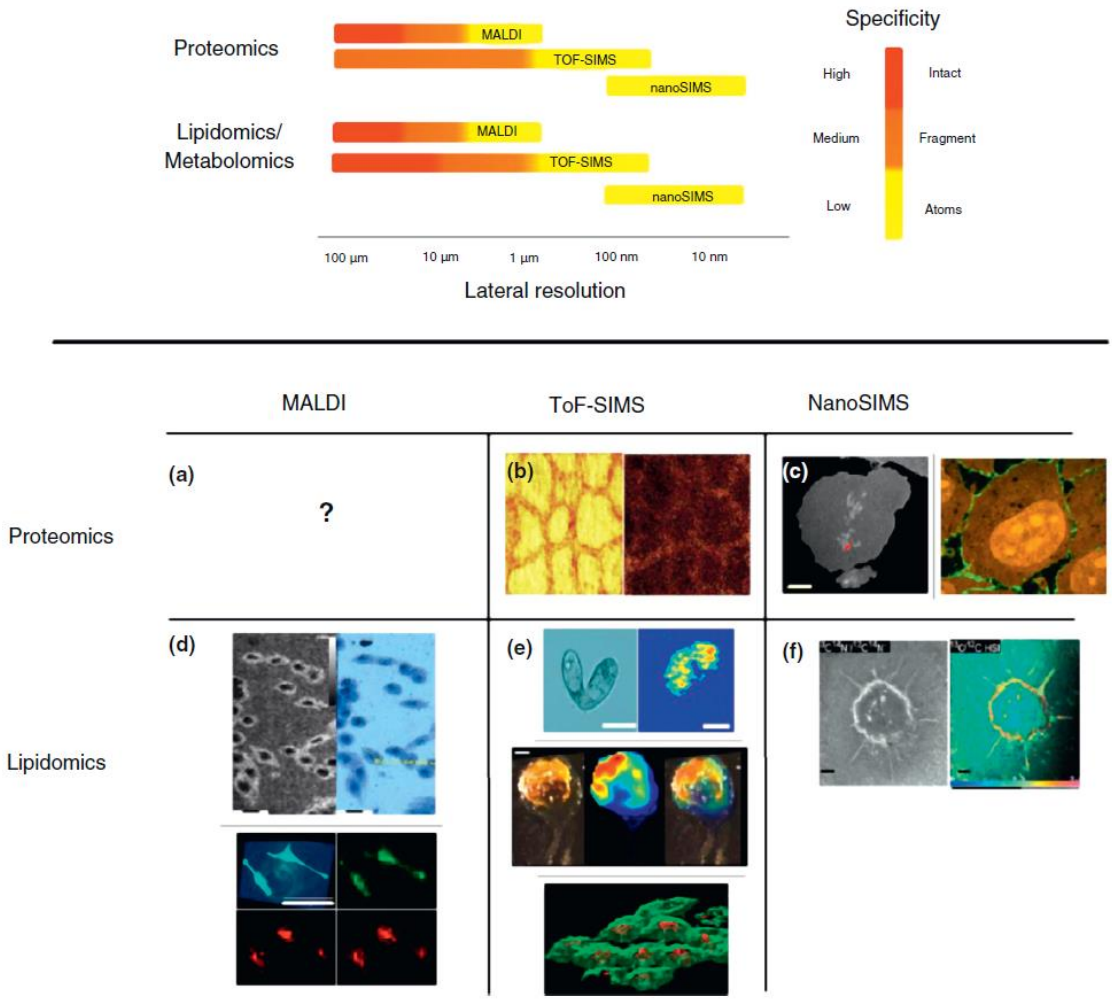

Figure 2.19: Comparisons between MALDI-MS, ToF-SIMS and NanoSIMS, and examples of applications of three techniques on proteomics and lipidomics. From Reference [122].

Fluorescence in Situ Hybridization (FISH) is another optically based technique that has been usefully combined with NanoSIMS analysis for biological research. Figure 2.20 shows fluorescence and NanoSIMS images of filamentous cyanobacteria samples exposed to ^{13}C-bicarbonate and ^{15}N-dinitrogen and labelled by FISH with a fluorine-containing ALF968F label [128]. These images show that this technique enables identification and functional analysis by the NanoSIMS at the same time. This combination of techniques also has been reported by other groups on environmental microbiology studies [129-131].

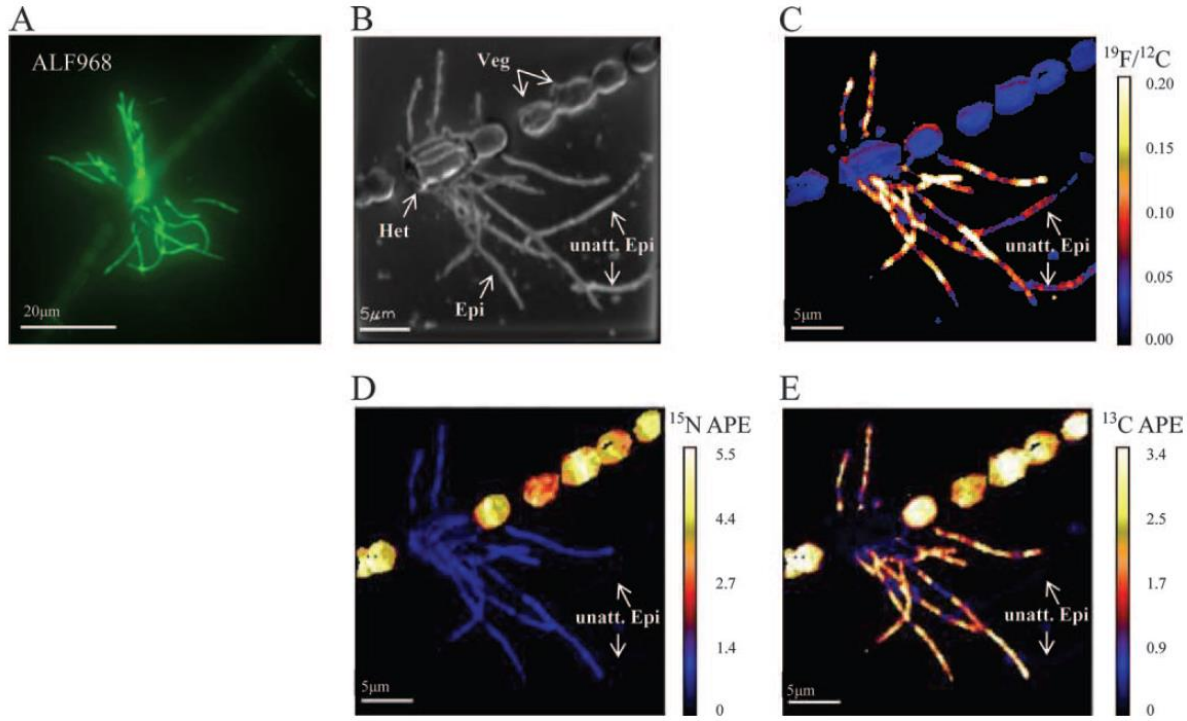

Figure 2.20: Fluorescence and NanoSIMS images on filamentous cyanobacteria samples exposed to ^{13}C-bicarbonate and ^{15}N-dinitrogen, and labelled by the FISH technique with a fluorine-contained probe (ALF968F). From reference [128].

There are also some other techniques which can provide useful complementary information for NanoSIMS analysis. ICP-MS was used to accurately measure the average concentrations of elements in bulk samples [132]. Synchrotron X-Ray Fluorescence can scan a large area with extremely high sensitivity for imaging trace elements in a biological matrix [101]. AFM has also been used extensively for lipid research to provide topographic information as a complementary technique for NanoSIMS analysis [112, 133]. Details of correlative NanoSIMS and AFM applications will be reviewed in Chapter 4.

2.4 Summary

In this chapter, the methods of stable isotope labelling and SIMS have been reviewed, and the design of the NanoSIMS and its characteristics discussed. The powerful abilities of the NanoSIMS to analyse biological sample have been reviewed, as well as its limitations. To overcome those limitations, and study complex biological systems, correlative analysis with NanoSIMS and complementary techniques has also been reviewed here.

3 Experimental Techniques

This chapter gives an overview of the experimental techniques and instruments used in the work reported in this thesis. More detailed descriptions of the sample preparation protocols and experimental methods developed for each specific project and different type of sample will be discussed in the subsequent chapters.

3.1 Sample Preparation

Sample preparation is a critical step in biological SIMS experiments. The goal of the biological sample preparation is to maintain native chemical composition and morphology for analysis, and also make samples suitable for the high-vacuum environment in the NanoSIMS. Good sample preparation can preserve both the structural and chemical information close to that formed in live cells and tissues. This section discusses the general sample preparation methods used in the projects described in this thesis. Each different sample type required distinct sample preparation methods, and these were discussed with my collaborators at the beginning of each project. Briefly, samples from the antimicrobial peptides and lipid bilayers were prepared by cryo-procedures, and cell and tissue samples were prepared by chemical procedures.

3.1.1 Rapid Freezing and Freeze Drying

To preserve the structures of antimicrobial peptides formed on the lipid bilayer surfaces the samples were plunged into liquid nitrogen and then freeze dried. This is the appropriate way to prepare samples from these very thin layers where the freezing can be sufficiently fast to immobilise all the molecules of interest. This method has been widely used to study chemical or structural information in supported lipid bilayers [72, 134, 135] with both static and dynamic SIMS.

3.1.2 Chemical Fixation and Dehydration

Chemical fixation was done on most other sample types to preserve the location of non-diffusible molecules such as nucleic acids, proteins and lipoproteins. This is the standard sample preparation

process for both electron microscopy [136] and SIMS [76, 87, 137]. My collaborators were confident that this method should allow the study of the molecules and structures of interest in a state relatively unmodified by the preparation process.

Glutaradehyde solutions in a phosphate buffer were used for fixation, and samples were also post-fixed and stained by osmium tetroxide in phosphate buffer to enhance the contrast in electron microscopy. The samples were sequentially dehydrated with increasing concentrations of acetone or ethanol (20, 30, 50, 70, 90, and 100%) for 30 min each.

3.1.3 Resin Embedding

Spurr's epoxy was used for all the resin embedded samples. Samples were infiltrated with increasing concentrations of Spurr's resin (25% for 1 h, 50% for 1 h, 75% for 1 h, 100% for 1 h, 100% overnight at room temperature), and then incubated overnight at 70^{o} C in a resin mould.

3.1.4 Microtomy

Resin blocks were taken from the resin moulds, and shaped with razor blades into trapezoidal form. All samples were cut by microtome to a section thickness of 500 nm by a diamond knife. The NanoSIMS sputters away the surface material during pre-implantation and analysis and therefore requires a relatively thick sample, but thin samples are better at dispersing the charge of the primary ion beam, so a sample thickness of 500 nm to a few micrometres was found to be optimal. Sections floating on water after microtomy were then picked up and mounted on NanoSIMS substrates. Figure 3.1 is a typical optical image of a section mounted on NanoSIMS substrates for analysis. Optical images of other sample sections studied in the NanoSIMS and by other techniques will be shown in the following chapters.

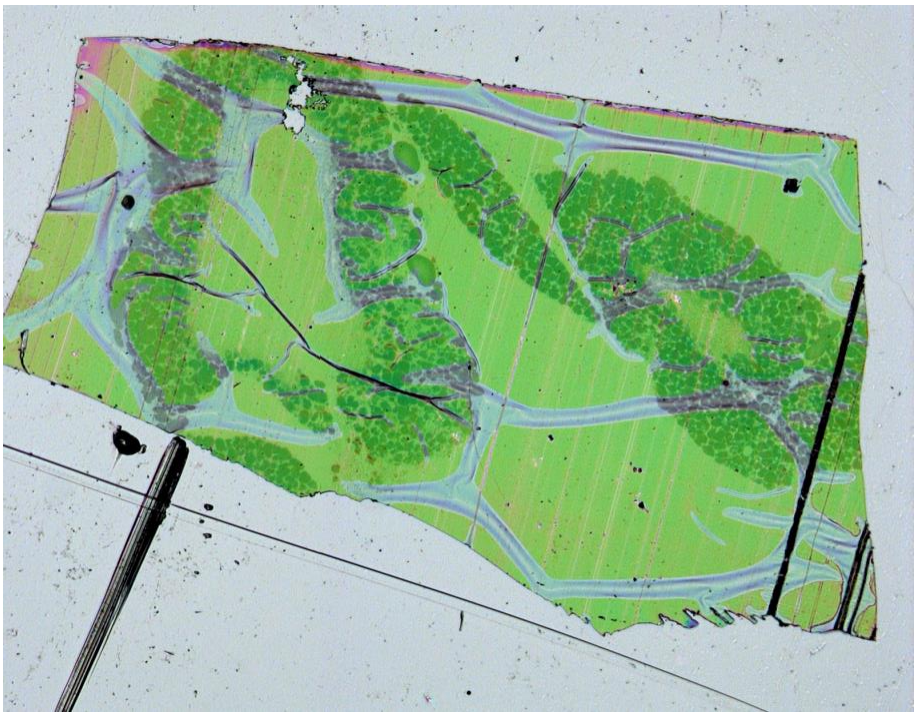

Figure 3.1: A resin embedded brown adipose tissue section cut to 500 nm and mounted on a plastic coverslip surface.

3.1.5 Platinum Sputter Coating

A Cressington 208HR high-resolution sputter coater was used to coat 5 nm platinum on all the samples to avoid charging in the NanoSIMS. Samples were not coated with platinum before backscattered electron imaging in order to visualize the contrast from heavy metal staining, they were then coated just prior to NanoSIMS analysis.

3.1.6 Substrates for Sample Mounting

Oxidized silicon substrates (University Wafer) were used to support the lipid bilayer and antimicrobial peptide samples. Plastic coverslips (Thermanox) cut to 1 cm diameter discs with a steel hole punch and coated with 15 nm platinum were used for cell culture and resin sections of cell and tissue samples (Figure 3.2). Coverslips with alpha-numeric grids (Cellattive, Nexcelom) were also used for correlative fluorescence microscopy and NanoSIMS analysis (Figure 3.3) since they made it easy to locate the same area in different microscopes.

Figure 3.2: Thermanox plastic NanoSIMS substrates for resin section samples, coated with 15 nm platinum on the surface.

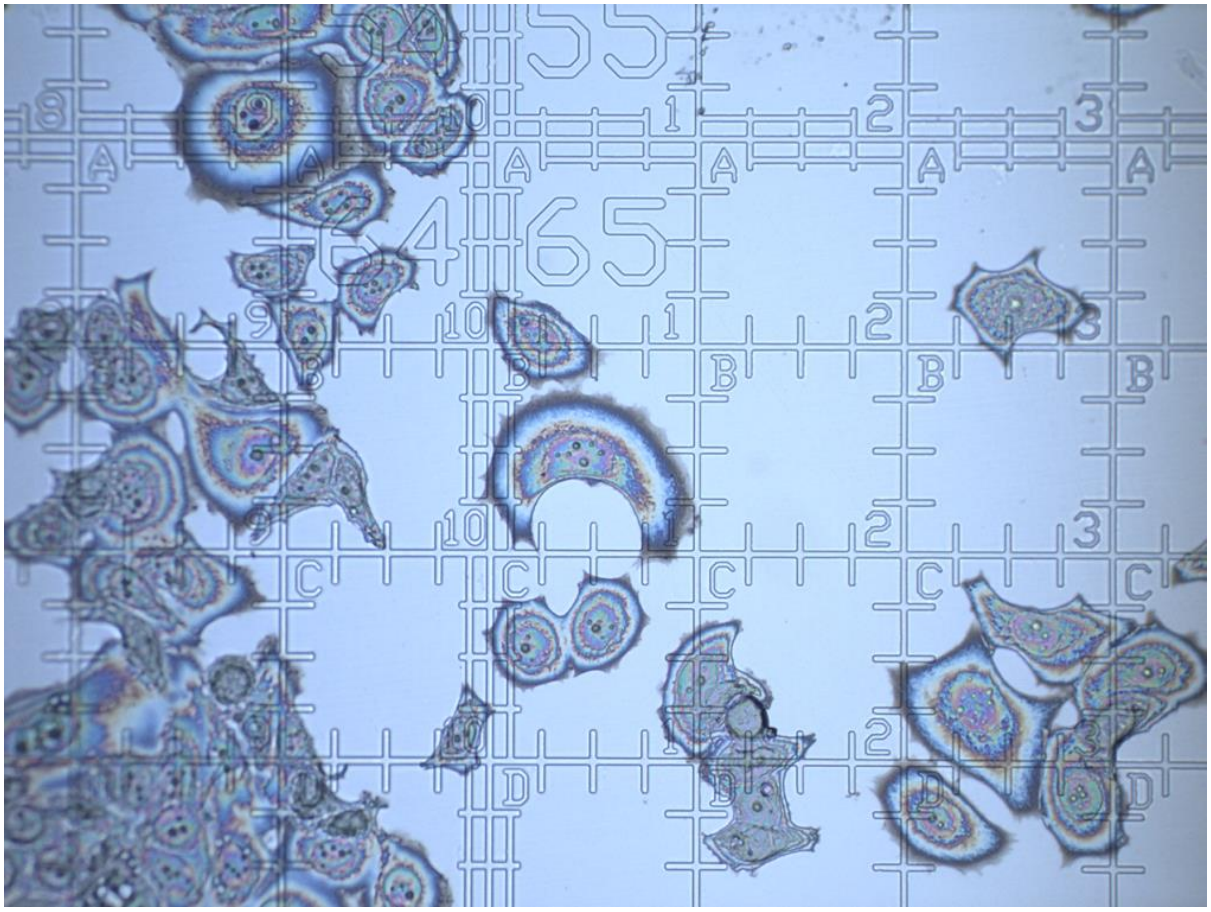

Figure 3.3: Plastic substrates with alpha-numeric grids were also used in this thesis for correlative analysis.

3.2 Light Microscopy

A Polyvar MET optical microscope was used to take optical images of all the samples. The images serve as navigation maps for subsequent electron microscopy and NanoSIMS imaging. Figure 3.4 is an example of using the optical image for navigating during correlative backscattered electron imaging and NanoSIMS analysis.

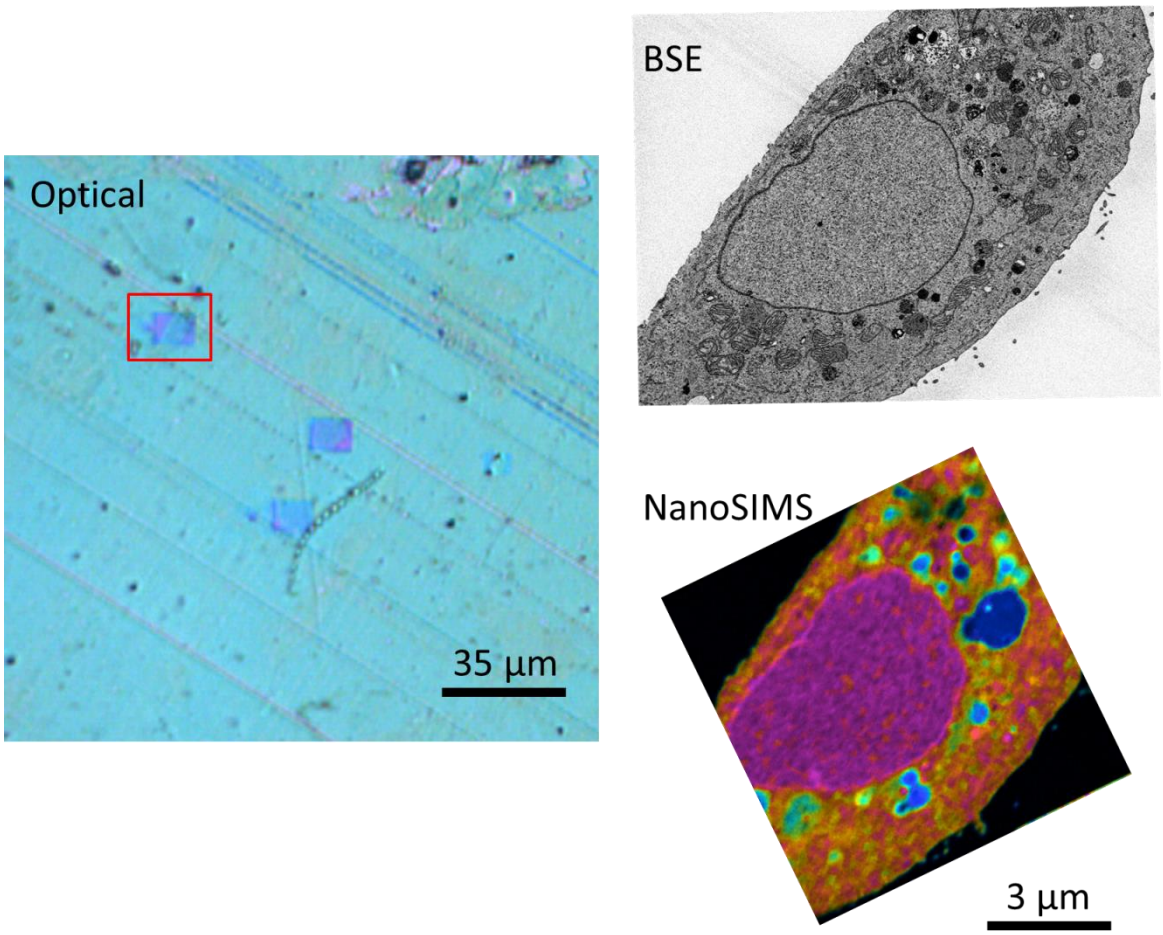

Figure 3.4: Optical image as a navigation maps for correlative electron microscopy and NanoSIMS imaging. The exact cell imaged by BSE and NanoSIMS were identified using the optical image.

3.3 Scanning Electron Microscopy

A JEOL 840A scanning electron microscope was used for low magnification secondary electron imaging, with a voltage of 10 kV and working distance of 15 mm. A dual beam NVision (Carl Zeiss) (Figure 3.5) was used to obtain backscattered electron images at higher magnifications. A low voltage 2 kV electron beam was selected to ensure surface sensitivity and achieve high resolution

backscattered electron imaging without excessive beam spreading. A short working distance of 5 mm was selected for imaging. More details of backscattered electron imaging are discussed in Chapter 4.

Figure 3.5: The Carl Zeiss NVision dual beam microscope I used for high resolution BSE imaging. From reference [138].

3.4 Focused Ion Beam milling

The same dual beam FIB instrument (Figure 3.5) was also used to cut surface of cell samples to expose structures deep under the surface, and create a flat surface for NanoSIMS imaging.

3.5 Atomic Force Microscopy

A ParkAFM atomic force microscope was used to obtain the topography images in this thesis. 35 Series tips from Mikromasch and tapping mode were used for imaging. In the tapping mode, the shear forces between tip and sample were low, and was chosen because shear forces can damage the sample especially when imaging soft materials. NanoSIMS analysis was done after AFM imaging,

which makes it particularly important to avoid damage from the AFM imaging. Figure 3.6 is a typical AFM high resolution image on soft materials, in this case DNA on a flat surface [139].

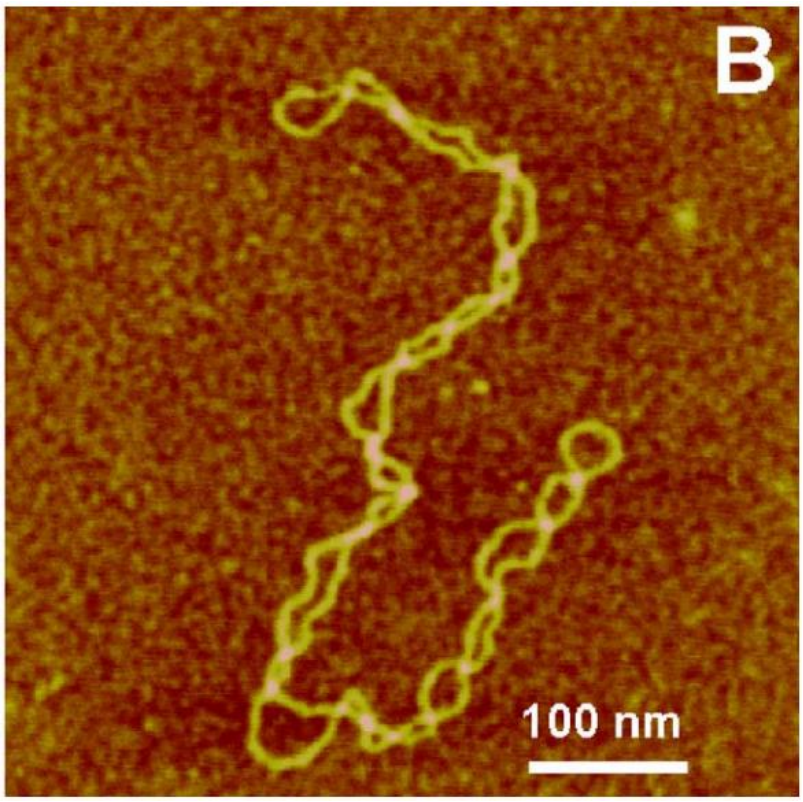

Figure 3.6: High resolution AFM image of DNA taken with tapping mode. From reference [139].

3.6 NanoSIMS

The NanoSIMS 50 (CAMECA) (Figure 3.7) was used to obtain the chemical maps from the sample surface. A detailed description of this instrument and previous applications of the technique to biological materials has been given in Chapter 2. In this thesis, all the experiments were carried out using the Cs^+ primary ion beam, and so negative secondary ions were collected to show chemical distributions and to quantify local variations in stable isotope-labelled molecule incorporation. Substrates were cut to the required size to fit into the Biology sample holder from CAMECA (Figure 3.8). The Biology sample holder can hold 8 samples as shown in Figure 3.8. Coated coverslip substrates, as shown in Figure 3.2 with semi-thin sample sections; a silicon substrate (bottom right)

with molecules on the surface, and a piece of metal standard (bottom middle) as shown in the Biological holder in Figure 3.8. Different samples for quantitative analysis, such as quantification of amino acid metabolism and lipid incorporation, were loaded in the same holder to avoid possible effects coming from sample exchange.

Figure 3.7: Oxford CAMECA NanoSIMS 50.

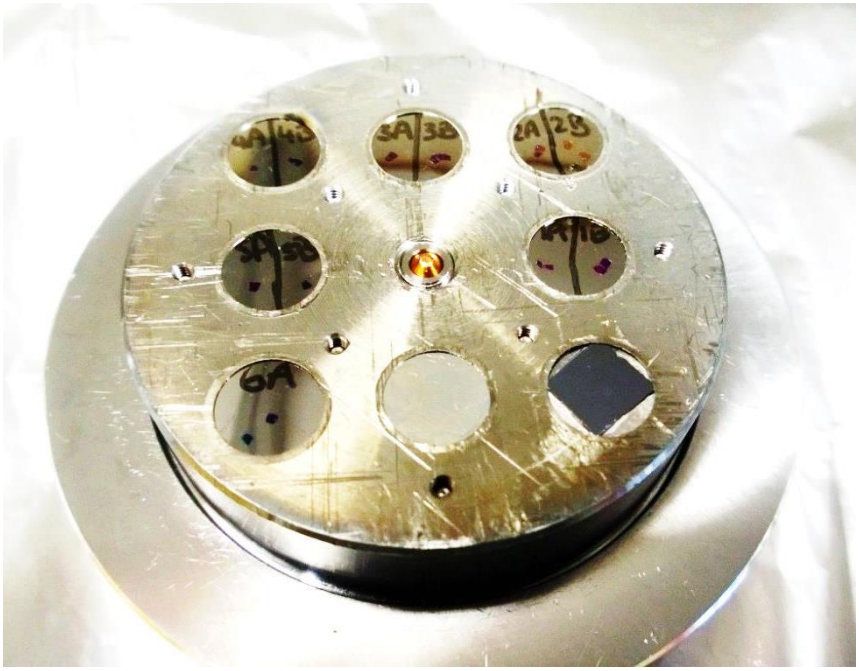

Figure 3.8: Biology sample holder from CAMECA mounted with samples on coverslips and silicon substrates.

3.6.1 Tuning the Instrument

It is very important when using the NanoSIMS that the 5 detectors are precisely tuned to the correct mass for the desired ion. Full tuning of the whole machine was carried out periodically, including the alignment of the secondary ion optics to maximize the secondary ion transmission and mass resolving power. During each experimental session most lens settings remain unchanged from the full tuning, and only a few aperture positions need to be changed to optimise for detection efficiency and to ensure accurate quantification.

At the start of each session, the primary ion beam current was checked with different positions of the D1 aperture (Table 3.1). The Oxford NanoSIMS 50 usually runs with a primary current of 80 – 120 pA with D1=0. The primary ion beam current can be changed depending on the type of samples and purpose of the analysis. If the desired analyte is present at very low concentrations then the highest possible primary current is needed. In order to set up for the detection of the selected ion signals, the magnet was set to a value to enable detector 5 to detect the heaviest ion signal in each experiment, such as ^{31}P or ^{191}Au. The other four detectors were set to approximately the correct position to detect the other interesting ion signals, such as $^{12}C^-$, $^{13}C^-$, $^{12}C^{14}N^-$ and $^{12}C^{15}N^-$. Then precise tuning was carried out by repeating (i) secondary ion beam (SIB) scans to select the highest ion transition efficiencies and (ii) high mass resolution (HMR) scans to select the right signals for detectors 1 – 5. There are several mass interferences in the low mass range, especially from organic samples. For example, mass 13 could be $^{12}C^1H^-$ or $^{13}C^-$ signals, with $^{13}C^-$ being slightly lighter than the $^{12}C^1H^-$. Figure 3.9 shows the selection of the left peak for $^{13}C^-$ detection. Careful selection of the correct signal is very important for NanoSIMS experiments.

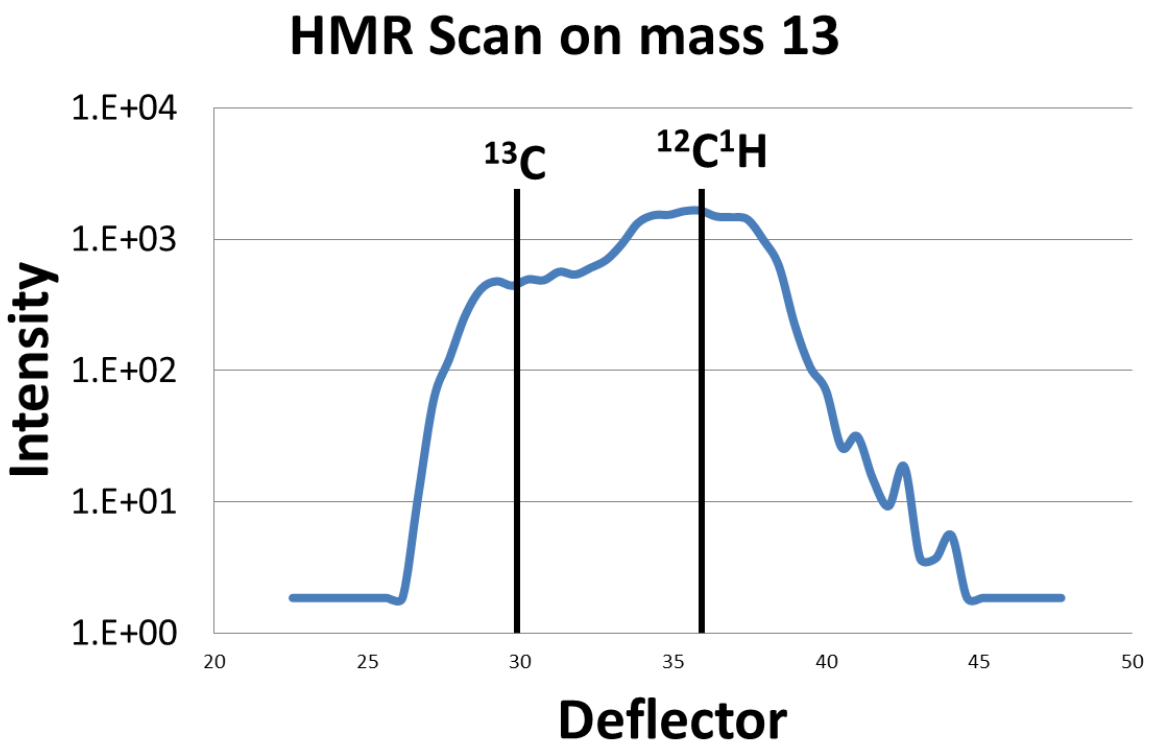

Figure 3.9: HMR scan on mass 13 showing the ability of the NanoSIMS to separate peaks with similar masses.

The EOS lens was fixed to give the highest signal from secondary ions and remains almost unchanged throughout the each session. C4X which centres secondary ions just before the mass spectrometer was also checked for the highest signals for each new sample and remain the same for the rest of the analysis.

Aperture	D1 diameter (µm)	Cs^+ current (pA)	Approximate beam Size/Resolution
D1=0	NA	80 – 120	NA
D1=1	750	9 – 14	120nm – 300 nm
D1=2	300	2 – 3	100 – 120 nm
D1=3	250	0.8 – 1.4	50 nm – 100 nm
D1=4	200	0.3 – 0.7	

Table 3.1: Positions of D1 aperture and corresponding primary ion beam current and beam size.

Setting up the 5 detectors performed either on standard samples or the real samples. Signals which were low on the real samples, such as trace elements, were tuned on standard samples to avoid incorrect tuning, and other stronger signals, such as $^{12}C^-$ and $^{12}C^{14}N^-$ were tuned on the actual samples. Signals on thin samples, such as lipid bilayers, were tuned on one area of the sample before moving to a nearby area to image immediately after the tuning.

Areas of interest can be chosen by using the optical camera installed on the NanoSIMS. This camera is extremely useful to localize the areas for correlative analysis. The Z value was set to focus the optical image, which also sets the optimal separation between the sample surface and the immersion lens assembly for SIMS analysis. After selecting the areas of interest, a high current mode can be selected by changing lens L1. This is useful because it allows the primary ion current to be increased to more than 2 nA for the implantation of Cs^+ to quickly reach the steady state yield of secondary ions for NanoSIMS analysis, as discussed in Chapter 2. HMR and SIB scans were repeated throughout a session to ensure that the NanoSIMS instrument was accurately tuned. The instrument was usually set to create a 256 × 256 pixel image from a selected area with a dwell time of 500 µs – 60,000 µs per pixel depending on the signal intensity and sample types. NanoSIMS analysis on thin samples, such as the lipid bilayer samples in Chapter 4, only required short dwell time since the NanoSIMS can quickly sputter away films of only a few nm thickness. To achieve reliable quantification, such as for the stable isotope labelling experiments discussed in Chapter 5, a longer dwell time or high primary beam current is required to get sufficient counts.

3.7 Data Analysis and Presentation

The OpenMIMS (Harvard) plugin of ImageJ was used for all the NanoSIMS image analysis. The basic function of this plugin is to open the NanoSIMS raw data and allow processing of the images. Images can be processed to show isotope ratio images and hue saturation images (HSIs) to display the variations of the isotope distributions on samples. Figure 3.10 is the colour scale used for all the HSIs in this thesis. Ion and isotope intensities are measured in the OpenMIMS plugin, and then calculated

and analysed by Microsoft Excel. Statistical analysis was done in Prism 5.0 to show the mean, standard deviation, max and min of those data. AFM images were analysed and processed by Gwyddion 2.30. Line scans created with this software can be used to show the topography of the surface.

Figure 3.10: CAMECA colour scale for HSIs.

4 Molecule Analysis – Interactions of Antimicrobial Peptides and Lipid Bilayers

4.1 Introduction

This chapter will discuss the application of NanoSIMS analysis to biological molecule samples with stable isotope labelling. The biological process focused on is the interaction between antimicrobial peptides (AMPs) and lipid bilayers (LBs).

4.1.1 Antimicrobial Peptides and Lipid Bilayers

Between the 1920s and 1950s, many investigators demonstrated the existence of antimicrobial substances in blood, leucocytes and lymphatic tissues [140]. Although some substances were rediscoveries of defined compounds, some of the small tissue polypeptides were unknown [141]. The polypeptides described could combine with negatively charged surface constituents of bacteria or viruses and disrupt cell functions [140]. The field of antimicrobial peptides was born at that time. It was Hans Boman who isolated purified AMPs from insects in 1981 [142]. Based on observing the lack of lymphocytes and antibodies in insects, he also pointed out that the innate immune system should have the capability to kill microbes rapidly for a species to live in microbe-rich environments [143]. According to Boman's view, the adaptive immune system in the human body is too slow compared with the growth rate of microbes, so adding AMPs to the innate immune system might be critical for human treatments. Shortly after Boman's discovery, AMPs were isolated and purified from amphibian and mammalian animals by Michael Zasloff [144] and Robert Lehrer [145] respectively.

There is a large diversity of AMPs in nature. As Boman's hypothesis states, such a large number of types of AMPs are due to an adaptive response to the various species of microbes existing in the environment [143]. AMPs possess not only antibacterial, antifungal and antivirus properties, but also antitumor effects and can stimulate cell proliferation amongst other properties. The discovery of

AMPs opened up great opportunities for new therapeutic strategies. After a few decades of development, a routine and relatively low cost process for synthesizing AMPs has been developed [143]. There are already some potential therapies under discussion. For example, human LL-37 has the potential to prevent lung infection [146], and AMPs also show great potential in skin diseases, such as wound repair and leprosy [147].

During the 1890s the first insights into the chemical nature of the outer boundary layer of cells were discovered by Ernst Overton, and now the structure of lipid bilayers is widely known [148]. The reason that AMPs can have strong effects on the immune system is that they can disrupt microbial phospholipid membranes by the creation of pores through the membrane which leads to cell death [141]. There have been several molecular models proposed for this interaction mechanism [141] (Figure 4.1) , such as the formation of (a) barrel-stave pores: peptides insert into the lipid bilayer with hydrophobic regions aligning with lipid core regions and hydrophilic regions aligned in the interior region of pores; (b) carpet models: peptides aligned as an extensive layer on the lipid bilayer with hydrophobic regions parallel to the lipids; and (c) toroidal pores: peptides induce lipid monolayer bending and pores with both peptides and lipid head groups in the interior regions of pores .

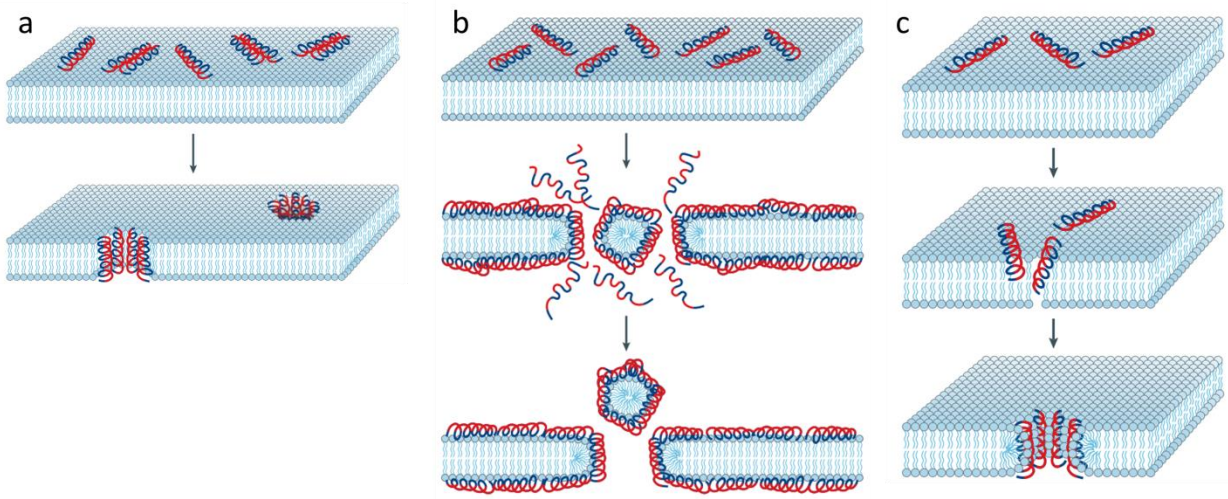

Figure 4.1: Modals proposed for the interation between AMPs and lipid bilayers: (a) barrel-stave pores; (b) torroidal pores; and (c) carpet models. From reference [141].

However, direct observation of these fundamental processes has not been obtained, and which is critical for a thorough understanding of the interaction mechanism. The most important reason for the lack of direct evidence is the complexity of the living cell membrane. Membrane binding of AMPs is kinetically driven and, in live cells, occurs over timescales of microseconds to minutes [149, 150]. Pores need not expand substantially because cell death can occur concomitantly as a result of membrane leakage and swelling under osmotic pressure and because AMPs can reach and bind to intracellular targets or disrupt processes that are crucial to cell viability (protein, DNA or cell wall syntheses) on the same timescales [149, 150]. Furthermore, microbial membranes are curved 3D architectures whose diameters do not exceed 2 μm. Pore formation in these membranes can cause significant variations in membrane tension, which can lead to "premature" membrane rupture before individual pores can expand substantially. Visualizing expansion in live cells depends on these interrelated factors, which makes direct observations problematic. By contrast, longer time and length scale studies are possible in supported lipid bilayers (SLBs) [151].

4.1.2 Supported Lipid Bilayer

As stated above, SLBs can provide ideal experiment models for fluid-phase membranes as they provide controllable analogues for membrane structures that are stable over the timescales needed for imaging work to gain direct evidence for mechanisms of interation with hostile molecules. They have been used for many interesting studies in the last two decades [152]. Figure 4.2 is an example of using SLBs (dioleoylphosphatidylcholine/dipalmitoylphosphatidylcholine) to study the functions of natural cyclic surfactin [153], and shows clearly the topography change of the SLBs incubated with SNC14 with time. Longo and his colleagues have extensively used SLBs to study the lipid separation and structures of lipid domains [154-156]. Importantly for my work, the SLBs provide a flat surface which can be easily imaged by Atomic Force Microscopy (AFM) [151] and the NanoSIMS [72, 103, 112], and this makes it possible to gain both chemical and structural information from the same sample surface. This chapter demonstrates the application of correlative AFM and NanoSIMS analysis to imaging the interaction between stable isotope labelled AMPs and lipid bilayers.

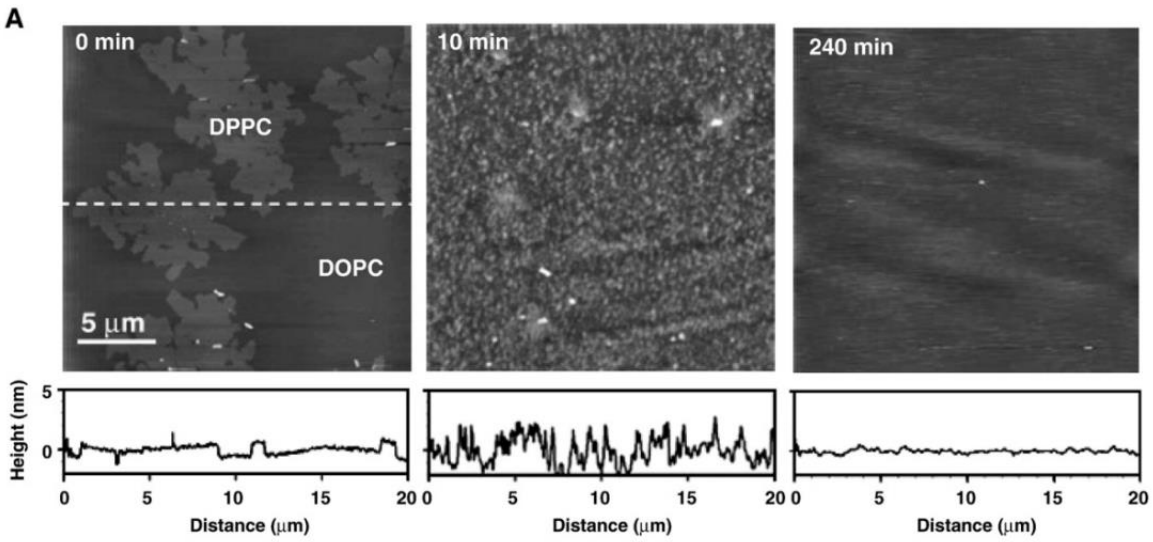

Figure 4.2: An application example of using SLBs to study functions of surfactants. From reference [153].

4.1.3 Correlative AFM and NanoSIMS analysis

The ability of the NanoSIMS to detect isotopic distributions has been discussed in Chapter 2. This ability has enabled some studies on molecule imaging [112]. Audinot et al. [157] from Luxembourg University, for example, used the technique to image single DNA molecules with ^{13}C and ^{15}N labels (Figure 4.3). The combination of high sensitivity and resolution enables single DNA strands to be clearly shown in the images. On the other hand, the development of modern AFM instruments makes it a popular technique in bionanotechnology, and it has been used for (1) mechanical property measurement on biological materials [158]; and (2) high resolution and high speed imaging on individual molecules [159] etc. Imaging individual molecules is getting easier and easier (Figure 4.4).

Most of the biological problems are so complicated that they need more than just structural information or only chemical information to reveal the key mechanisms that are operating. The samples for AFM and NanoSIMS analysis are perfectly matched, since imaging single molecules on flat surfaces or on thin films is relatively simple. SLB samples can be analysed by both AFM and

NanoSIMS in the same area, and this advantage has also enabled a few discoveries in the last decade [103, 160]. For instance, Kraft et al. made full use of correlative analysis and conducted a series of studies based on the two techniques (Figure 4.5) [72, 112, 133].

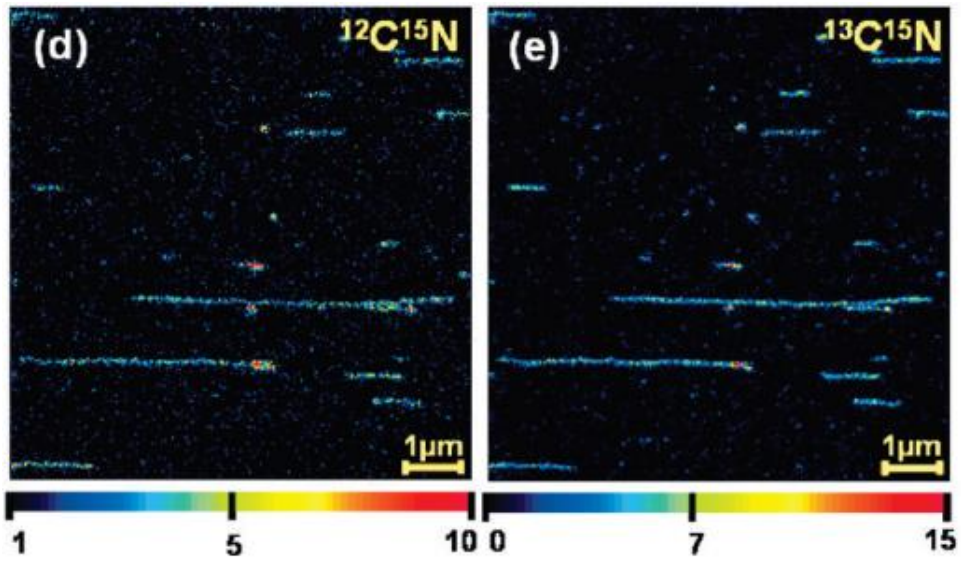

Figure 4.3: ^{13}C and ^{15}N labelled DNA strands imaging with the NanoSIMS [157].

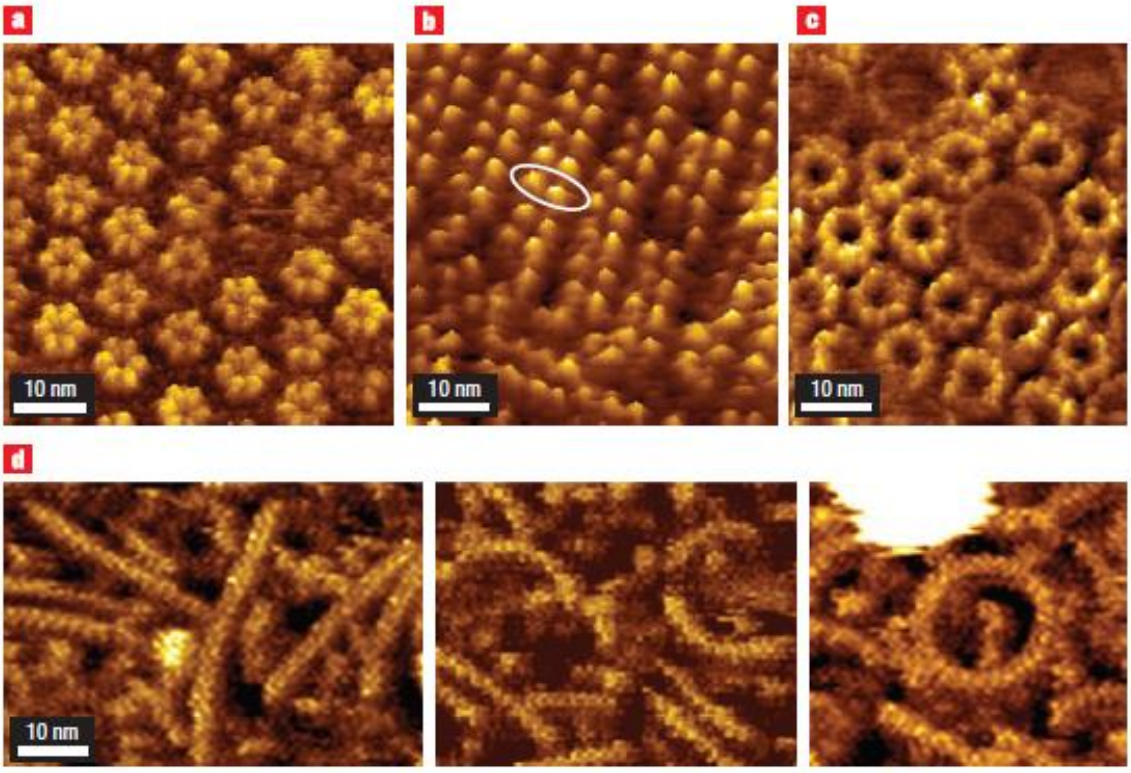

Figure 4.4: Individual molecule imaging with AFM. (a) hexameric pores formed by human communication channels; (b) Rows and dimers formed by bovin rhodopsin; (c) assembly of light harvesting complexes; and (d) Rings formed by the anti-cancer drug taxol. From references:[159].

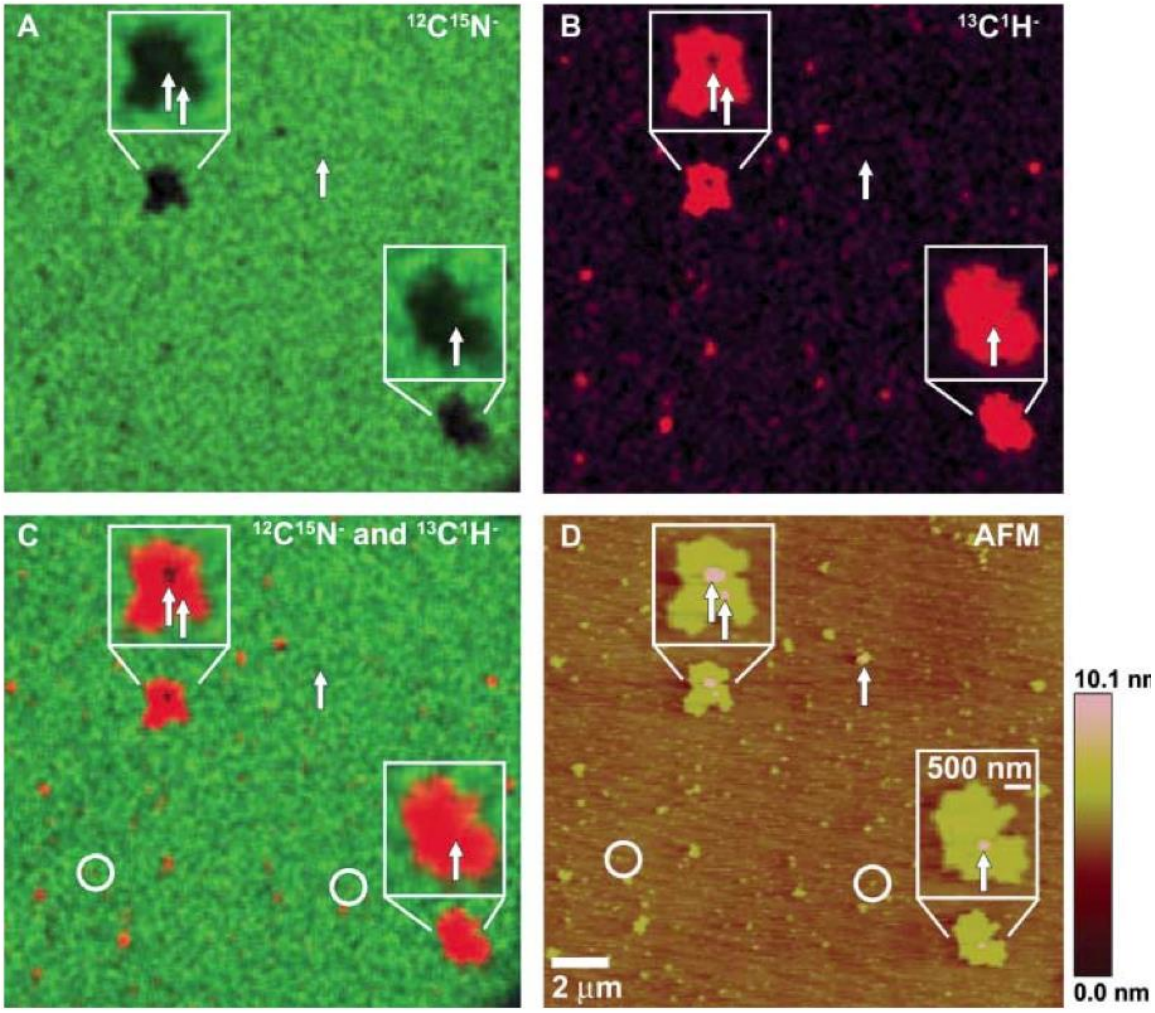

Figure 4.5: Correlative analysis on lipid phase separation by AFM and the NanoSIMS with ^{13}C and ^{15}N-labelled lipids. From reference [72].

4.1.4 Aim of the Project

Collaborating with Dr. Maxim Ryadnov, Paulina Rakowska, and Dr. Santanu Ray at the National Physical Laboratory, I have studied the mechanism of interaction between AMPs and lipid bilayers with correlative AFM and NanoSIMS analysis. Modifying the AMP molecules only by stable isotope labelling, we can be sure that they behave the same as natural molecules, and the structural and chemical information can reveal the mechanism of the interaction with a SLB experimental model for a membrane.

4.2 Materials and Methods

4.2.1 Peptide Design

This part of work is done by the team at the National Physical Laboratory led by Dr. Max Ryadnov. Experiments using amhelin were designed, synthesized, and characterized according to protocols published by my collaborators [161].

4.2.2 Supported Lipid Bilayer Preparation

The lipids, 1,2-dilauroylphosphatidylcholine (DLPC) and 1,2-dilauroyl-sn-glycero-3-phospho-(1'-rac-glycerol)(DLPG), 75%/25% (wt/wt) used for liposome construction were from Avanti Polar Lipids. The lipids were weighed, dissolved in chloroform-methanol (2:1, vol/vol), dried under a nitrogen stream, and placed under vacuum overnight. The resulting film was hydrated to 10 mg/mL total lipid concentration in 10 mM phosphate buffer, pH 7.4. The suspension was then extensively vortexed, sonicated (30 °C), and extruded using a hand-held extruder (Avanti Polar Lipids) (fifteen times, polycarbonate filter, 0.05 µm) to give a clear solution containing small unilamellar vesicles (SUVs).

Oxidized silicon substrates (University Wafer) were cut into ~0.72-cm^2 pieces and ozone-cleaned. The SUV solution was poured over the substrate in a culture dish and shaken for 2 h to enable lipid bilayer deposition on the surface. The substrates were then plunged into a dish of water and shaken for 3 min (three times) to remove excess vesicles.

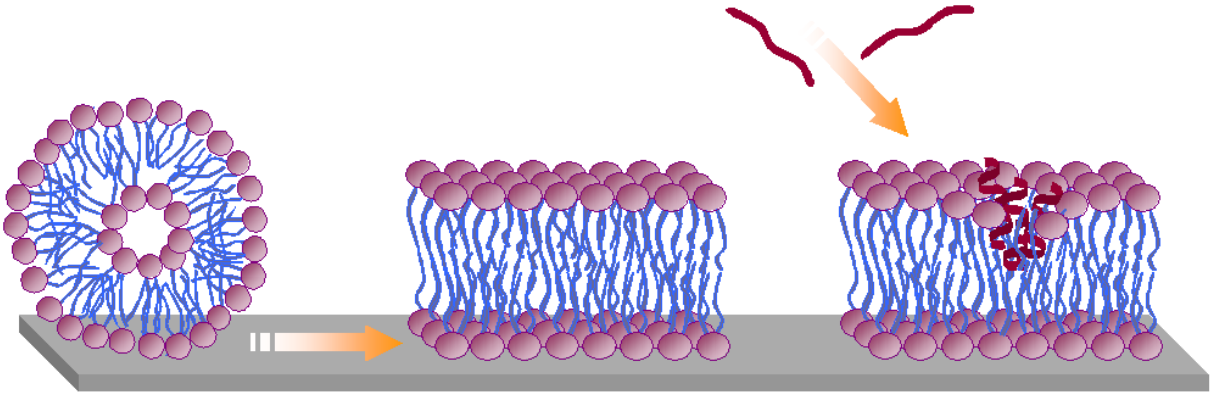

Figure 4.6: Schematic of the SLB preparation and incubation of AMPs. From reference [162].

4.2.3 Treatment

The surface lipid bilayer was then treated with a 10-μM ^{15}N-amhelin (labelled at all alanine and leucine residues and purchased from AnaSpec) solution (10 mL) for 30 min followed by washing to remove peptide excess (this step was omitted for control samples). Another sample was also prepared treated by unlabelled amhelin by the same process. The control sample is SLBs without any AMP treatment (Figure 4.6).

4.2.4 Preparation for Imaging

The substrate was transferred without drying into a 2 mL container filled with water, which was plunged into a chamber with liquid nitrogen to quickly freeze the entire sample. The lid of the container was replaced with a perforated lid, and the sample was freeze-dried. The same procedures were performed on bare SLBs.

4.2.5 Imaging

The SLBs on oxidized silicon substrates provide flat surfaces for AFM and NanoSIMS imaging. Topographic AFM images were recorded using tapping mode AFM on a ParkAFM instrument as described in Chapter 3. Images (5μm by 5μm) were taken on the sample surface, and all AFM images were flattened and processed with Gwyddion 2.30. Imaged regions were located using optical microscopy as a reference for subsequent NanoSIMS imaging (Figure 4.7).

The same areas imaged by AFM were found in the NanoSIMS instrument, and $^{12}C^{14}N^-$ and $^{12}C^{15}N^-$ secondary ions were collected to identify the location of the unlabelled amhelin or ^{15}N-amhelin. Three other signals were also recorded simultaneously to give information on sample morphology: $^{12}C^-$, $^{16}O^-$ and $^{31}P^-$. Ratio images ($^{12}C^{15}N^-/^{12}C^{14}N^-$) (10 by 10 μm, 256 by 256 pixels) were collected with a small primary aperture (D1=4) to match the pixel size in the images with the incident ion beam diameter (~70 nm). All data was collected without preliminary $^{133}Cs^+$ implantation to avoid sputtering away the thin samples, and the dwell time was set to 8,000 μs/pixel to collect only information from the top few nanometres of the sample, as will be explained in section 4.3.2. The

images were processed using the ImageJ plugin, OpenMIMS (MIMS, Harvard University; www.nrims.harvard.edu), and processed with a median filter with one pixel radius. The median filter works by replacing signal intensity in each pixel by the median of neighbouring pixels, and it is a widely used process for reducing the noise in images [163].

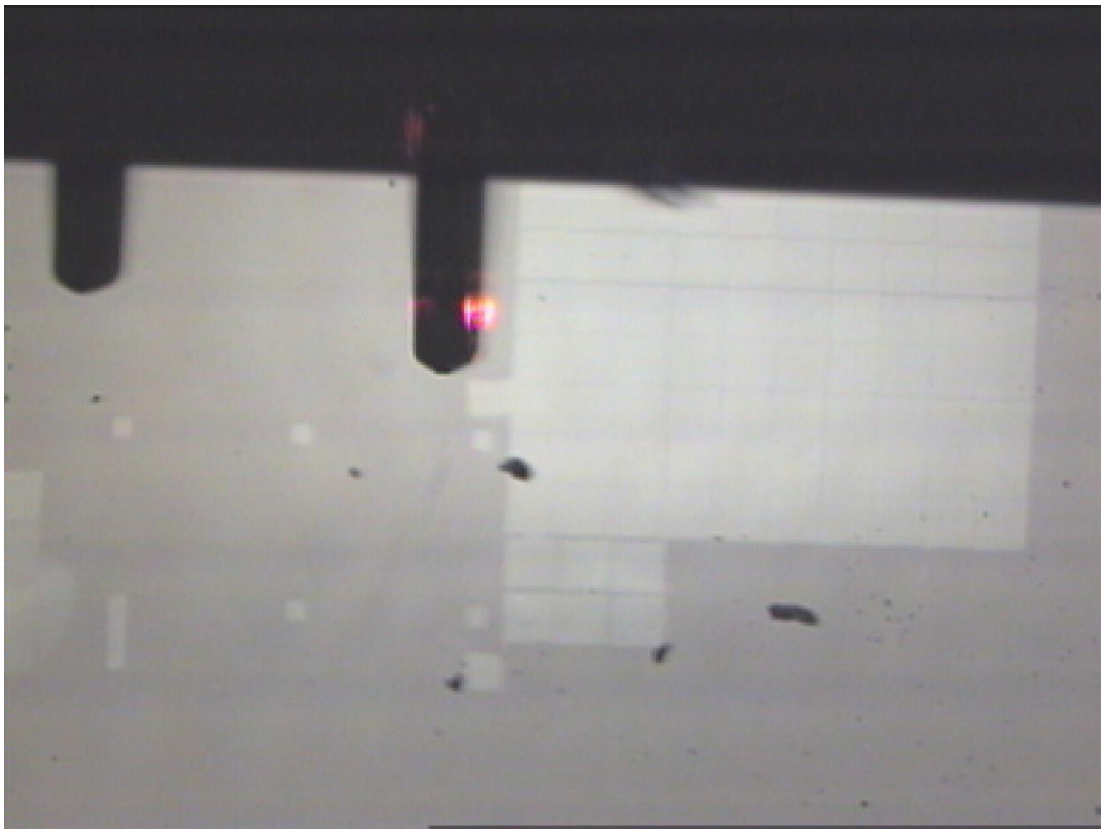

Figure 4.7: Optical image during AFM imaging. Bright squares are NanoSIMS analysed areas.

4.2.6 Intact Bacterial Cells

To observe amhelin action on bacterial cells, the results of some preliminary experiments on intact E. Coli are also included in this chapter. E. Coli were deposited on the oxidized silicon substrates and treated with ^{15}N-amhelin for 5 min. The substrates were plunged into a dish of water and shaken for 3 min (three times) to remove excess amhelin. The samples were then air-dried and coated by 2 nm Pt for SEM and NanoSIMS imaging. An NVision dual beam FIB instrument was used to conduct SEM imaging. $^{12}C^{14}N^-$ and $^{12}C^{15}N^-$ secondary ions were collected to identify the location of ^{15}N-amhelin in the NanoSIMS.

4.3 Results and Discussions

This section discusses the experiments involved to visualize the interaction between AMPs and lipid bilayers, including NanoSIMS setup, imaging strategy and experiments on negative control, positive control and real samples.

4.3.1 NanoSIMS Basics

The $^{12}C^-$, $^{16}O^-$, $^{12}C^{14}N^-$, $^{12}C^{15}N^-$, and $^{31}P^-$ signals were collected during the NanoSIMS imaging. Signals all required careful tuning to avoid isobaric mass interferences. Figure 4.8 shows typical HMR scans from an amhelin-treated SLBs sample. The peaks are not flat due to the low signals from the thin film sample. The peak of $^{12}C^{15}N^-$ can be seen clearly separated from the $^{13}C^{14}N^-$ peak, which enables us to tune the signal to detect the distribution of ^{15}N-amhelin. There is no mass interference for the $^{12}C^-$ signal.

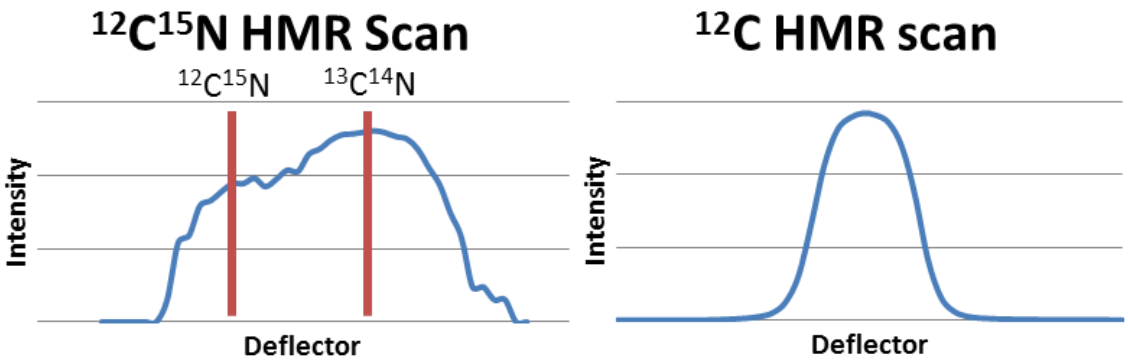

Figure 4.8: HMR scans on the ^{15}N-amhelin treated SLBs sample.

4.3.2 Thin Sample Imaging Strategy

The flat surface of the SLB samples is ideal for both AFM and NanoSIMS imaging. Figure 4.9 is a schematic of correlative AFM and NanoSIMS analysis. The AFM can measure the topography and phase information from the sample surface (light green), then the NanoSIMS can be used to gain chemical information from the blue volume of the sample, which is only a few nanometres thick. We can control the imaging protocol to make sure the NanoSIMS is only imaging the sample. In this way, we can get both structural information and chemical information from this type of thin sample on a

flat substrate. An important part of the experimental design is selecting the counting parameters to use to give the most accurate chemical information in the NanoSIMS without removing the thin sample altogether.

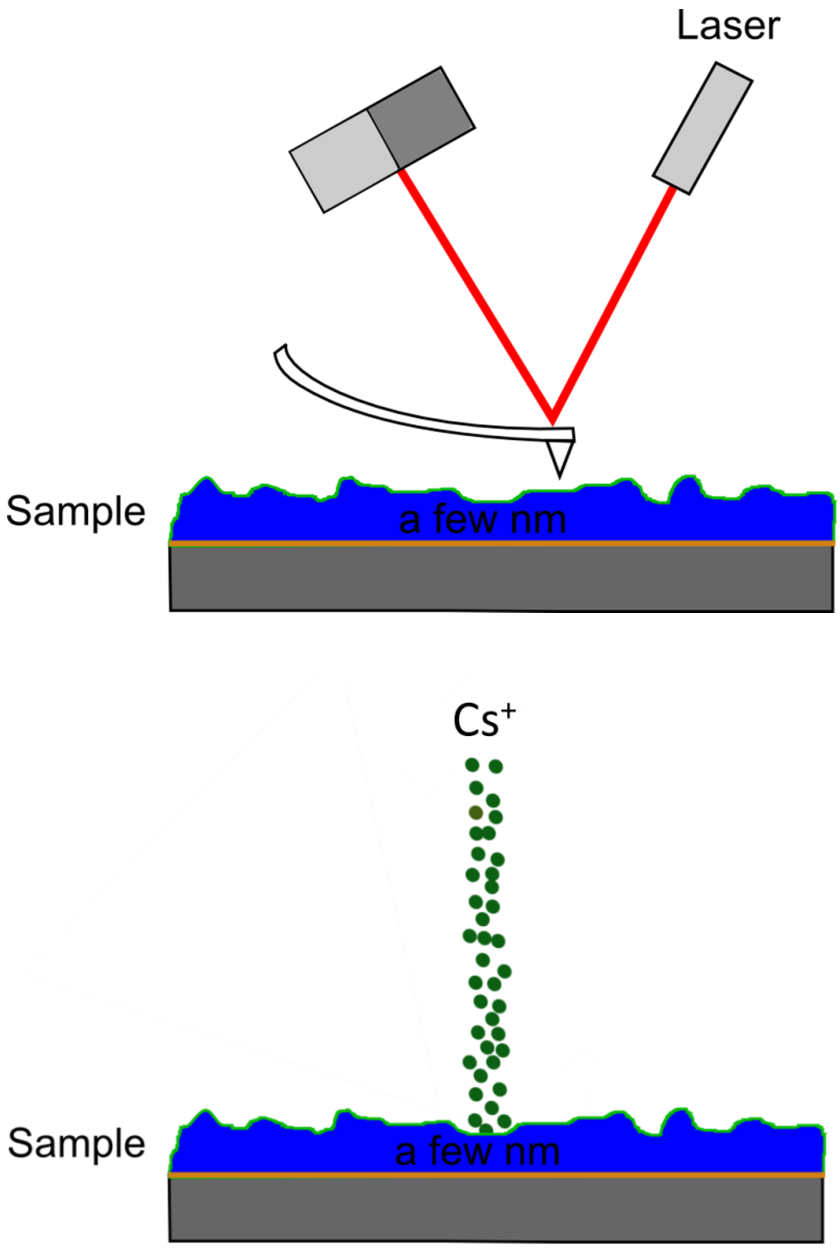

Figure 4.9: Schematic of correlative AFM (top) and NanoSIMS (bottom) imaging on thin samples. Graphs are not to scale.

A typical optical image from a sample imaged by both AFM and NanoSIMS is shown in Figure 4.10. The NanoSIMS imaging leaves obvious marks on the sample surface due to sputtering by the primary

ion beam. The patterned bright squares are from 'chained analysis' from the NanoSIMS, which make good marks for correlative AFM and NanoSIMS analysis.

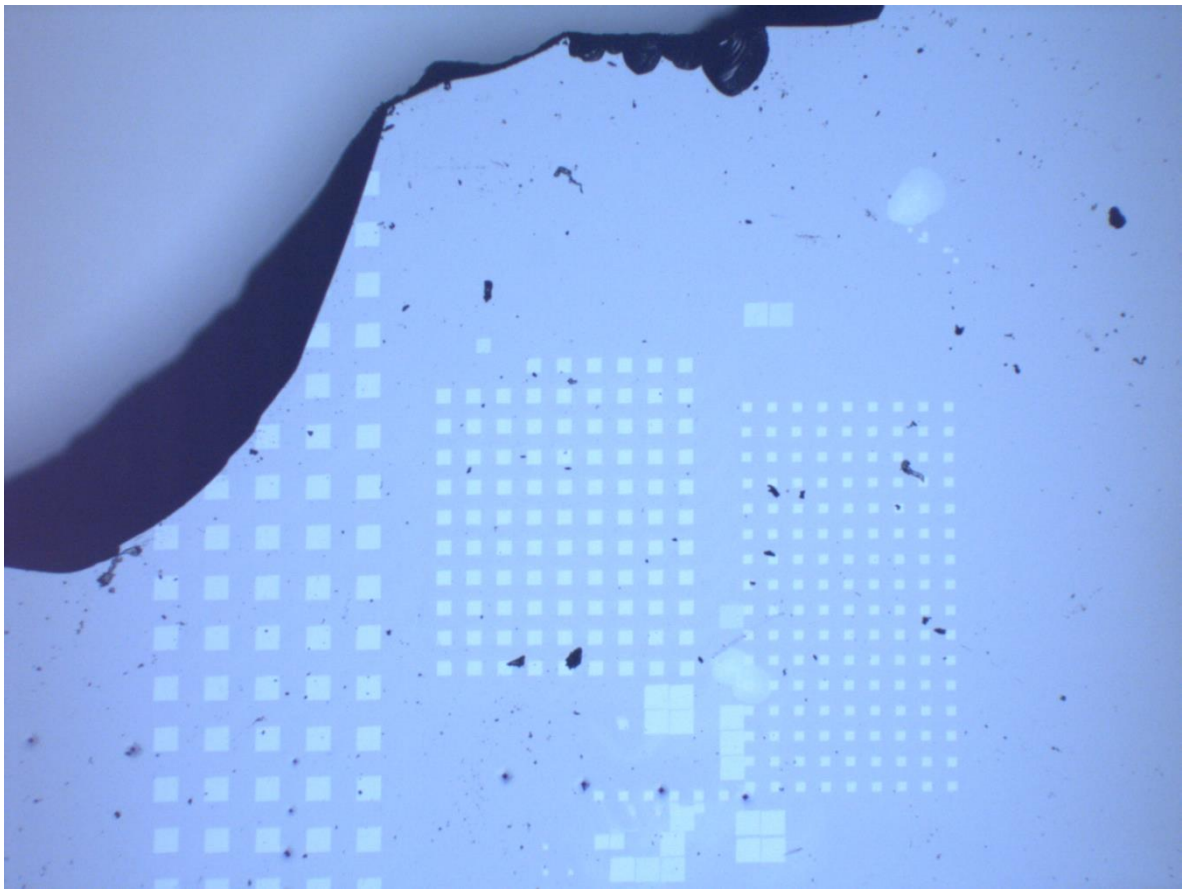

Figure 4.10: Optical image of the NanoSIMS imaged areas on the sample surface.

As a destructive instrument, the NanoSIMS signals are generated from sputtering of material from the surface. The thickness of SLBs is only a few nanometres, which means the NanoSIMS can remove the entire sample quickly, and there is no chance to implant enough Cs^+ to reach steady state for the selected signals, see section 2.2.1. Figure 4.11 shows the disappearance of the $^{12}C^{14}N^-$ signal over 10 frames of imaging, a total of 10,000 µs/pixel. To ensure the imaging volume is from the SLB samples, the NanoSIMS total dwell time was set to 8,000 µs/pixel dwell time with about 0.3 pA primary current resulting in a dose of Cs^+ about 1.0×10^{15} ions/cm^2, either by summing short slices or a single long scan. Unlike other insulating samples, coating with Pt is not necessary for this type of thin film

samples because excess charge is removed by the Si substrate. Figure 4.11 contains images starting on the SLB surface right after tuning in a nearby area.

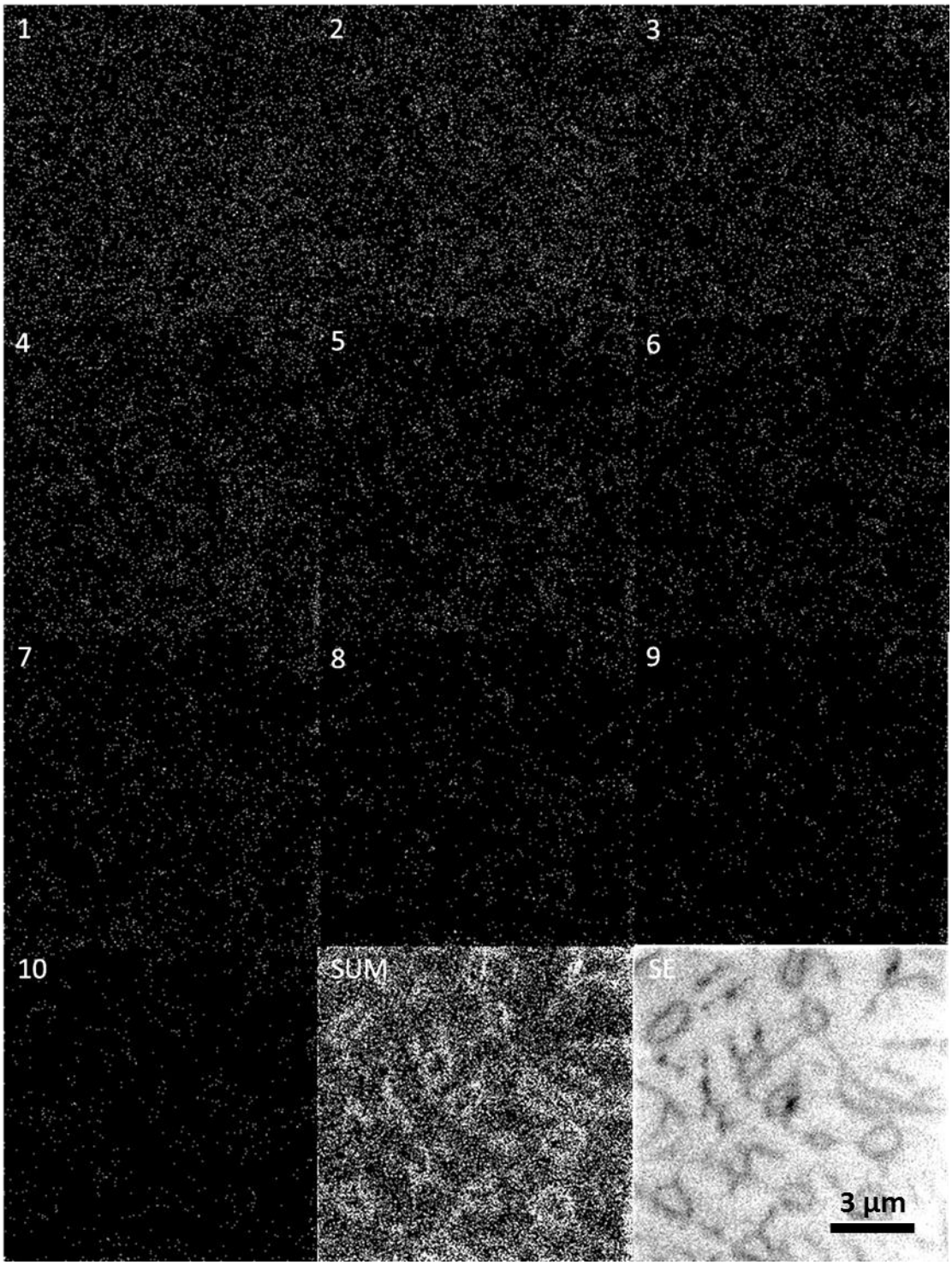

Figure 4.11: Thin sample NanoSIMS imaging: a series of NanoSIMS images on the same area using the $^{12}C^{14}N^-$ signal and 1,000 µs/ pixel dwell time in a 256 pixel by 256 pixel image. The signal almost disappears after 10 frames of imaging. The sum of all 10 images is shown in the SUM image in which the $^{12}C^{14}N^-$ distribution and circular structures can now be seen, and correlated to structures in the SE image.

4.3.3 Bare Lipid Imaging

The bare lipid bilayer samples were imaged by AFM. There are no obvious features in a typical AFM image (Figure 4.12), and the height is quite homogenous across the sample. The synthesized lipid bilayers were also imaged with the NanoSIMS (Figure 4.13), collecting both $^{12}C^{15}N^-$ and $^{12}C^{14}N^-$ signals from each area. Figure 4.13 are images on different areas of the sample surface. The average $^{15}N/^{14}N$ ratio measured from images is about 0.37%, which is close to the natural abundance, and was set as the background value for the natural $^{15}N/^{14}N$ ratio for these experiments. As expected, the $^{12}C^{15}N^-$ signals and $^{12}C^{14}N^-$ signals are homogenous over the surface because the lipid bilayer is uniform and smooth.

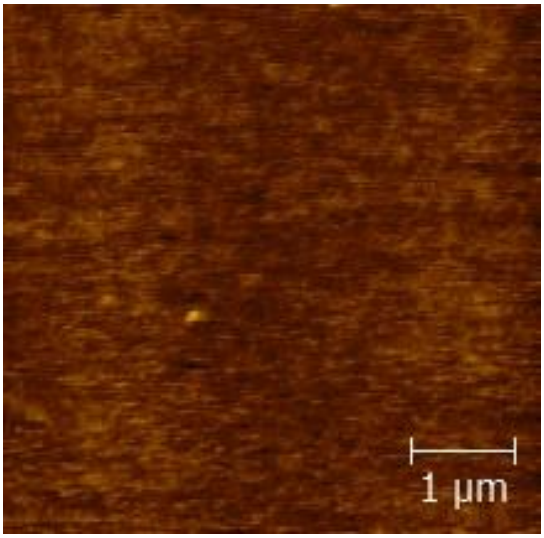

Figure 4.12: AFM image of bare lipid bilayer sample. Height scale: 0 - 3 nm.

4.3.4 Unlabelled Amhelin Treated SLBs

In a typical AFM image of an amhelin-treated SLBs sample, Figure 4.14, we have seen a very detailed structure due to the interaction between the amhelin and the SLB. We can see circular structures on the sample surface with various diameters from tens of nanometres to 1 µm. There are also some 'filament-like' structures (arrowed) running across the surface connecting the large structures. A line scan cross the AFM image (Figure 4.14) shows the height of the structures is 3 nm above the surface of the SLBs. This was the first image obtained showing the structures formed by the interaction of amhelin with the SLBs.

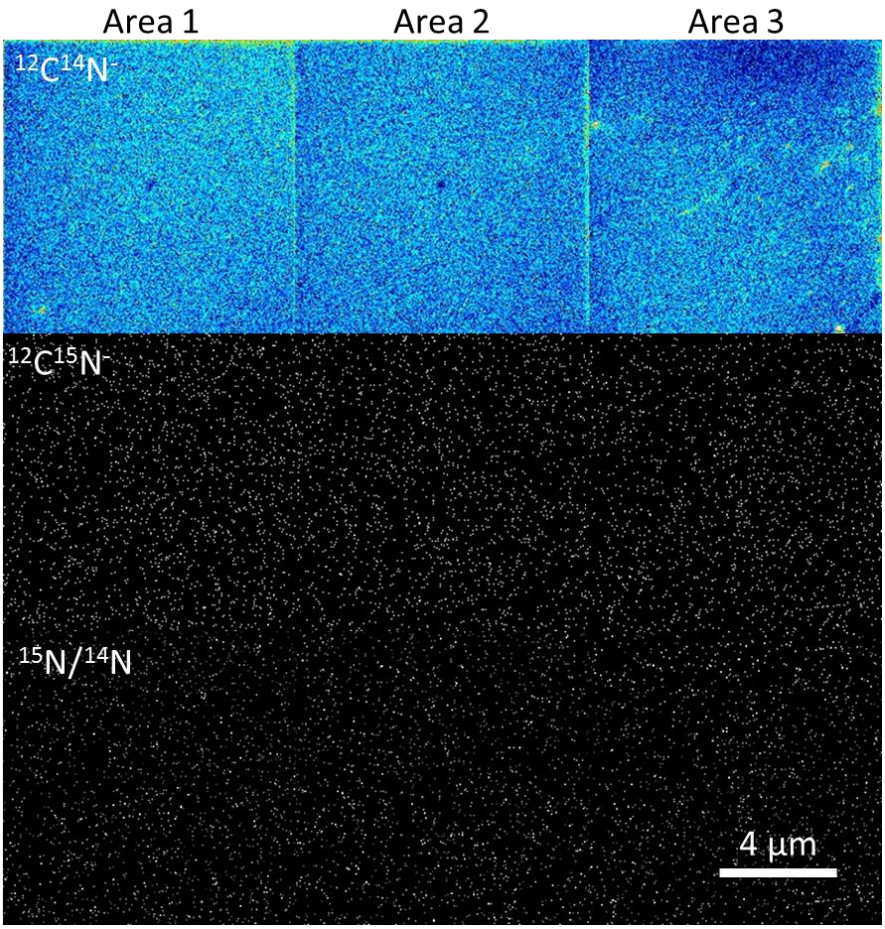

Figure 4.13: NanoSIMS images of bare lipid bilayer samples imaged as a control. $^{12}C^{14}N^-$ and $^{12}C^{15}N^-$ images were obtained and the ratios were calculated.

Figure 4.15 gives typical $^{12}C^{14}N^-$ images from the NanoSIMS of an amhelin-treated sample. These same structures are visible over large areas of the sample surface, and have been mapped over a continuous 140 × 60 µm^2 area, and 8400 µm^2 in total. We are able to see the similar structures to those in the AFM images, which suggests that these characteristic features can yield higher $^{12}C^{14}N^-$ signals than other parts of the sample. The size of the structures varies from below 100 nm to a few micrometres. Comparing the concentration of nitrogen atoms in the synthesized lipid bilayers and amhelin, there is only one nitrogen atom per molecule in DLPC, and every amino acid residue has at least one N atom in amhelin. It is thus likely the high $^{12}C^{14}N^-$ signals in these images originate from amhelin. A line scan through the lower image (red line) shows that the $^{12}C^{14}N^-$ signal from the circular and 'filament-like' structures is about 10 counts, and the background, possibly from SLBs, is only about 2 counts.

However, due to potential artefacts in the signals in the NanoSIMS, including topography, matrix effects etc. as discussed in section 2.2.2, we cannot be sure that the structures we see in the $^{12}C^{14}N^-$ images are formed by local variations in the concentration of amhelin. This needs stable isotope labels to confirm the suggestion that we are imaging features formed by AMPs on the lipid bilayer.

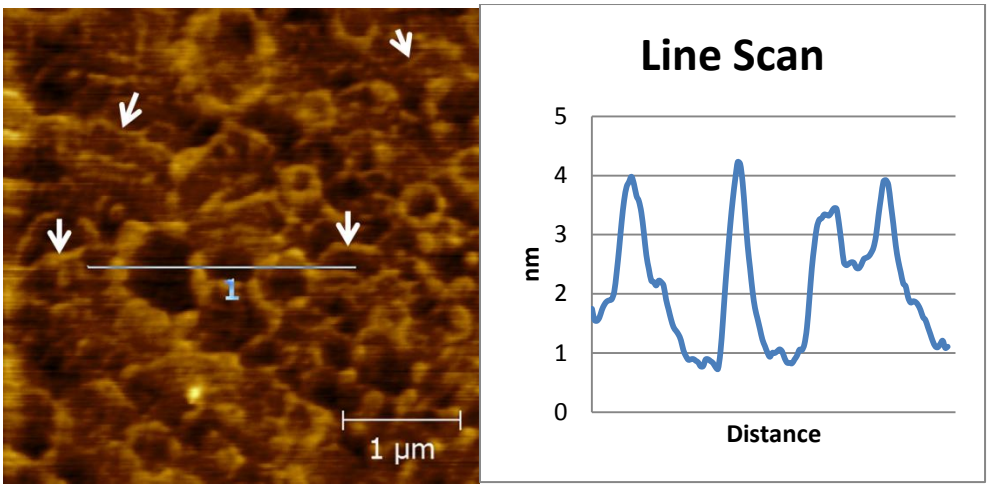

Figure 4.14: AFM image and line scan of amhelin treated SLBs sample.

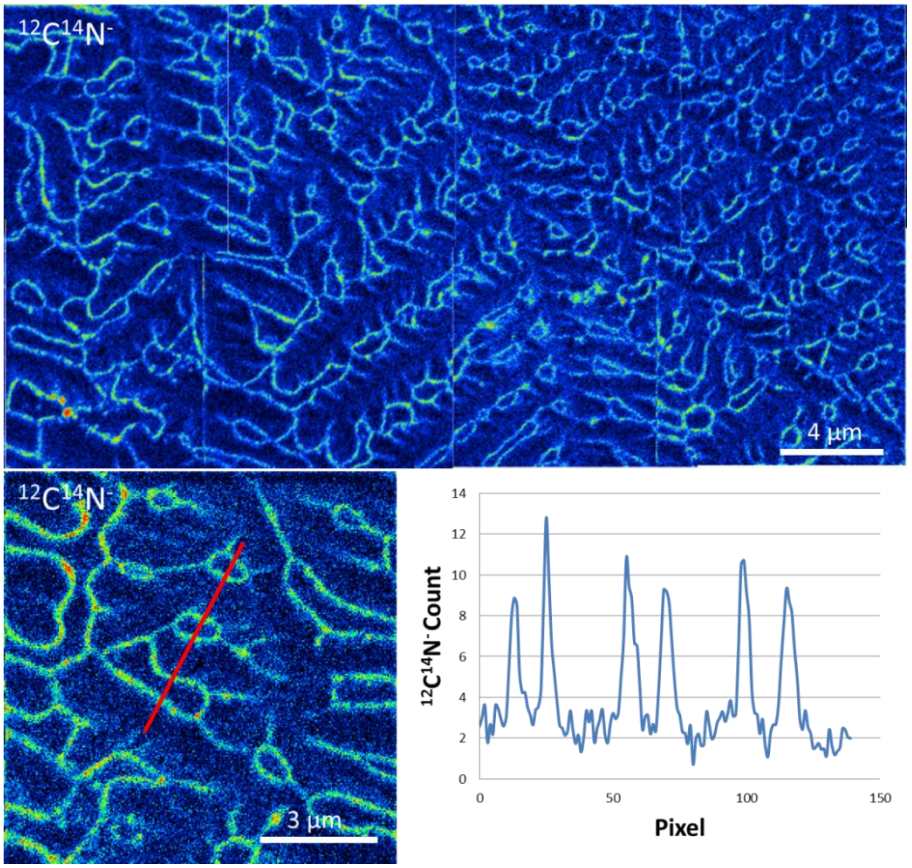

Figure 4.15: NanoSIMS $^{12}C^{14}N^-$ images of amhelin-treated lipid bilayers. Scale: 0 – 20. Line scan across the pore structures identified by red line.

4.3.5 Labelled Amhelin Treated SLBs

In the AFM image of ^{15}N-amhelin treated SLB sample in Figure 4.16 , the structures do not look exactly the same as in the unlabelled sample. This might because of variations in the AMP-SLB interaction, and effects from small changes in the environment (temperature, humidity and concentration etc.) during sample processing. However, we can see circular structures with various diameters and also filament-like structures connecting the circular structures, which may be an indication of the dynamics of AMP molecules moving over the sample surface. The line scan (blue) in Figure 4.16 shows about 3 - 4 nm height difference between the flat surface (presumably the SLB) and the edges of the circular structures. As we argued in reference [164], although the heights of the edges were fairly consistent, the depth values of the perforations could not be determined reliably. The holes would appear as deep as ∼2 nm with respect to the surrounding surfaces, but an explicit crosssection analysis was hampered by high noise levels from the surfaces in the 1- to 2-nm range. The peaking itself may become negligible under equilibrium conditions at which the outer leaflet lipids detach irreversibly, and too fast to be observed without deliberately arresting the system by freezing. An insight into this scenario can be obtained only in solution, which has been done by my collaborator with time-lapse AFM in water [164]. The result shows pores started forming after the first 10 min incubation of amhelin, and continued to grow in size and number over a period of 2h. The lipids are likely to dissolve in the form of micelles, possibly including peptides. On removal of larger amounts of the SLB, material increasingly precipitates on the surface. It also shows that the pores appeared as expanding holes, suggesting the displacement of outer lipids from the surface into the water, which is characteristic of equilibrated systems [165]. The depths of perforations reached ∼2.7 nm, consistent with the amhelin spanning the bound hydrophobic core of the bilayer [164].

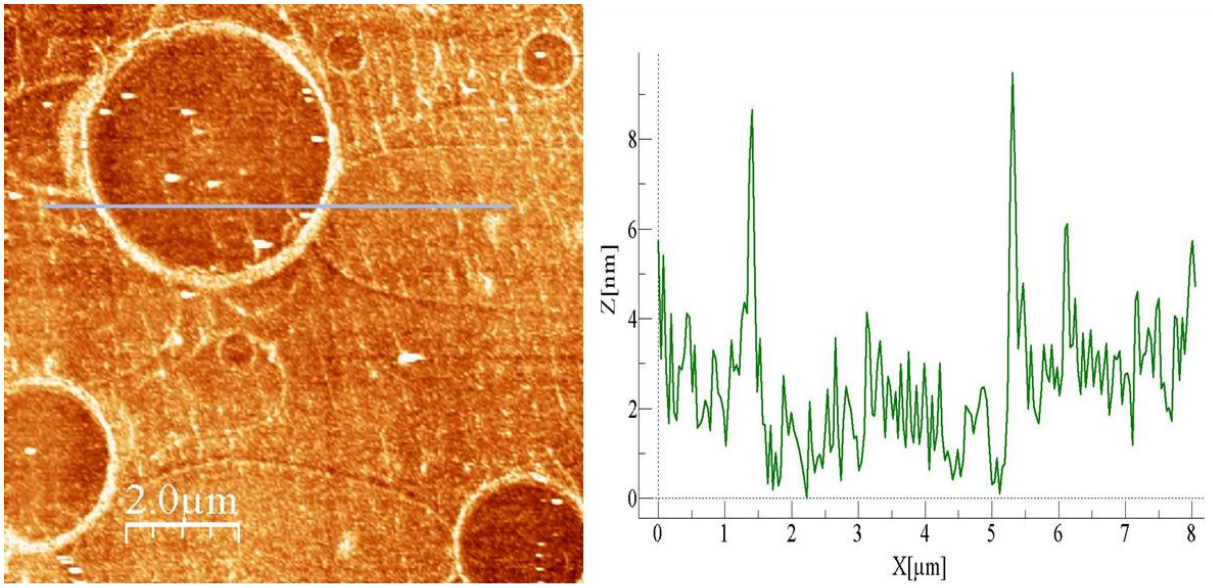

Figure 4.16: AFM and line scan of a selected area (7 µm by 7µm) from the ^{15}N-amhelin treated SLB sample.

NanoSIMS imaging was conducted on the same sample. The $^{15}N/^{14}N$ image in Figure 4.17 shows a distinctive distribution of ^{15}N in and outside the circular structures. It is obvious that there is no ^{15}N-amhelin inside the structures since we only measure the natural abundance of ^{15}N there. The surface outside the circular structures seems to be covered by ^{15}N-amhelin. In some circles, we can see an obvious high ratio of $^{15}N/^{14}N$ at the edge of the holes, about 0.2 (20%), much higher than the $^{15}N/^{14}N$ ratio inside the pores. These structures are visible over large areas of this sample surface, and total areas about 15,000 µm^2 were imaged showing similar features. In total, 126 pores have been imaged with the NanoSIMS with diameters ranging from 700 nm to 8.3 µm (average diameter 2.76 µm ± 1.3 µm), and the distribution of sizes of the holes is shown in Figure 4.17.

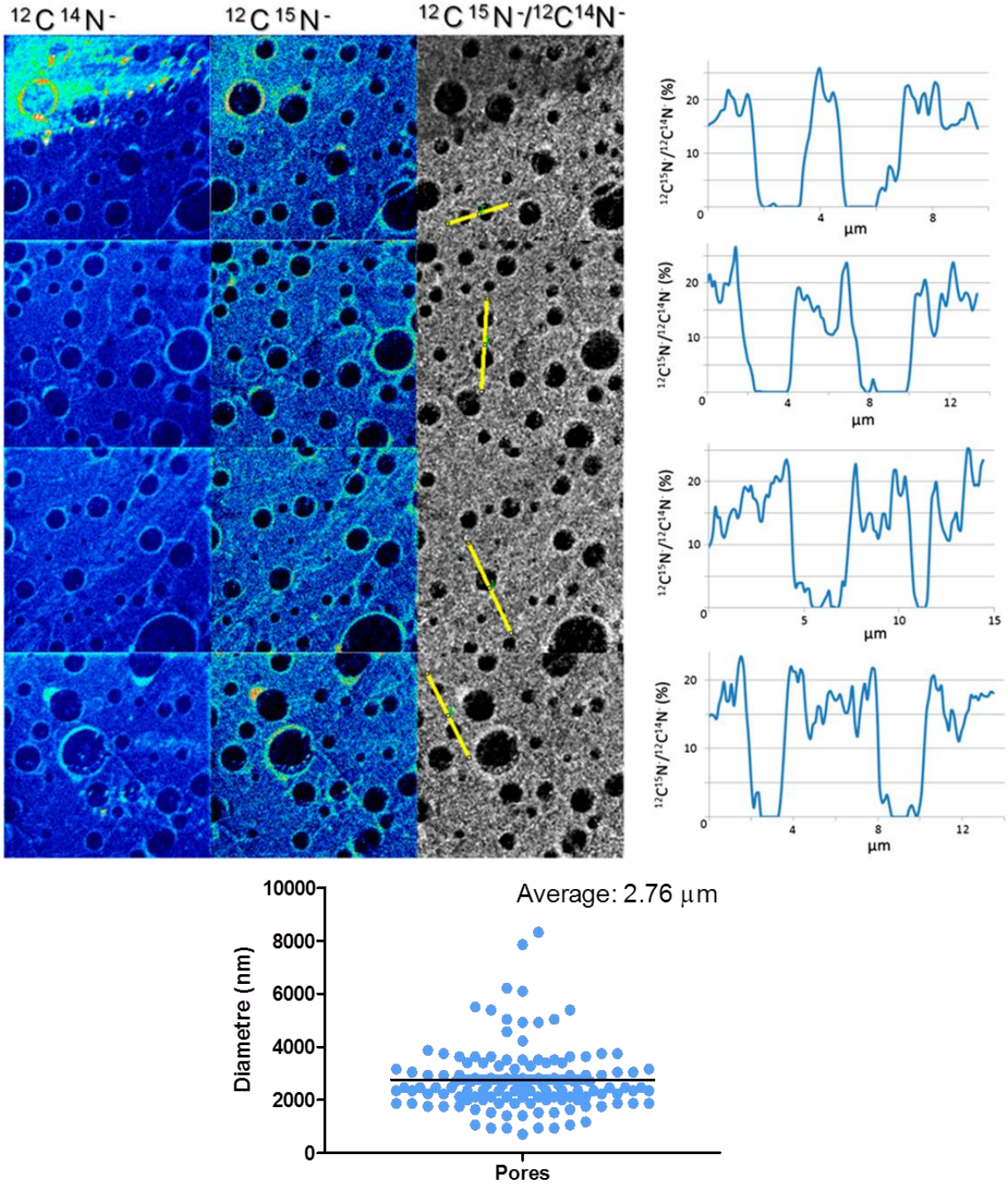

Figure 4.17: NanoSIMS $^{15}N/^{14}N$ ratio images, line scans and analysis of the diameters of the circular structures formed by ^{15}N-amhelin. Size of images: 30 µm × 30 µm.

The NanoSIMS and AFM imaging have been conducted on the same areas of this sample, Figure 4.18. This area of about 10 µm by 25 µm shows 9 pore features. The surface is covered by less ^{15}N-amhelin than in the previous images since the $^{15}N/^{14}N$ ratio line scan shows low ratios both inside and outside the pore, with a 0.2 (20%) $^{15}N/^{14}N$ ratio at the edge. Features running across the surface and

connecting the individual pores again can be seen in both AFM and NanoSIMS images, which we interpret as accumulations of peptide molecules and may again be evidence for migration of the peptides across the SLB surface. Overlapping AFM and NanoSIMS images were produced by Photoshop (Figure 4.19). This way of presenting results can provide a direct view of both chemical and structural information, and convincingly demonstrates that I have been able to image exactly the same features by both techniques. The surface outside the pores is covered by ^{15}N-amhelin in this area. This data from both AFM and NanoSIMS provides strong evidence that the pores in the SLB are formed by amhelin.

Real time changes in the pore formed in SLBs incubated with amhelin have also been imaged by my collaborator with time-lapse AFM in water [164]. The results show small pores started to form after 10 min incubation which continue to grow in size and number over a period of 2 h, culminating in the total removal of the lipid from the mica surface. Collectively our findings provide evidence for pore expansion, or an E-state, of amphipathic antimicrobial peptides interacting with lipid bilayers (Figure 4.20). The E-state promotes cooperative peptide migration through the lipid matrix and can persist to complete membrane disintegration. Our proposed model of pore expansion is the synergistic interplay of two physical processes. In the first, peptide adsorption induces surface tension changes on membrane surfaces, which, when sufficiently large, lead to poration. The pore formation promotes peptide migration from the surface to the edges of the pores, and the NanoSIMS images have been very important in confirming the concentrations of labelled AMPs at these locations. This variation of surface tension with composition (Gibbs surface excess) is driven by amphipathic peptides having a higher affinity for the membrane edges [166, 167]. The process is likely to reduce the surface tension between peptide and lipid bilayers, thereby stabilizing the pores.

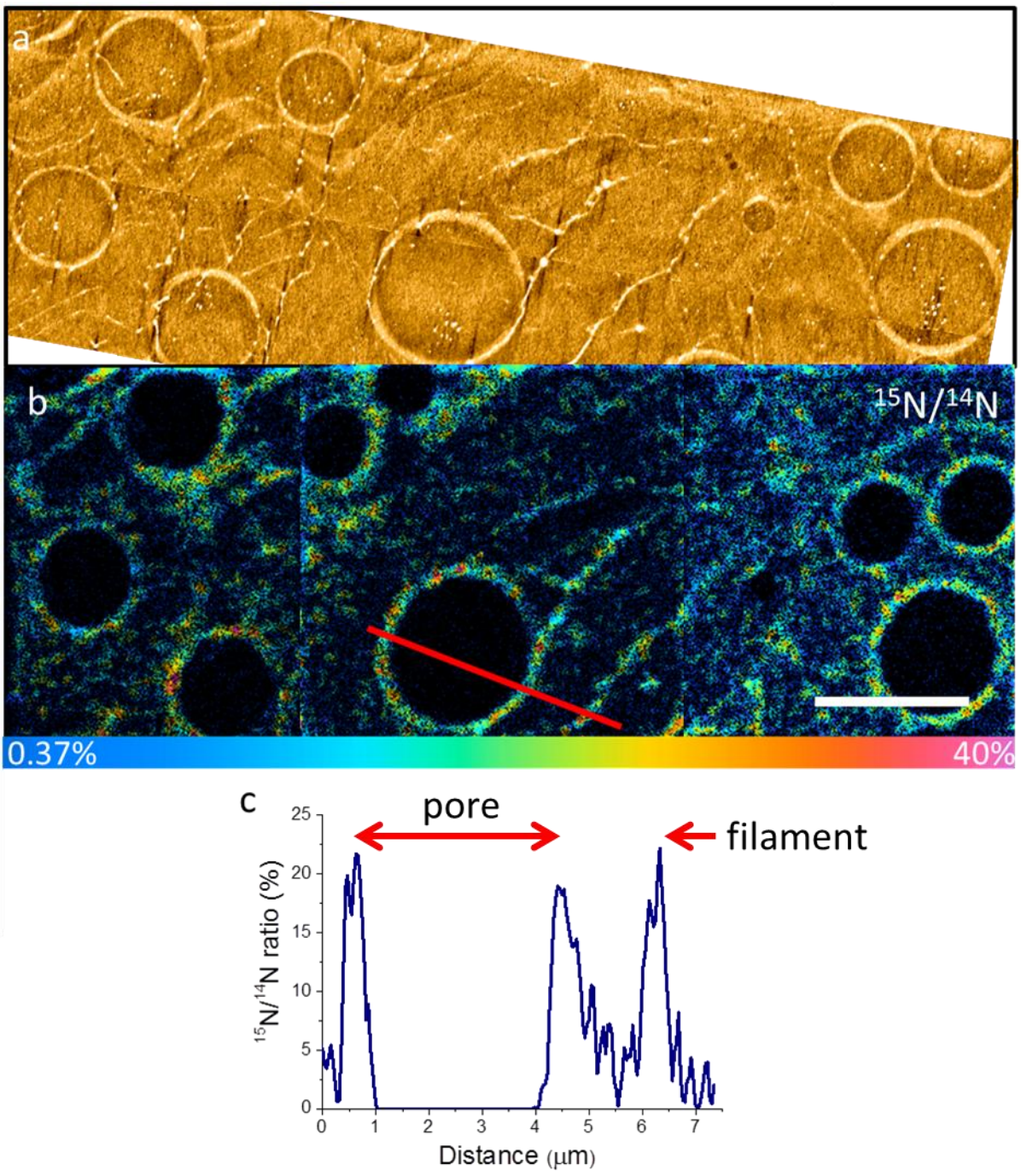

Figure 4.18: Correlative analysis on the ^{15}N-amhelin treated SLB sample. (a) AFM images; (b) NanoSIMS images with line scan; (c) $^{15}N/^{14}N$ ratio line scan identified in (b).

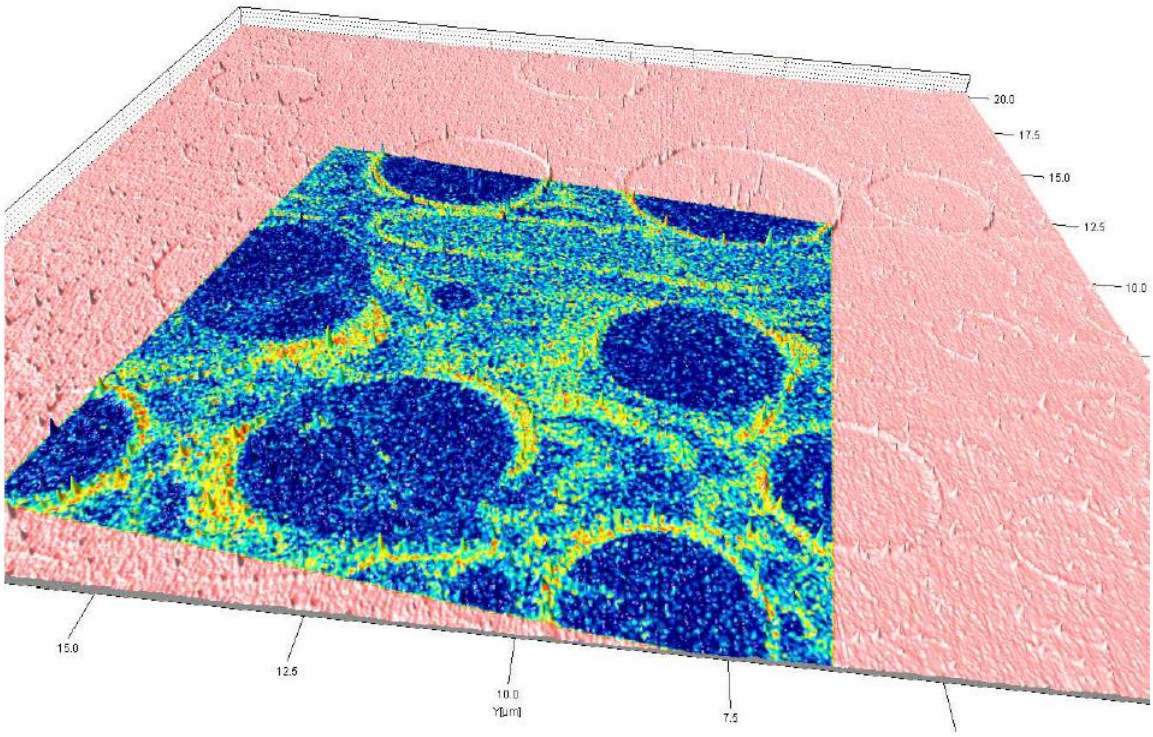

Figure 4.19: Overlap of NanoSIMS and AFM images of the same area of the ^{15}N-amhelin treated SLBs.

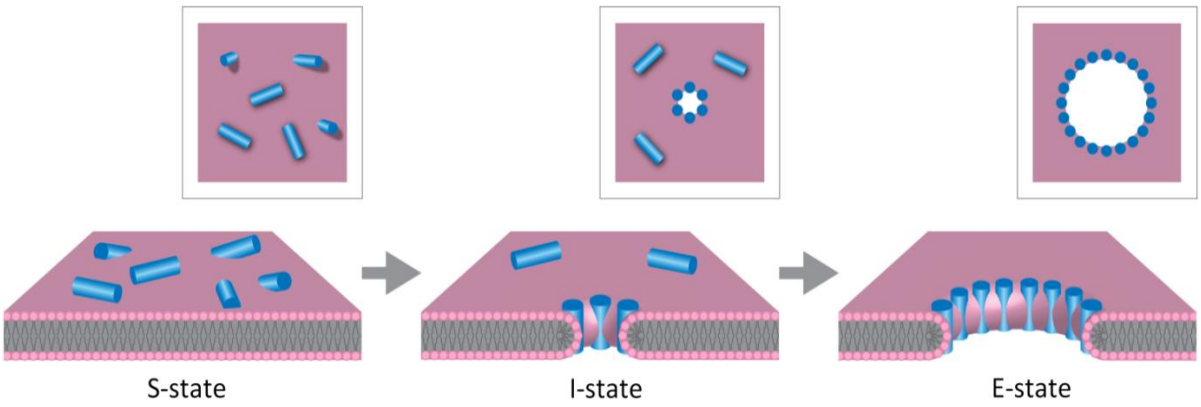

Figure 4.20: Proposed mechanism of the interaction between amhelin and lipid bilayers. Published in reference [164].

Stabilization of pores is challenged by strong electrostatic repulsion between inserted helices in the pore edges. In live cells, this conflict can be avoided both because excess peptide on cell membranes can migrate through small pores directly into the cytoplasm, targeting intracellular components, and because continuous peptide incorporation and diffusion in lipid bilayers can be preempted by membrane swelling [168-170]. Careful consideration of our AFM and NanoSIMS data suggested that

for flat and extended 2D lipid matrices, pore expansion is more thermodynamically favourable and the rate is determined by both incorporation and repulsion of peptides to the pore edges. In this way, inserting helices can be viewed as charged equipotential surfaces with a degree of translational freedom [167, 171] conforming to toroidal type poration, which is characterized by shallow energy minima leading to substantial variations in pore sizes [167, 168, 172].

Thus, my results supported a biological explanation of the effect of antimicrobial peptides as nonspecific and fast-reacting molecules that target microbial membranes, and whose action depends on concentration and matrix availability rather than on pore uniformity and global structural parameters such as folding topology.

4.3.6 AMP Interaction with Intact Bacterial Cells

^{15}N-labelled AMPs were also used to study the interaction between AMPs and intact bacterial cells. The aim was to try and image the structures formed by AMPs on the surface of the intact bacterial cells, and also visualize the AMPs inside bacterial cells. SEM and NanoSIMS analysis has been conducted on those samples.

The high resolution SEM images (Figure 4.21) show the treated E. coli surfaces have some structures that might suggest damage to the external membrane, and the surfaces are slightly rougher than the control sample surface. However, we need to be careful in interpreting these SEM images, since the samples are platinum coated to make them conductive which may give fine surface features, and also the sample preparation protocols may affect the surface structures. NanoSIMS analysis was carried out on these samples.

In the NanoSIMS ratio images (Figure 4.22), it is clear that the substrates are covered by ^{15}N-labelled amhelin that has not been effectively washed from the substrate (or possibly AMPs come from damaged bacterial cells) and that these signals from the substrates decrease as the primary ion dose is increased. Since during sequential imaging we are sputtering the surface of the sample, the $^{15}N/^{14}N$ ratio change can be measured through the depth of individual cells. In three of the four

measured bacterial cells, the first frame of the image has the highest $^{15}N/^{14}N$ ratio, which suggests that the ^{15}N-amhelin covers the surface of the bacterial cells and rather little peptide has penetrated into the cells. The variation of $^{15}N/^{14}N$ ratio from frame 2 to frame 9 is small, which means that I can detect is no obvious segregation of ^{15}N-amhelin inside specific layers of the bacterial cells. It is difficult to make a direct correlation for how much ^{15}N-labelled amhelin enters the cells and the health of these cells, because of the 'knock on' effect where ^{15}N atoms on the sample surface may be 'detected' apparently below the position on the surface from which they originated.

Due to the resolution limit of the NanoSIMS, the surface imaging limitation of the samples, and the complications from the sample preparation, I was not able to make a direct correlation of $^{15}N/^{14}N$ with surface structures imaged directly on the bacterial cell surface. However, SEM and NanoSIMS analysis has shown its potential on this type of analysis, and with more careful experimental design could provide important in direct observation of the interaction of AMPs with bacteria.

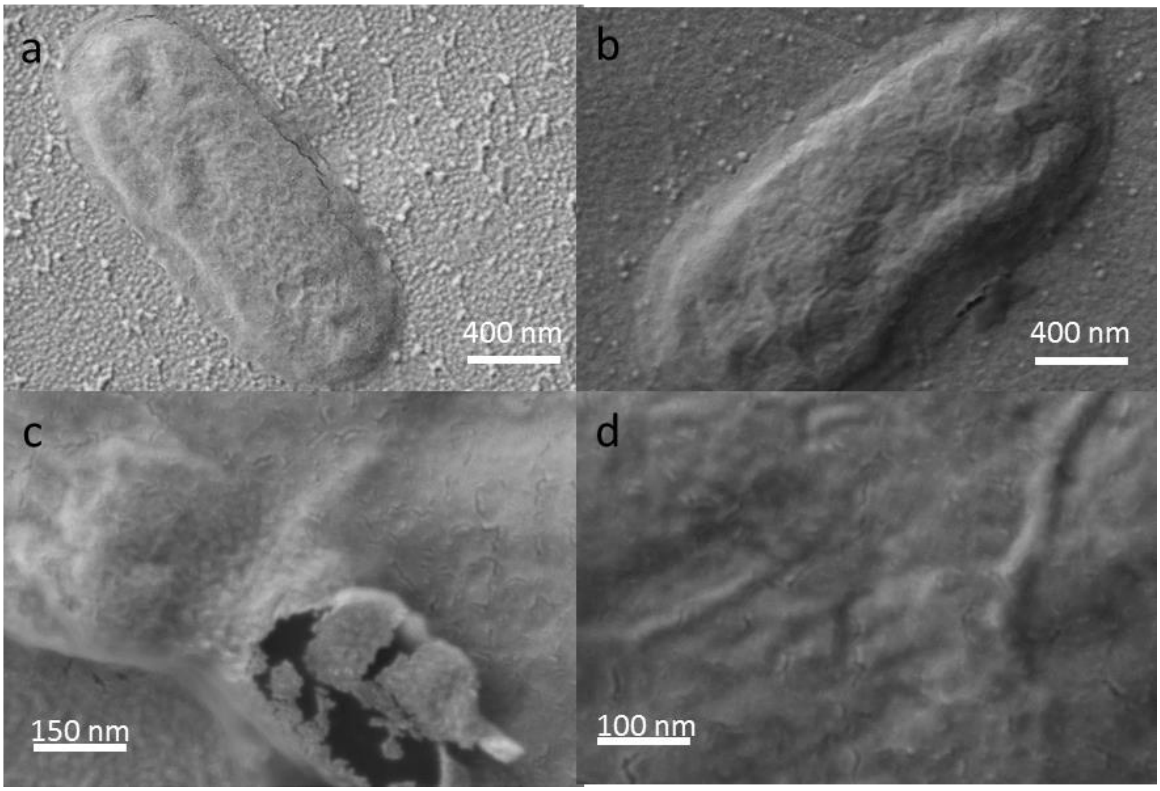

Figure 4.21: High resolution SEM images show the surface of the amhelin treated E. coli. (a) an overview of the surface of a single E. coli after treatment with amhelin for 60 min. (b) control sample without the treatment. (c) High magnification of surface of the treated E. coli. (d) High magnification image of the control sample surface.

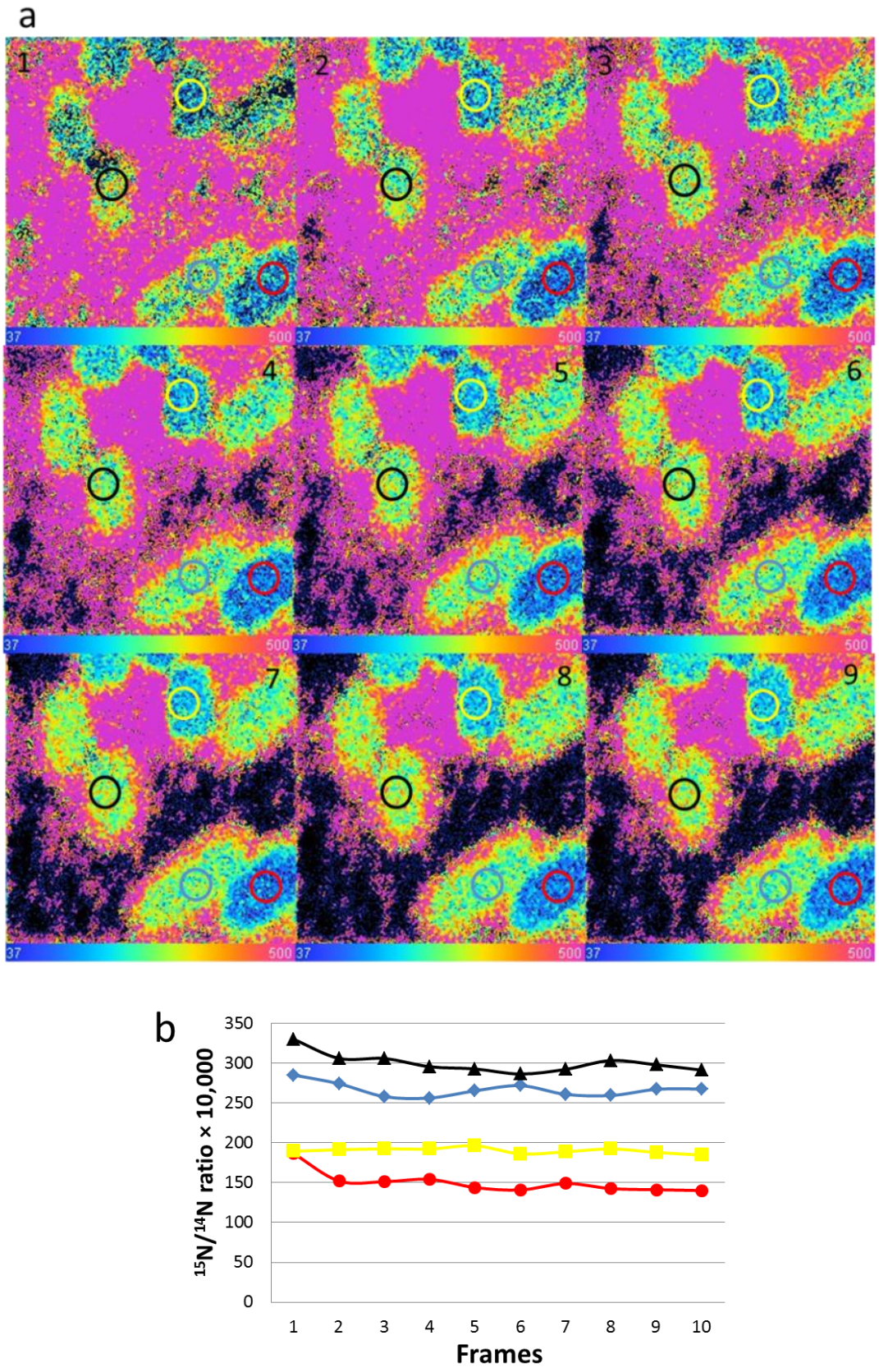

Figure 4.22: (a) 9 frames $^{15}N/^{14}N$ images on the same area with D1=4 (current ~ 0.5 pA). (b) Measurement of the $^{15}N/^{14}N$ ratio through the depth of E. Coli cells, corresponding to the black, blue, yellow and red circles identifying individual cells. Size of images: 5 µm × 5 µm.

4.4 Applications of Correlative AFM and NanoSIMS Analysis

This chapter demonstrates another application of correlative NanoSIMS and AFM analysis, which has provided the first direct evidence for expanding pores formed by amhelin in lipid bilayers. The success of this analysis depends on the use of SLBs and flat substrates providing an ideal surface for imaging. With this kind of correlative analysis, the interaction mechanism of other types of AMPs and membranes can be easily imaged with well-designed experiments and this analysis protocol. It also can be easily applied to study other molecular interaction and single molecule behaviour.

4.5 Summary

This chapter described the first chemical images of the interaction between an AMP and lipid bilayers, which is also an example of correlative AFM and NanoSIMS analysis. The established analysis protocol has many potential applications. Further work in this area would include the design of a sample holder for this kind of analysis to make the image alignment easier, and software to automatically align and present correlative NanoSIMS and AFM images would also be very useful.

5 Single Cell Analysis – Glutamine Metabolism in Cancer

5.1 Introduction: Single Cell Analysis

Cells are basic functional units in almost all organisms, and the sizes of the cells vary considerably depending on their function and location in different types of tissue. There are two main types of cells; eukaryotic and prokaryotic cells, and the basic differences between these are whether the cell has a nucleus and other distinguishing features including size, organelles, distribution of DNA in cells and metabolic pathways etc. [173]. This chapter will focus on my work on eukaryotic cells. Figure 5.1 is a schematic of a eukaryotic cell, which usually contains nucleus, Golgi, endoplasmic reticulum (ER), ribosome, mitochondria and lysosomes etc. The scale of these structures ranges from a few nanometres to a few micrometres.

Figure 5.1 has been removed due to copy right restrictions. The original image can be found in the reference.

Figure 5.1: Schematic of a eukaryote cell. From reference [174].

This section discusses single cell analysis methods and experiments on cell cultures. Cell culturing has been used as laboratory technique since the 1900s, and has become a routine laboratory method since the 1950s [175]. It has a wide range of applications including studies on cell metabolism, tests on drugs and chemical compounds etc. Even though studies on cell cultures are done on 'single cells', most of the studies use averaged results from the analysis of many cells.

Single cell analysis has some advantages in comparison to these traditional analysis methods: Single cell analysis can reveal a more accurate representation of cell-to-cell variations instead of the average results from bulk measurements and also makes it possible to fully understand the cellular specificity of complexity of tissue microenvironments under physiological conditions [176]. The small sizes of the internal structures are one of the challenges in single cell analysis, and the sensitivity limitations of some experimental techniques also makes single cell analysis difficult [177].

Mass spectrometry has been a commonly used and useful technique for biomedical research, in particularly in metabolism studies for decades as noted in Chapter 2. Mass spectrometry techniques have been developed and significantly improved for the study of metabolism in the last century, and resulted in interesting studies [29, 178, 179]. However, all these studies were performed on hundreds to thousands of cells and produced averaged results. In the last two decades, the developments of imaging Mass Spectrometry techniques enable scientists to visualize specific molecular information which was previously buried in the average data. A significant improvement is the lateral resolution of imaging mass spectrometry techniques [180]. Biologists are now not only able to image the whole body of small animals with good MALDI-MS [181] but also can have sub-micron resolution with secondary ion mass spectrometry [180]. The spatial resolution of the NanoSIMS makes it possible for single cell analysis as a useful method for many studies [87, 88].

As in Chapter 4, the NanoSIMS is the main technique I have used in the work reported this chapter. With its combination of high lateral resolution and high sensitivity for both elements and isotopes, it has the ability to directly image the chemical distributions in single cells. Figure 5.2 contains

NanoSIMS images of the distribution of a ^{15}N-labelled peptide vector reported by Romer et al [182]. The excellent lateral resolution of the NanoSIMS is clearly shown in these images allowing both elements and isotopes to be easily detected. The subcellular structures of the nucleus and cytoplasm are clearly revealed by using the NanoSIMS to detect different ionic signals.

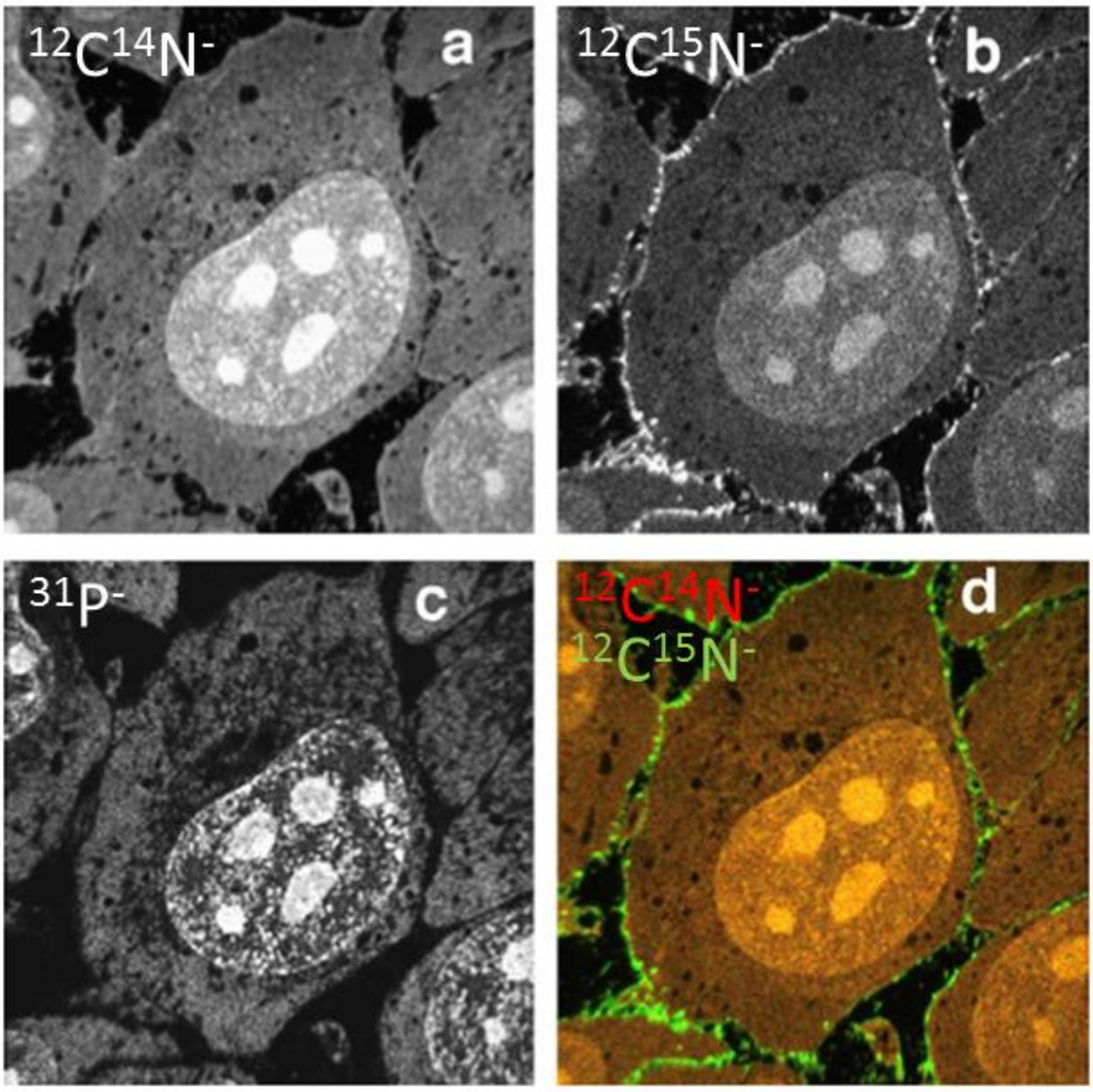

Figure 5.2: NanoSIMS images on ^{15}N-labelled proteins on the cell membranes. a. $^{12}C^{14}N^-$, b. $^{12}C^{15}N^-$, c.$^{31}P^-$ and d. overlap of $^{12}C^{14}N^-$ (red), $^{12}C^{15}N^-$ image (green). From reference [182]. Size of images: 35 µm × 35 µm.

5.1.1 Correlative NanoSIMS and complementary techniques for single cell analysis

The potential of the NanoSIMS for single cell analysis has resulted in it becoming an increasingly important technique to study processes in biological systems at the subcellular level [84, 88, 94, 95].

However, limitations of non-molecular-specific information and lack of structural information still make a complete understanding of a biological process difficult if solely based on chemical distributions. To make full use of the advantages of the NanoSIMS, and to compensate for these limitations, combining correlative techniques with NanoSIMS analysis has been proven to be very useful for single cell analysis as discussed in Chapter 2. All of these techniques have their own specialities, and all have brought us more information than available from NanoSIMS analysis alone, and answered many important questions in various areas of study.

Morphological and structural information is important to study single cell metabolism. To obtain this information, scientists have tried fluorescence microscopy and NanoSIMS to image on the same intact cell [109], and also tried TEM and NanoSIMS on consecutive sections of the same tissue [132]. The limitation of correlating fluorescence microscopy and NanoSIMS analysis is that the imaged volume is so different and the difficulty of imaging the same plane (depth) from intact cells. Additional labels required for imaging also makes sample preparation complicated. Correlative analysis with NanoSIMS and TEM is difficult because finding the same area of the sample can be challenging, as they are from different sections on different substrates. One way to avoid this problem is to cut one section which is very thin so that it is suitable for both techniques, but this may result in very fragile NanoSIMS samples. To overcome the limitations of the two method approaches which have been used in the last decade, this chapter will report another way to conduct metabolism studies at a subcellular level: correlative backscattered electron (BSE) and NanoSIMS analysis.

The BSE signal from scanning electron microscopy is an important imaging mode in materials science research. Backscattered electrons are electrons that are scattered from the surface of a specimen due to elastic interactions of primary electrons with the nuclei of atoms. The fraction of electrons backscattered by heavy elements (high atomic number) is higher than from light elements (low atomic number). Consequently, the BSE signal is able to reveal contrast based on the average atomic

number of atoms in the specimen. Hence it can show the distributions of heavy elements on a sample surface with excellent spatial resolution. Biologists started to use this signal to image biological samples about 40 years ago [183], and it has been used in many interesting studies [184, 185]. With recent developments of the SEM technique and BSE detectors, its applications on structural biology studies are becoming more popular, especially in the neuroscience area [186, 187]. The requirements of the samples and sample preparation protocols for BSE and NanoSIMS imaging are very similar, and that BSE can reveal structural information at subcellular level with higher resolution. This makes BSE an ideal candidate to do correlative analysis with the NanoSIMS.

In this chapter, an example of NanoSIMS analysis of single cells with correlative BSE imaging: glutamine metabolism in single cancer cells will be discussed. This project has been carried out with colleagues in the Weatherall Institute of Molecular Medicine at Oxford University.

5.2 Introduction: Glutamine metabolism in cancer

5.2.1 Cancer

Cancer is no longer an unfamiliar word or disease for human beings. It has become one of the leading causes for death around the world, causing 13% of all deaths in 2007 [188]. Cancer was discovered a long time ago. We can even say it was known from the beginning of recorded history. The oldest description of cancer we have found in Egypt dates back to 3000 BC [189]. In the UK, the statistics show that the incidence of cancer for both men and women has increased in the last few decades (Figure 5.3) [190].

5.2.2 Cancer biology

As the diagnoses of cancers increase, more and more attention has been attracted to this area. Many scientists and doctors are trying to understand the causes of cancer and to develop effective therapies and drugs to treat the various types of cancer. Most scientists have agreed the following definition: ‘abnormal growth of cells caused by multiple changes in gene expression leading to

dysregulated balance of cell proliferation and cell death and ultimately evolving into a population of cells that can invade tissues and metastasize to distant sites, causing significant morbidity and, if untreated, death of the host' [191].

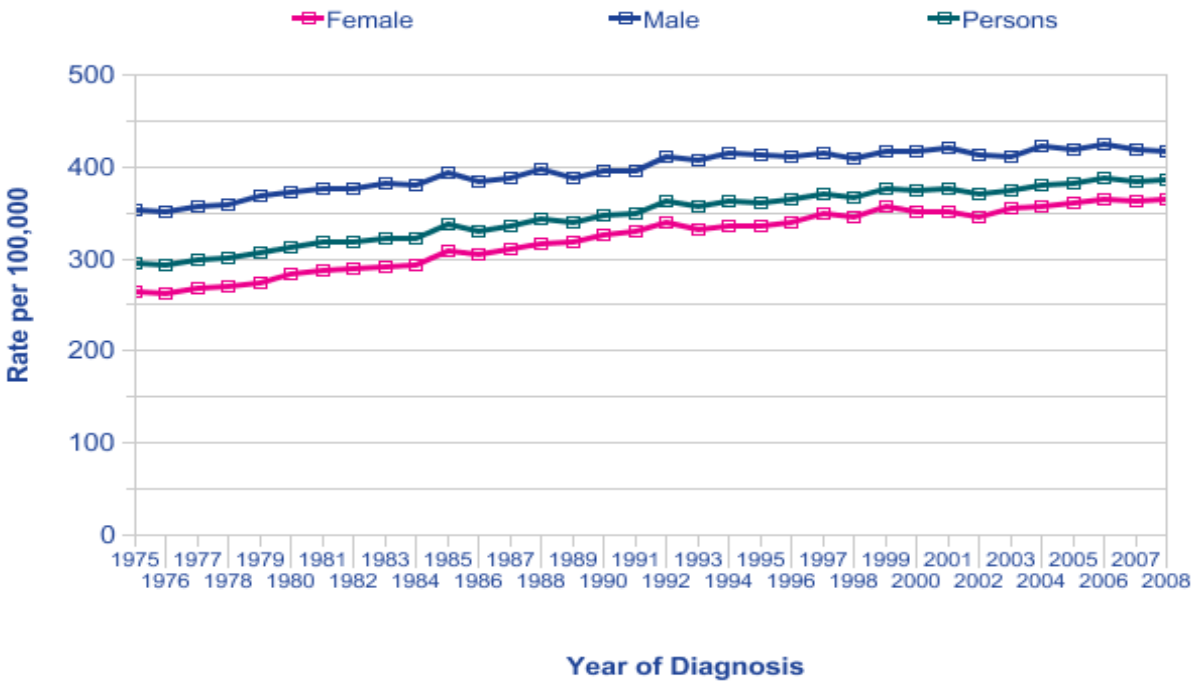

Figure 5.3: Trend of cancer diagnosis in the UK [190].

As stated in this definition, the most important characteristic of cancer is uncontrolled cell growth, which results from alterations in the genes. The uncontrolled growth of cancer cells breaks the balance of cell replication and cell death, and can result in a very large population of tumour cells [191] that can invade surrounding healthy tissues [148]. For normal cells, there is a precise mechanism controlling the size and population in a specific tissue. This means that division and proliferation processes accelerate when new normal cells are needed and decelerate when there are too many cells, so maintaining a balanced population. This does not happen in cancer tumours [192].

In detail, the hallmarks of cancer can be summarized as stated in the reference [193]: (a) continuous cell division; (b) oncogenes give sustained growth signals; (c) loss of function of tumour suppressor genes bypassing anti-growth signals; (d) apoptosis; avoidance of cell death; (e) angiogenesis; ensuring blood vessel growth because the transcription factor for inducing the formation of new

blood vessels, HIF, is activated under hypoxic conditions [148] as discussed further below; (f) metastasis; the spread to other sites. The first 4 aspects result in the loss of control we discussed above. Metastasis makes cancer extremely difficult to treat, resulting in harm to the entire organ, even the entire body.

5.2.3 Cancer Metabolism

Nowadays, targeting the metabolism of cancer cells is an important treatment for cancer, and metabolisms are good targets for effective therapies. It is now widely acknowledged that the metabolism of cancer cells is remarkably different from that of the normal cells from which cancer cells are derived. The metabolism of glucose is the most important metabolism in cancer cells, as it is in other cells in the human body. More than 80 years ago, the Nobel Prize winner Otto Warburg discovered the altered metabolism in cancer cells for the first time [194], showing that cancer cells have a higher glycolysis metabolism even in conditions of sufficient oxygen supply. In other words, cancer cells produce more lactate due to an increase of glycolysis. This effect has been discovered in different types of cancers though it is not universally applicable for all types. The glucose uptake also increases in cancer cells because of the low efficiency of ATP production in glycolysis and the high growth rate [195]. However, the increased glucose uptake is still insufficient to provide sufficient energy for cancer cells. In the 1950s, scientists recognized the importance of glutamine as a nutrient for cancer cells [196], and identified another important metabolism, glutaminase, as well as glycolysis [197]. Glutamine is a nonessential amino acid in humans, but it is also the most abundant free amino acid. It is an important nitrogen source for protein and nucleotide synthesis, and it is the signal to maintain the activation of target of rapamycin (mTOR) pathway to uptake essential amino acids. What is more, glutamine can also be the primary mitochondrial substrate [198]. A detailed summary of cancer metabolisms are shown in Figure 5.4.

The metabolisms of cancer are described as the disease's Achilles's Heel, and even the Holy Grail by some scientists [195, 196, 199] in terms of the development of cancer therapies. Targeting

metabolisms is a relatively new therapy compared with conventional surgery and radiotherapy. Targeting metabolism therapy works because cancer cells will undergo autophagy and cell death if there is insufficient bioenergetic supply [200]. So the metabolic regulators and enzymes responsible for the energy supply could be good targets to kill cancer cells. Some research has already shown that metabolism is effective target in therapies [201], and understanding these metabolisms in detail will be a critical first step to design these types of targeted therapies.

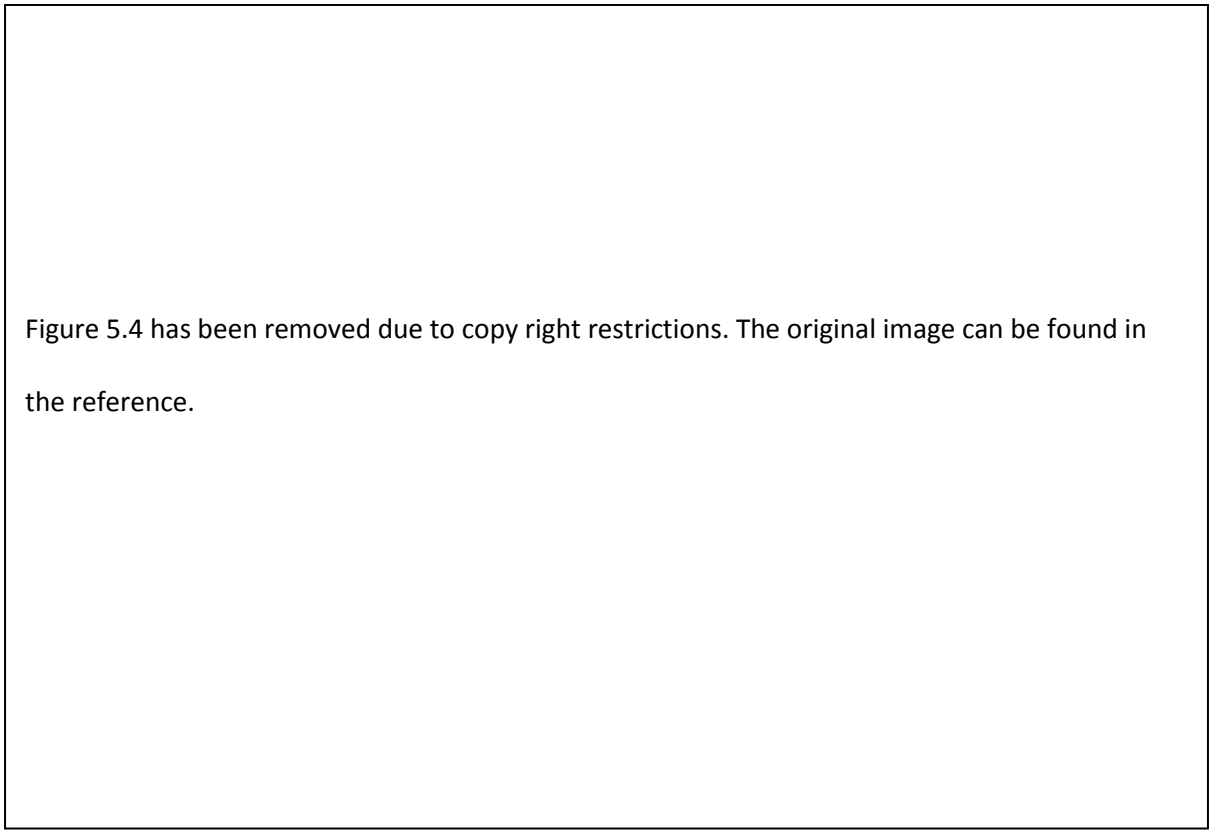

Figure 5.4: Schematic of overview of the cancer metabolism. From reference [202]. The glutamine metabolism pathway is seen at the bottom of the diagram.

5.2.4 Project Aim

This chapter is about glutamine metabolism in cancer. Having a clear understanding of the glutamine metabolism would be extremely useful to design potential targeted therapy to treat cancers. This project is collaboration with Prof. Adrian Harris, Prof. David Ferguson and Dr. Elena Favaro from the Weatherall Institute of Molecular Medicine at Oxford University, to develop correlative NanoSIMS

and BSE analysis methodologies on single cell metabolism studies and getting a better understanding of the glutamine metabolism.

5.3 Materials and Methods

In this project, both intact cells and resin embedded sections were prepared and analysed.

5.3.1 Intact Cell analysis

Intact cells were used to explore the incorporation of glutamine into cancer cells. A FIB sample preparation method was also tried on intact cell samples.

5.3.1.1 Sample Preparation

The breast cancer MCF7 cell line was provided by Cancer Research UK Cell Services. MCF7 were grown in a DMEM media supplemented with 10% fetal calf serum, 1% Pen Strep. They were removed from the flasks using trypsin and seeded into 6-well dishes containing platinum coated alpha-numerical gridded coverslips for subsequent experiments. Cells were then fixed in 4% paraformaldehyde (PFA) for 20 minutes at room temperature followed by a graded series of dehydration washes in 20%, 30%, 50%, 70%, 90% and 100% of ethanol for 5 minutes each. Cells were then coated with 5 nm platinum in a Cressington 208HR high-resolution sputter coater to render the surface conductive for NanoSIMS imaging.

5.3.1.2 Focused Ion Beam

The NVision dual beam FIB-SEM was used to cut the top part of the cells to flatten the cell surface and expose the nucleus. A 30 kV gallium beam was used in the instrument and the beam was aligned as parallel as possible to the substrate.

5.3.1.3 Imaging

Fixed and dehydrated cells on platinum-coated coverslips were imaged by optical microscopy to select the cells to image in the NanoSIMS. Cells mostly lying on the flat areas of the grids were selected to avoid the topography effect from raised sections on the grids. The cells were pre-

sputtered with a high current Cs^+ beam to enable the secondary ion signals to reach steady state and to expose the nucleus for imaging. A dose of 2.5×10^{17} Cs^+ ions/cm^2 was used for this purpose. Then the cells were imaged with a low current Cs^+ beam (D1=2, D1=3 and D1=4). The choice of the D1 aperture depends on the requirements for image resolution. A dwell time of 30,000 µs/pixel was used for imaging.

5.3.2 Resin embedded section analysis

Resin embedded section samples were used to study the glutamine metabolism at a subcellular level, and also provided the flat samples for correlative BSE and NanoSIMS analysis.

5.3.2.1 Sample Preparation

The same MCF7 cells were used for resin embedded sections. Cells were cultivated for 24 h in L-Glutamine-free Advanced Dulbecco's modified Eagle's medium (DMEM, Gibco) supplemented with 10% fetal bovine serum and 4 mM alpha-^{15}N-L-Glutamine (Cambridge Isotope Laboratories, Inc). Cell pellets were fixed in 4% glutaraldehyde in 0.1 M phosphate buffer and processed as for routine electron microscopy. The samples were post-fixed in 2% osmium tetroxide in 0.1 M phosphate buffer, washed in distilled water and treated with uranyl acetate. Samples were then dehydrated in ethanol and treated with propylene oxide prior to embedding in Spurr's epoxy resin.

5.3.2.2 Imaging

500-nm sections were cut in a microtome and mounted on 15 nm platinum coated coverslips for imaging. Areas of interest were recorded by optical microscopy and the sections were then transferred to the NVision FIB for BSE imaging. The BSE signal is sensitive to atomic number contrast [203], which enables us to image biological samples stained with heavy metals. With a low energy incident beam, the interaction volume decreases rapidly [204], which makes low voltage images extremely surface sensitive, and in a modern SEM we can achieve a lateral resolution of a few nanometres [205]. Here, BSE images were taken with a 2 kV incident beam with a standard aperture (30 µm) and 5-mm working distance. Sections were then coated with 5 nm of platinum in a

Cressington 208HR high-resolution sputter coater to render the surface conductive for NanoSIMS imaging. The Cs^+ primary beam in the NanoSIMS was first used to remove the platinum on the surface at selected locations, and at the same time implanted a low Cs^+ dose of 6.5×10^{15} ions/cm^2 to ensure that as little as possible of the section surface is removed before imaging. Maintaining the surface sensitivity for both BSE and NanoSIMS imaging is important to ensure that precisely the same material is analysed in both techniques. This is not possible when correlating a surface-sensitive technique and optical fluorescence imaging, for instance, where the optical signals can originate from different depths in the section.

Small apertures (D1 = 3 or D1 = 4) were used for imaging single cells to match the primary beam size to the pixel size. The instrument was tuned for $^{12}C^-$, $^{16}O^-$, $^{12}C^{14}N^-$, $^{12}C^{15}N^-$, and $^{31}P^-$ ions to give morphological information and allow calculation of the $^{15}N/^{14}N$ ratio. NanoSIMS images were collected with a dwell time of 30,000 μs/pixel for 256 pixel × 256 pixel images and processed. A median filter with radius of 3 pixels is applied to the HSI images to reduce the noise in images as stated above. The BSE and NanoSIMS images can then be aligned, and the local ratio of $^{15}N/^{14}N$ can be measured quantitatively by ImageJ. Data collected from ImageJ was imported into Prism 5.0, Excel and Origin for analysis.

5.4 Results and Discussions

This section will discuss (1) the study of glutamine incorporation by exposing the cell culture to ^{15}N-labelled glutamine; (2) preparation of flat surfaces inside fixed cells with a focused ion beam; (3) development of correlative BSE and NanoSIMS analysis and (4) direct subcellular imaging on the effects of hypoxic conditions and PYGL gene knockdown on glutamine metabolism.

In this project, α-^{15}N-labelled glutamine (Figure 5.5) was used for all the experiments, and will be described as ^{15}N-labelled glutamine throughout this chapter. The labelled glutamine is used for synthesis of proteins, nucleotides and glucosamine in the cells (Figure 5.6), which are the metabolites imaged in this chapter.

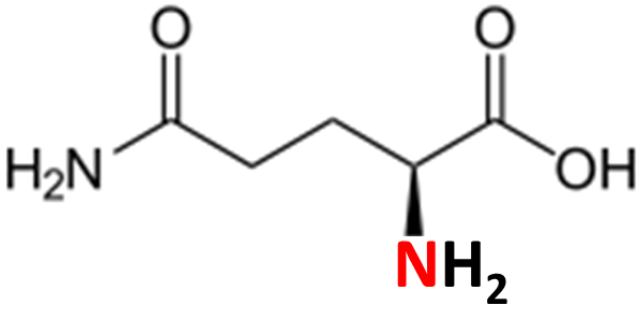

Figure 5.5: Glutamine molecule. α-^{15}N identified in red.

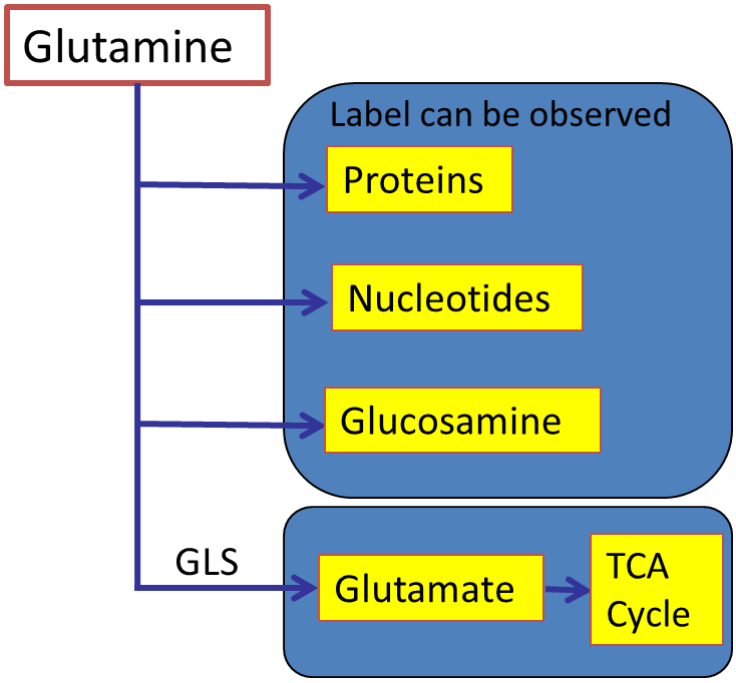

Figure 5.6: Summary of the glutamine metabolism in cancer cells, drawing based on [196].

5.4.1 Optical Images

Single cells on both intact cell samples and resin sections were imaged by optical microscopy before BSE and NanoSIMS imaging to identify areas of interest. The marker coverslips coated with 15 nm Pt were used for intact cell samples, and grids and numbers on the coverslips were used to select cells to analyse. As shown by the arrows in Figure 5.7. I avoided imaging cells sitting on top of the grids as described above. Optical imaging can also show the cells in resin sections, as seen in Figure 5.7. Cells on the flat areas of the sections were chosen to avoid possible charging and topography effects.

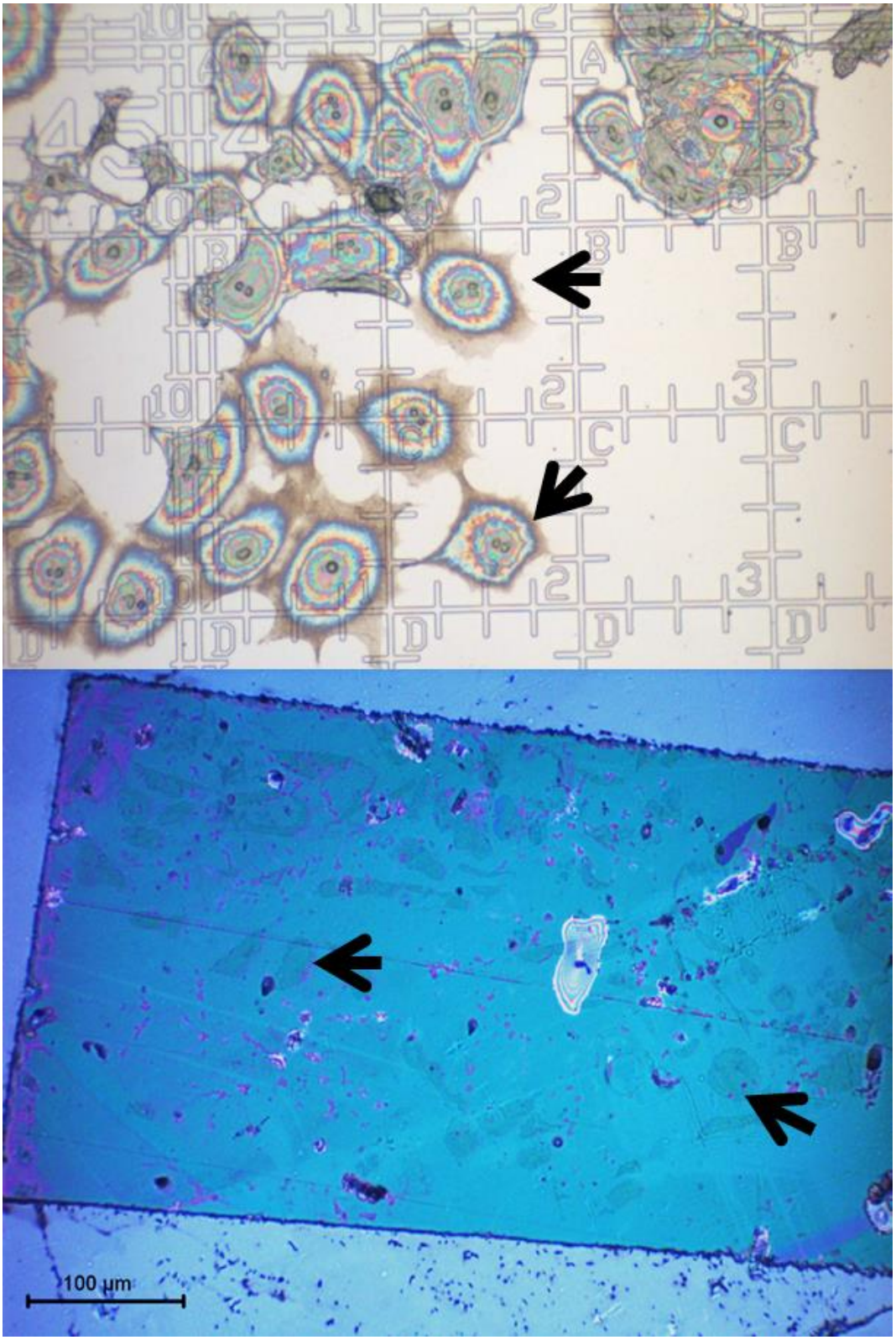

Figure 5.7: Optical images of intact cell samples on grids (100 µm × 100 µm squares) (a) and resin embedded samples (b). Arrows identify the areas selected for subsequent analysis.

5.4.2 NanoSIMS Tuning

As noted in Chapter 2, reaching steady state is important for reliable signal quantification in the NanoSIMS, and also improves the signal intensity and image quality. In the intact cell analysis, it also defines what depth into the sample surfaces the images are recorded from. In this case, pre-sputtering is required both to achieve steady state for all the signals and also to remove surface material to image deep inside the cells.

Using the normal selection of $^{12}C^-$, $^{16}O^-$, $^{12}C^{14}N^-$, $^{12}C^{15}N^-$, $^{31}P^-$, and $^{32}S^-$ ions, the $^{12}C^{15}N$ signal must be tuned precisely when attempting to measure accurately the local $^{15}N/^{14}N$ ratio. Apertures ES=2 and AS=1 were selected to separate the $^{12}C^{15}N$ peak from other peaks with mass 27 (Figure 5.8), including naturally occurring $^{13}C^{14}N^-$ ion.

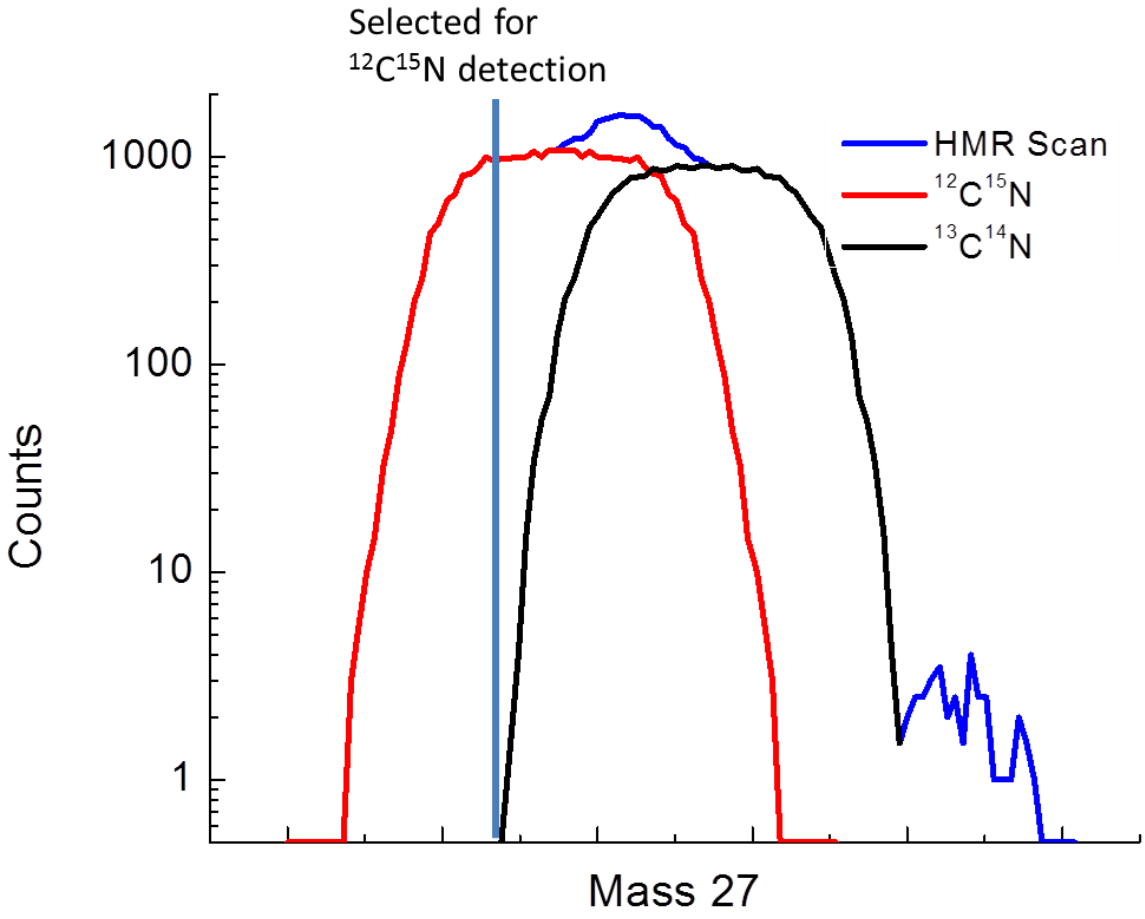

Figure 5.8: Tuning of $^{12}C^{15}N^-$ on cell samples exposed to ^{15}N-labelled glutamine.

Depth profiles were carried out on the intact cell samples to decide the dose of Cs^+ for pre-sputtering. Imaging of cells with exposed nuclei is preferred in this case to obtain information from both nucleus and cytoplasm. Figure 5.9 is a depth profile of the 5 selected signals on one intact cell and corresponding images of the cell at different stages. The sputtering depth can be estimated from equation 3.1. The sputtering yield can be calculated by SRIM [206], and the sputtering yield of carbon, nitrogen, oxygen under a 16 keV Cs^+ ion beam of normal incidence is 1 – 4 atoms/ion.

$$\text{Sputtering Depth} = \text{Dose} \times \text{Sputtering Yield} \times \text{Volume of an atom} \qquad \text{(Equation 3.1)}$$

All signals start low on these intact cell samples and increase significantly with the Cs^+ dose. After a dose of about 10^{17} ions/cm^2 Cs^+ (~150 nm sputtered from the sample surface), all the signals have reached steady state, and so this is a suitable stage for quantitative imaging. Other factors that contribute to the change of secondary ion signals are the removal of cells and sputtering of substrates. The thickness of dehydrated cells on coverslips is a few micrometres at the nucleus with thin cytoplasm at the edges reducing down to a few hundred nanometres. Secondary ion signals remain stable from a dose of 1×10^{17} ions/cm^2 to 3×10^{17} ions/cm^2 Cs^+ which is the window for reliable NanoSIMS imaging on these intact cell samples. After a longer period of sputtering, some of the signals started to decrease due to the removal of the edges of the cell starting with the dose of ~3×10^{17} ions/cm^2 (~450 nm sputtered), as shown in Figure 5.9. Secondary electron images show the shrinking of the area of the cell due to sputtering. The cytoplasm started disappearing first since it is much thinner than the nucleus area of the cell. Figure 5.9 also shows that after about 3.0×10^{17} ions/cm^2 dose of Cs^+, the $^{12}C^-$ signal increases again, because the polymer substrate yields a higher $^{12}C^-$ signal than the cell sample.

Another factor which needs to be considered is the dose required to expose the nucleus for analysis. The NanoSIMS has the ability to remove the sample surface to image deep inside cells. Figure 5.10 contains $^{31}P^-$ images showing the nucleus after different sputtering times on the same cell. It is clear that the nucleus area increased with the time of sputtering, which means subsequent images are

originating from deeper into the cell. To obtain nuclear and cytoplasmic information, all images on these intact cell samples were taken with a dose of about 2.5×10^{17} Cs^+ ions/cm^2.

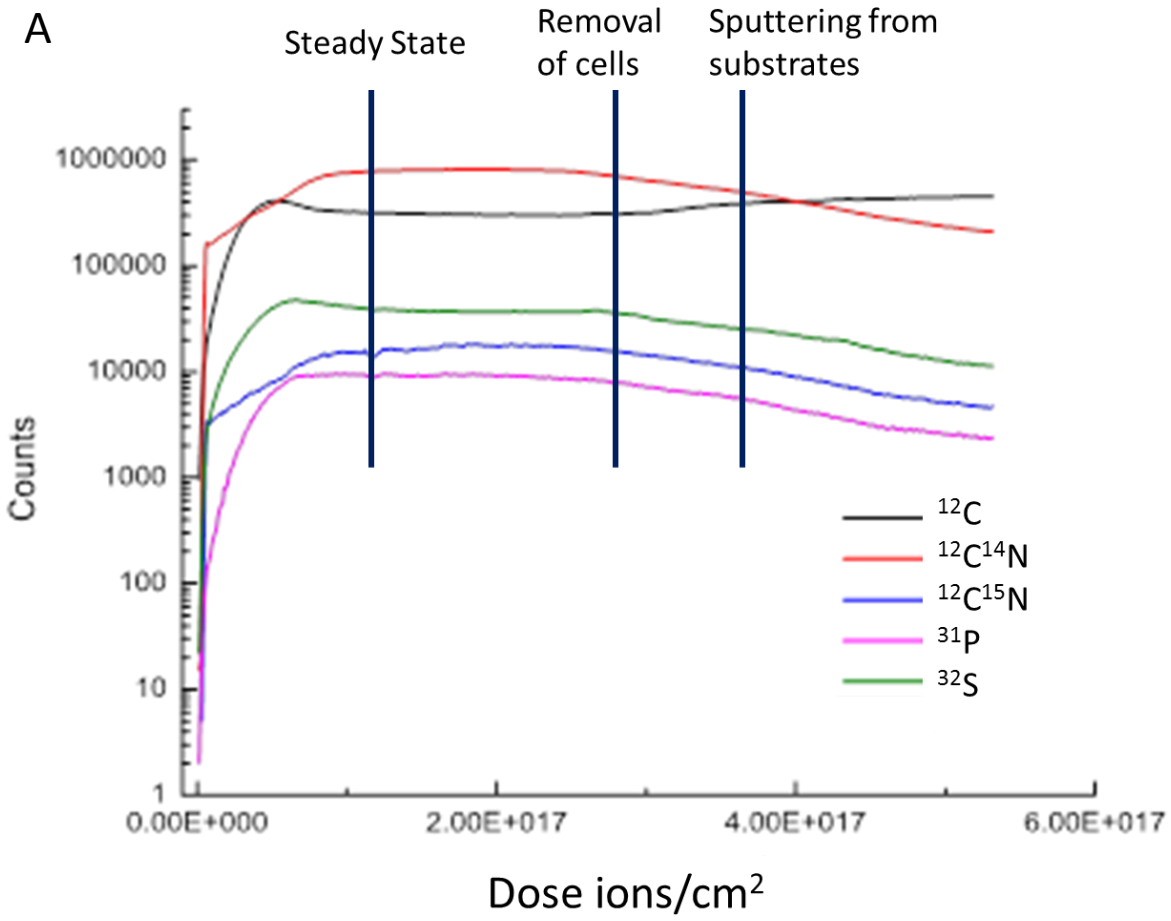

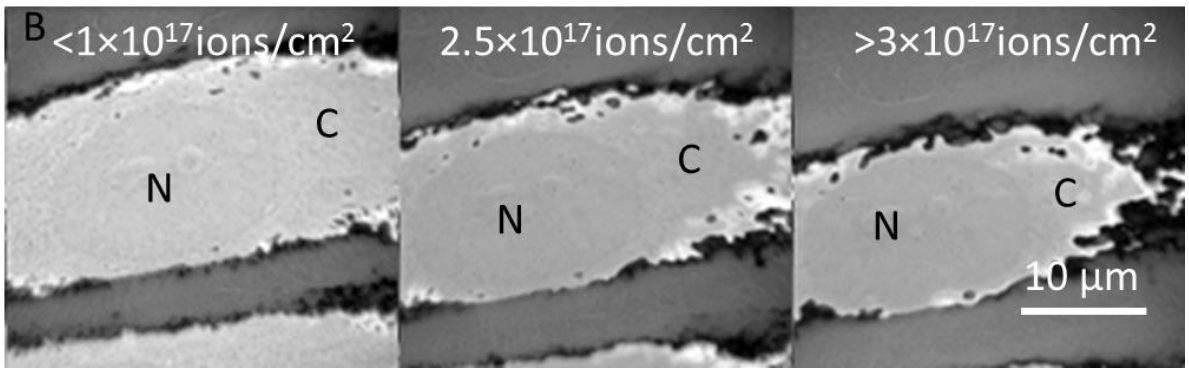

Figure 5.9: (A) Depth profile of $^{12}C^-$, $^{12}C^{14}N^-$, $^{12}C^{15}N^-$, $^{31}P^-$ and $^{32}S^-$ signals from intact MCF7 cells, showing the steady state, removal of cells and increased sputtering from the substrate. (B) corresponded secondary electron images of the cells from different stages of the depth profile, with nucleus (N) and cytoplasm (C) identified.

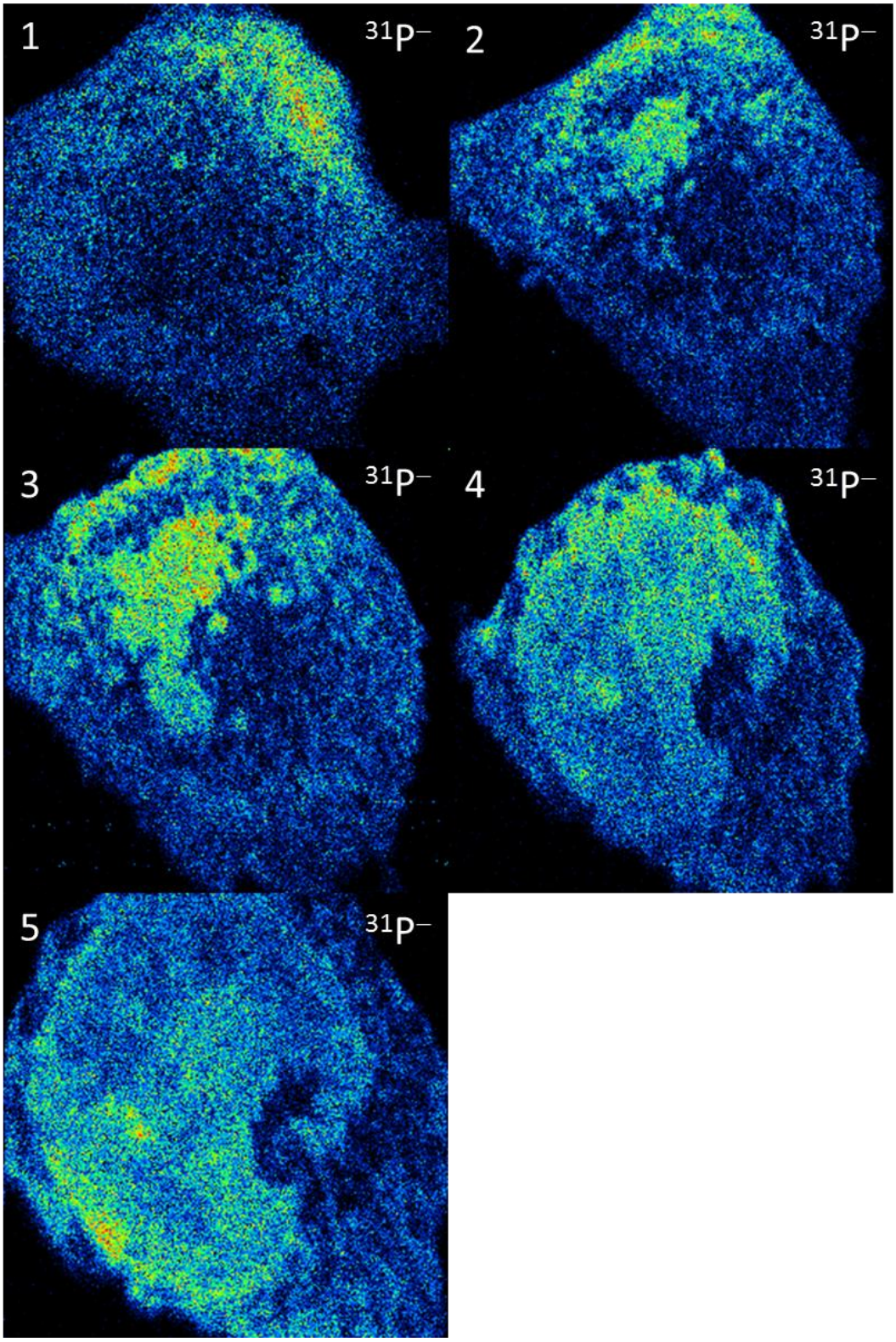

Figure 5.10: $^{31}P^-$ images of the same cell after different pre-sputtering times. Images in CAMECA colour scale. Size of images: (1) 35 µm, (2) 35 µm, (3) 30 µm, (4) 25 µm , and (5): 20 µm.

Figure 5.11 shows 5 selected ion images and the secondary electron image from an intact control cell which was not exposed to ^{15}N-labelled glutamine. The $^{12}C^{14}N^-$ image shows the effect of surface

topography on the local signal intensity, and this topography is also seen in the SE image. The $^{31}P^-$ and SE images show the nucleus area clearly. The average $^{15}N/^{14}N$ ratio is 0.37% which is very close to the natural abundance of ^{15}N. Control cells were analysed in every NanoSIMS session to set a ^{15}N background for calibration of the isotopically enhanced $^{15}N/^{14}N$ ratio.

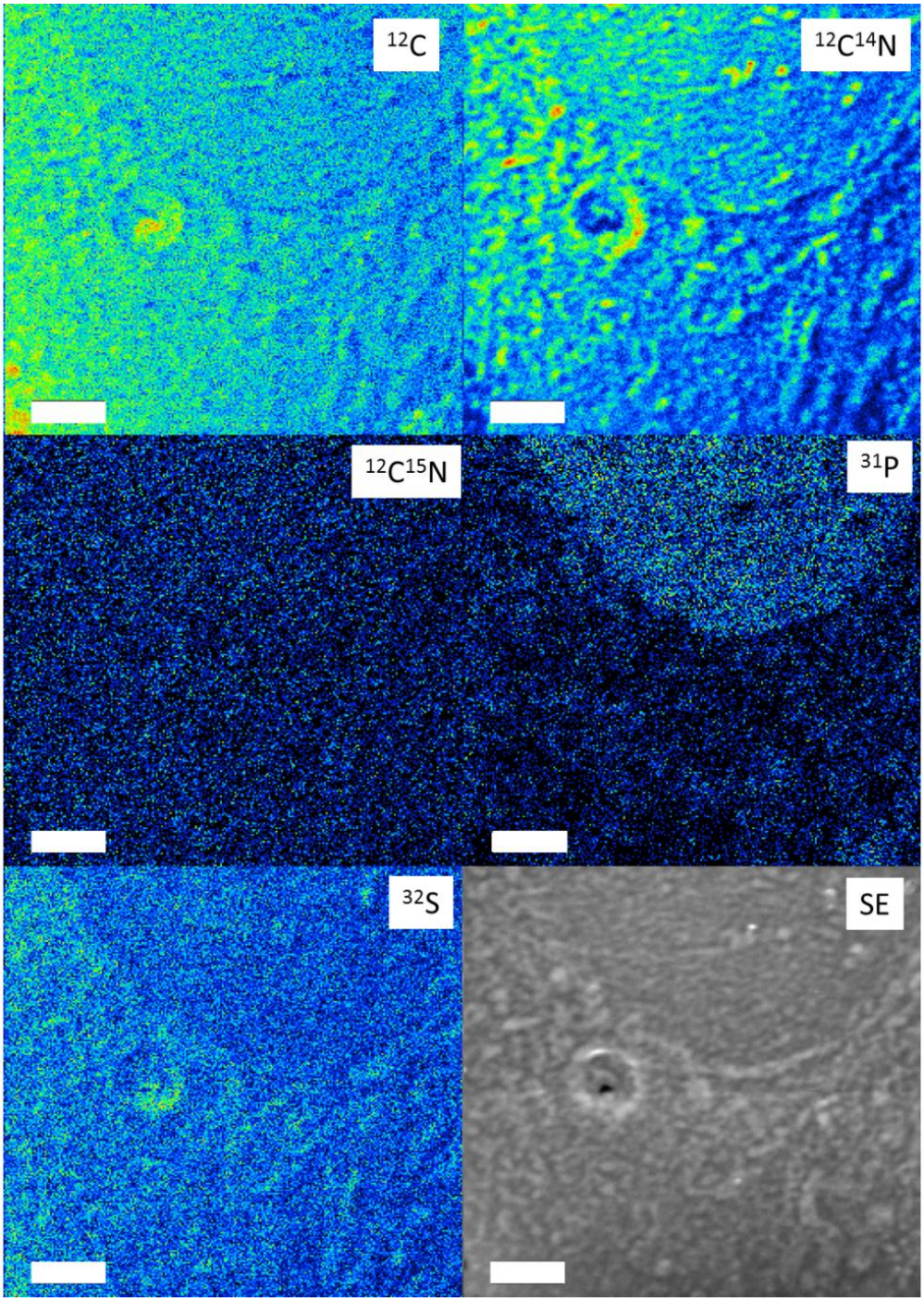

Figure 5.11: $^{12}C^-$, $^{12}C^{14}N^-$, $^{12}C^{15}N^-$, $^{31}P^-$, $^{32}S^-$ and secondary electron NanoSIMS images on an intact control cell. Ion images in CAMECA colour scale, SE image in grey scale. Scale bar: 2 µm.

5.4.3 Focused Ion Beam Sample Preparation

Focused ion beam sample preparation is a technique which uses a finely focused ion beam to conduct site specific sputtering or milling. It has been extensively used in materials science [207], particularly in semiconductor research [208]. FIB milling is also starting to be used more widely in biological studies, such as tomography studies with FIB-SEM [205, 209], and Cryo-FIB to prepare TEM samples from specific sites [210].

As noted in Chapter 2, the topography effect is a major factor for introducing artefacts into SIMS signals. Figure 5.11 shows the effect of topography on the $^{12}C^{14}N^-$ image of intact cells. In order to reduce the topography of cell surfaces to obtain reliable chemical distributions in these samples, FIB milling can be used to create a flatter surface for NanoSIMS imaging. I have explored the possibility of carrying out this kind of sectioning on complete cells cultured on coverslips.

Figure 5.12 is the picture of the alignment of the sample with the Ga^+ source inside the NVision. The ion beam was aligned as parallel as possible to the substrate to create a flat surface of the cell for imaging. The intact cells can first be visualized with the ion beam, to ensure alignment of the substrates. The top of the cells can then be cut off to expose the inside of individual cells (Figure 5.13). This image also shows the effect of the ion beam on the cell surface and on the substrate. The substrate is also cut due to imperfect alignment of the beam, which also results in milling of the substrates.

NanoSIMS analysis was conducted on this area with ^{12}C, ^{16}O, $^{12}C^{14}N$, $^{12}C^{15}N$ and ^{31}P images and SE signals as shown in Figure 5.14. Comparing with Figure 5.11, the surface is much flatter and there is less beam damage on the surface due to the reduced pre-sputtering time needed with the 16 kV Cs^+ beam. The images show that in this region there are three cells closely attached. The improved surface flatness in particularly clearly shown in the SE image which is almost featureless. The $^{31}P^-$ image is helpful in positioning the 3 individual nuclei, and nucleoli can be seen most clearly in the $^{12}C^{15}N^-$ and $^{31}P^-$ images. This sample was exposed to ^{15}N-labelled glutamine for 24 hours. The $^{15}N/^{14}N$

image (Figure 5.15) shows a very obvious variation in ^{15}N concentration in the three cells, and local variations in single cells. The top right cell shows a higher $^{15}N/^{14}N$ ratio, which means that it incorporated more ^{15}N-labelled glutamine in the 24 hour exposure period. In all three cells, the $^{15}N/^{14}N$ ratio is higher in the nucleolus than in other areas in the nucleus.

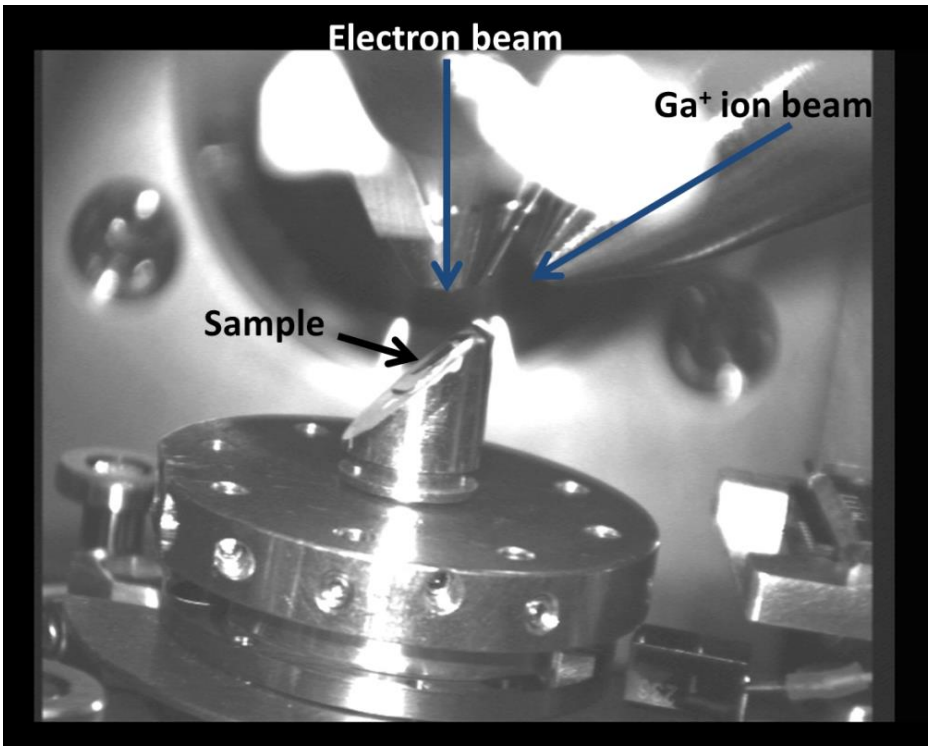

Figure 5.12: Picture of the sample alignment inside the FIB chamber.

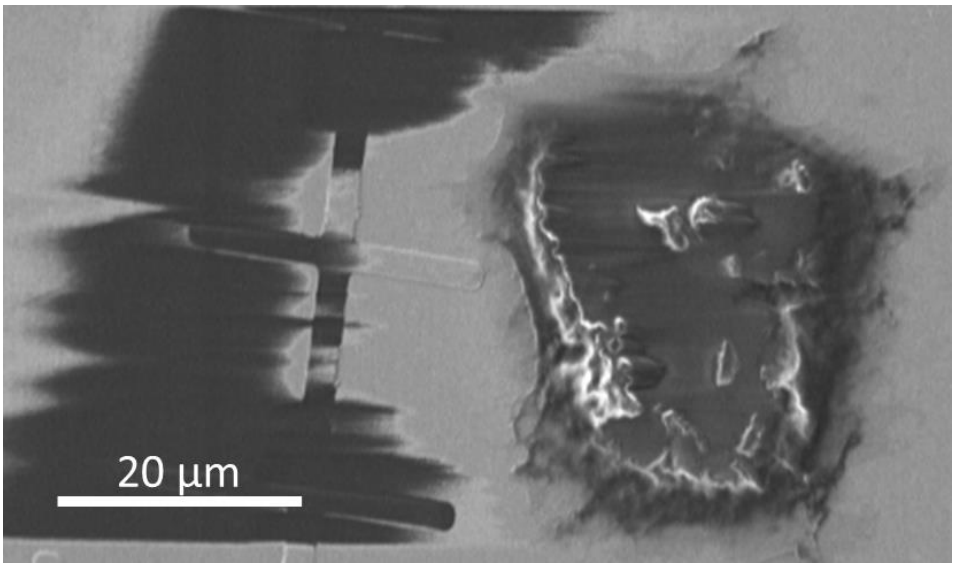

Figure 5.13: Secondary electron image of the cell after sectioning with the FIB.

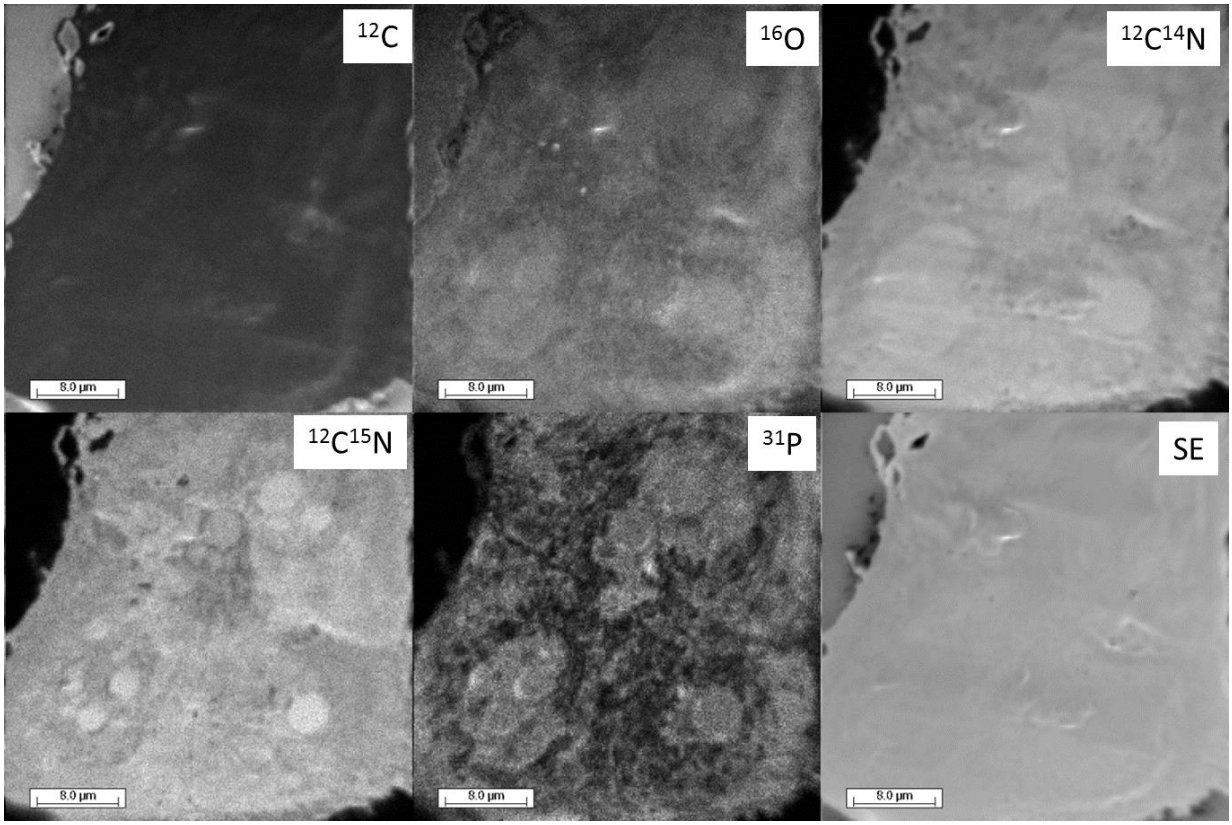

Figure 5.14: ^{12}C, ^{16}O, $^{12}C^{14}N$, $^{12}C^{15}N$, ^{31}P and SE NanoSIMS images of a group of FIB cut cells. Scale bars: 8 µm.

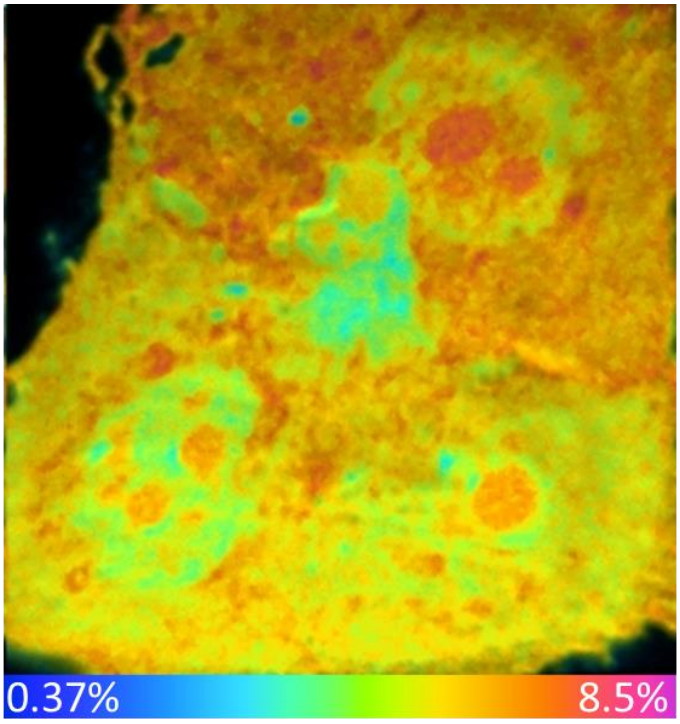

Figure 5.15: $^{15}N/^{14}N$ HSI NanoSIMS image of the FIB cut cells. Size of images: 35 µm × 35 µm.

The flatter surface also makes it more possible to reconstruct a 3D-view of the cell by imaging frame by frame on the same area. The cross-section view is stretched in the Z direction to show how the $^{15}N/^{14}N$ ratio and $^{31}P/^{12}C$ ratio changes in depth through the cell. The changes in colour in the z direction probably mean the transition between two areas or structures within the cell. Figure 5.16 also shows obvious correlations of high $^{15}N/^{14}N$ ratio areas with the low $^{31}P/^{12}C$ areas identified by red boxes.

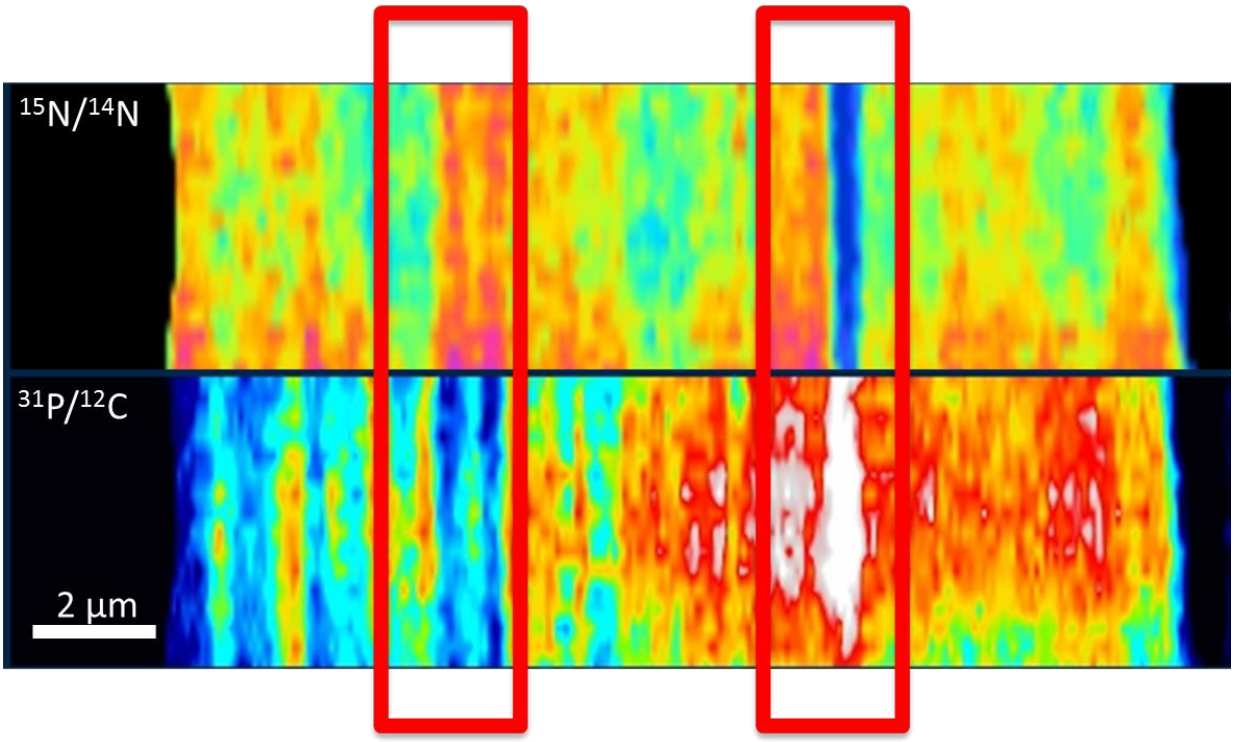

Figure 5.16: A side view of a reconstructed $^{15}N/^{14}N$ (top) and $^{31}P/^{12}C$ (bottom) ratio images. Thickness of the view is about 500 nm.

FIB sample preparation could be also useful on resin embedded samples. The NVision is an instrument equipped with both ion beam and electron beam. The sputtering ability of the ion beam has been demonstrated above. The backscattered electron signal enables the NVision to visualize structures in single cells in great detail, which can be used to choose areas of interest and then expose these areas of interest for NanoSIMS analysis with ion beam milling.

This is a proof of principle experiment for sample preparation by FIB milling. This method has been proven useful to create a flatter surface and reduce the Cs^+ dose needed for pre-sputtering, but it is very time-consuming, so this method was not used for the NanoSIMS experiments in this thesis.

5.4.4 Glutamine Incorporation – Exposure Time

Cells exposed to ^{15}N-labelled glutamine for 2, 8, 16 and 24 hours were analysed by the NanoSIMS. Figure 5.17 consists selected representative images of cells exposed for different lengths of time, and the relationship between the $^{15}N/^{14}N$ ratio in individual cells and exposure time to ^{15}N-labelled glutamine. Five to ten cells were analysed for each exposure time. All images are set to different colour scales to show the contrast within single cells. Variations in ^{15}N concentration between cells are visualized here, even for cells prepared under the same conditions. This is an advantage of the NanoSIMS measurement, obtaining results from single cells rather than averaged results from many cells.

The overall $^{15}N/^{14}N$ ratio in the cells seems to increase roughly linearly with exposure time to ^{15}N-labelled glutamine, and in the first 24 hours the cells are still taking up glutamine. This increase can also be seen in the concentration scales in the 4 selected images, where the peak concentration increases from 0.45% to 9 %. The average $^{15}N/^{14}N$ ratios are around 0.8%, 1.8%, 3.3% and 4.7% for cells exposed to ^{15}N-labelled glutamine for 2, 8 and 24 hours respectively, and the rate of incorporation of ^{15}N is 0.18% per hour. I presume that this increase in $^{15}N/^{14}N$ corresponds to the incorporation of labelled α-N by all three pathways, including proteins, nucleotides and glucosamine, as shown in Figure 5.6.

5.4.5 Subcellular Analysis

In order to visualize ^{15}N variations inside the single cells seen in the images above, higher magnification and higher resolution images were taken. Figure 5.18 is a mosaic of six 10 µm by 10 µm $^{15}N/^{14}N$ HSI images from a single cell. The D1 aperture was put to number 4 to achieve high spatial resolution to take these images, and local variations of the $^{15}N/^{14}N$ ratio are clearly seen.

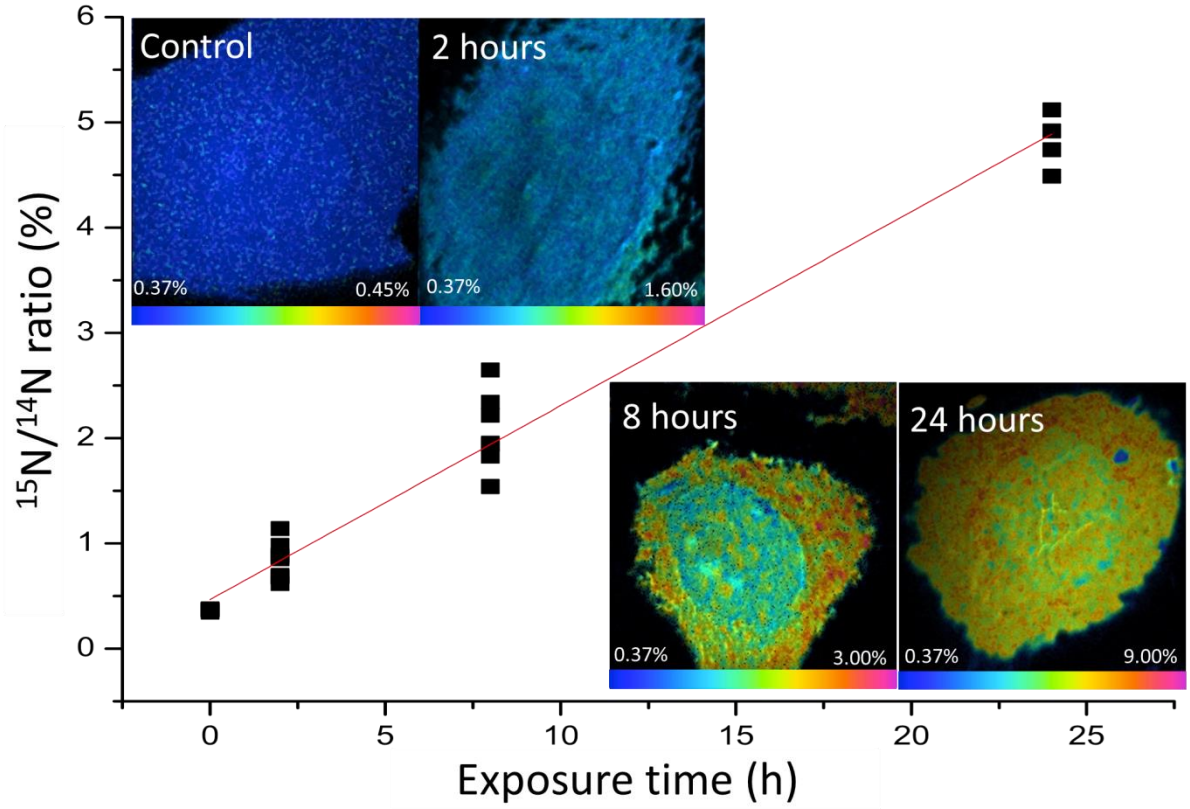

Figure 5.17: The relationship between the measured $^{15}N/^{14}N$ ratio and exposure time to ^{15}N-labelled glutamine, and representative $^{15}N/^{14}N$ images for each exposure time. Size of images: 30 µm × 30 µm. Line scans of two selected areas show the quantitative variations in the $^{15}N/^{14}N$ ratio in cytoplasm and nucleus respectively. The variation in the nucleus along line scan 2 is 55% over a distance of only 300 nm. The highest measured ratio in the cytoplasm reached 6.0%. I assume that these variations in the ^{15}N represent the distribution of the metabolites of glutamine. By using the $^{15}N/^{14}N$ ratios strong effects of surface topography should be avoided since both CN isotope signals should respond the same way to topography enhancements to the local signal intensity.

Although from these high resolution images we can see variations in ^{15}N concentration, it is hard to identify the organelles or cellular structures from which the higher ^{15}N signals originate. To gain a better understanding of subcellular metabolism it is important to obtain the structural information on these same cells, so correlating the NanoSIMS images with complementary techniques was significant focus of my work in this project.

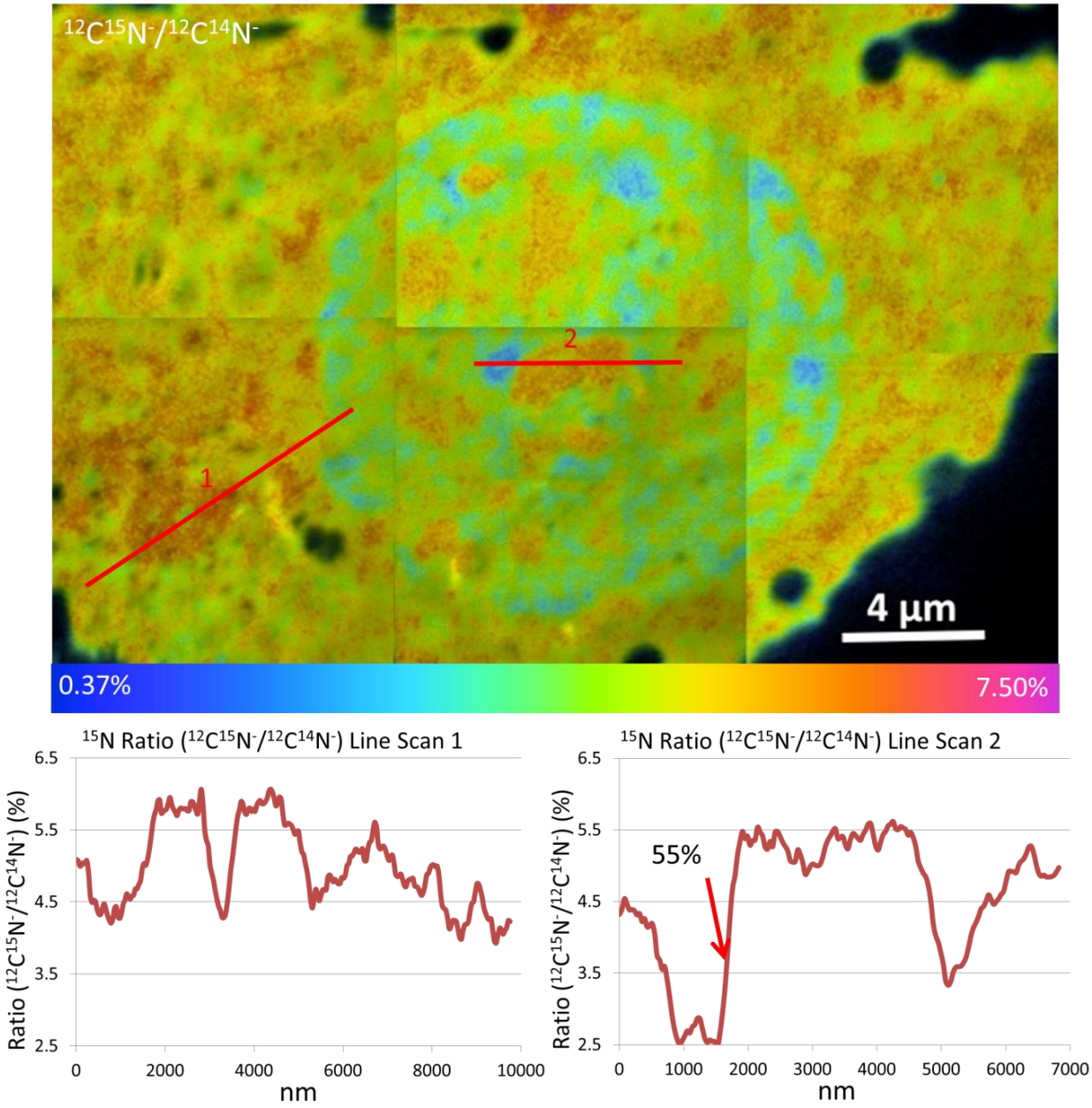

Figure 5.18: Mosaic of NanoSIMS $^{15}N/^{14}N$ HSI images of an intact cell. Line scans across two areas in the cytoplasm and nucleus show the variation of the $^{15}N/^{14}N$ ratio.

5.4.6 Analysis of Intact Cells with Correlative NanoSIMS and Complementary Techniques

This section will discuss a few methods which I have explored to correlate the chemical information obtained by the NanoSIMS to other information to improve the understanding of subcellular metabolisms on intact cells.

Optical techniques have the advantage of being non-destructive, and developments of fluorescence labelling methods make it easy both to reveal molecular specific information and to show the organelles with different types of trackers [211, 212]. Working with Dr. Adrian Harris and Dr. Elena Favaro, I have combined conventional florescence imaging with chemical analysis. The first part of this work was to establish reliable methodologies for sample preparation and multi-modal imaging.

Figure 5.19 shows correlative NanoSIMS and fluorescence images on the same cell, exposed to ^{15}N-glutamine for 24 hours. The cell was imaged by confocal microscopy in solution, and was labelled with fluorescence probes on the nucleus (purple) and ER (yellow) respectively. Then this cell was chemically fixed and dehydrated on the coverslip. The same cell was localized using the alphanumeric grids on the coverslip and imaged by the NanoSIMS to visualize the chemical and isotopic information. The ^{15}N/^{14}N HSI image clearly shows the local variations in the ^{15}N/^{14}N ratio, with a high ratio in the nucleus and a few low ratio areas in the cytoplasm. However, there is no obvious correlation between the ^{15}N distribution and the ER. This is an example of the feasibility of correlative NanoSIMS and fluorescence microscopy on intact cells. This method could be useful to visualize if the molecules of interest are localized in the certain organelles or structures [109], or colocalize with a fluorescence labelled protein in single cells.

AFM is another technique which gaining more and more attention in the biological community [159]. It has been successfully used to study AMP and lipid bilayer interactions as discussed in Chapter 4. Figure 5.20 contains AFM and NanoSIMS images on the same cell. The AFM image shows the details of the topography on the surface of the cell. The highest parts of the cell are the two nucleoli. The NanoSIMS images were taken from the same cell to show the chemical distribution, which also shows a strong topography effect. The AFM is not only a topography imaging technique, but also has the ability to measure cell adhesion and elasticity [213, 214]. If these types of information and chemical information are needed to understand a biological mechanism, this method could be especially useful.

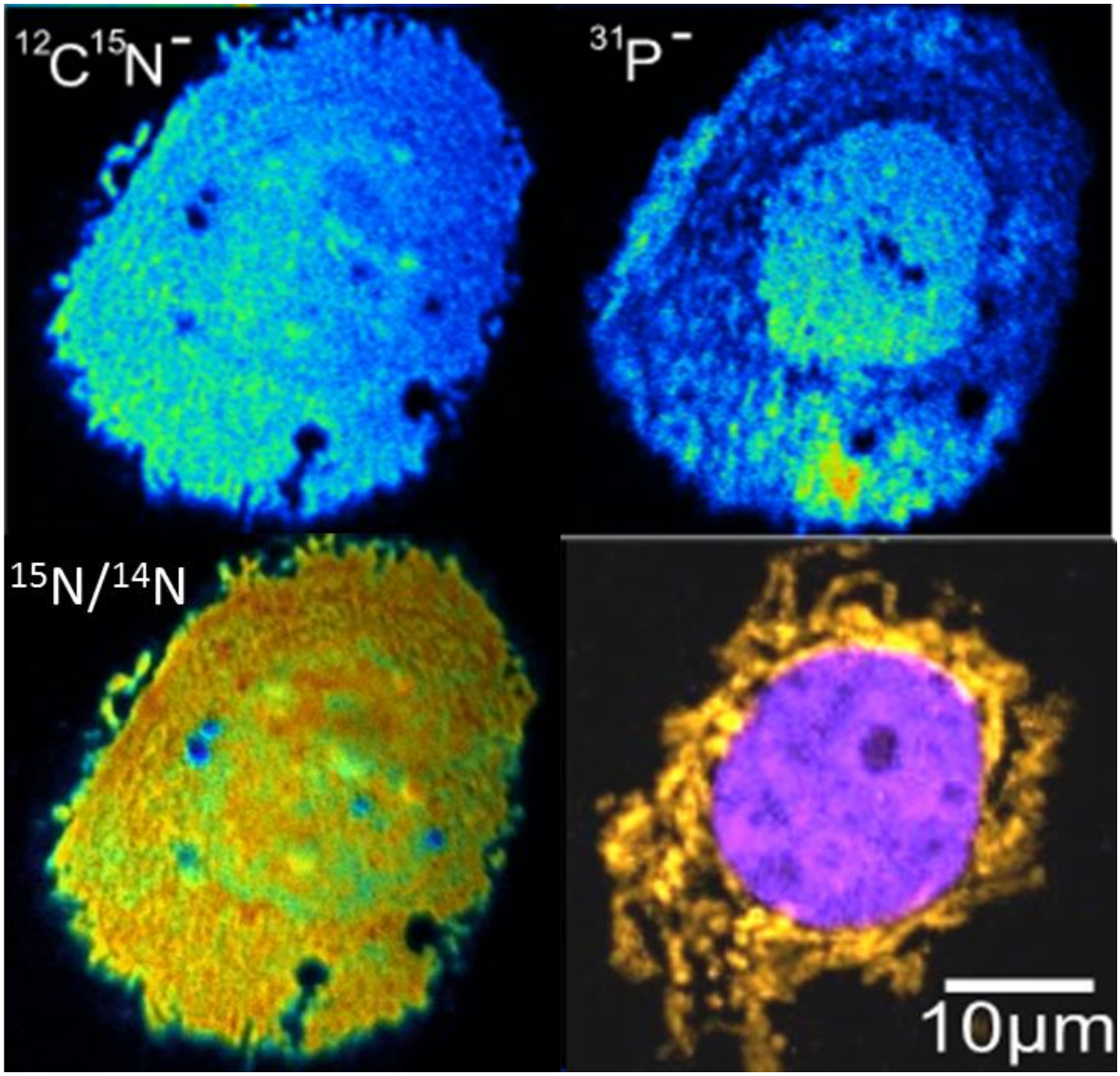

Figure 5.19: Correlative NanoSIMS and confocal microscopy (bottom right) imaging on the same intact cell sample.

So correlative fluorescence microscopy, AFM and NanoSIMS can enable us to obtain different information from the same intact cells. However, there are also some limitations of these two methods. Firstly, the depth resolution of the fluorescence microscopy is not as good as the NanoSIMS, which means the information obtained from fluorescence microscopy combines information from different depths through the cell, while the NanoSIMS images are only from a layer of tens of nanometres thick on the surface. The difficulty of this correlative imaging technique would be to image the same volume of the cell, which may affect the final data interpretation. The other limitation of correlative fluorescence microscopy and NanoSIMS imaging is the complexity of

fluorescence labelling. Even though there have been very many developments of all types of labelling compounds and methods, the complexity of the sample preparation especially if many types of the organelles or molecules are to be labelled is still a problem. Correlative AFM and NanoSIMS imaging has been shown in Chapter 4 to give interesting results, but this method is only suitable to image the cell surface, and gives no information through the thickness of the cell. In order to overcome these limitations of these two techniques for studying subcellular metabolism, I have developed reliable protocols to conduct correlative Backscattered Electron (BSE) and NanoSIMS imaging to study metabolism in single cells, and which can potentially be more widely applied. To overcome the limitations of correlative fluorescence microscopy, AFM and NanoSIMS analysis, this section will discuss the protocols for correlative BSE and NanoSIMS analysis.

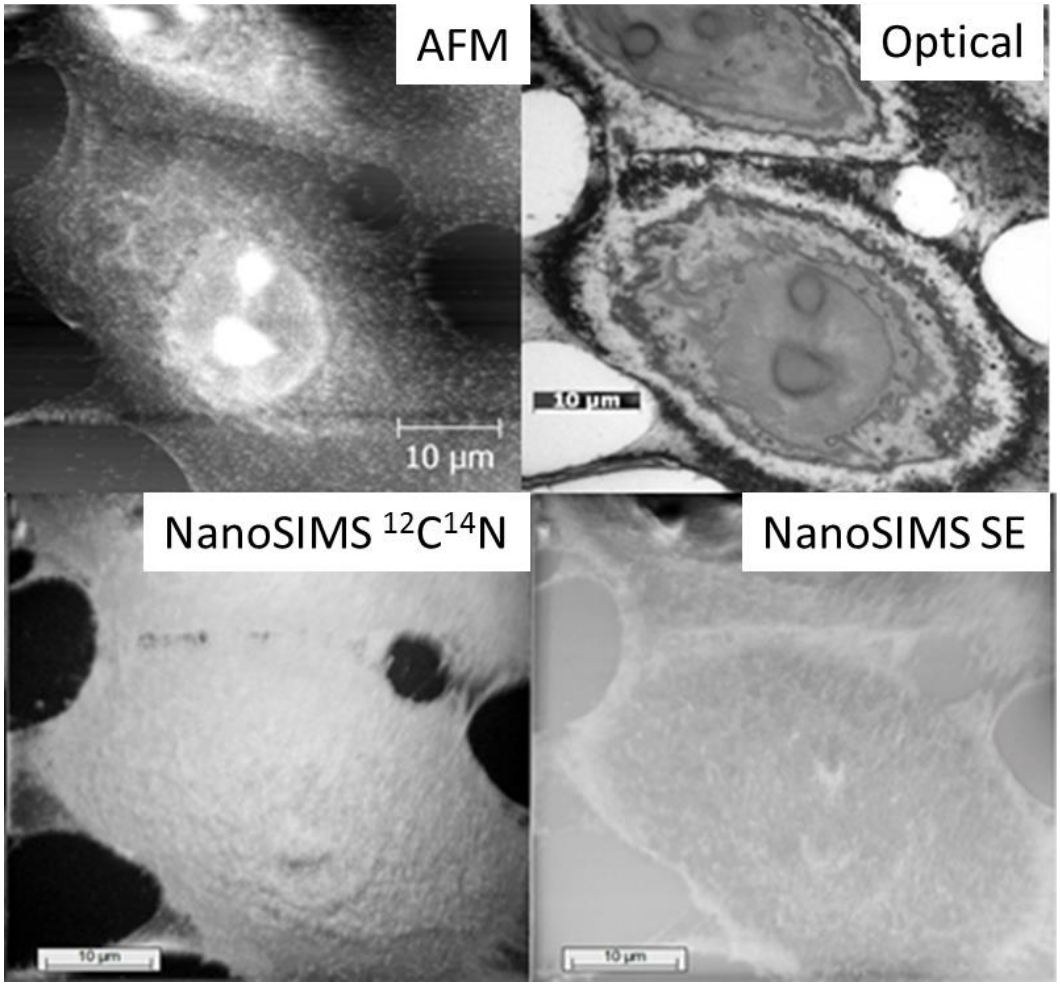

Figure 5.20: Correlative AFM, optical and NanoSIMS imaging on intact cell samples. Scale bars: 10 µm.

5.4.7 Correlative NanoSIMS and BSE imaging

5.4.7.1 Selecting the Cs^+ dose for correlative BSE and NanoSIMS imaging on thin sections

While determining the steady state conditions for these sectioned samples it was found they responded slightly differently to the Cs^+ implantation compared to intact cells, and also to achieve similar image volume for both techniques, the Cs^+ dose needs to be as low as possible. Figure 5.21 shows how the counts for $^{12}C^-$ and $^{12}C^{14}N^-$ varied as a function of Cs^+ dose on a 5 nm platinum coated 500 nm section of heart tissue sample with a primary ion beam current of 1.3 pA and 5 µm raster size. The $^{12}C^{14}N^-$ signal stabilises immediately after sputtering away the platinum coating at a primary ion dose of about 6.5×10^{15} ions/cm^2. This rapid stabilization enables imaging of the top surface of the sample for tracking ^{15}N-labelled molecule distribution in the same material imaged in the AFM, as shown in Chapter 4. This also makes it possible to conduct correlative BSE and $^{15}N/^{14}N$ NanoSIMS analysis of a very similar imaging volume. The primary ion dose required for reliable analysis of $^{13}C^-$ and $^{12}C^-$ was set to about 6.5×10^{16} ions/cm^2 to ensure steady state for the $^{12}C^-$ signal.

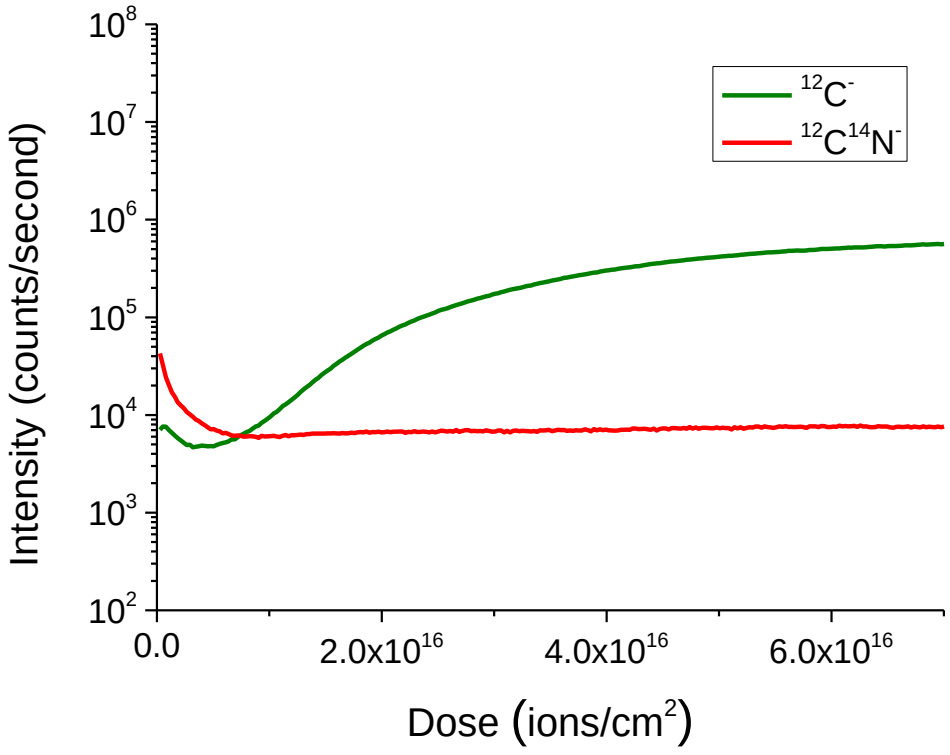

Figure 5.21: Depth profile of $^{12}C^-$ and $^{12}C^{14}N^-$ on a 500 nm section coated with 5 nm of platinum.

5.4.7.2 Developing the Correlative BSE and NanoSIMS analysis method

The BSE signal is very sensitive to atomic number contrast, so samples stained with OsO_4 as is common for electron microscopy analysis are also suitable for BSE imaging. As described above, a modern scanning electron microscope can also offer a spatial resolution for low voltage BSE imaging of a few nanometres, and samples prepared for BSE are also ideal for NanoSIMS imaging. I have found that 500 nm sections are appropriate for both BSE imaging and NanoSIMS analysis. The use of low accelerating voltages means that the BSE signals are generated from the top 2 – 3 nm of the section surface, very similar to the volume analysed with NanoSIMS imaging.

As an indication of the kind of data that can be obtained by combining BSE and NanoSIMS, I have selected a typical data set in Figure 5.22. As described in section 5.3.2, MCF7 cells were exposed to ^{15}N-glutamine and fixed, dehydrated, embedded, and cut to sections for analysis. Organelles can be revealed very clearly in the BSE images (Figure 5.22a), which can then be used to identify the location of chemical information in the NanoSIMS image (Figure 5.22b). These images show that the nucleolus is heavily labelled with ^{15}N; the ^{15}N/^{14}N ratio is about 4.6% after 16 h of exposure, more than ten times higher than the natural abundance of ^{15}N. There is also heavy labelling of the nucleus, Golgi, and ER (Figure 5.22c). Analysis of 10 cells has shown average ^{15}N/^{14}N ratios of about 3.0% ± 0.5%, 3.6% ± 0.3%, 3.4% ± 0.3% in the nucleus, Golgi and ER respectively (Figure 5.22d). This data shows that combining these techniques is able to reveal quantitative chemical information in specific areas, and the imaging experiment is designed to ensure that the imaged volumes in the two techniques are as similar as possible. In this chapter, the effects of hypoxic conditions and PYGL gene knockdown will be studied with this method.

5.4.7.3 Effects of Hypoxic Condition on Glutamine Metabolism in Cancer

Hypoxia is a condition when the tissue has a reduced oxygen supply below the normal level. Hypoxia is common condition since very rapid growth requires a larger than normal oxygen supply and unless there is an enhanced vascular structure, hypoxic conditions are easily achieved around growing

tumours. Hypoxic conditions have been proved to induce a variety of biolgical responses in cells [215]. These hypoxic-induced pathways are also reported as good candidates for targeted therapy [216]. More details on hypoxia in cancers can be found in the reference [217]. This section will focus on correlative BSE and NanoSIMS analysis of cells cultured under normal and hypoxic conditions where we can follow the glutamine metabolism at specific sites in the cells.

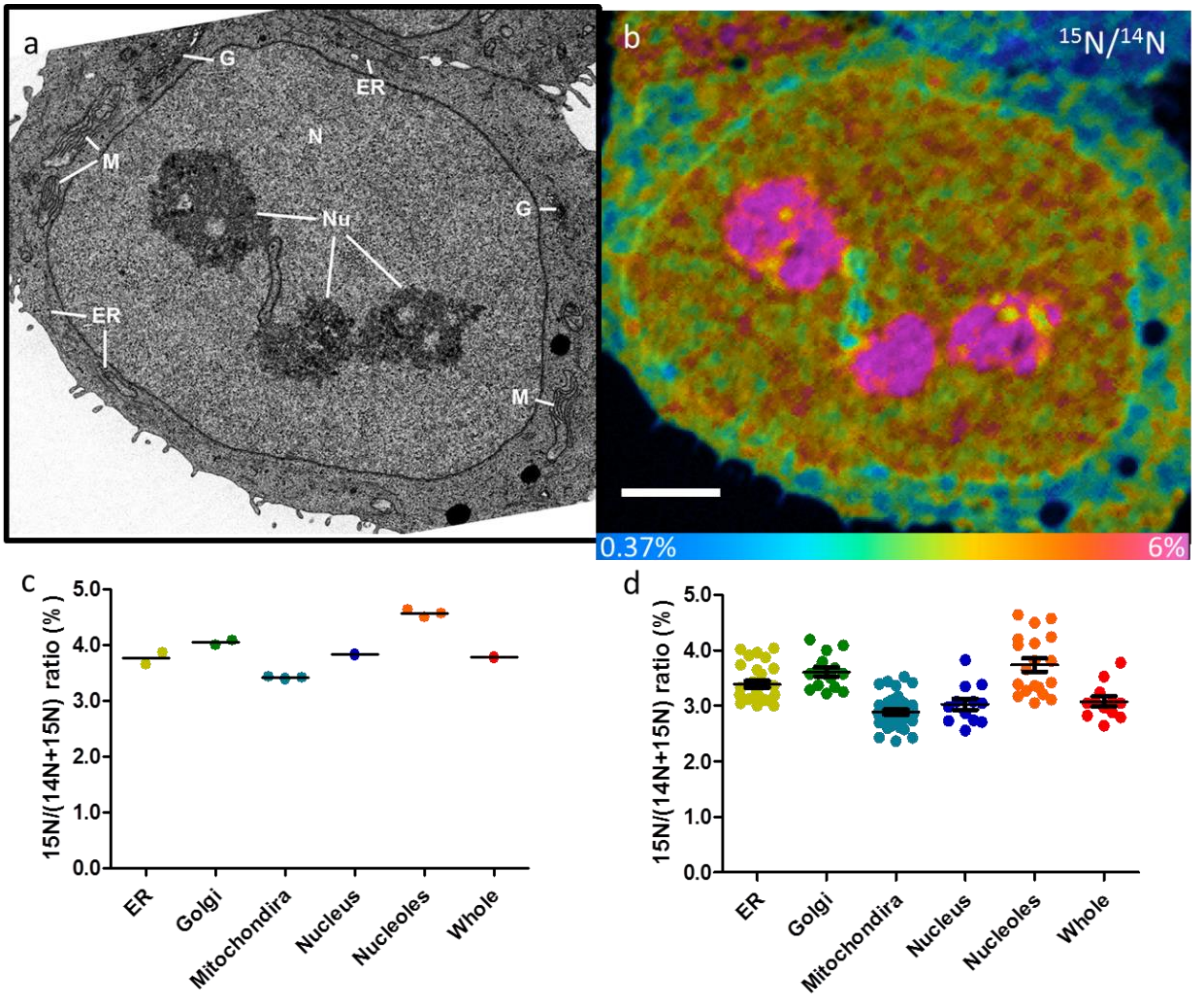

Figure 5.22. Correlative BSE and NanoSIMS imaging on single cells. (a) BSE image of a typical MCF7 cell exposed to ^{15}N-glutamine for 16 h. The organelles are identified with white lines: nucleolus (Nu), nucleus (N), Golgi (G), ER (ER), and mitochondria (M). (b) $^{15}N/^{14}N$ HSI NanoSIMS image of the same cell enables quantitative measurement of the $^{15}N/^{14}N$ ratio in specific organelles. (c) $^{15}N/^{14}N$ ratio in different organelles of the cell. (d) Statistical analysis of 10 single cells showing $^{15}N/^{14}N$ ratios in organelles. Scale bar, 3 µm. Colour scale of $^{15}N/^{14}N$ ratio image: 0.37% – 6%.

Another factor that will be studied in this section is the effect of glycogen phosphorylase (PYGL). PYGL is gene one of the 99 genes included in the hypoxia metagene [218]. My collaborators have

showed its importance on supporting cell proliferation [218]. The knockdown of PYGL would result in the accumulation of glycogen, which is a store of glucose. More detailed research also revealed that glycogen degradation by PYGL can provide a source of G6P, which can be used to maintain the reduction of NADPH and glutathione, and the synthesis of nucleotides, as shown in Figure 5.23 [218]. This section will analyse PYGL gene knockdown effects on glutamine metabolism in cancer.

5 samples were prepared to study the effects of the hypoxia condition and PYGL gene knockdown:

- Sample 1: Control cells.
- Sample 2: Cells exposed to ^{15}N-labelled glutamine for 16 hours.
- Sample 3: PYGL gene knockdown cells exposed to ^{15}N-labelled glutamine for 16 hours.
- Sample 4: Cells exposed to ^{15}N-labelled glutamine for 16 hours under hypoxic conditions.
- Sample 5: PYGL gene knockdown cells exposed to ^{15}N-labelled glutamine for 16 hours under hypoxic conditions.

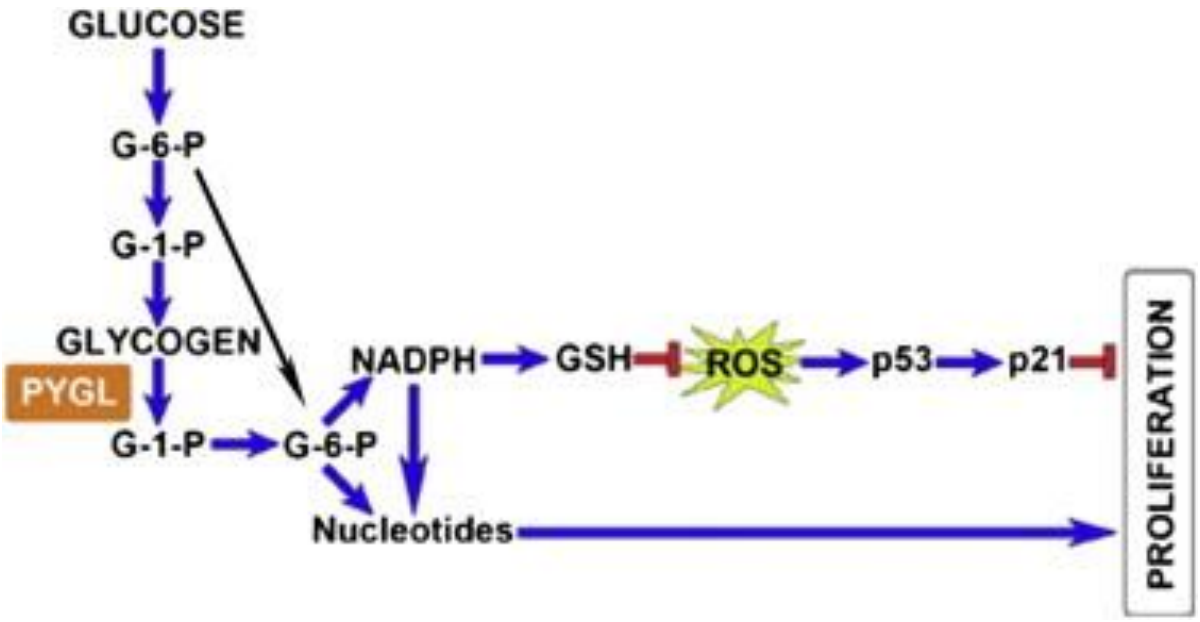

Figure 5.23: Summary of the PYGL gene effect on the glucose and glycogen metabolism. From reference [218].

The analysis method showed in Figure 5.22 was used to obtain ^{15}N/^{14}N ratio data in the nucleus, nucleolus, mitochondrion, ER, and Golgi and the ratios in the whole imaged cell were also measured. Figure 5.24 gives selected representative ^{15}N/^{14}N images of the 5 samples. All the images were set to

the same colour scale, and the overall impression from the colour differences of the images shows that:

- The control cells have, as expected, the natural abundance of $^{15}N/^{14}N$.
- There is a significant colour change in the cells exposed to ^{15}N-labelled glutamine for 16 hours showing a substantial increase in $^{15}N/^{14}N$ ratio.
- Sample 3 shows more red areas which means that the $^{15}N/^{14}N$ ratio in those cells is generally higher than the sample 2.
- There are also some low ratio areas observed in sample 3 cells.
- The images from sample 4 are greener than from sample 2 and sample 3, which mean the hypoxic condition reduced glutamine incorporation into those cells.
- The $^{15}N/^{14}N$ ratio in sample 5 is generally higher than in sample 4.

Quantified, site specific, results can be obtained from ImageJ and the correlative BSE images. Figure 5.25 gives selected BSE images of some of 70 cells analysed in this project. All the organelles are clearly revealed in these images. Combined with 15 of individual images like those in Figure 5.24and Figure 5.25, and extracting the measurements showing in Figure 5.22, we are able to achieve the results shown in Figure 5.26 and Figure 5.27.

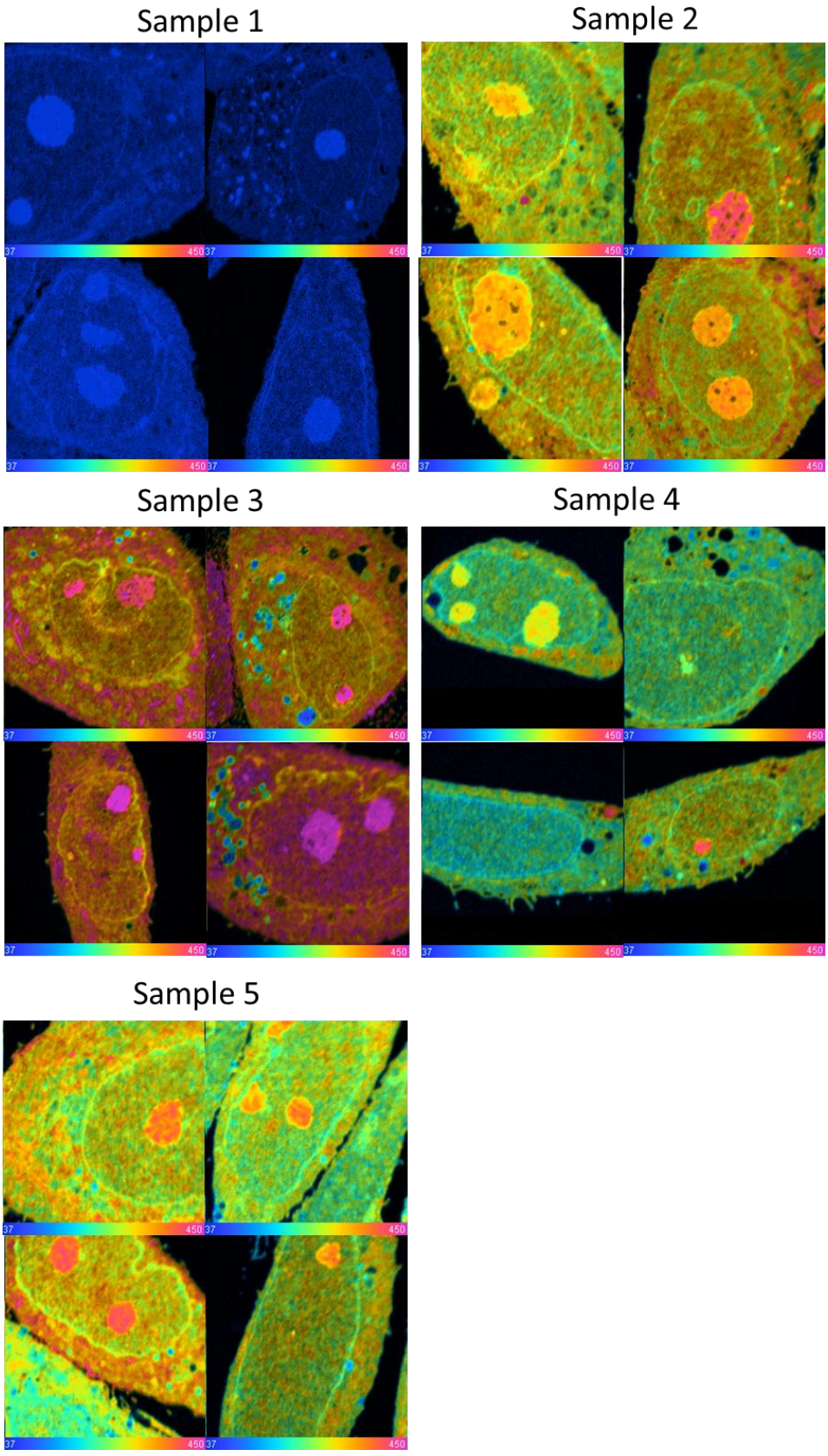

Figure 5.24: Selected representative $^{15}N/^{14}N$ HSI images of the samples used to test the effects of hypoxia and PYGL gene knockdown. Size of images: 20 µm × 20 µm. Ratio scale: 0.37% - 4.5%.

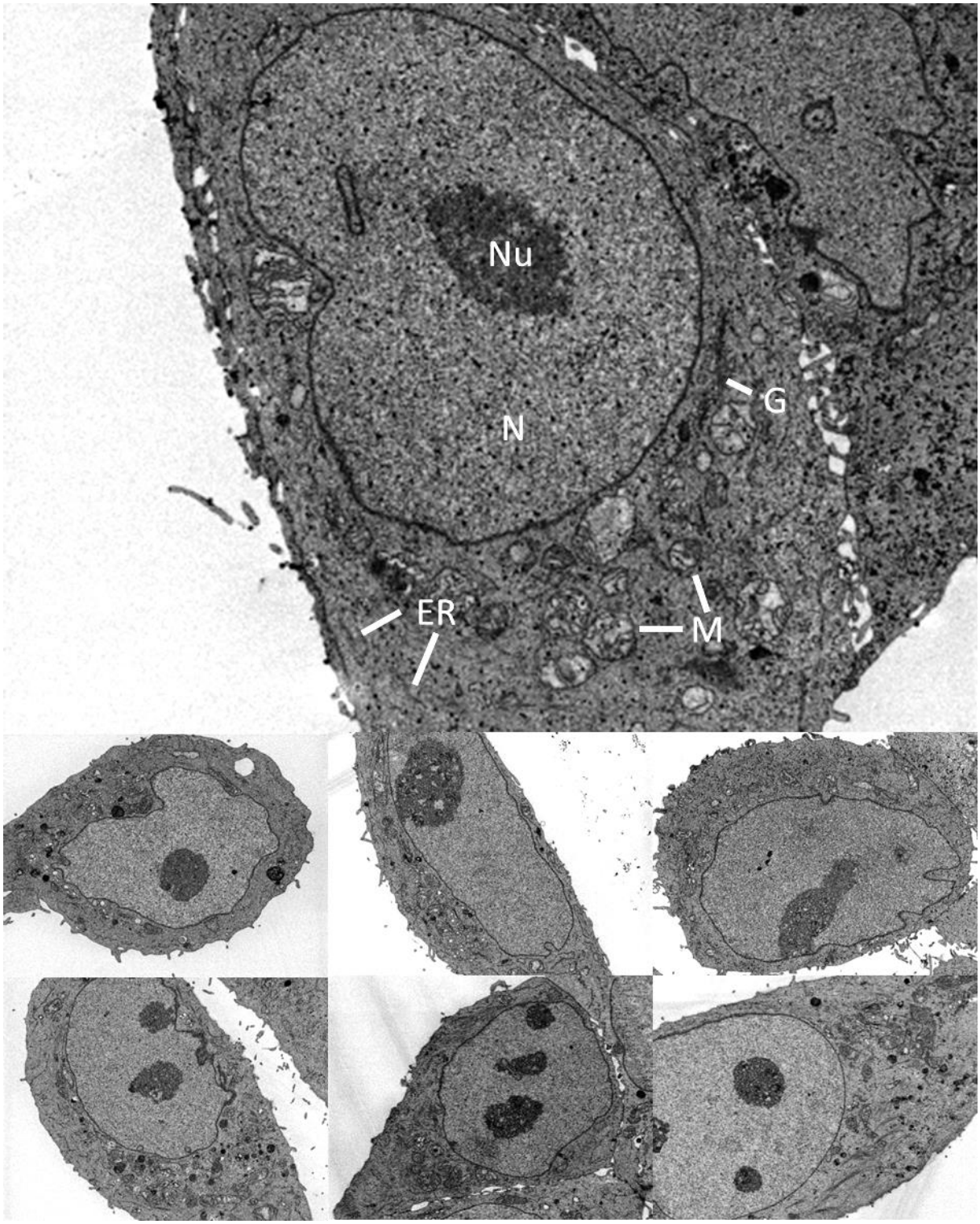

Figure 5.25: Selected BSE images of analysed cells. Nucleus (N), Nucleolus (Nu), ER (ER), Golgi (G) and mitochondria (M) are identified in the top image. Size of images: 15 µm × 15 µm.

Figure 5.26 and Figure 5.27 summarise the results from cells analysed with correlative BSE and NanoSIMS analysis. The measured $^{15}N/^{14}N$ ratios in different organelles are shown in Figure 5.26 for samples 2, 3, 4 and 5. This data shows both significant variation of ^{15}N incorporation into single cells with the same treatment, and significant variations in ^{15}N concentrations are found in different organelles. The ratios in Golgi and nucleoli are highest, and mitochondria show slightly lower $^{15}N/^{14}N$ ratios. This set of experiments was carried out while developing my experimental protocols, and only 10-15 cells were imaged and analysed for each condition. The limited number of data points in this figure are only used to show the capability of the method, and the inherent scatter in this kind of data. Many more images would needed for a rigorous statistical analysis. To compare the effects of the treatments of the 5 samples, Figure 5.27 gives the ratio results by organelle. The control sample (sample 1) has, as expected, an average ratio of 0.373% ± 0.003% (mean ± SD). The cells exposed to ^{15}N-labelled glutamine for 16 hours incorporated ^{15}N into the cells, and the $^{15}N/^{14}N$ ratio reached 3.39%, 3.61%, 3.74%, 3.03% and 2.89% in ER, Golgi, nucleolus, nucleus and mitochondrion respectively. More interestingly, the $^{15}N/^{14}N$ ratio in the PYGL gene knockdown cells shows a higher $^{15}N/^{14}N$ ratio in all the organelles and also in the whole cell. This means that blocking one pathway of PYGL increased the activity of glutamine metabolism. These increases are 19.2%, 15.0%, 20.1%, 15.8%, and 14.9% in ER, Golgi, nucleoli, nuclei and mitochondria respectively. In sample 4, the hypoxic condition decreased the incorporation of glutamine in 16 hours, and the effect of the hypoxia is different in different organelles. Nucleoli and nuclei are the two structures were affected most, 10.0%, 3.0%, 19.7%, 20.8% and 23.9% decrease in ER, Golgi, nucleoli, nuclei and mitochondria respectively. Two tailed t tests were carried out on all the data, and the results show that the hypoxic condition for the PYGL gene knockdown cells also shows significantly ($P<0.0001$) increased $^{15}N/^{14}N$ ratios in the nucleoli and nuclei, but the effects on other organelles are not statistically significant. We can understand this result because the PYGL knockdown blocked the glycogen pathway to produce G-6-P, which is an important source for nucleotides synthesis. The increase of the $^{15}N/^{14}N$ ratio is 11.3% and 13.3% in nuclei and nucleoli respectively.

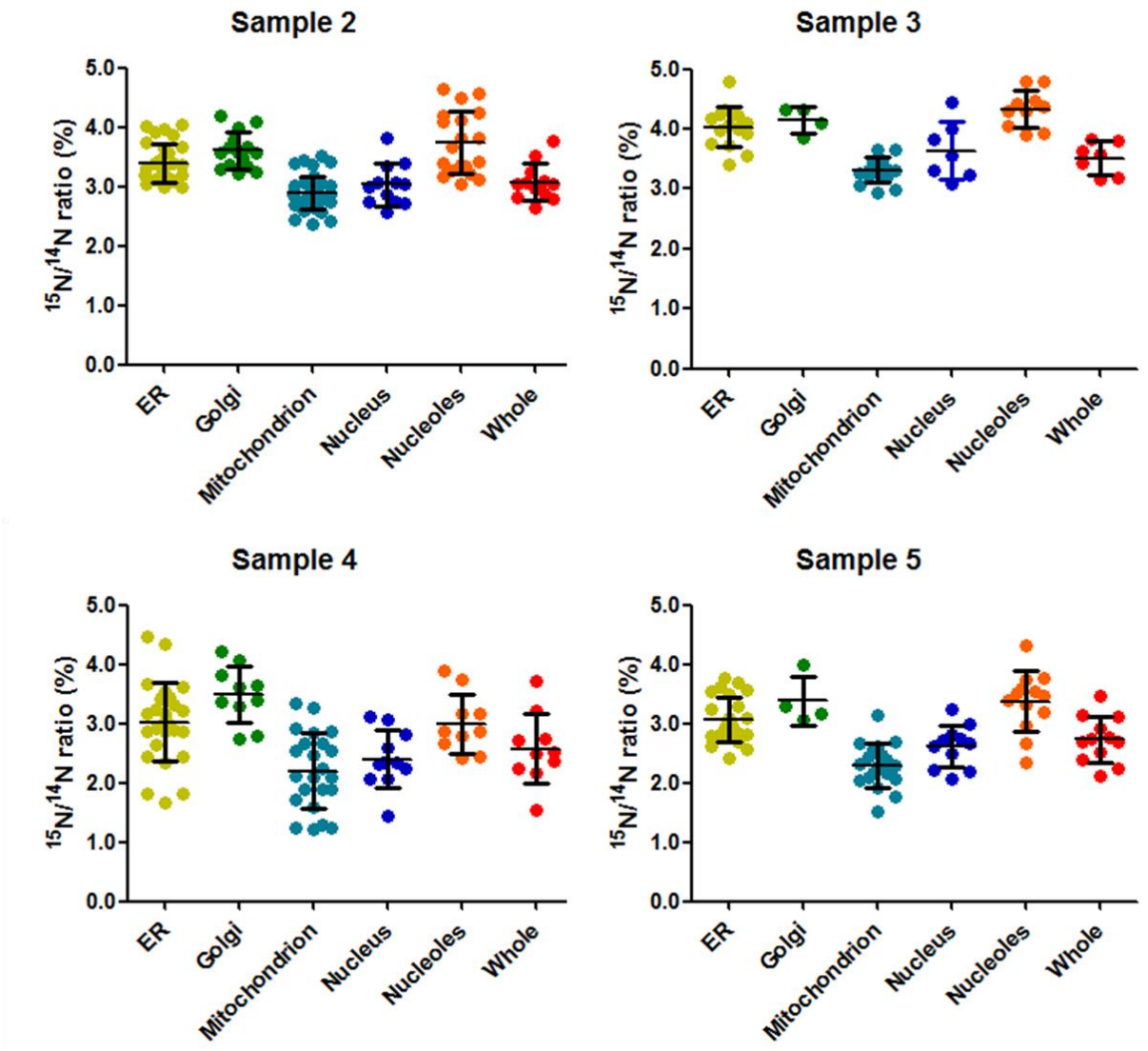

Figure 5.26: Sample view of the quantitative effects of the hypoxic condition and PYGL gene knockdown on glutamine metabolism in MCF7 cells.

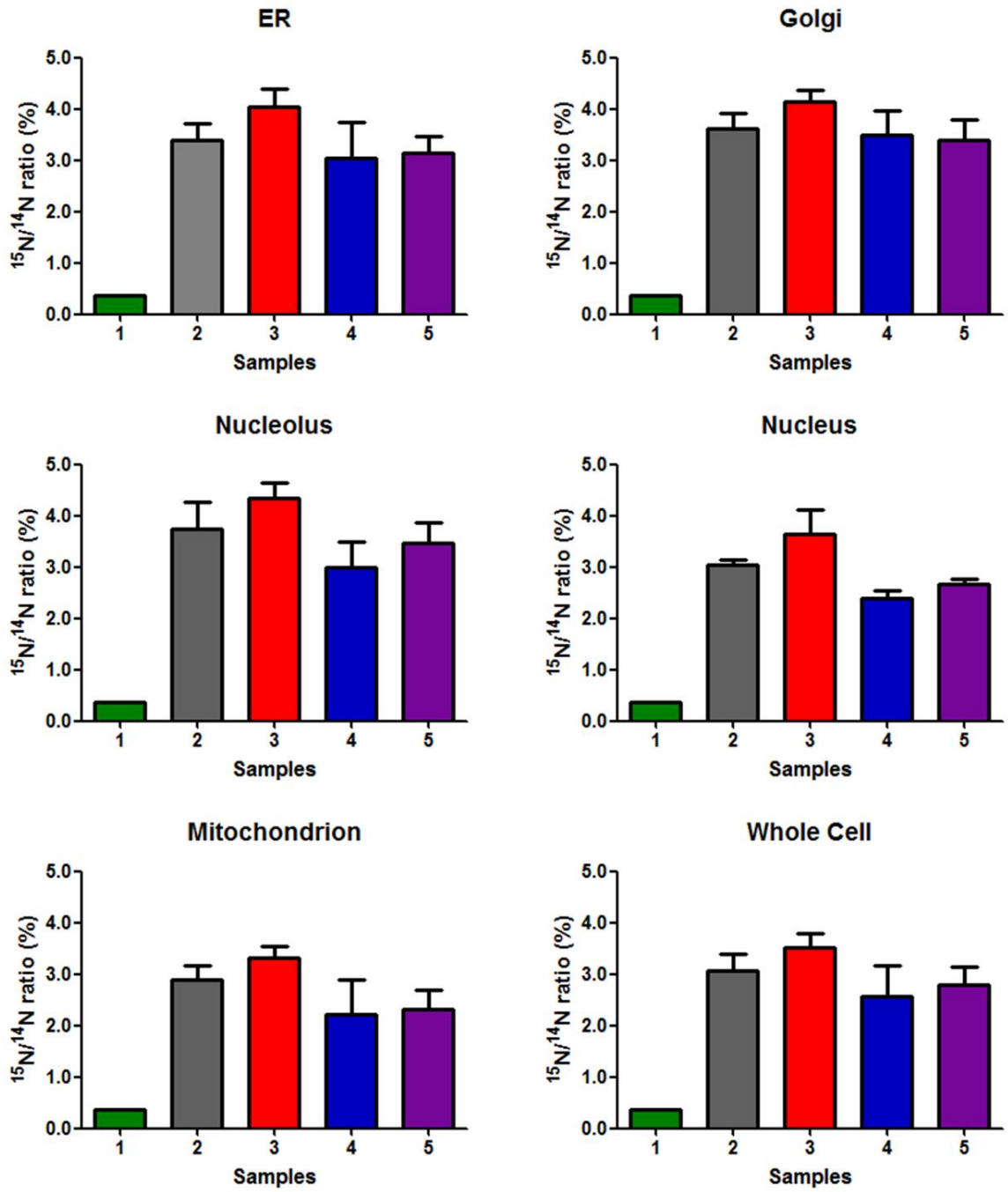

Figure 5.27: Organelle view of the quantitative effects of the hypoxic condition and PYGL gene knockdown on the glutamine metabolism in MCF7 cells.

In summary, the results here show that the hypoxic condition decreased the ^{15}N incorporation to all the organelles in the cells. The PYGL gene knockdown blocked the glycogen pathway, which can increase glutamine incorporation to all the organelles. The PYGL gene knockdown cells in a hypoxic

condition can increase the glutamine incorporation into the nucleus and nucleolus, but not significantly to other organelles.

5.4.7.4 Advantages of Correlative BSE and NanoSIMS analysis

Correlative EM and NanoSIMS analysis has been successfully used in many interesting studies [84, 96, 132]. All the EM images in those works were taken by TEM and mostly on consecutive sections. Figure 5.28 is a schematic of the comparison between correlative BSE and NanoSIMS analysis and correlative TEM and NanoSIMS analysis. Firstly, the BSE signals originate from the top few nanometres of the section. Simulations have shown that the interaction volume of a 2kV primary electron beam is about 10 nm, with most backscattered electrons originating from the top 1 nm [205]. The NanoSIMS also images a volume close to the surface for $^{15}N/^{14}N$ ratio information. Due to a low dose primary of ion implantation and secondary ion signal tuning on the surface, a thin layer of material (~10 nm) on the surface is removed before NanoSIMS imaging. A sequential TEM section will be cut before or after the NanoSIMS section, which makes the structural images recorded originate from a different volume of material than is studied by NanoSIMS. This may not be a problem if the structures or organelles of interest are large enough to appear in both sections, but will be misleading if the structures are smaller than 2 - 300 nm. Another advantage of correlative BSE and NanoSIMS analysis is that BSE imaging has more flexibility. It can image the section mounted directly on the coverslips while TEM still requires samples mounted on special TEM grids. The flat surface of the sections for BSE imaging also allows us to image areas up to a few square millimetres. However, the TEM grids will limit the areas can be imaged, and areas of interest need to be localized inside the squares in the grids. Finally, the thickness of the BSE samples is more suitable for NanoSIMS imaging than the 100 nm sections for TEM imaging as they are less fragile.

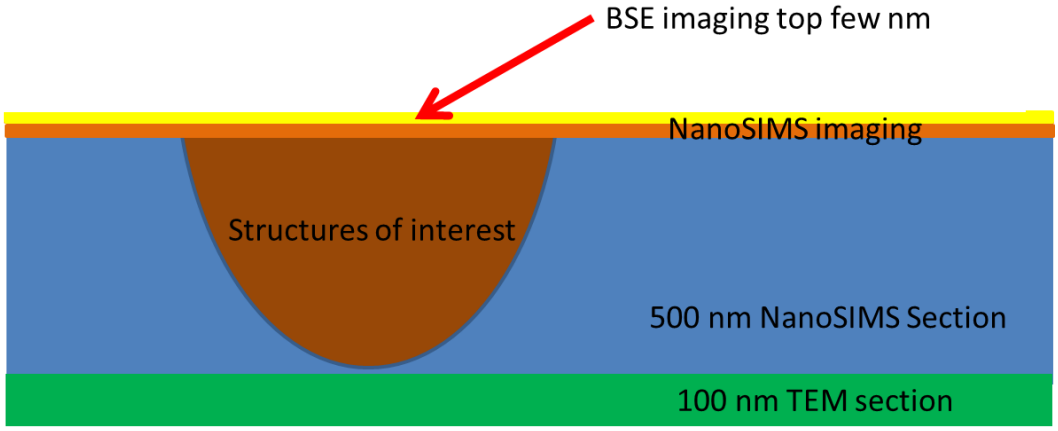

Figure 5.28: Schematic of the comparison between correlative TEM, BSE and NanoSIMS analysis. Image volume of BSE (yellow), NanoSIMS (orange), and the possible location of a sequential TEM section (green) are identified.

5.5 Summary

In this chapter, I have discussed the application of stable isotope labelling and NanoSIMS analysis to metabolism studies in single cells. The incorporation rate of the glutamine was measured in the intact cell samples, and showed a linear relationship between the $^{15}N/^{14}N$ ratio in cells and exposure time to ^{15}N-labelled glutamine. The rate of increase is 0.18%/hour. A FIB sample preparation method was also tested on intact cell samples, and is able to create a flatter surface for NanoSIMS imaging and minimize the topography effects than in the intact cell samples. A 3D image was also created from these FIB cut samples that is more representative of the real cell structures than a 3D image obtained from intact cell samples. Correlative fluorescence microscopy, AFM and NanoSIMS imaging was tried on the intact sample, which can provide different types of information. Both combinations are useful for some studies, but also have several limitations and were found not to be useful for this study.

Reliable protocols have been developed to conduct correlative NanoSIMS and BSE imaging, which enables us to observe both high resolution morphological and chemical information from the same cell surface. Hypoxic conditions and PYGL gene effects on the glutamine metabolism in cancer cells were chosen as examples to explore the abilities of these techniques, ensuring that the imaged

volume of the BSE and NanoSIMS is as similar as possible. The quantified effects of hypoxic condition and PYGL gene knockdown were studied, and quantitative effects on specific organelles were measured. The turnover speed in specific organelles can also be measured by studying cells exposed to the labelled glutamine for different periods under different conditions in conventional pulse/chase experiments. This correlative NanoSIMS and BSE imaging method can reveal the chemical information in specific organelles or areas of interest in single cells. This method can be extensively applied to track molecules in single cells and study biological processes at the subcellular level.

6 Tissue Analysis – Tracking Lipolysis Products

6.1 Introduction

This chapter discusses applications of NanoSIMS analysis to biological tissue samples with stable isotope labelling. The process we are focused on is lipid metabolisms and tracking the transport of the lipolysis products.

6.1.1 Lipid Uptake Mechanism

Lipids are a class of hydrophobic or amphipathic small molecules which include a broad group of molecules like fats, fat-soluble vitamins, waxes, sterols, monolycerides, diglycerides, phospholipids and others [219]. They have important functions in living organisms, such as energy storage, in the structural components of membranes as mentioned in Chapter 3, and they also act as important signalling molecules [220].

At the scale of the whole organism, the uptake of lipids is a complicated process starting with formation of micelles taken up by intestinal mucosal cell; transformation from nascent chylomicrons to mature chylomicrons and formation of lipoprotein lipase in the capillary cells and taken up by adjacent tissues. The chylomicron remnants will go through another complex process to enable more lipids to be taken up by tissues for use and storage. Regarding fatty acid take up by adjacent cells, triglycerides (TGs) cannot be transferred through biological membranes, so triglycerides within the core of triglyceride-rich lipoproteins (TRLs), chylomicrons and very low-density lipoproteins (VLDL) need to be hydrolysed by lipoprotein lipase (LpL) along the luminal side of capillaries when the chylomicrons are in the bloodstream [221].

Recent developments in the understanding of lipolysis include the discovery of the glycosylphosphatidylinositol anchored high density lipoprotein binding protein 1 (GPIHBP1) [221]. For decades, the mechanism by which LPL reached its site of action within the capillary lumen was unknown. In 2007, Stephen Young's team discovered a GPI-anchored protein, GPIHBP1, which has

been proved to have a critical function in lipolytic processing of TRLs, possibly by forming a platform for lipolysis by binding both LPL and chylomicrons [221, 222]. This discovery solved a long-standing mystery in plasma lipid metabolism and suggested how the LPL was transported to the luminal surface of capillaries. Since the discovery, their group has conducted a series of further studies on GPIHBP1 [223-226].

After the discovery of GPIHBP1, Figure 6.1 shows a current summary of our understanding of intravascular and intracellular lipolysis. In the intravascular lipolysis process, LPL is bound to the luminal surface of capillary endothelial cells and hydrolyses TGs in chylomicrons and VLDLs to enable the products, fatty acids and monoacylglycerols (MGs) to be taken up by the parenchymal cells. MG can be further catabolized by MGL to produce fatty acids and glycerol. Fatty acids can be stored as TGs after re-esterifition or oxidized as an energy source. As for intracellular lipolysis, MGs, TGs and diglycerides in lipid droplets can be hydrolysed and release fatty acids to enter oxidative or biosynthetic pathways in many tissues [222]. However, even with the important discovery of GPIHBP1, there are still some key questions that remain unclear in this lipolysis process. For example, (1) why TRLs stop at the luminal face of capillaries so that the lipolysis can happen rather than simply "flowing by" in the bloodstream; and (2) how the fatty acids are transported through the capillaries to the parenchymal cells. With the ability of the NanoSIMS to conduct subcellular imaging on ^{13}C-spiked molecules, these questions can be addressed.

6.1.2 NanoSIMS Analysis of Tissue Samples.

Imaging mass spectrometry is getting more and more attention from the biological community as noted in Chapter 2. Secondary ion mass spectrometry, MALDI, LA-ICP-MS and DESI have all been used successfully to study molecular distributions in tissue samples, for instance elemental distributions in heart tissue by LA-ICP-MS [227] and BDNC distribution with MALDI-MS [228]. SIMS instruments have the highest spatial resolution among these techniques. A recent ToF-SIMS study

visualized cholesterol, amyloid and glia in an Alzhemeimer's disease transgenic mouse brain [229]. ToF-SIMS has also been extensively applied to image lipids, Figure 6.2 [230].

Figure 6.1 has been removed due to copy right restrictions. The original image can be found in the reference.

Figure 6.1: Schematic of intravascular lipolysis and intracellular lipolysis. From reference [222].

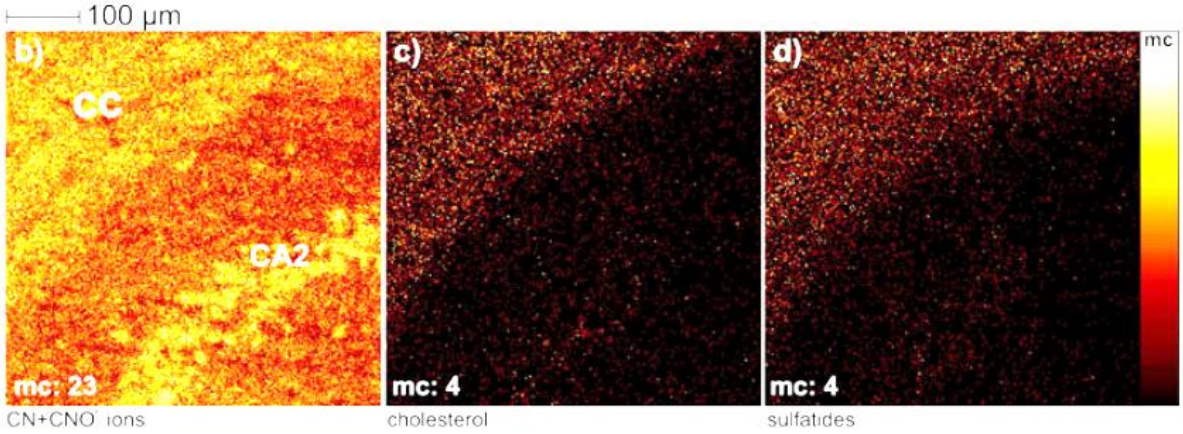

Figure 6.2: ToF-SIMS reveals the distribution of CN/CNO^-, cholesterol and sulphatide in an Alzhemeimer's disease transgenic mouse brain. All three species colocalize partially in corpus callosum (CC) and the *Cornu Ammonis* (CA) subfield only shows high CN/CNO^- signal. From reference [229].

In the last decade, the NanoSIMS also has been applied to the study of tissue samples by several groups. Senyo et al. used the NanoSIMS to study mammalian heart renewal by pre-existing cardiomyocytes, and quantified the turnover rate of healthy and damaged mature hearts by feeding the mouse with ^{15}N-labelled nucleotides [86]. Figure 6.3 shows the ability of the NanoSIMS to image large areas of tissue samples and analyse new cells formed after myocardial infarction. Lechene et al. studied the distributions of fixed nitrogen by bacterial cells in L. pedicellatus [76].

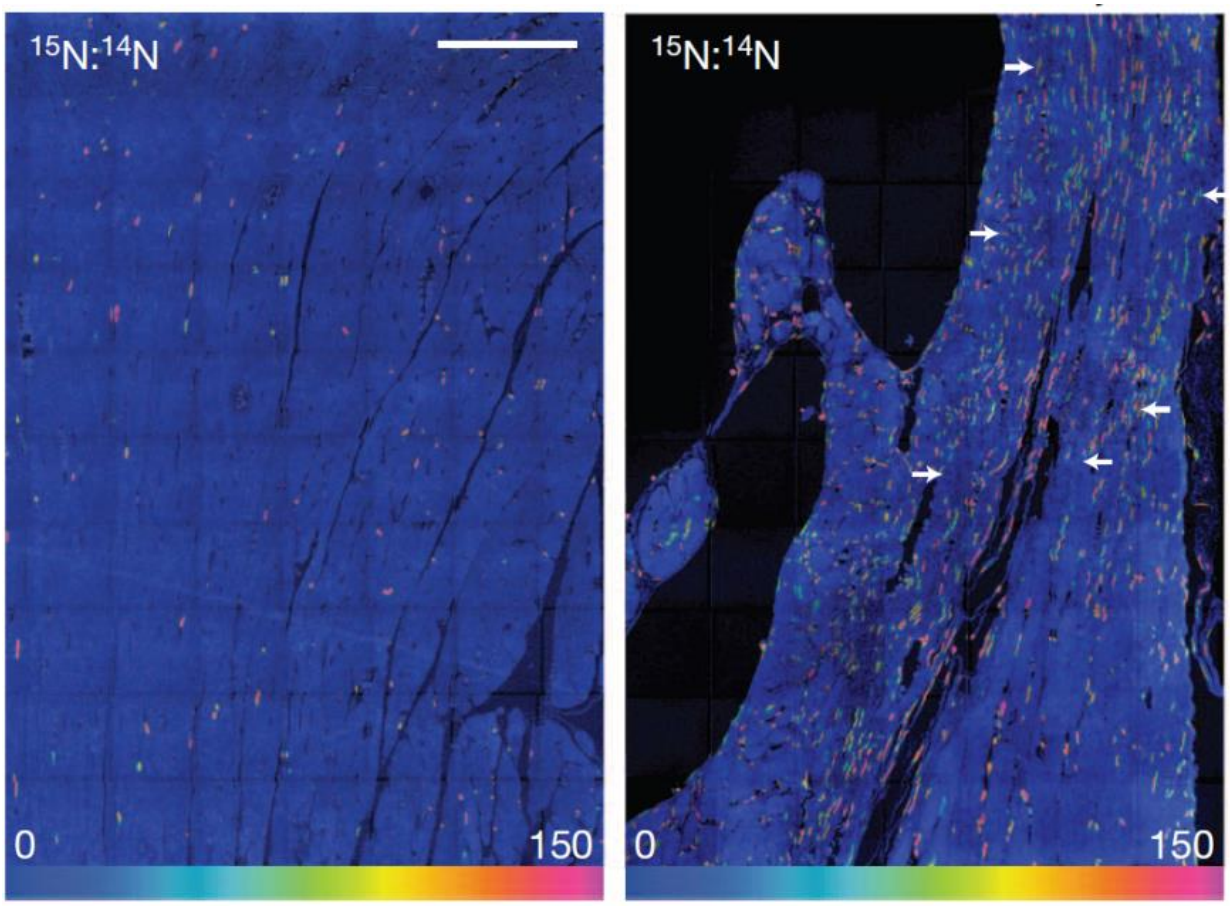

Figure 6.3: Tissue imaging by the NanoSIMS: The mammal heart renewal rate was recorded using ^{15}N-thymine on both healthy (left) and damaged heart (right). Scale bar, 90 µm. From reference [86].

The NanoSIMS also has the ability to obtain 3-D chemical information. Figure 6.4 is a 3D image of ^{15}N/^{14}N in a 2 µm thick volume and shows the tips of the hair-cells have a high protein turnover rate. The ability of visualize stable isotopes in 3D could provide a better understanding of many biological process, and it was also used in my project.

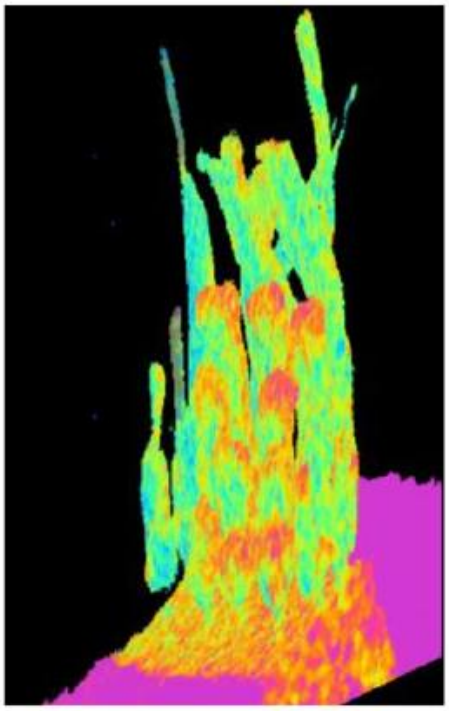

Figure 6.4: 3D Tissue imaging example of hair cell turnover in a mouse. From reference [88].

6.1.3 Backscattered Electron Imaging on Tissue Samples

Previous chapters described the development of BSE imaging on biological materials; and recent work has shown that BSE can obtain detailed microstructural information from a large area of tissue samples. Helmstaedlter et al. reconstructed connectomes of the inner plexiform layer in the mouse retina [186], and several other successful applications have focused on brain samples [231]. Figure 6.5 shows serial images of a brain tissue obtained from mouse samples in a FIB-SEM instrument, which can be reconstructed to a 3D volume if necessary.

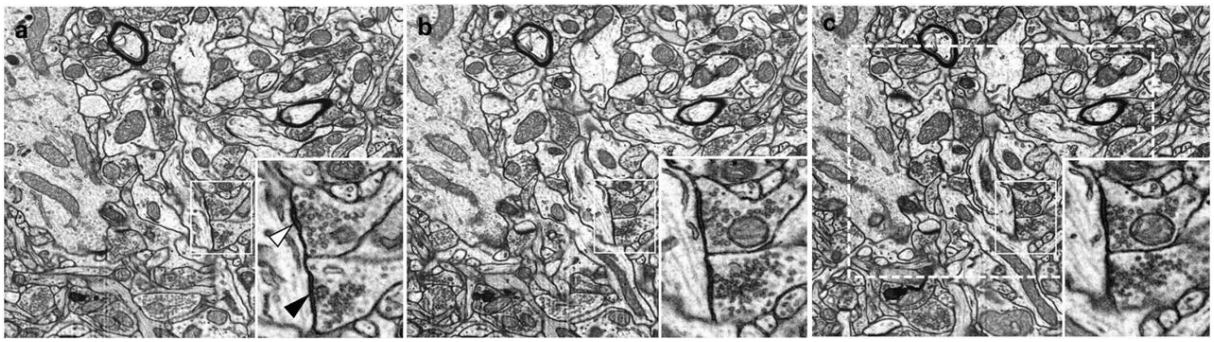

Figure 6.5: BSE images from serial sections from brain tissue sample. Width of images, 8.4 µm. From Reference [231].

6.1.4 Aim of the Project

Working with Prof. Stephen Young, Prof. Loren Fong and Dr. Chris Goulbourne in Department of Medicine at UCLA, I studied the lipolysis process by conducting correlative BSE and NanoSIMS on the same samples. This chapter will show the tracking of the lipolysis products in subcellular structures in various tissues, and contributes to understanding in more detail the effects of GPIHBP1.

6.2 Materials and Methods

This section discusses the materials and methods for this project, including sample preparation, imaging and data analysis. All the animal experiments were done by my collaborators at UCLA, and all procedures were conducted under the oversight of the UCLA Animal Research Committee, and monitored by UCLA veterinarians.

6.2.1 Materials

Wild type *mice (Gpihbp1*$^{+/+}$), expressing Gpihbp1, and Gpihbp1 knockout mice (*Gpihbp1*$^{-/-}$) were used in these experiments. ^{13}C-labeled Algal fatty acids (Sigma 487937) were used to form the labelled TRLs and lipid droplets. ^{15}N-labelled antibody was isolated by Dr. Chris Goulbourne and used to label the location of GPIHBP1. During this project, brown adipose tissue (BAT), intestine, heart, liver and skeletal muscle (SKM) tissue samples are prepared and imaged.

6.2.2 Sample Preparation

To study the effects of GPIHBP1 on lipid metabolisms, labelled fatty acids (120 mg) were dissolved in 200 µl ethanol and 1.7 ml sunflower oil; 200 ml of the suspension was administered to mice twice per day for four consecutive days.

To collect ^{13}C-spiked Triglyceride-rich lipoproteins (TRLs) for margination and lipid uptake studies, labelled ^{13}C-TRLs were harvested from *Gpihbp1*$^{-/-}$ mice after delivering a mixture of ^{13}C-labeled Algal fatty acids (Sigma 487937) by gavage. TRLs were isolated by ultracentrifugation (Figure 6.6) and 50

µg was injected into a wild-type or *Gpihbp1*$^{-/-}$ mice, and mice then were left for different lengths of time before sacrifice and sample fixation.

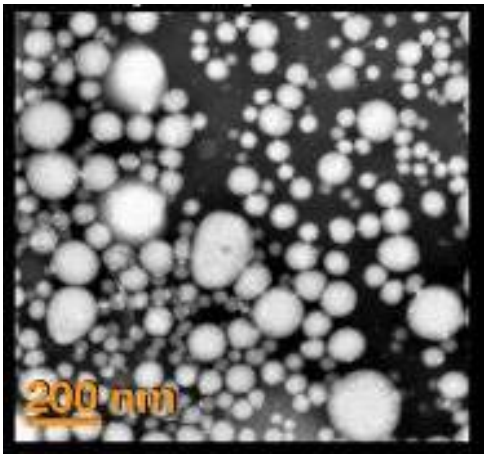

Figure 6.6: Chylomicron particles can be collected from *Gpihbp1*$^{-/-}$ mouse blood. From Dr. Chris Goulbourne.

All tissues from the mice subjects were perfusion-fixed in situ with 2.5% glutaraldehyde containing 2 mM $MgCl_2$ in 100 mM cacodylate buffer (pH 7.4) and incubated in the fixation solution at 4 °C overnight. The following day, the tissues were incubated in an equal volume of 1% osmium tetroxide. The samples were then washed three times in distilled water (10 min each). Samples were next treated with 1% osmium tetroxide in 100 mM cacodylate buffer for 1 h, washed in distilled water four times (10 min each), and then treated with 1.2% aqueous uranyl acetate overnight at 4^{o} C in the dark. The samples were sequentially dehydrated with increasing concentrations of acetone (20, 30, 50, 70, 90, and 100%) for 30 min each, followed by three additional treatments with 100% acetone for 20 min each. Samples were then infiltrated with increasing concentrations of Spurr's resin (25% for 1 h, 50% for 1 h, 75% for 1 h, 100% for 1 h, 100% overnight at room temperature), and then incubated overnight at 70^{o} C in a resin mold. 500 nm thick sections were cut using a Diatome diamond knife on an Ultramicrotome. The sections were placed on a platinum coated coverslip and left to dry.

Test samples of cultured endothelial cells were also carried out to investigate the transport of lipids. Cultured cells were fixed in 2.5% glutaraldehyde and processed in a similar way as tissue samples,

stated above. Cultured cells were embedded into resin with coverslips as a reference for navigating imaging.

6.2.3 Imaging

Sections were transferred into the Zeiss NVision FIB to conduct BSE imaging. BSE images were taken under the same conditions as for the single-cell imaging studies described in Chapter 5. All the BSE-imaged areas were also studied in the NanoSIMS to allow direct correlation of the chemical information with the sample structure. 40 μm × 40 μm NanoSIMS images were taken to study reasonably large areas of sections from BAT and heart tissue, and 10 μm × 10 μm images were taken to show the subcellular distributions in selected areas. The $^{13}C/^{12}C$ ratio was used to reveal the distribution of ^{13}C-labeled lipids; the $^{16}O^-$, $^{12}C^{14}N^-$, and $^{31}P^-$ signals were also collected to show the morphology of the samples. A large primary aperture (D1 = 2) was used, matching the beam size and pixel size, as discussed in Chapter 3, to acquire images (40 × 40 μm, 256 × 256 pixels) on brown adipose tissue, and a smaller primary aperture (D1 = 3 or D1 = 4) was used to achieve higher spatial resolution images of capillaries in heart or brown adipose tissue. The $^{13}C/^{12}C$ HSI images were processed using the OpenMIMS plugin in ImageJ software, and processed by a median filter with three-pixel radius to reduce the noise in images as stated above.

6.3 Results and Discussion

This section discusses the results from mice treated in different conditions to get a better understanding of lipid metabolisms by visualization. The methods of conducting tissue analysis with the NanoSIMS are also discussed.

6.3.1 Optical Images

Optical images (Figure 6.7) were taken on all the tissue samples to enable the NVision to localize the areas of interest. The contrast in the brown adipose tissue (BAT) sample is due to the lipid droplets showing dark under the optical microscope. The intestine sample also can show the shape of cross sections through the microvilli. Optical images were also taken after BSE imaging for correlative

NanoSIMS analysis. The rectangular shapes (arrowed) in the BAT, heart and skeletal muscle samples are the areas imaged by BSE. Most of the areas contain capillaries, which are the main target of imaging in this project. High magnification optical images can show distributions of capillaries, which is useful to locate areas of interest for study in other instruments.

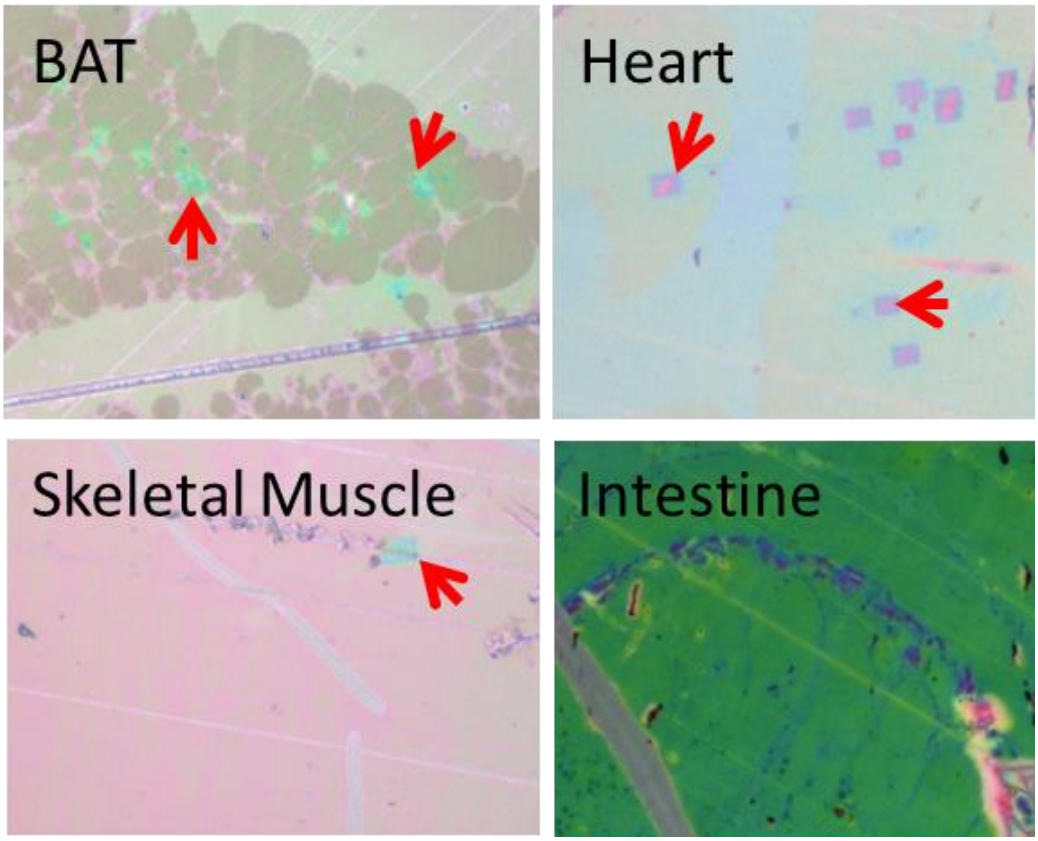

Figure 6.7: Optical images of some tissue samples analysed by BSE and NanoSIMS. The rectangular shapes on the sections (indicated with red arrows) are areas imaged by BSE, which allows easy identification of the exact same area using the NanoSIMS optical microscope.

The in vitro methods have also been used to track the transport of lipolysis products through endothelial cells. The cells cultured on coverslips are embedded in resin with the coverslip, which can then be used to help find the cells. Optical images (Figure 6.8) were also taken for navigating BSE and NanoSIMS experiments. The endothelial cells are attached to one side of the coverslips and can be localized with BSE, and can then be found in the NanoSIMS.

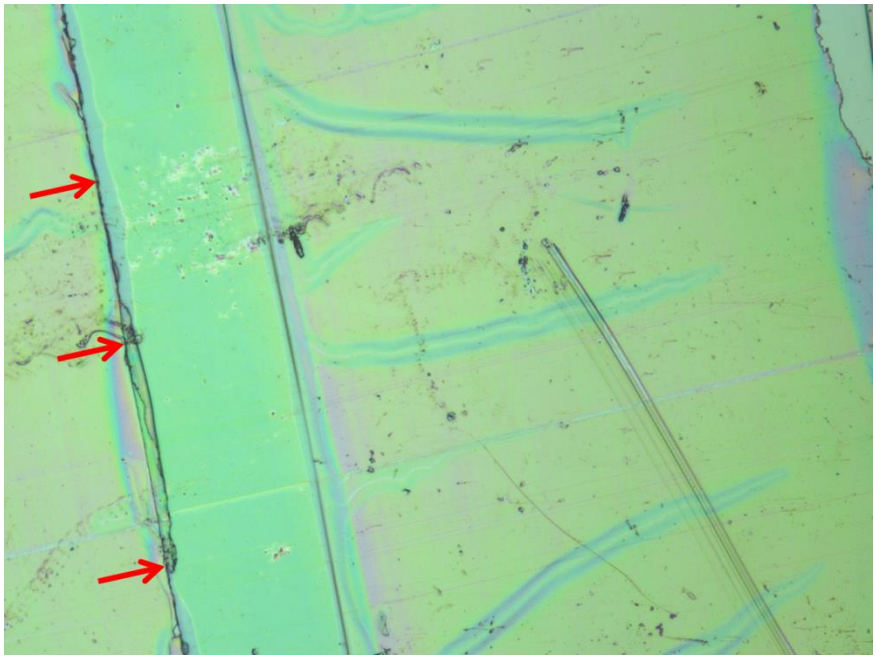

Figure 6.8: Optical image of cultured cell with coverslips in the resin section. Red arrows identify the locations of cells attached to one side of the coverslip.

6.3.2 NanoSIMS Signal Tuning

As shown in Chapter 4 and Chapter 5, ^{13}C and $^{12}C^{15}N$ signals can be easily tuned for in the NanoSIMS, and ^{12}C and $^{12}C^{14}N$ signals were recorded for isotopic ratio measurements.

6.3.3 Tissue Samples Fed with Control Diet

^{12}C, ^{13}C and $^{12}C^{14}N$ images were obtained from control samples (Figure 6.9), which are tissues from mice fed no ^{13}C-fatty acids. The morphology of three types of tissues can be clearly seen in the $^{12}C^{14}N$ images. Heart muscle cells and capillaries were observed in the heart tissue, and many lipid droplets showing low signals in $^{12}C^{14}N$ image can be seen in the BAT tissue. In all samples, the ^{13}C distribution is homogeneous, as expected, and the ratios calculated from all the samples are close to the natural abundance of ^{13}C, 1.1%. Control samples were imaged in each NanoSIMS session to use as a background to normalize the $^{13}C/^{12}C$ ratios.

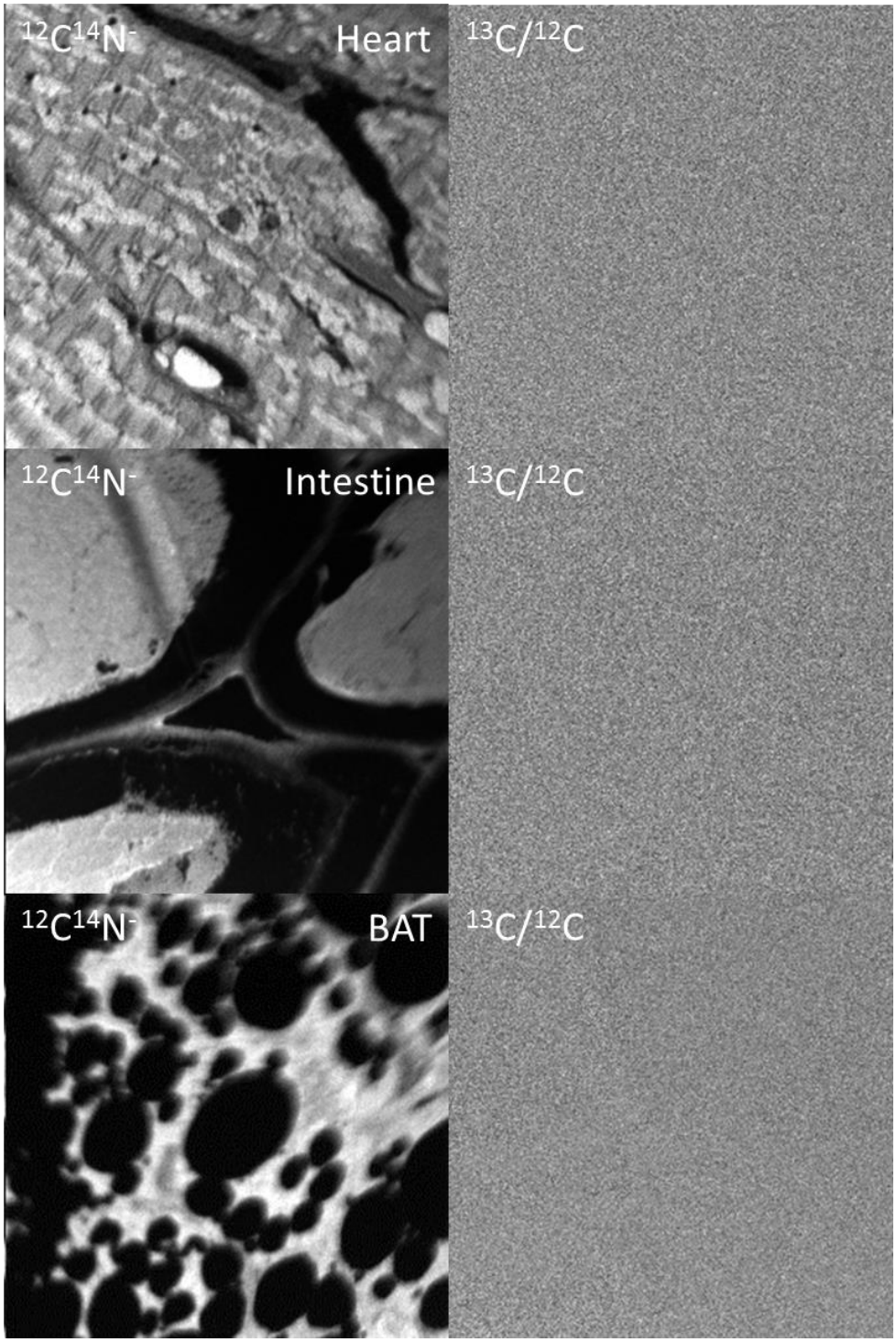

Figure 6.9: $^{12}C^{14}N$ and $^{13}C/^{12}C$ ratio image of control tissue samples from mouse fed with normal diet without extra ^{13}C-labelled molecules. Ratio scale, 0 – 2%. Size of images, 40 µm × 40 µm.

6.3.4 ^{13}C-labelled Lipids Distribution after 4-day Gavage

Tissues from mice gavaged with ^{13}C-labelled lipids were quantitatively analysed to study effects of GPIHBP1 on lipid metabolisms. The four parts of this section will discuss typical results on these different types of tissue.

6.3.4.1 Intestine

The intestine is the first step in the absorption of lipids from the feeding process as shown in Figure 6.10. Figure 6.11 is a mosaic of images totalling 200 µm by 100 µm covering intestinal tissue harvested from a mouse fed with ^{13}C-fatty acids for four days. Mucosal cells, blood vessels, capillaries, villus, and microvilli structures are observed in this area. The $^{13}C/^{12}C$ image shows the distribution of ^{13}C-fatty acids, inside and outside cells. Higher $^{13}C/^{12}C$ ratios were also observed in the cytoplasm than the nucleus, which might be due to the transportation of lipids through the cytoplasm.

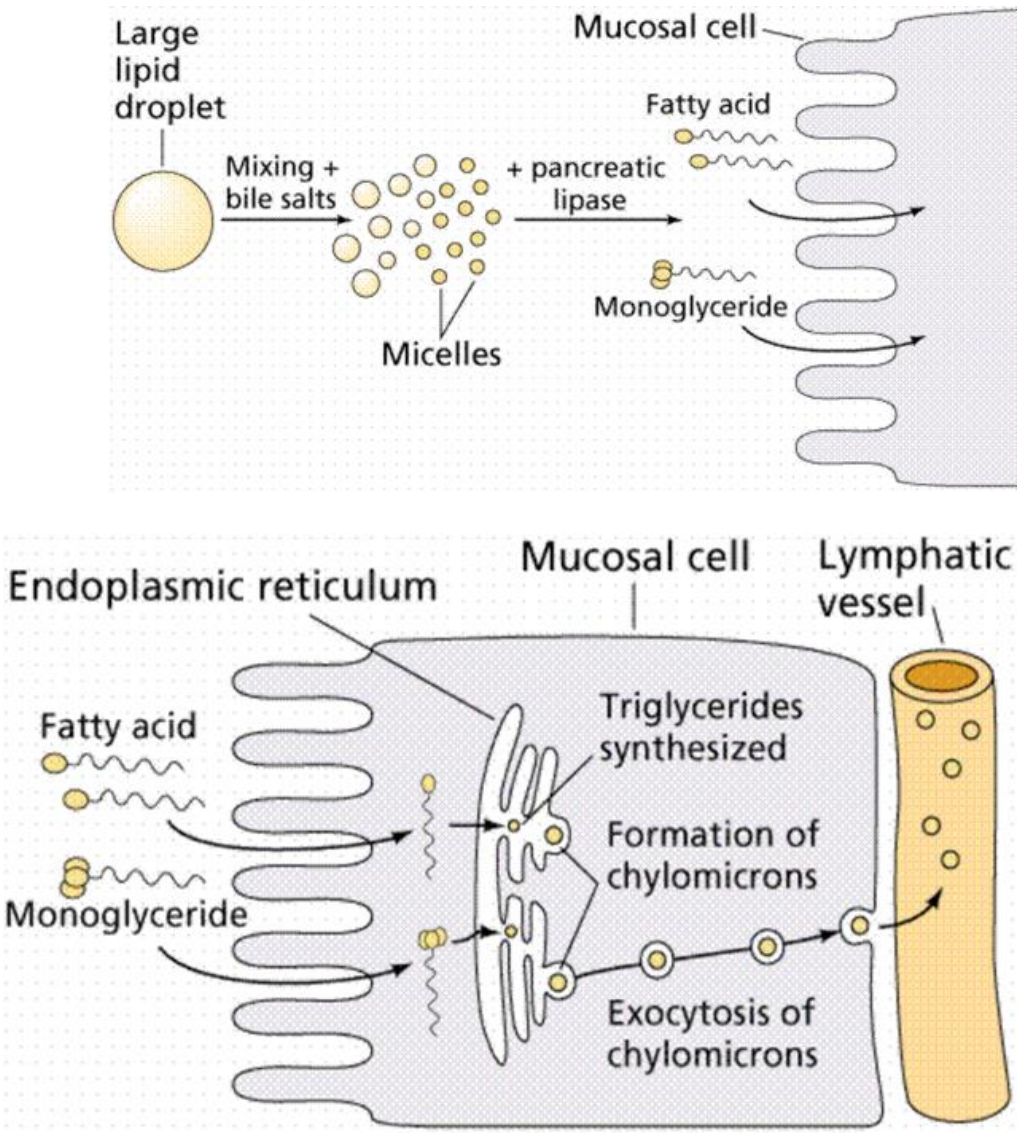

Figure 6.10: Schematic of process by which the intestine takes up lipids. From reference [232].

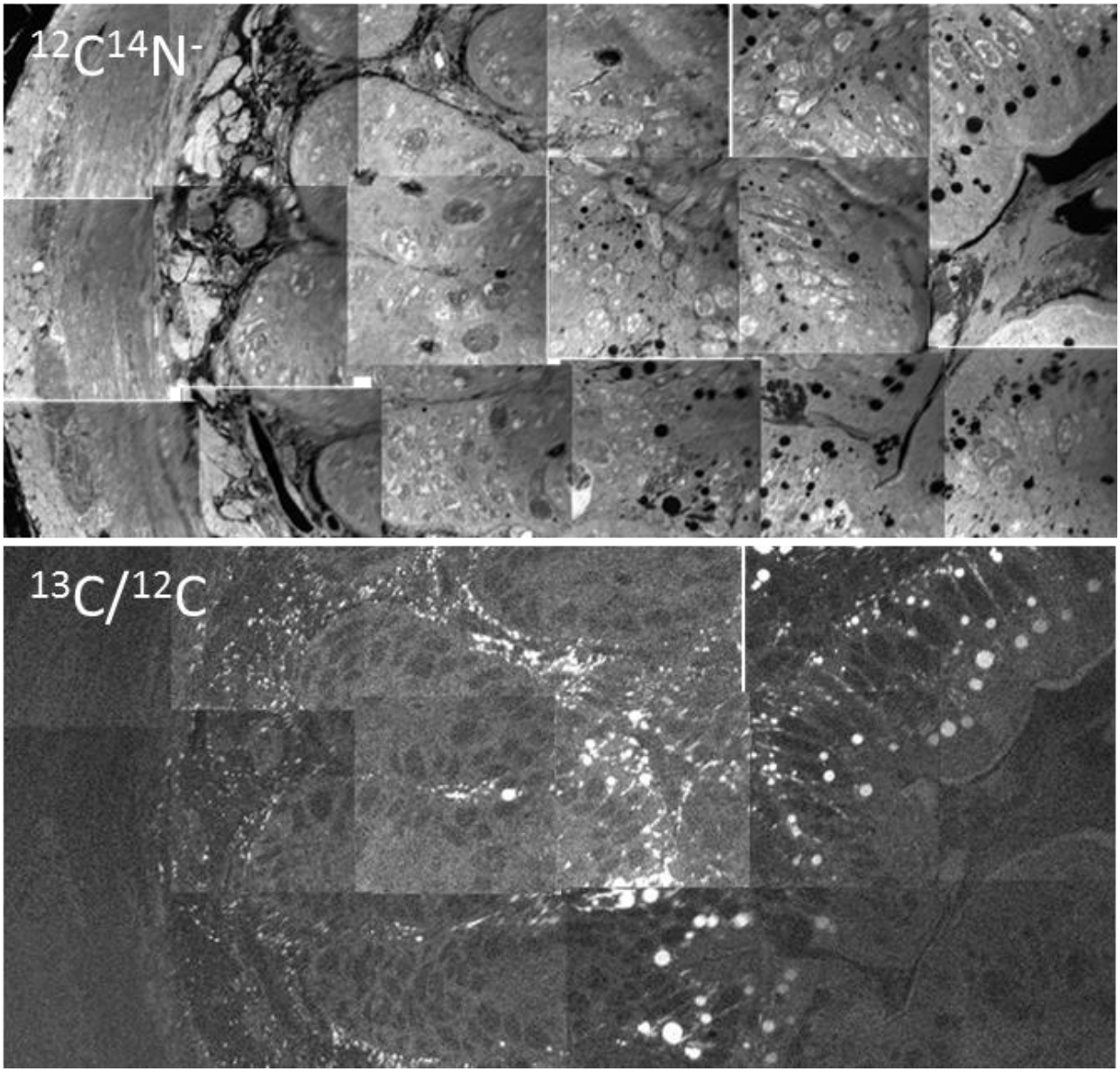

Figure 6.11: $^{12}C^{14}N^-$ and $^{13}C/^{12}C$ images from a 200 µm by 100 µm area of an intestine tissue from a mouse fed with ^{13}C-fatty acids for 4 days. Ratio scale: 1.1% - 2.0%.

Figure 6.12 shows higher resolution NanoSIMS images from intestine tissue. The $^{12}C^{14}N^-$ image nicely shows the morphology of the intestine cells. Mucosal cells (top) and a blood vessel (bottom) are clearly showing in the images, corresponding to the lipid uptake schematic in Figure 6.10. Lipids are taken up into mucosal cells and form chylomicrons, showing as particles, which are then transported to vascular system, and are removed during perfusion-fixation. The size of the ^{13}C-labelled particles in these images range from 200 nm to 5 µm in diameter, with a $^{13}C/^{12}C$ ratio about 1.8%.

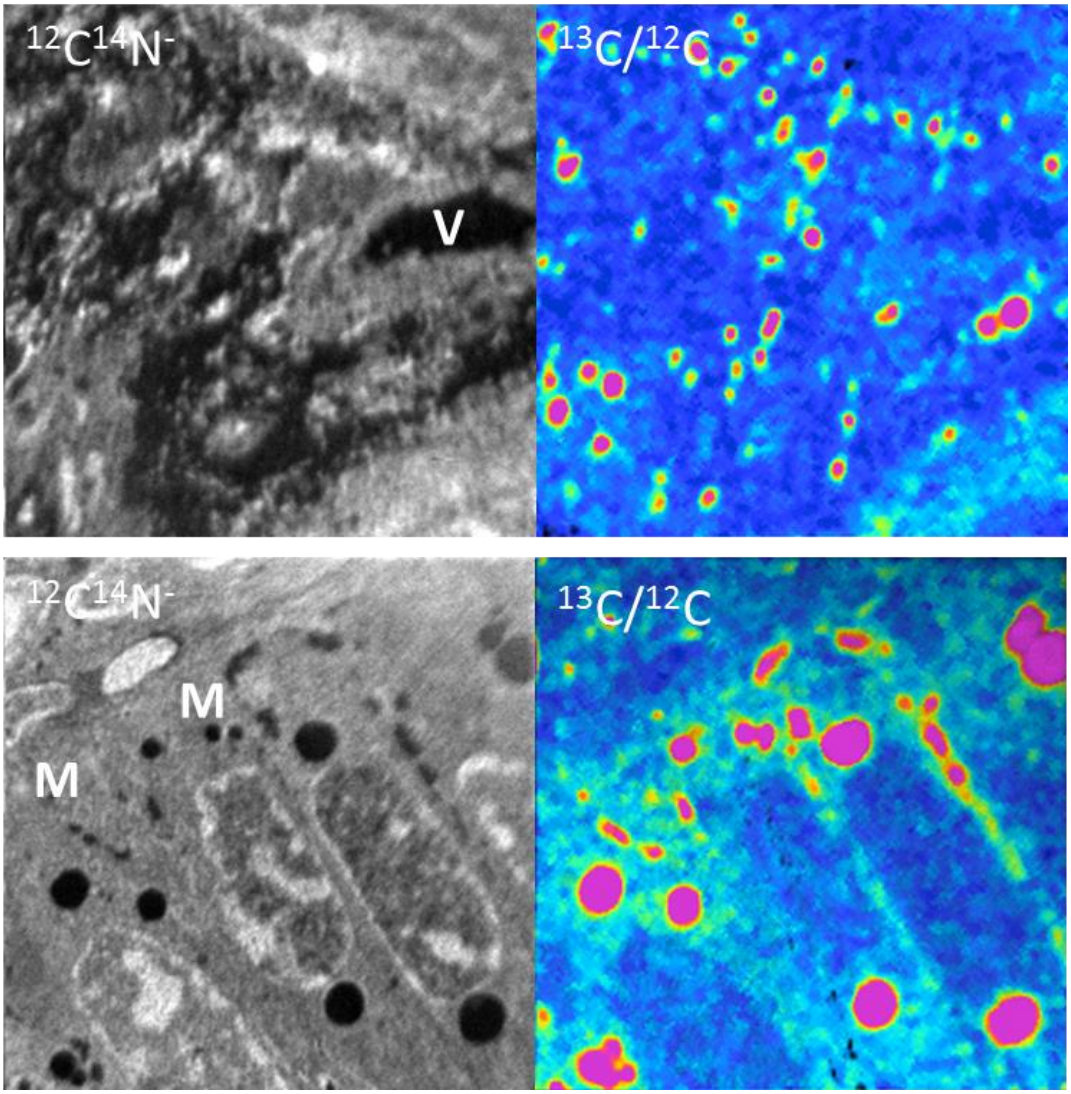

Figure 6.12: $^{12}C^{14}N^-$ and $^{13}C/^{12}C$ images of a 15 µm by 15 µm area of Intestine tissue from a mouse fed with ^{13}C-fatty acids for 4 days. Mucosal cells (M) and a blood vessel (V) are identified. Ratio scale: 1.1% - 2.0%.

6.3.4.2 Liver

Liver is a critical tissue in fatty acid metabolism. It plays an important role in fatty acid treatments, including the processing of chylomicron remnants and also lipoprotein formation, such as VLDL and LDL [233]. In addition, the liver is not a GPIHBP1 expressing tissue, and the uptake of the fatty acids is partly due to the leaky capillary endothelial cells. Figure 6.13 contains two 40 µm by 40 µm areas of liver tissue from the same mouse. Lipid droplets and capillaries are visualized in both images, but there is no sign in the $^{13}C/^{12}C$ ratio images of the lipid droplets labelled by the ^{13}C-fatty acids fed to the mouse.

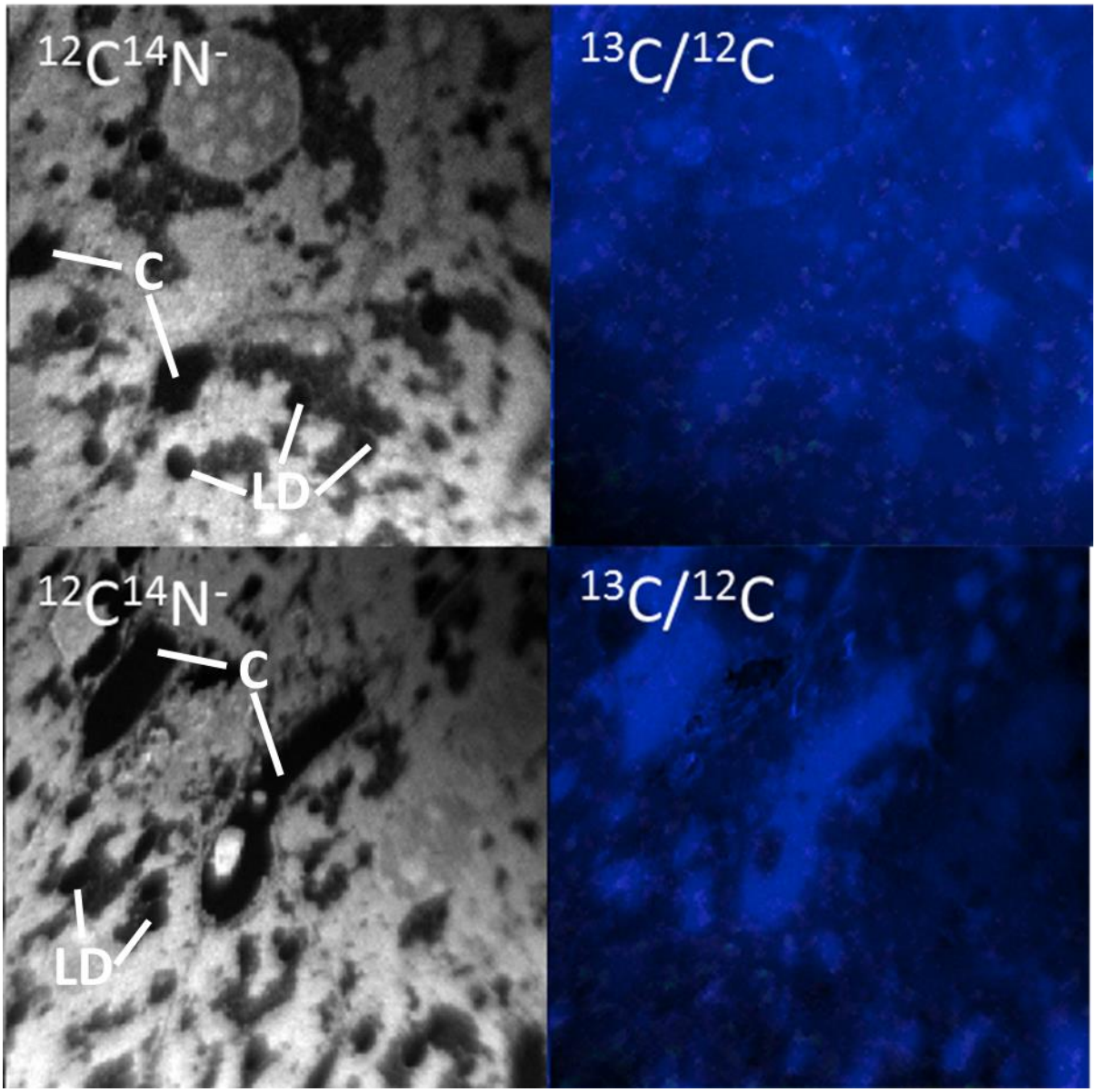

Figure 6.13: $^{12}C^{14}N^-$ and $^{13}C/^{12}C$ images of a 40 µm by 40 µm area of liver tissue from a mouse fed with ^{13}C-fatty acids for 4 days. Capillaries (C) and lipid droplets (LD) are identified. Ratio scale: 1.1% - 2.0%.

6.3.4.3 Skeletal Muscle

SKM is also a GPIHBP1 expressing tissue, and uses lipids as a main energy source. Figure 6.14 shows a 40 µm by 40 µm image of a typical region of SKM tissue. The low signal $^{12}C^{14}N^-$ areas are lipid droplets in the muscle, which are also labelled with ^{13}C. The $^{13}C/^{12}C$ ratio in these lipid droplets is ~1.6%, 50% higher than the natural abundance.

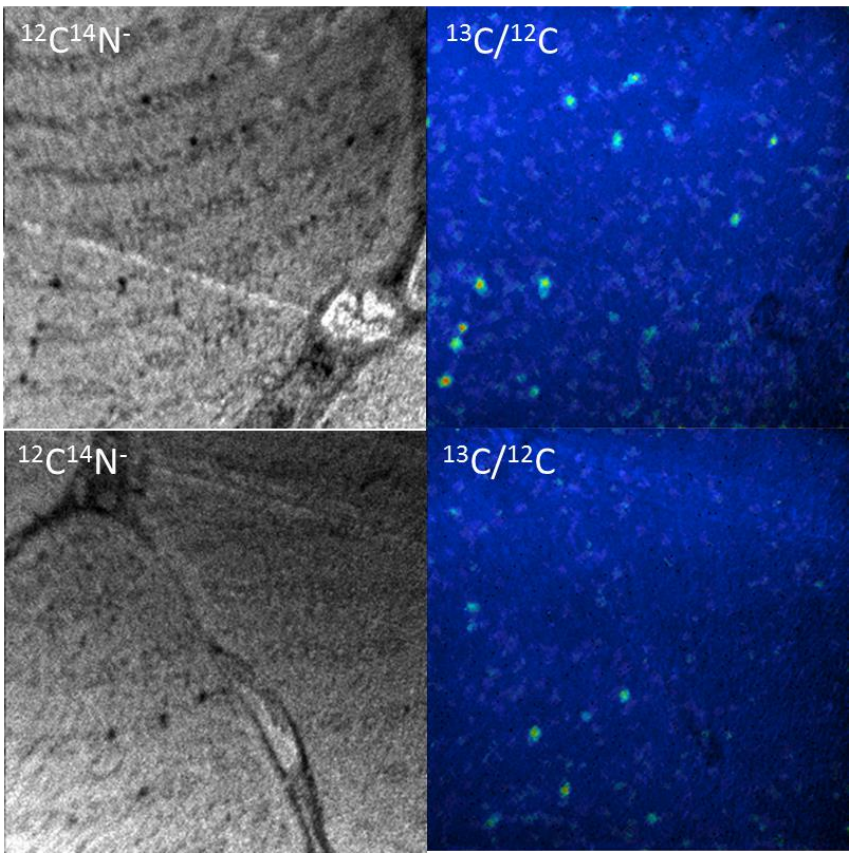

Figure 6.14: $^{12}C^{14}N^-$ and $^{13}C/^{12}C$ images of a 40 µm by 40 µm area of SKM tissue from a mouse fed with ^{13}C-fatty acids for 4 days. Ratio scale: 1.1% - 2.0%.

6.3.4.4 Brown Adipose Tissue

BAT is the tissue which can transfer energy from food to create heat in the organism [234]. The lipids in the lipid droplets are created both from taken up of fatty acids and also synthesised with glucose. Figure 6.15 contains $^{12}C^{14}N^-$ and $^{13}C/^{12}C$ images of a typical 40 µm by 40 µm area of a BAT tissue from a mouse fed with ^{13}C-fatty acids for 4 days. The $^{13}C/^{12}C$ image clearly shows the lipid droplets are strongly labelled by extra ^{13}C, with an average ratio about 1.8%.

High resolution NanoSIMS images have also been taken on the same BAT sample, Figure 6.16, lipid droplets (LD), capillaries (C) and parenchymal cells (P) are observed in both areas, as well as the nucleus of the endothelial cells (N). The lipid droplets are bigger than in then other tissues, and they are homogeneously labelled within each lipid droplet, but different lipid droplets show different amount of labelling. The $^{13}C/^{12}C$ ratio in these lipid droplets ranges from 1.7% - 1.9%. There are also two lipid droplets observed in the top left capillary endothelial cell (red arrows), which might show

the transport process of lipid through the endothelial cells or the build-up of lipid droplets in the endothelial cells. This will be further discussed with correlative BSE and NanoSIMS imaging in section 6.3.6.

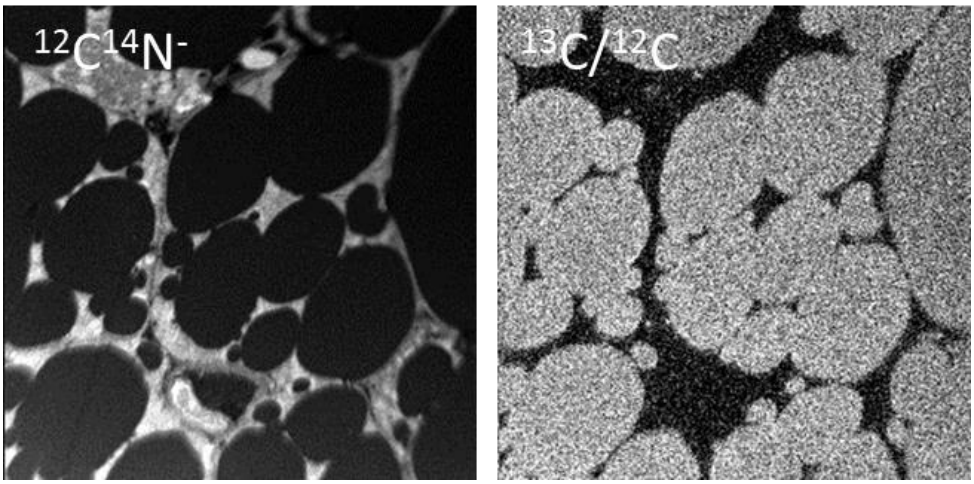

Figure 6.15: $^{12}C^{14}N^-$ and $^{13}C/^{12}C$ images of a 40 µm by 40 µm area of BAT sample from a mouse fed with ^{13}C-fatty acids for 4 days. Ratio scale: 1.1% - 2.0%.

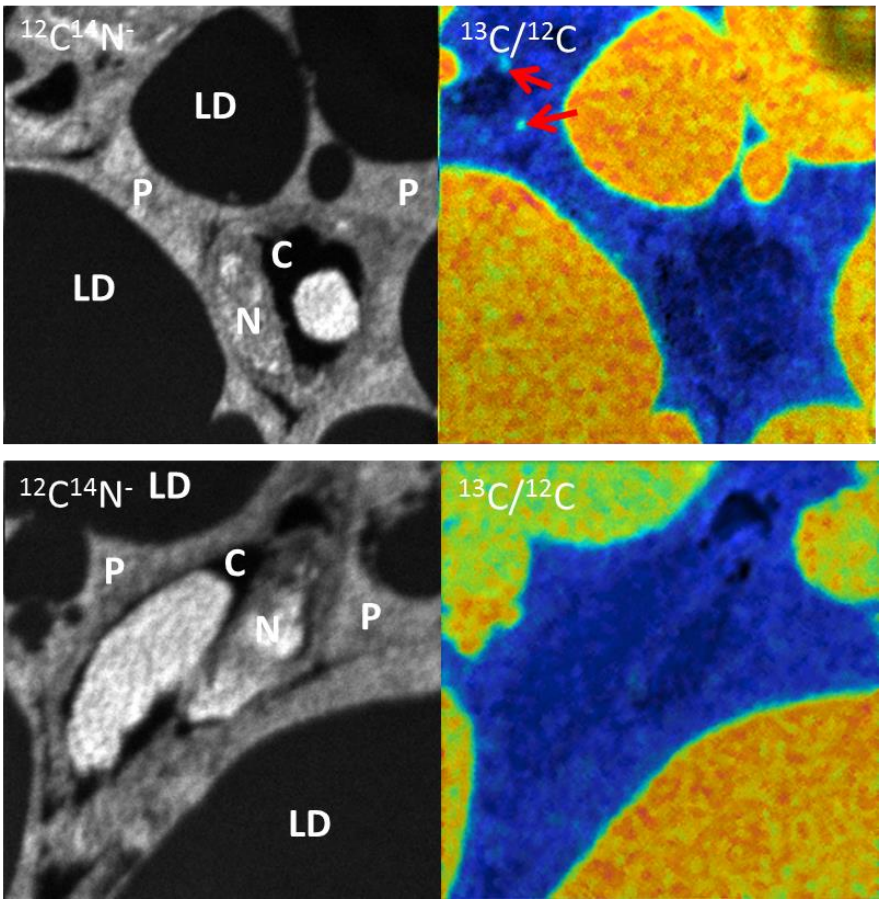

Figure 6.16: $^{2}C^{14}N^-$, $^{31}P^-$ and $^{13}C/^{12}C$ images of 15 µm by 15 µm area of BAT tissue from a mouse fed with ^{13}C-fatty acids for 4 days. Ratio scale: 1.1% - 2.2%.

6.3.4.5 Heart

Lipids are the major cardiac fuel, and heart tissue has the most robust expression of lipoprotein lipase for lipids uptake from lipoproteins [235]. A large area of heart sections was scanned in the NanoSIMS (Figure 6.17). The $^{12}C^{14}N^-$ images show clearly the heart muscle cells and the capillaries in the area. After 4 days of the ^{13}C-fatty acid diet, the low intensity $^{12}C^{14}N^-$ areas correspond to the high ratios of $^{13}C/^{12}C$. The high $^{13}C/^{12}C$ areas are lipid droplets built up in the muscle cells, with $^{13}C/^{12}C$ ratios about 1.8%.

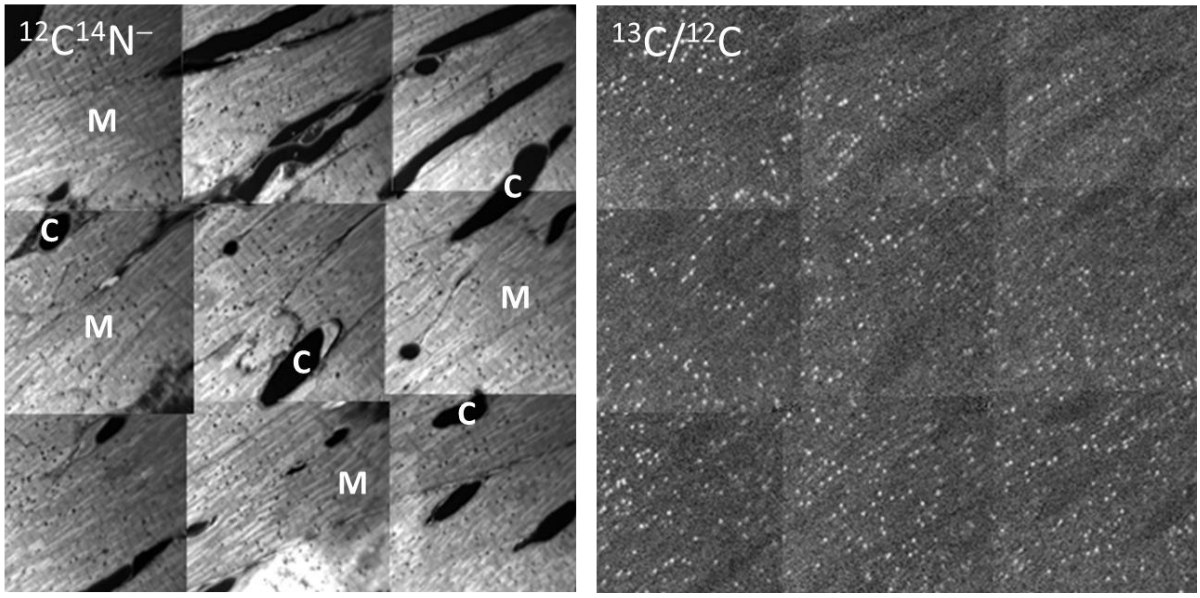

Figure 6.17: $^{12}C^{14}N^-$ and $^{13}C/^{12}C$ image on an area of 100 µm by 100 µm area of heart tissue from a mouse fed with ^{13}C-fatty acids for 4 days. Heart muscle cells (M) and capillaries (C) are identified. Ratio scale: 1.1% - 2.0%.

Figure 6.18 shows high resolution NanoSIMS images of wild type mouse heart tissue. The $^{12}C^{14}N^-$ images are showing the heart muscle cells and a capillary (C). The $^{13}C/^{12}C$ ratio images show that lipid droplets in the muscle tissue are labelled with the ^{13}C-fatty acids fed to the mouse. The lipid droplets are also corresponding to the low signal area in the $^{12}C^{14}N^-$ images, which is partly due to the low concentration of nitrogen and phosphorus in the lipid droplets. There are 73 labelled lipid droplets observed in these two images, and the sizes range from 200 nm to 1 µm, with $^{13}C/^{12}C$ ratio about 2.0%.

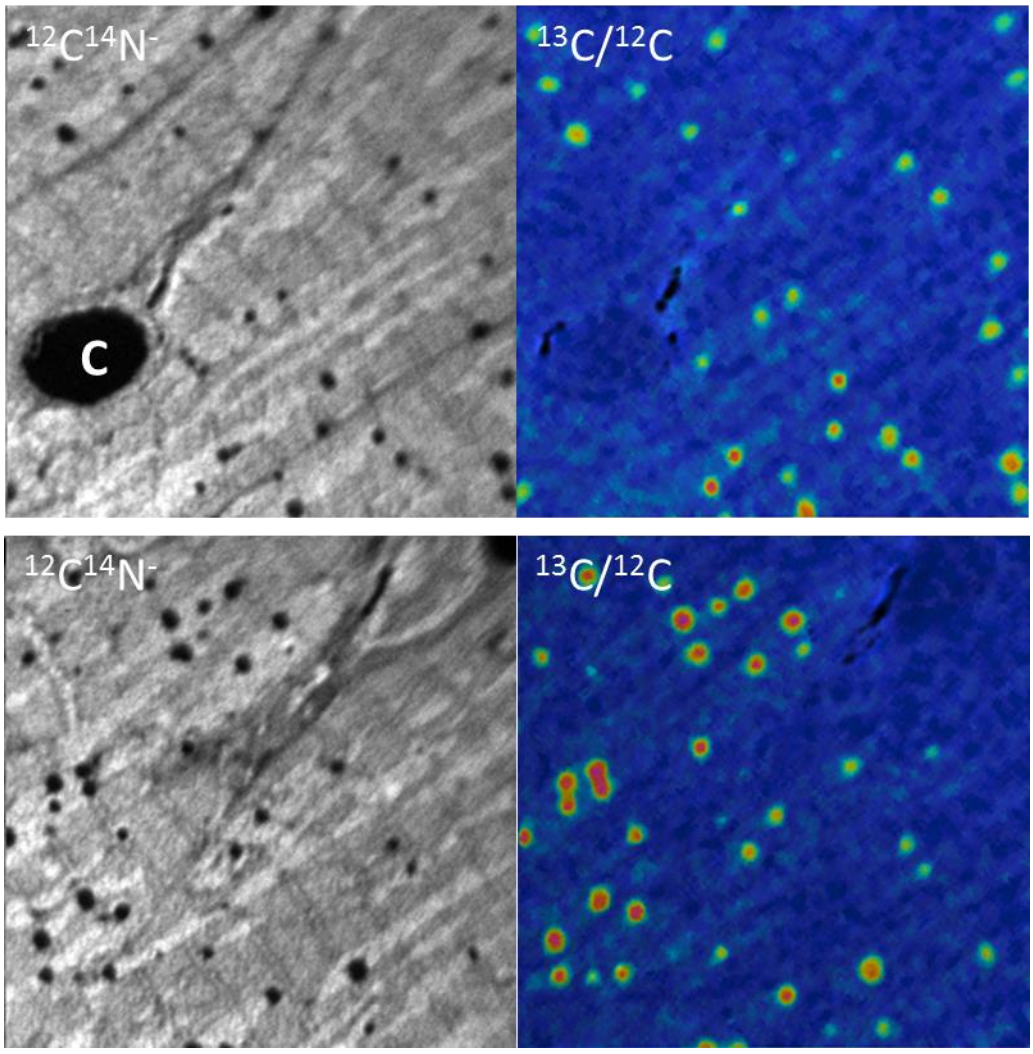

Figure 6.18: $^{12}C^{14}N^-$ and $^{13}C/^{12}C$ images of two typical 15 µm by 15 µm areas of heart tissue from a mouse fed with ^{13}C-fatty acids for 4 days. A capillary (C) is identified. Ratio scale: 1.1% - 2.2%.

A depth profile was conducted to allow reconstruction of a 3D view of the lipid droplets in the heart tissue. Figure 6.19 shows 16 frames of $^{13}C/^{12}C$ images on the same area. The images show three lipid droplets (LD), a large one in the top right (parenchymal cells), and small ones in a parenchymal cell, a capillary endothelial cell. During the depth profile, we can see changes in the three lipid droplets. The lipid droplet in the capillary endothelial cell was sputtered through and disappeared, and the small one in the parenchymal cell appeared and disappeared during the imaging. The big one hardly changed. The whole section was removed after imaging, and calculating from the dose used in these 16 frames, an estimated 150 nm of material was removed in these images (most material was removed during implantation of the Cs^+). The black areas at the edge of the images are due to the

drift of the sample. A reconstructed 3D image is also shown in this figure, in which we can see the 3D view of the three lipid droplets.

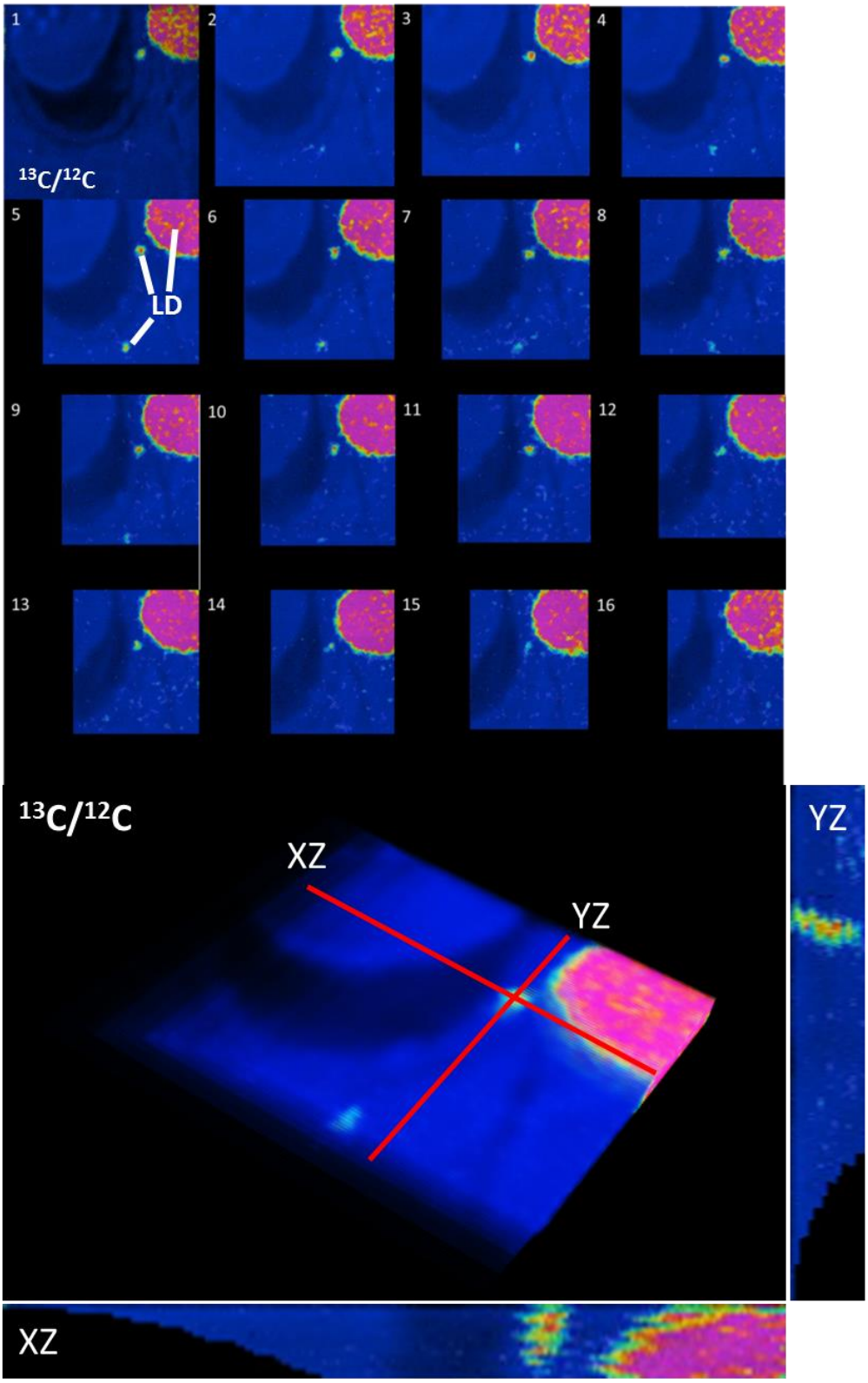

Figure 6.19: Depth profiling $^{13}C/^{12}C$ images of lipid droplets in capillary endothelial cell and parenchymal cells in heart tissue. Lipid droplets (LD) are identified. Size of images: 6 µm × 6 µm.

Wild type heart samples injected with ^{15}N-labelled antibodies were also imaged. Figure 6.20 shows 16 images from the same area. The $^{15}N/^{14}N$ images nicely show the distribution of the ^{15}N-labelled antibodies. Due to the high depth resolution of the NanoSIMS, we can clearly see the patchy distribution of the antibodies, which could only with difficulty be resolved by a conventional fluorescence microscopy or even confocal microscopy. The 3D reconstructed image at the bottom of the 16 frames shows the connecting of the ^{15}N-labelled antibodies looking through the volume from the top. This is a good example of the different results that can be obtained from fluorescence and NanoSIMS images.

6.3.5 GPIHBP1 Deficiency Mouse

The same set of experiments were done on the *Gpihbp1*$^{-/-}$ mice. Figure 6.21 shows typical $^{12}C^{14}N^-$ and $^{13}C/^{12}C$ HSI images of different tissues in the deficient mouse fed with ^{13}C-fatty acids for 4 days. The BAT images show low $^{12}C^{14}N^-$ signal in the lipid droplets just as in the wild type mouse sample, and the $^{13}C/^{12}C$ image shows some incorporation of the ^{13}C-fatty acid into the lipid droplets after 4 days feeding, but the $^{13}C/^{12}C$ ratio is lower than in the wild type mouse. The two high $^{13}C/^{12}C$ ratio areas can be identified as capillaries (red arrows) in the $^{12}C^{14}N^-$ image.

The $^{12}C^{14}N^-$ mouse heart image shows some lipid droplets in the area, but in the $^{13}C/^{12}C$ image only 4 of them are labelled by ^{13}C-fatty acids fed to the mouse; significantly fewer than in the wild type mouse, and the $^{13}C/^{12}C$ ratios in these 4 lipid droplets are also lower than in the wild type heart. The 3 capillaries (red arrows) in the 30 µm by 30 µm area all show a high $^{13}C/^{12}C$ ratio, which may suggest that the ^{13}C-fatty acids fed to the *Gpihbp1*$^{-/-}$ mouse could not be taken up as they are in a wild type mouse. The $^{12}C^{14}N^-$ and $^{13}C/^{12}C$ image of the SKM do not showing any ^{13}C incorporation in the imaged area. The liver, as stated above is the final step of the lipid uptake process, and shows high $^{13}C/^{12}C$ labelled areas and lipid droplets.

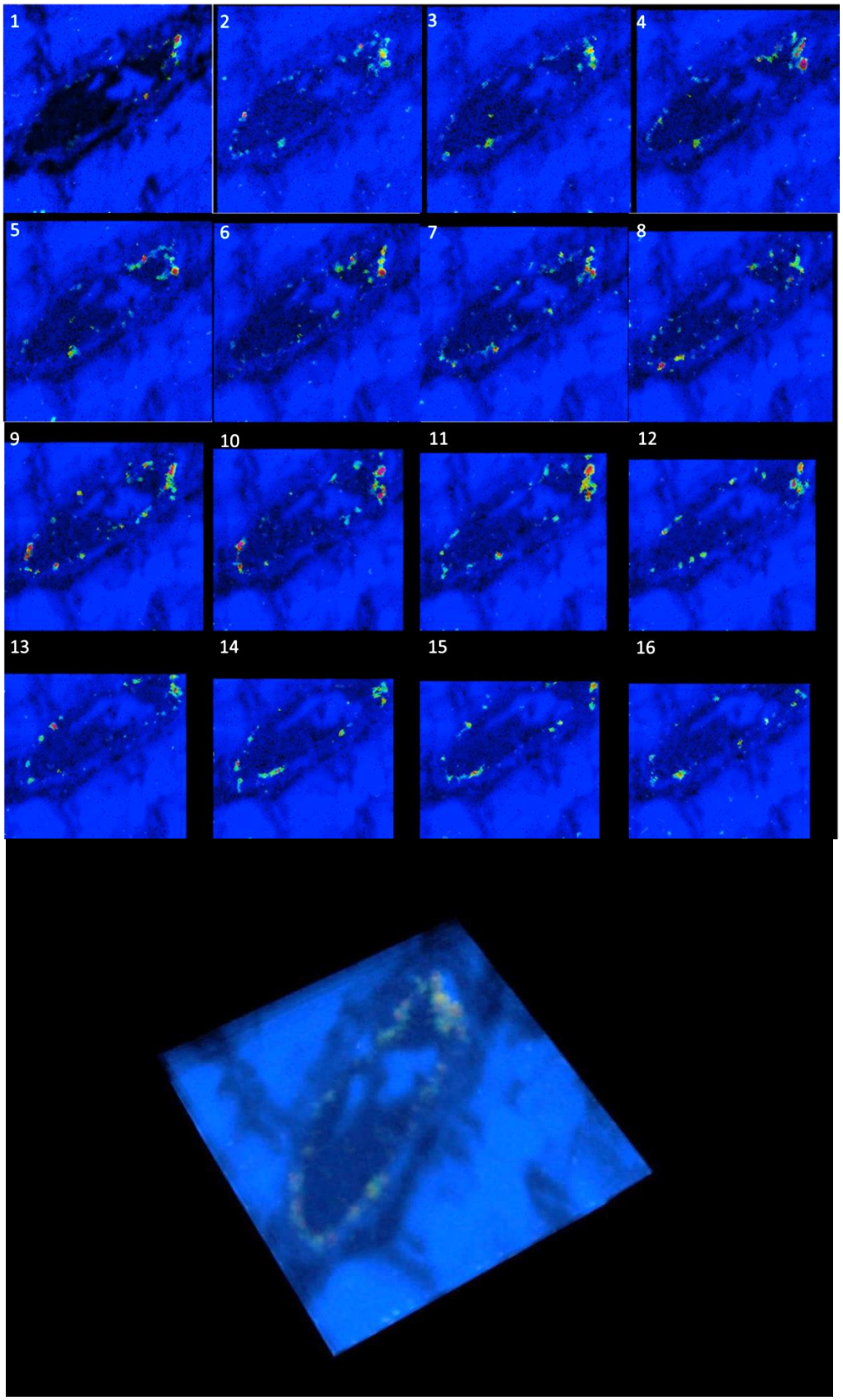

Figure 6.20: Depth profiling $^{15}N/^{14}N$ images of a capillary in heart tissue labelled with ^{15}N-antibody for GPIHBP1. Size of images: 10 µm × 10 µm.

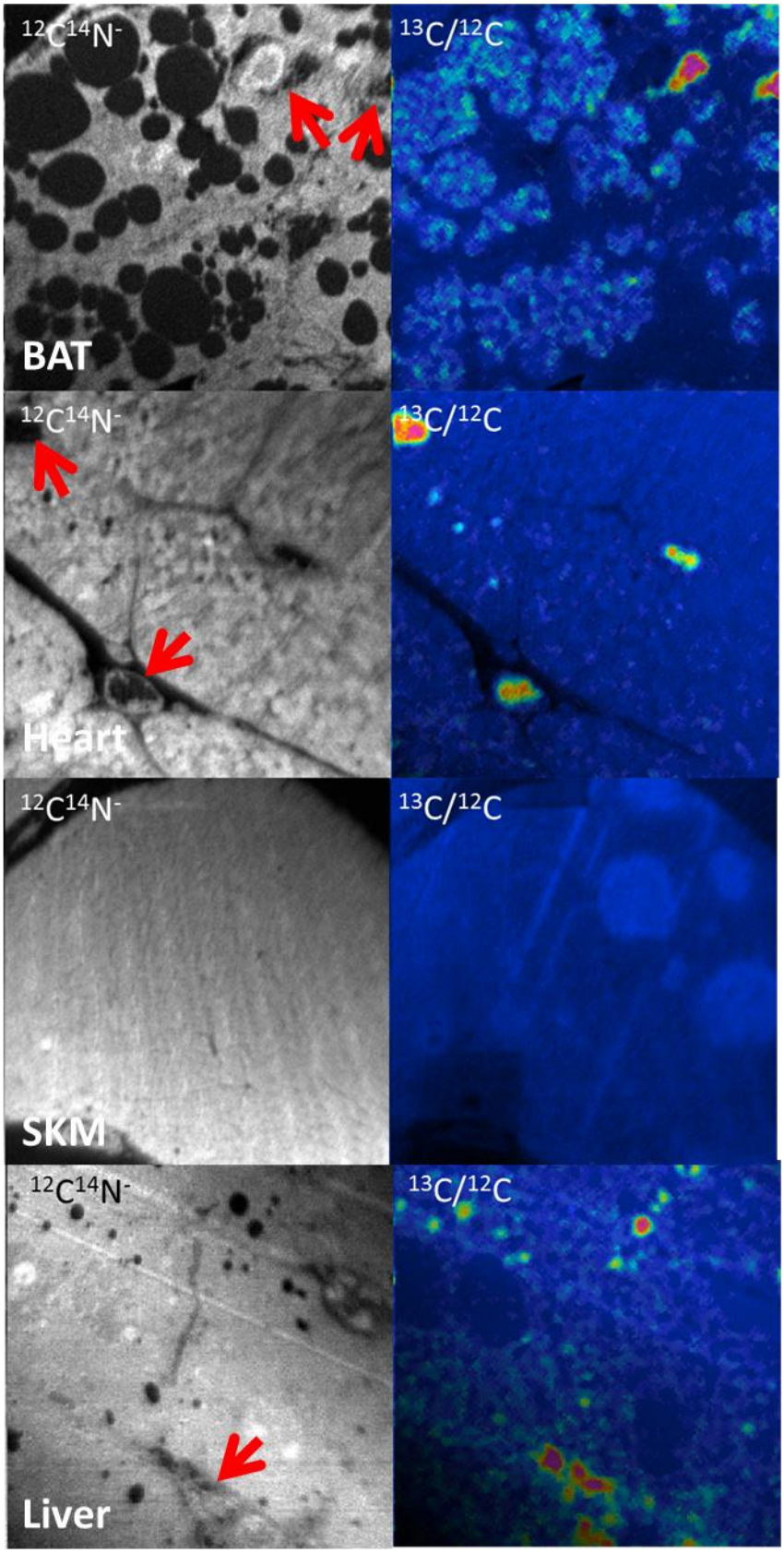

Figure 6.21: Typical NanoSIMS $^{12}C^{14}N^-$ and $^{13}C/^{12}C$ HSI image on *Gpihbp1*$^{-/-}$ mouse tissue samples. Capillaries are identified by red arrows. Size of images: 35 µm × 35 µm.

Measurements of the $^{13}C/^{12}C$ ratio in the lipid droplets were performed with the OpenMIMS plugin in ImageJ, and the data analysed by Prism 5.0 is shown in Figure 6.22 (data presented as mean ± SD). The increase of the $^{13}C/^{12}C$ ratio was calculated from $Increase = \frac{\frac{^{13}C}{^{12}C}ratio - 1.1\%}{1.1\%}$ to show changes of $^{13}C/^{12}C$ ratio above the natural abundance after 4 day feeding with the ^{13}C-fatty acid diet. Analysis shows a lower increase of the $^{13}C/^{12}C$ ratio in the lipid droplets in the GPIHBP1 expressing tissues, including BAT, heart and SKM. The results show 455%, 56% and 630% more than the $^{13}C/^{12}C$ ratio increase in wild type BAT, heart and SKM respectively than in the *Gpihbp1*$^{-/-}$ mouse. In liver tissue, which does not express GPIHBP1, results show more increase of the $^{13}C/^{12}C$ ratio in the *Gpihbp1*$^{-/-}$ mouse liver, 479% higher than the wild type liver. As an important step of the lipid metabolism, lipids that cannot be taken up in other tissues all end up in the liver. *Gpihbp1* expressing mouse tissues show significant lower $^{13}C/^{12}C$ ratio in *Gpihbp1*$^{-/-}$ mouse than the ratio in wild type mouse, whereas liver results show the opposite. These results again proved the importance of GPIHBP1 in lipid metabolism, without it lipids cannot be efficiently taken up by tissues, and potentially result in serious diseases.

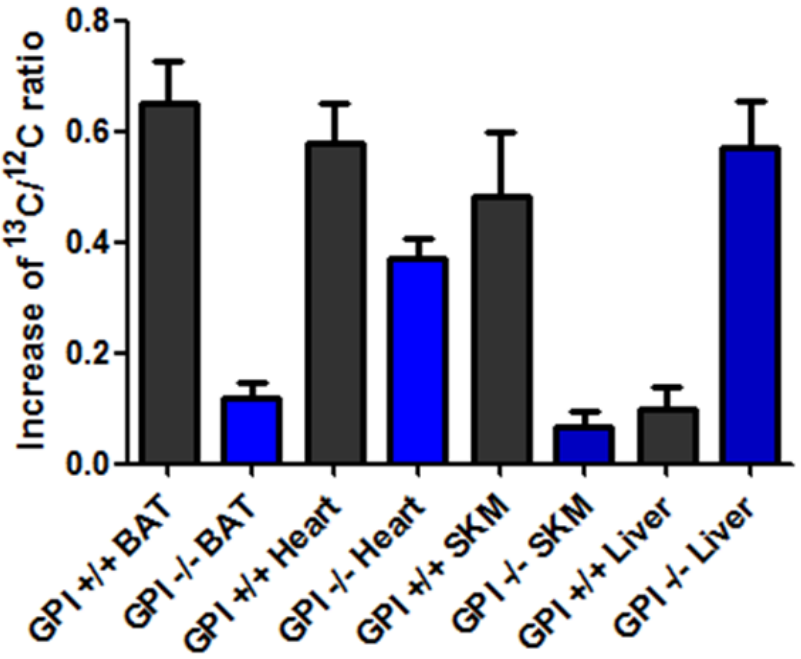

Figure 6.22: Effect of GPIHBP1 on the lipid uptake in 4 types of tissue in wild type and *Gpihbp1*$^{-/-}$ mice.

6.3.6 Correlative BSE and NanoSIMS Imaging on Tissue Samples

All the samples analysed in this chapter were stained with OsO_4 as for a TEM sample, and BSE imaging was conducted on various tissue sections. In all the images, the subcellular structures are nicely revealed. All the imaging was conducted on 500 nm tissue sections, which are also good for NanoSIMS imaging. The BSE imaging is a useful technique to provide morphology information, and it is also useful to select areas of interest for NanoSIMS imaging, since it is much quicker and more efficient than imaging large areas in the NanoSIMS. Figure 6.23 shows a mosaic image of low a magnification BSE analysis of heart tissue.

Establishing a correlative BSE and NanoSIMS imaging protocol has been discussed in Chapter 4, and I also applied this method to the tissue samples used to track the lipolysis products in tissues. Figure 6.24 shows correlative images of a 200 µm by 100 µm area. The BSE image show the detailed morphology of the heart tissues, with myocytes and a few capillaries observed in this area. With this method, we are able to relate the $^{13}C/^{12}C$ chemical information to the morphology at a large scale. The images here show some lipid droplets incorporating the ^{13}C-fatty acids, but more obviously the inside of the capillaries have the highest $^{13}C/^{12}C$ ratio. This shows again the ^{13}C-fatty acids were retained in the capillaries due to the deficiency of *Gpihbp1* in this mouse.

Higher resolution correlative BSE and NanoSIMS images were taken (Figure 6.25) on both *Gpihbp1*$^{+/+}$ and *Gpihbp1*$^{-/-}$ BAT tissues. The *Gpihbp1*$^{+/+}$ images show that large lipid droplets in parenchymal cells are heavily labelled with ^{13}C, with a $^{13}C/^{12}C$ ratio of 2.1%, and show as dark particles in the BSE image. These large BAT lipid droplets were also shown in the low magnification images in Figure 6.15. The high resolution BSE and NanoSIMS images on the *Gpihbp1*$^{-/-}$ mouse show darkly labelled features inside the capillaries, and the NanoSIMS image confirmed that they are the ^{13}C-fatty acids retained in the capillaries. Some incorporation of the ^{13}C is also imaged in the large lipid droplets in the *Gpihbp1*$^{-/-}$ samples, with a $^{13}C/^{12}C$ ratio of ~1.2% in lipid droplets, which is 42.9% lower than the ratio in the lipid droplets in *Gpihbp1*$^{+/+}$ mice.

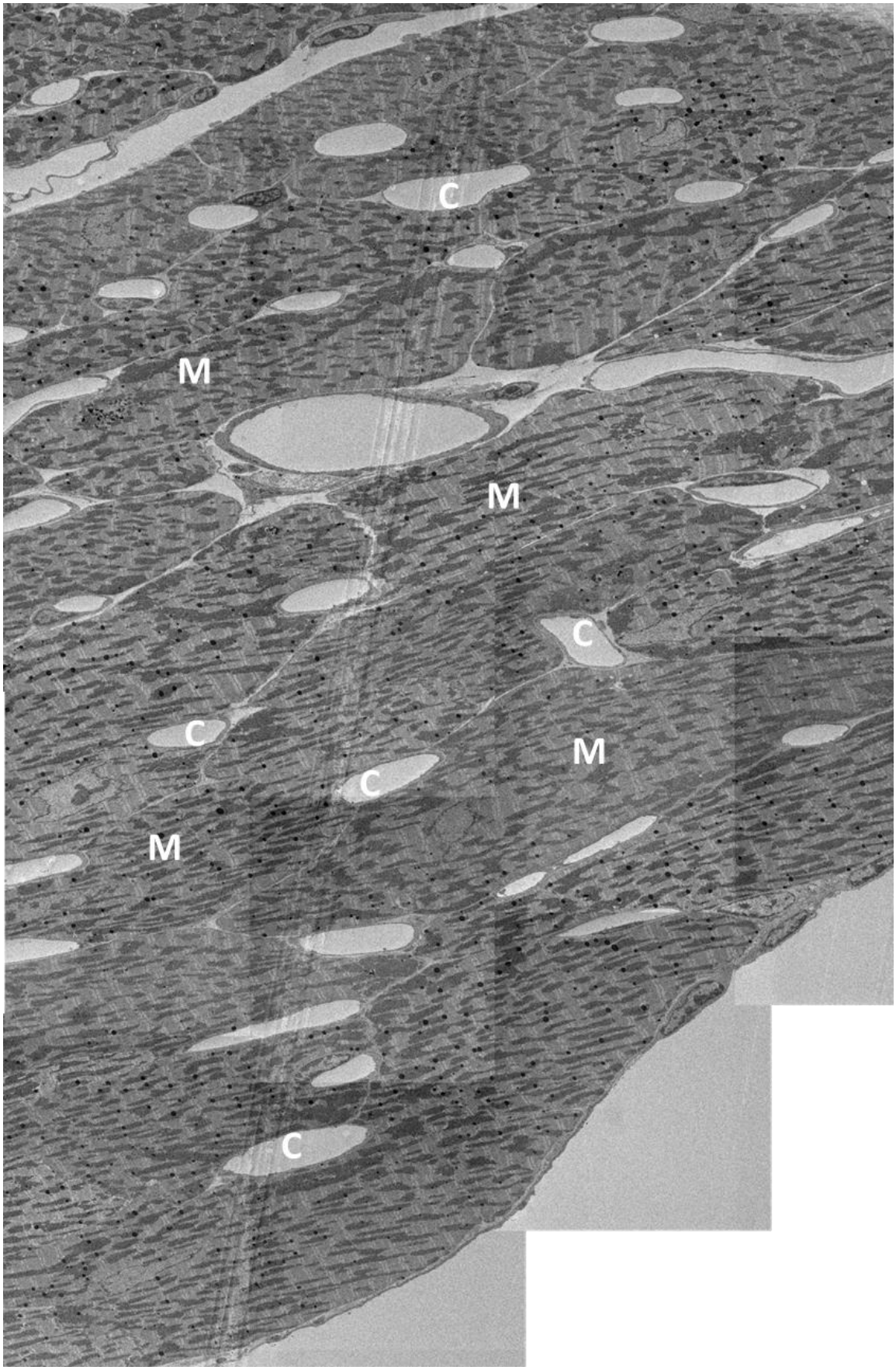

Figure 6.23: Low magnification BSE images scanning a large area (150 µm × 230 µm) of a wild type mouse heart tissue. Four capillaries (C) and myocytes (M) are identifiedl.

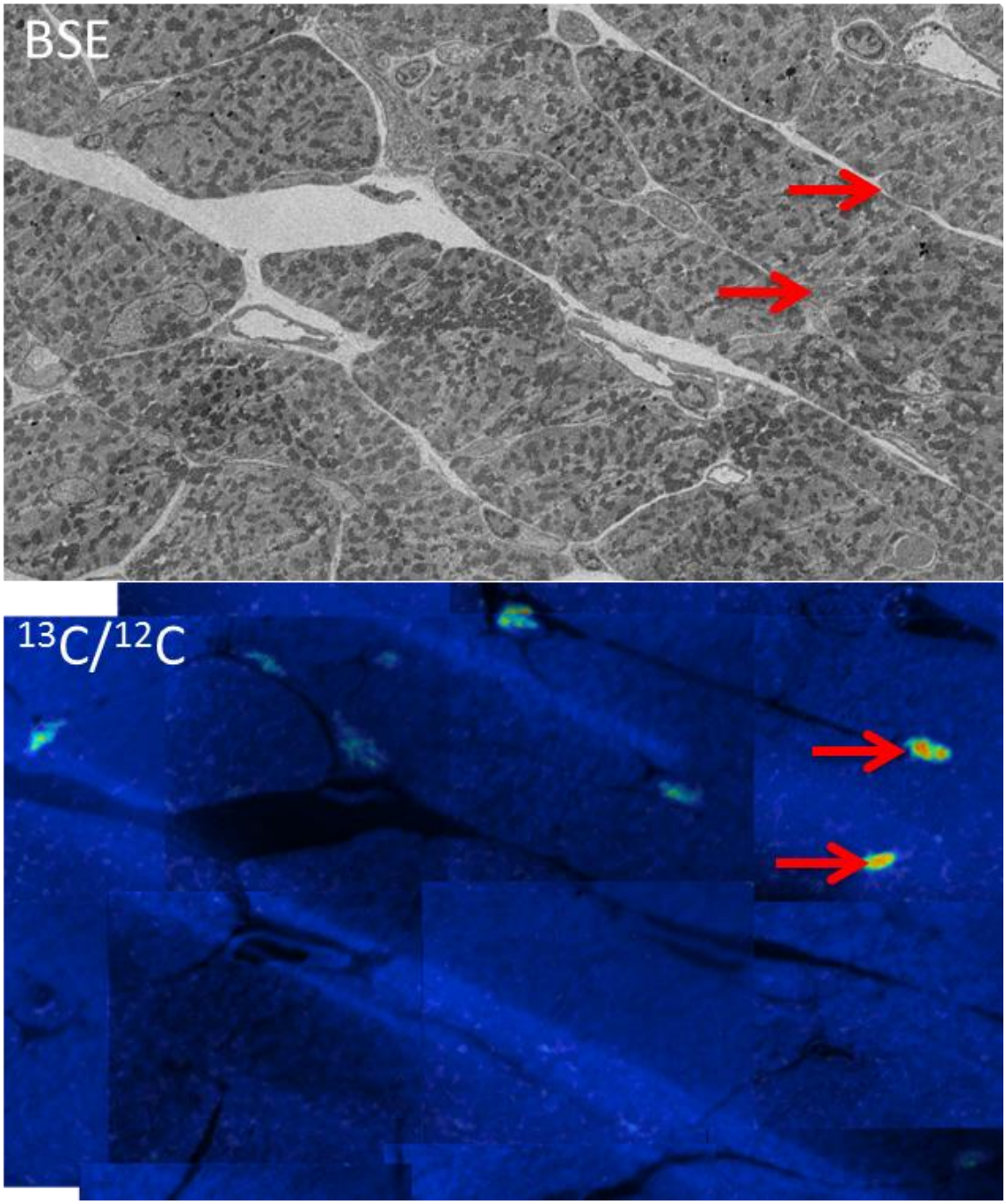

Figure 6.24: Large area correlative BSE and NanoSIMS image on a *Gpihbp1*$^{-/-}$ heart. Two capillaries are identified by red arrows.

Correlative BSE and NanoSIMS imaging was also conducted on both *Gpihbp1*$^{+/+}$ and *Gpihbp1*$^{-/-}$ heart tissue (Figure 6.26). As in the BAT tissue, lipid droplets observed in *Gpihbp1*$^{+/+}$ heart were obviously strongly labelled with ^{13}C, with a $^{13}C/^{12}C$ ratio of ~2.4%, whereas in *Gpihbp1*$^{-/-}$ heart, lipids were retained in capillaries, showing as dark features in the BSE image and high $^{13}C/^{12}C$ ratio in the NanoSIMS image.

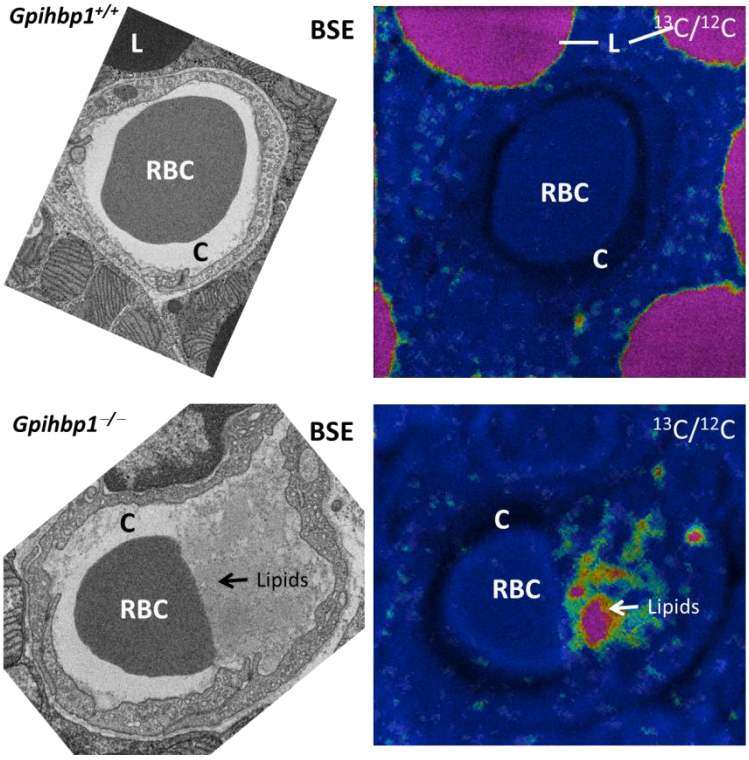

Figure 6.25: High resolution correlative BSE and NanoSIMS imaging on BAT samples from wild type and *Gpihbp1*$^{-/-}$ mouse. Capillaries (C), red blood cells (RBC), lipid droplets (L) and labelled lipids were identified. Width of NanoSIMS images: 10 µm.

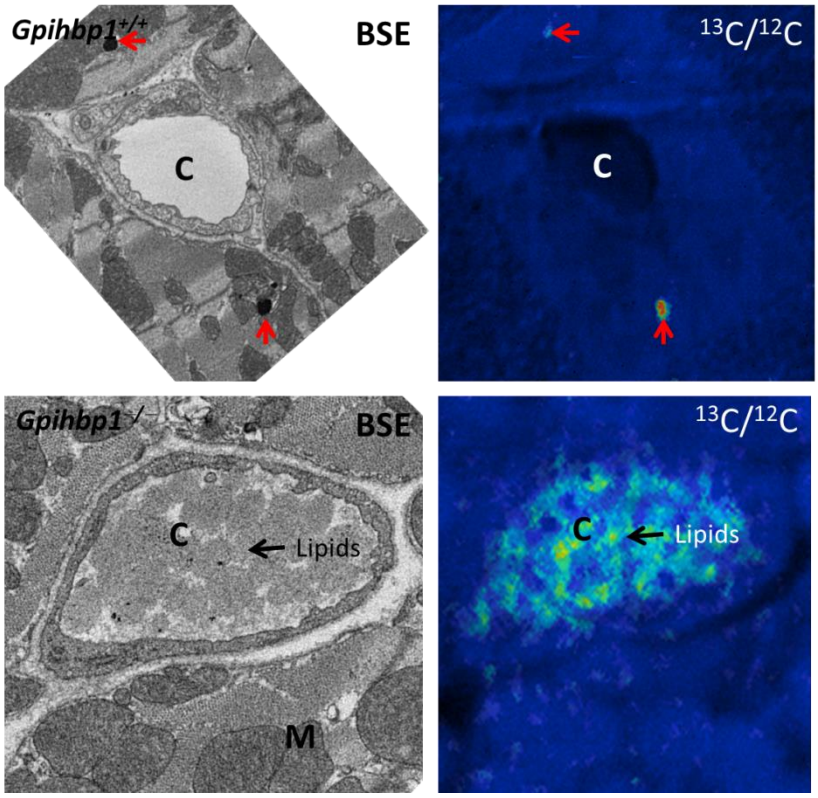

Figure 6.26: High resolution correlative BSE and NanoSIMS imaging on heart tissues from wild type and *Gpihbp1*$^{-/-}$ mice. Capillaries (C) and myocytes (M) and Lipid droplets (red arrows) were identified. Width of NanoSIMS images: 10 µm.

6.3.7 TRL Margination

The triglycerides within the core of chylomicrons, TRLs and very low-density lipoprotein (VLDL) can be hydrolysed by lipoprotein lipase (LPL) in the capillary lumen, mainly in heart, skeletal muscle and adipose tissue [236]. For lipolysis to proceed, TRLs in the bloodstream need to stop at the luminal face of the capillaries. The "receptor" on the endothelial cells responsible for capturing TRLs in the bloodstream remains unclear. One possibility that has been discussed in several articles [237, 238] is that TRLs marginate along the surface of capillaries by interacting with heparan sulfate proteoglycans (HSPGs) lining the capillary endothelial cells. However, direct observations of TRL margination in capillaries have lagged behind these suggestions, at least in part because of the absence of experimental approaches to visualize and quantify TRL margination within the microvasculature. I applied correlative BSE and NanoSIMS imaging to directly visualize the margination and investigate the mechanism for TRL margination in capillaries. My colleagues and I hypothesized that TRL margination might require GPIHBP1 and/or GPIHBP1-bound LPL. We began by testing whether TRLs could be shown trapped along capillaries in *Gpihbp1*$^{-/-}$ mice. My collaborators labelled TRLs (d < 1.006 g/ml lipoproteins from *Gpihbp1*$^{-/-}$ mice) with Alexa555 and injected them intravenously (along with FITC-labelled tomato lectin labelling endothelial cells) into wild-type and *Gpihbp1*$^{-/-}$ mice. After 30 sec, the mice were perfused with PBS to remove unbound lipoproteins, fixed in situ, and tissue samples prepared for microscopy. As expected, the tomato lectin is found bound to endothelial cells (both in capillaries and larger blood vessels). However, the TRLs bound only to heart capillaries in wild-type mice and did not bind to the larger blood vessels arrowed in Figure 6.27 where GPIHBP1 expression is absent [239]. TRL margination was nearly absent in heart capillaries of *Gpihbp1*$^{-/-}$ mice.

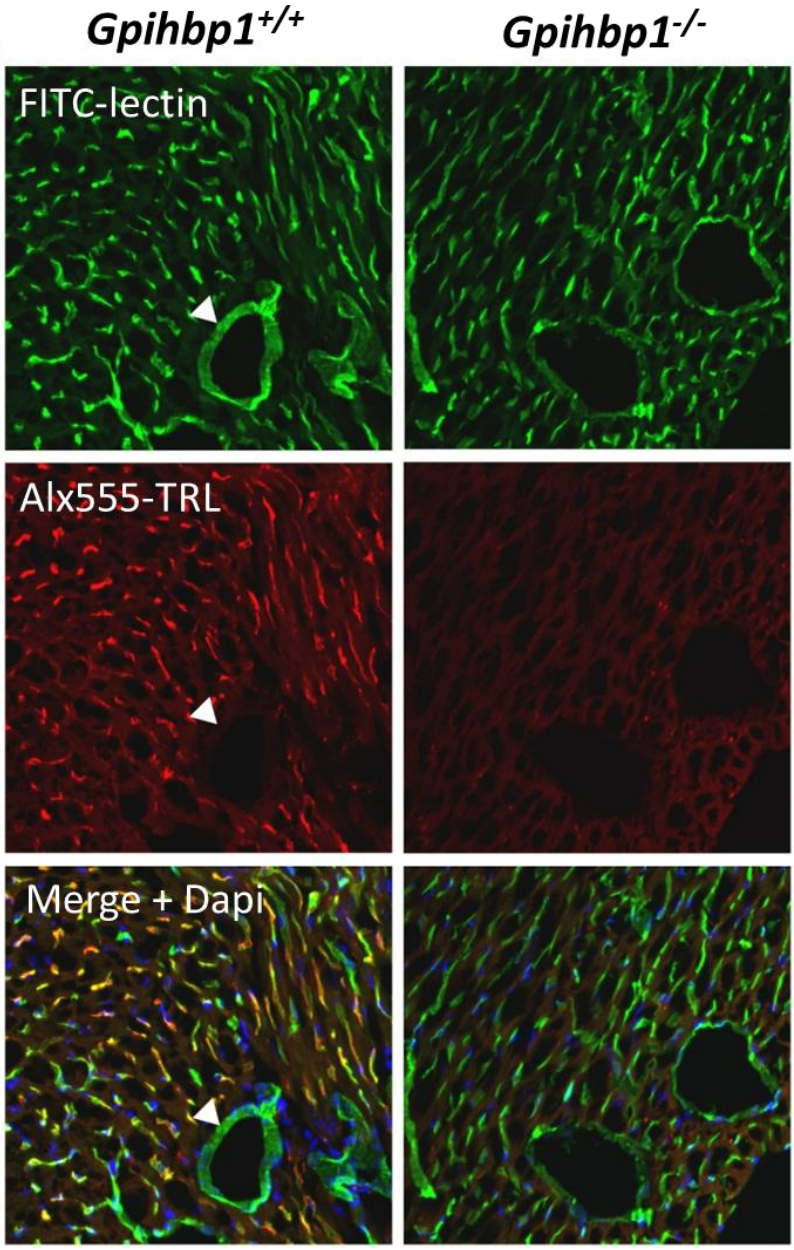

Figure 6.27: Typical fluorescence images of *Gpihbp1*$^{+/+}$ and *Gpihbp1*$^{-/-}$ heart injected with FITC-lectin, labelling endothelial cells, and Alx555 labelled TRLs, showing the distribution of the TRLs in capillaries in the *Gpihbp1*$^{+/+}$ heart, but not in *Gpihbp1*$^{-/-}$ heart tissue or large blood vessels.

Heart tissues from *Gpihbp1*$^{+/+}$ and *Gpihbp1*$^{-/-}$ mice fed with ^{13}C-fatty acids for 4 hours were also imaged by BSE. Figure 6.28 shows very clearly that there are many TRLs marginating along the luminal surface of the capillary endothelial cells. In total a few hundred TRLs have been observed in the *Gpihbp1*$^{+/+}$ samples. The sizes of these TRLs vary from tens of nanometres to almost 1 micrometre. The different sizes are partly due to the differences of the actual sizes of the TRLs, but is also a result of cutting through different sections of the TRLs. The *Gpihbp1*$^{-/-}$ BSE images show no

marginated TRLs along the luminal side of the capillary endothelial cells, and previous images (Figure 6.26) also showed many darkly labelled particles accumulated in capillaries rather than marginating along the luminal side.

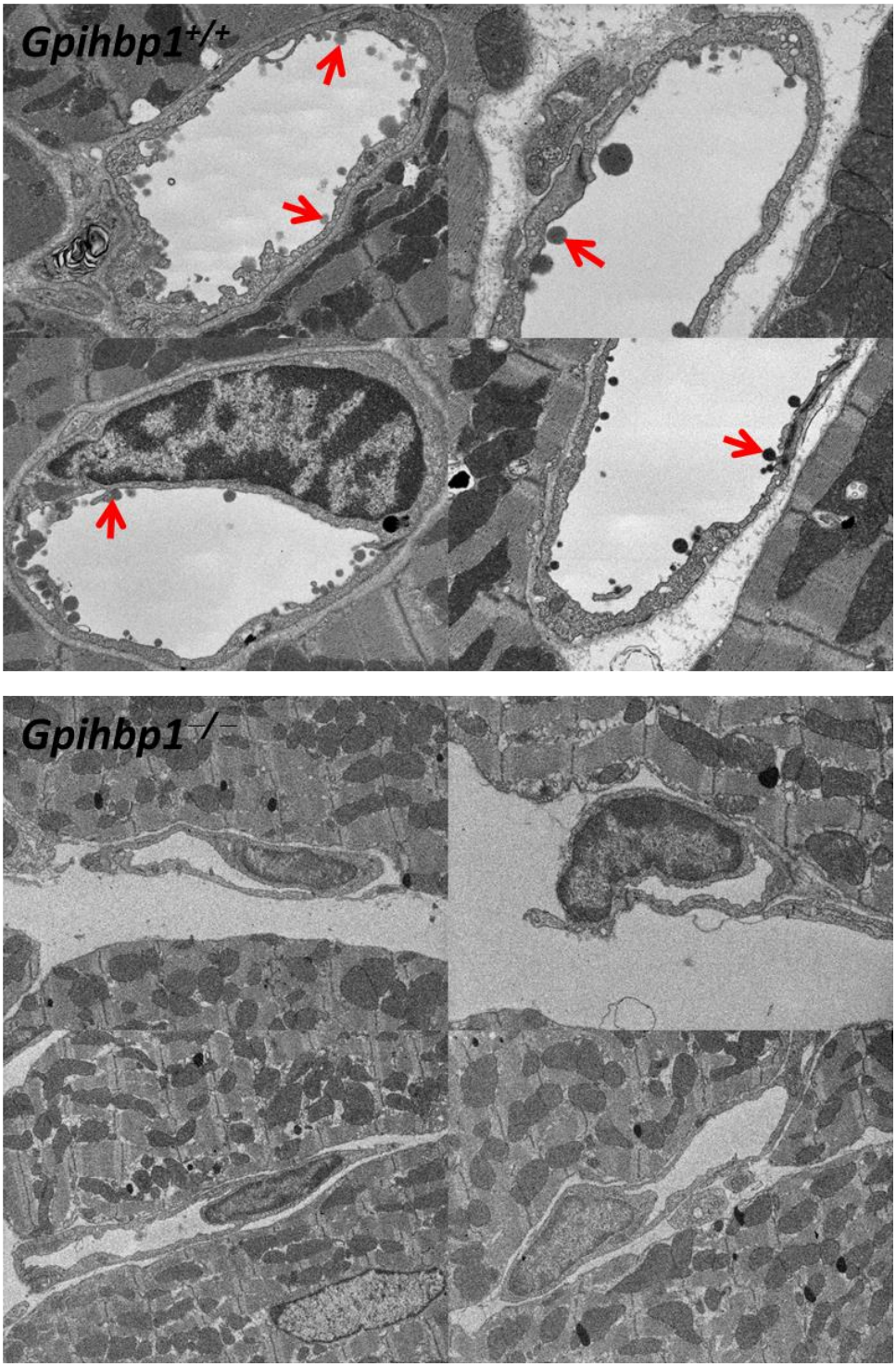

Figure 6.28: Details of BSE images of marginated TRLs (red arrows) in a *Gpihbp1*$^{+/+}$ sample but not in *Gpihbp1*$^{-/-}$ sample. Size of images: 10 µm × 10 µm – 15 µm × 15 µm.

The identity of ^{13}C-spiked TRL particles along the surface of capillaries was confirmed by correlative NanoSIMS and BSE imaging (Figure 6.29). These images are from samples injected with ^{13}C-TRLs harvested from a *Gpihbp1*$^{-/-}$ mouse after administering ^{13}C-labeled fatty acids by gavage for 4 days. After 8 min, the heart was perfused extensively, fixed, and tissue sections analysed by NanoSIMS imaging. The ^{13}C-label was often observed to be located in lipoproteins at the luminal surface of capillaries, corresponding to TRLs on the endothelial cell surface in BSE images. These results offered a direct visualization of TRLs margination in a *Gpihbp1*$^{+/+}$ mouse, but not in a *Gpihbp1*$^{-/-}$ mouse.

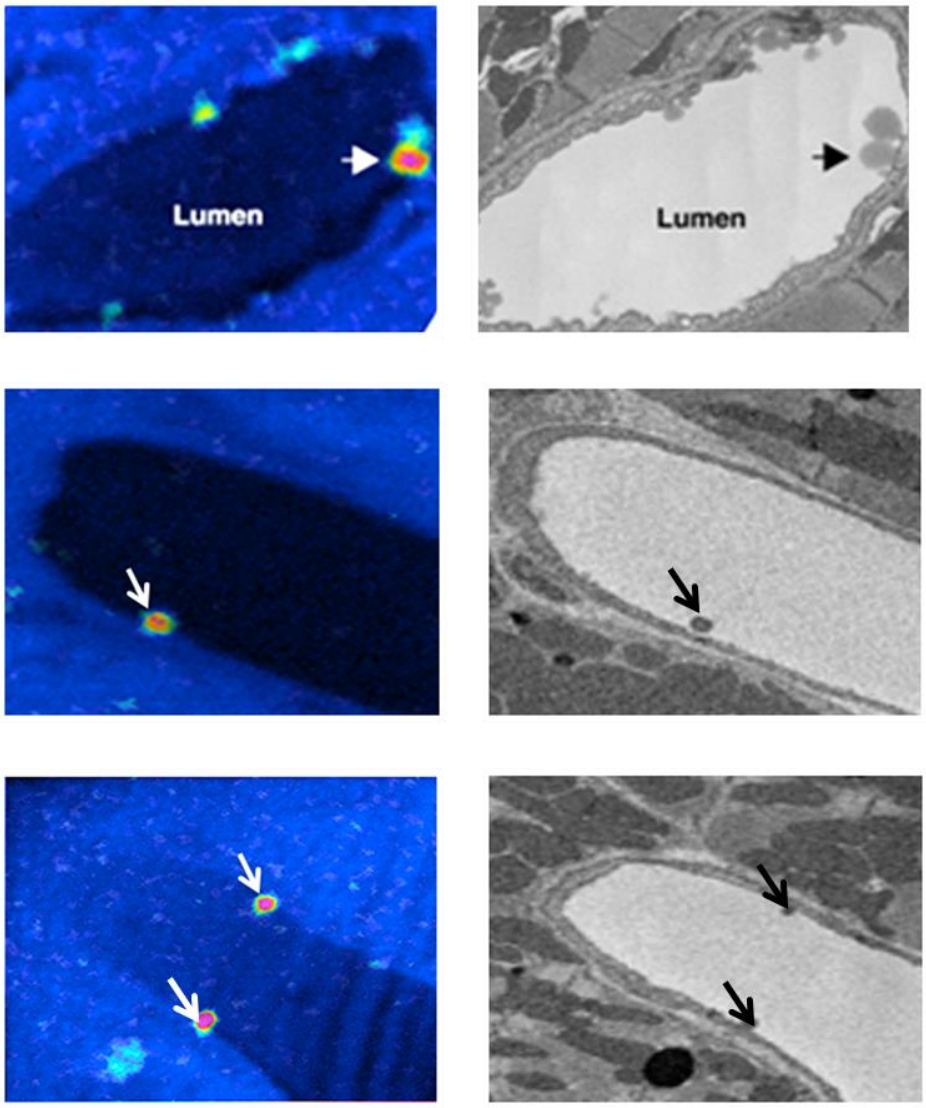

Figure 6.29: Correlative BSE and NanoSIMS images on marginated lipoproteins (arrows) on the luminal surface of the capillary endothelial cells in *Gpihbp1*$^{+/+}$ heart tissue. Width of NanoSIMS images: 10 µm.

6.3.8 ^{13}C and ^{15}N Double Labelling Imaging

As noted in Chapter 2, the NanoSIMS 50 is able to detect 5 selected secondary ion signals. The detection of ^{13}C with ^{12}C and ^{15}N with ^{14}N enables us to label two different molecules in the same samples, which can be used to localize two molecules at the same time. Figure 6.30 is an example of experiments I have done to explore at the same time the distribution of ^{13}C-fatty acids and ^{15}N-labelled antibodies. The images from both areas have shown the distribution of the antibodies to GPIHBP1 alongside the capillary and some fatty acids taken up through the endothelial cells to the lipid droplets in parenchymal cells at the same scan. This is a proof of principle imaging, which shows this technique could be useful to experiments aiming to localize two different molecules.

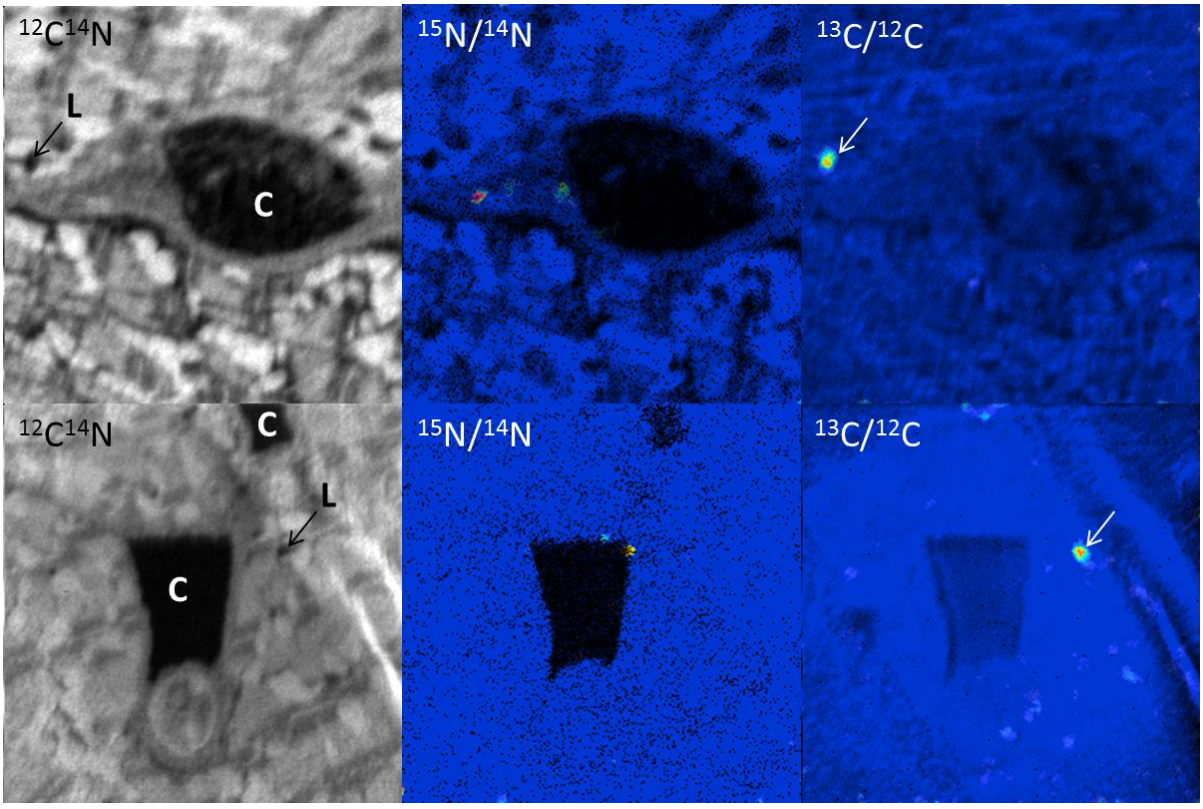

Figure 6.30: $^{12}C^{14}N^{-}$, $^{13}C/^{12}C$ and $^{15}N/^{14}N$ NanoSIMS images obtained in the same acquisition on a wild type heart tissue injected with ^{13}C-TRLS and ^{15}N-labelled antibodies. Capillaries (C) and lipid droplets (L) are identified. Size of images: 10 µm × 10 µm.

6.3.9 Transport of the Lipolysis Products through Capillary Endothelial Cells

Another mystery in the lipolysis story is how the products of TRL lipolysis (i.e., fatty acids) are transported across the capillary wall and delivered to the underlying adipocytes and myocytes. In

the past, others have suggested that TRL-derived lipid might diffuse laterally within the plasma membrane of endothelial cells and then move across endothelial cells in "membrane-lined channels" [240]. However, there is no clear understanding of how lipids move across endothelial cells towards the parenchyma. I have also attempted to address this problem with combined NanoSIMS and BSE imaging.

The images in Figure 6.31 are selected from hundreds of areas imaged by BSE. They are selected by identifying darkly labelled particles inside the capillary endothelial cells, which might be stages in the transportation process of the lipolysis products. They are difficult to find, and in total approximately 1000 capillaries have been imaged to capture some examples of the transport process.

As discussed in the previous sections, correlative BSE and NanoSIMS imaging has been successfully used in studying the transport of the labelled lipids through the endothelial cells. NanoSIMS analysis of the selected BSE imaged areas shows darkly labelled particles inside endothelial cells as shown in Figure 6.32. The $^{12}C^{14}N^-$ images show low signals from the location of the dark particles in the BSE images, and the $^{13}C/^{12}C$ images of the same area show that the dark particles are highly labelled with ^{13}C from the ^{13}C-TRLs injected to the *Gpihbp1*$^{+/+}$ mouse.

Figure 6.33 summarizes all the stages of the lipolysis product transportation we have imaged; including TRL margination (top) showing labelled TRLs alongside the luminal side of the capillary; transport through endothelial cells (middle) showing localized ^{13}C-lipids in the endothelial cell; and take up to the lipid droplets in the parenchymal cells (bottom) showing high $^{13}C/^{12}C$ in the lipid droplet. To make a strong conclusion that the lipids are also transported through the endothelial cells though vesicles, rather than only by diffusion, I need more correlative NanoSIMS and BSE images to identify vesicles that have high $^{13}C/^{12}C$ ratios. A 3D correlation would also be helpful to gain a clear understanding of this mechanism. However, even the evidence already collected strongly suggests that the some fatty acids were transported through endothelial cells in vesicles.

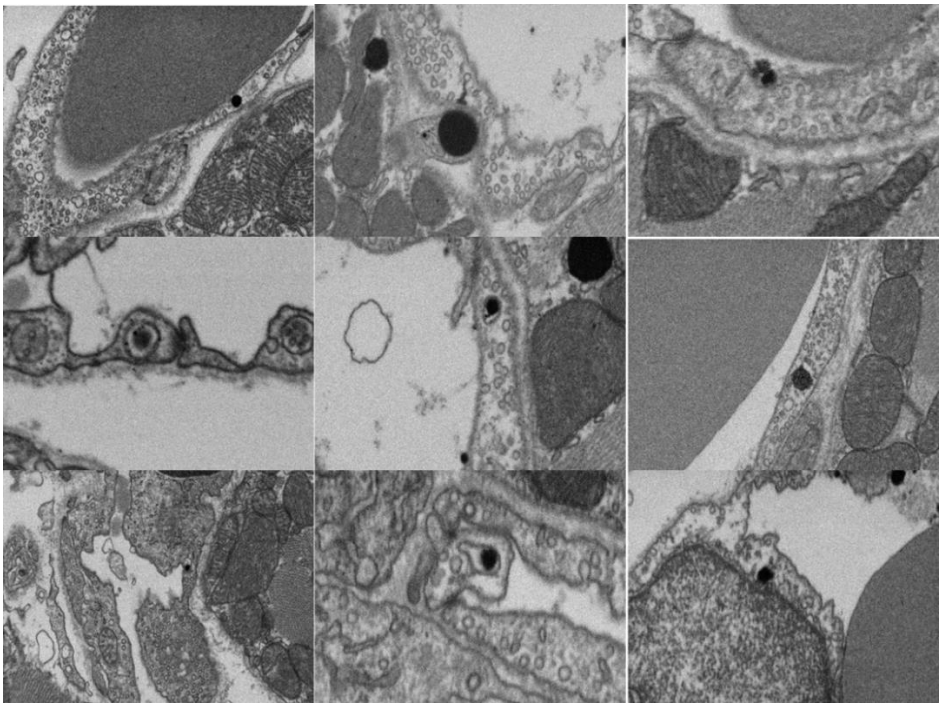

Figure 6.31: BSE images showing the darkly labelled particles 'entering' or inside the endothelial cells, and these areas are selected as areas of interest for NanoSIMS imaging. Width of images: 5 µm – 8 µm.

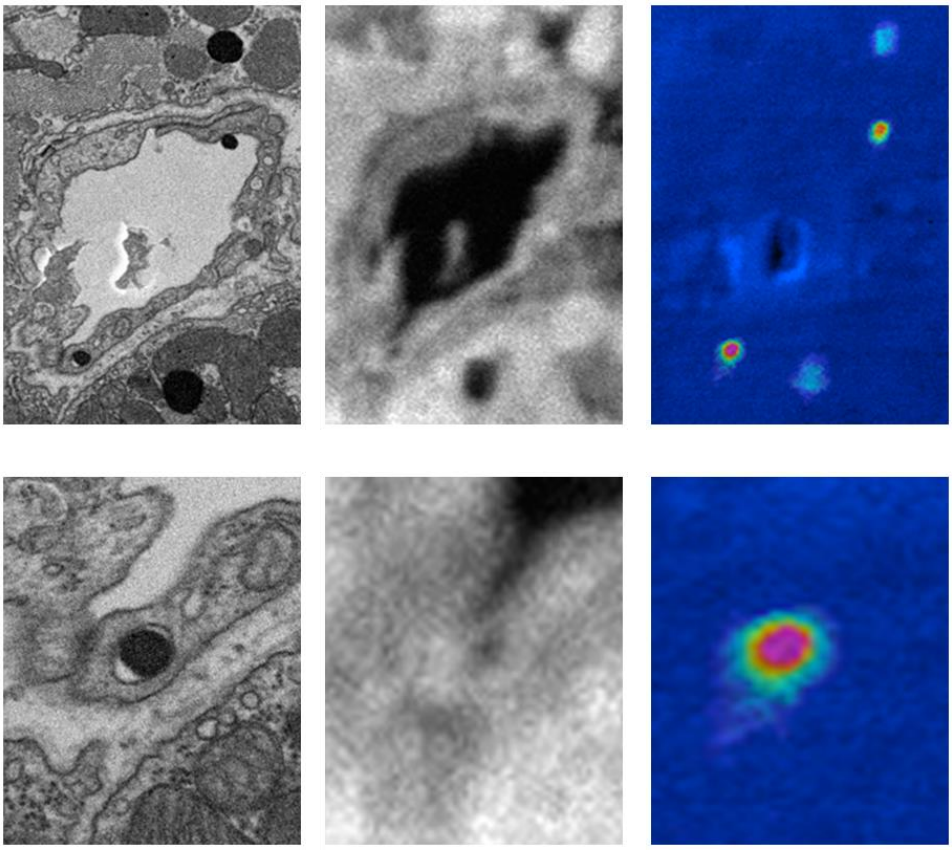

Figure 6.32: A set of correlative BSE (left), NanoSIMS images, $^{12}C^{14}N^-$ (middle) and $^{13}C/^{12}C$ (right) on a darkly imaged particle in endothelial cells, which are also labelled by ^{13}C. Width of images, 8 µm (top), 3 µm (bottom).

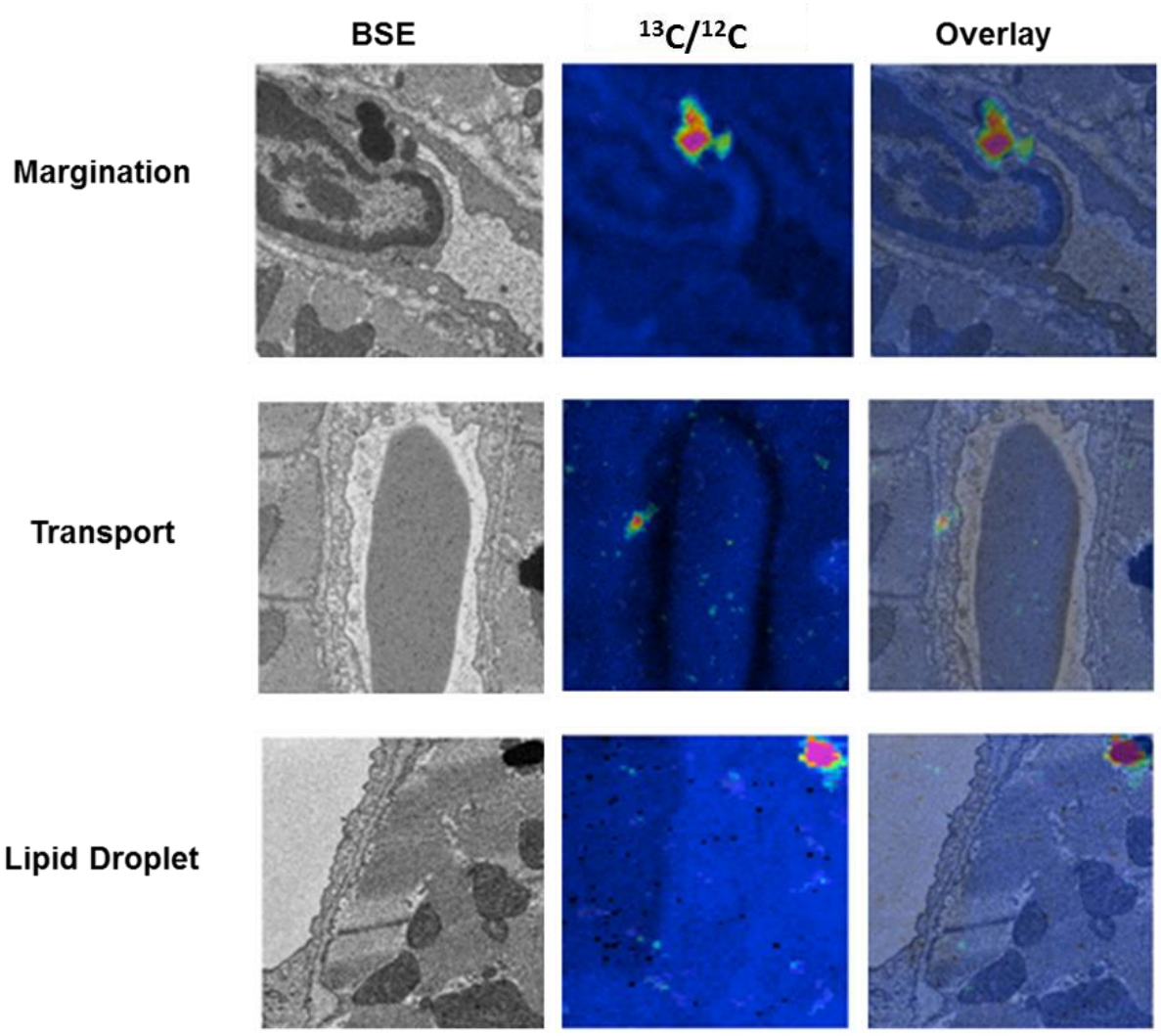

Figure 6.33: Three stages of transport of lipolysis products imaged with correlative BSE and NanoSIMS. Width of images, 8 µm.

6.3.10 Gold Nanoparticle Conjugated Antibodies

Gold nanoparticle conjugated antibodies were also injected to the mouse to visualize the GPIHBP1 distribution in vivo. The heavy Au particles are easily recognized in the BSE images. From the BSE images in Figure 6.34, the gold particles are clearly localized along the endothelial cells in the *Gpihbp1*$^{+/+}$ heart tissue, and not observed in the *Gpihbp1*$^{-/-}$ heart tissue. This is a complementary experiment to the fluorescence and ^{15}N-labelled antibodies experiment described above.

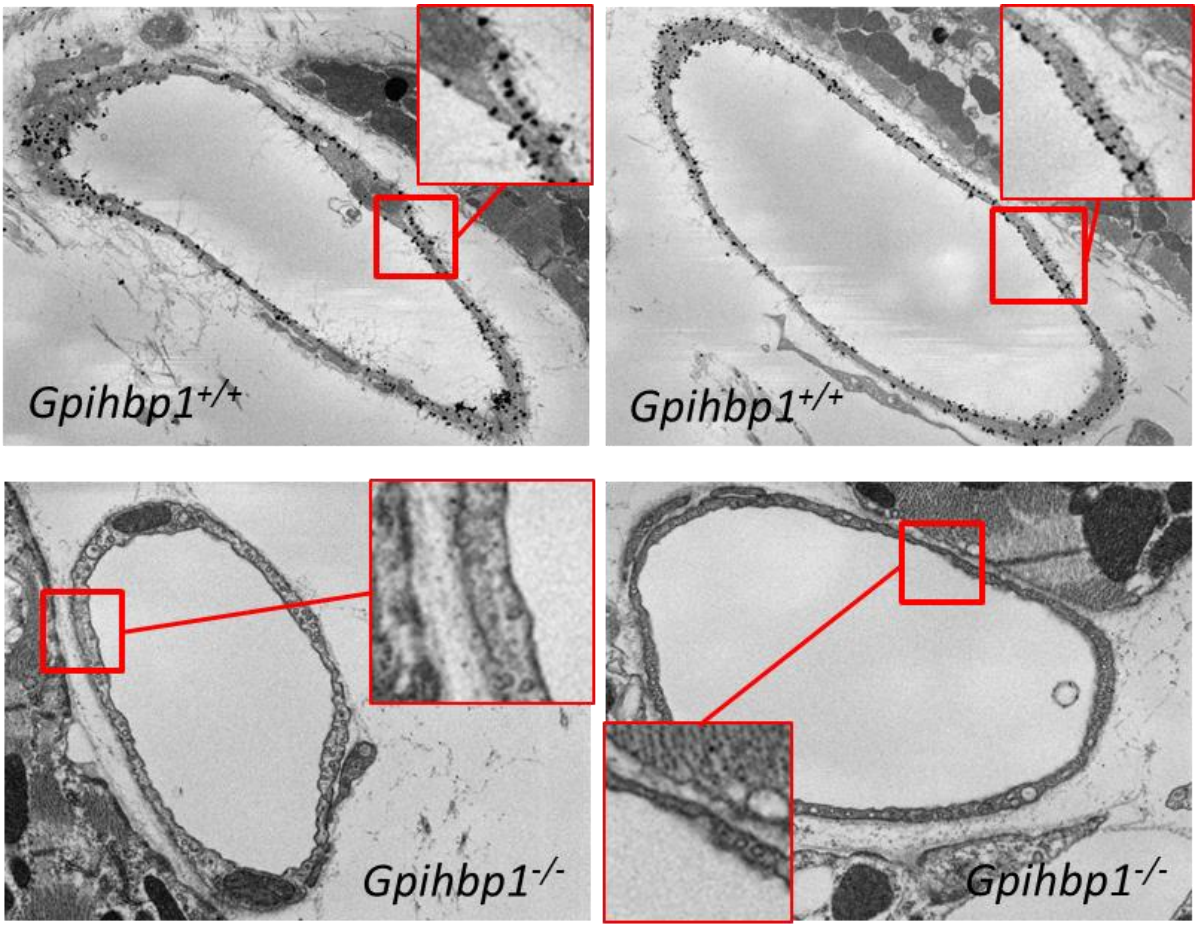

Figure 6.34: BSE images of gold nanoparticle conjugated antibodies targeted to GPIHBP1 in *Gpihbp1*$^{+/+}$ and *Gpihbp1*$^{-/-}$ mouse, showing the absence of gold nanoparticles in the *Gpihbp1*$^{-/-}$ sample. Width of images: 15 µm.

6.3.11 Cultured Capillary Endothelial Cell analysis

Cultured cells experiments have been tried as a model to visualize the transportation of lipids through endothelial cells. The problem with cultured cell samples is that the topography of the sections I cut with coverslips embedded in resin is too severe for the NanoSIMS imaging as discussed in Chapter 2. Some darkly labelled particles can be identified by BSE on sectioned samples prepared as described in section 6.2.2 (Figure 6.35), but none of them are found to be strongly labelled with ^{13}C by NanoSIMS imaging. One possibility is that endothelial cells grown directly on to the impermeable substrates lose polarity and do not behave as endothelial cells *in vivo*. One way to maintain the polarity of endothelial cells is to use porous membranes for cell culture. The porous

membrane allows cells to have multidirectional exposure to the environment, which mimics a three dimensional *in vivo* setting [241]. The advantage of doing the experiments in vitro is the quick sample preparation and ease of localizing areas of interest, and more work can be done with this model experiment to achieve useful results.

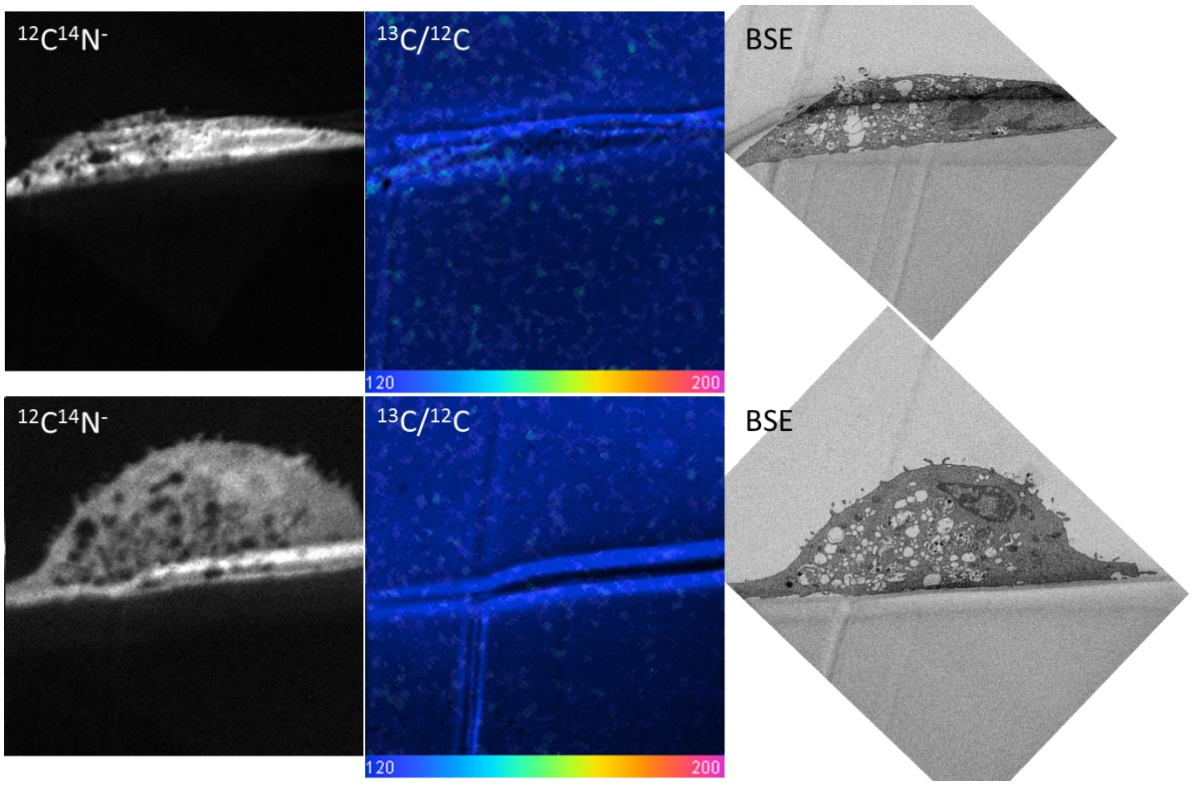

Figure 6.35: Cultured endothelial cell images exposed to ^{13}C-TRLs. Width of images: 15 µm.

6.4 Summary

This chapter shows the application of NanoSIMS analysis to understand the mechanism of lipolysis for the first time, and also the use of correlative BSE and NanoSIMS to image tissue samples. The ability of the NanoSIMS to image stable isotopes is again proved to be useful in studying metabolic processes, and this chapter is an example of studying metabolism in various tissues of the same mouse to get a better understanding of a complex biological process at the whole body level.

In summary, my colleagues in UCLA and I have accomplished the following goals with this project:

1. This chapter demonstrated the NanoSIMS can be used to image the uptake of isotopically labelled lipids in tissue samples, including BAT, heart, SKM, and liver sections. All of them have shown results consistent with the current understanding of lipolysis.
2. The effects of GPIHBP1 have been visualized by using ^{13}C-fatty acids and tracking the products of lipolysis in various tissues with high resolution. We have seen a very significant decrease of ^{13}C incorporation in GPIHBP1-expressing tissues. Statistically significant results have been obtained.
3. Correlative BSE and NanoSIMS images have been applied to study the subcellular chemical information in specific structures in these tissue samples.
4. Three stages of the transport of lipolysis products have been imaged by BSE and NanoSIMS. The results have shown that the presence of GPIHBP1 is a critical factor in controlling lipoprotein margination. Highly localized ^{13}C-fatty acids are imaged in the vesicles, which strongly suggests some transport of the fatty acids through capillary endothelial cells are with the vesicles.
5. ^{15}N labelled and gold-conjugated antibody labelling experiments have been conducted in vivo, which shows the detailed distribution of GPIHBP1 on the endothelial cells.

7 Conclusions

This thesis has demonstrated the potential of NanoSIMS analysis for the study of biological mechanisms and processes, especially when combined with stable isotope labelling. The presumption is that this kind of labelling results in molecules that behave the same as the natural ones, and the ability of the NanoSIMS to detect quantitatively all isotopes with high lateral resolution and high sensitivity makes it possible to directly image the distribution of molecules, or metabolites of these molecules, after fixation from the in vitro or in vivo state. ^{13}C and ^{15}N were used in this thesis to label fatty acids, amino acids and proteins, and I have been able to use the high mass resolution in the NanoSIMS to accurately detect the secondary ion signals from labelled ions avoiding mass interferences, as was shown in the experimental chapters. Three distinct sample types were analysed, which allowed me to explore biological processes ranging from interactions at the molecular scale, single cell metabolism and molecule tracking in tissue samples. Two reliable correlative imaging protocols have been developed, including combined AFM and NanoSIMS imaging, and combined BSE and NanoSIMS imaging. In addition, the correlation of fluorescence microscopy and NanoSIMS analysis has been briefly discussed.

Chapter 4 presented an application of stable isotope labelling and NanoSIMS analysis at the molecular scale, and it is also an example of correlative AFM and NanoSIMS analysis. The chapter showed the first direct images of the structures formed by AMPs on lipid bilayers by using ^{15}N-labelled peptides. My observations were part of a multi-technique project to reveal the pore expansion mechanism between the amhelin and models for cell membranes. The analysis protocols that I established with my colleagues in NPL have the potential to be widely applied to study molecule interactions with experimental models on a flat sample surfaces. Results from this work have been presented in 2 publications [164, 242].

Single cell analysis with the NanoSIMS and complementary techniques was demonstrated in Chapter 5. Both intact cell samples and resin embedded sections were used to study glutamine metabolism in single cells. FIB was explored as a sample preparation technique to create a flat surface for the NanoSIMS to image. The images showed that flat surfaces could be obtained, and this makes it easier to construct 3D chemical images than from intact cells. This is a technique that could be developed in further work.

The results presented in Chapter 5 on conventional resin embedded samples have revealed the incorporation rate of ^{15}N-labelled glutamine over different exposure times; from which we could extract quantitative data to show that the $^{15}N/^{14}N$ ratio increased at 0.18%/hour over 24 hours. Subcellular analysis has showed obvious variations in local incorporation in different samples and also between cells treated under the same conditions. Correlative fluorescence, AFM and NanoSIMS analysis were tried on intact cell samples, and these other techniques can provide different information to correlate to the chemical information obtained by the NanoSIMS. I concentrated on obtaining morphological and chemical information from the same sample by correlative BSE and NanoSIMS analysis. The protocol was designed to make the imaging volume of the two techniques as similar as possible, to provide more accurate information to study the glutamine metabolism. This method was applied to study the effect of hypoxic conditions and PYGL gene knockdown effects on the glutamine metabolism in populations of single cells. Quantitative results were presented in Chapter 5, and proved that hypoxic conditions can reduce glutamine incorporation to all the organelles, and PYGL knockdown increased glutamine incorporation into all organelles. PYGL knockdown under hypoxic conditions has an obvious effect in the nucleus and nucleolus, but less on other organelles, which suggested that the blocked glycogen metabolism upregulated the glutamine pathway for nucleotide synthesis. The advantage of single cell analysis to reveal cell-to-cell variations is also clearly shown in this chapter.

Tissue imaging with NanoSIMS and complementary techniques was discussed in Chapter 6. The chapter demonstrated NanoSIMS imaging of ^{13}C-labelled fatty acids, and the ability to track the molecules in various tissues, including BAT, heart, skeletal muscle and liver tissue. The observed distributions of the labelled fatty acids in those tissues are consistent with the current understanding of lipolysis. The effects of GPIHBP1 were emphasized in the chapter. GPIHBP1 has been proved to have the ability to transport the LPL into the luminal side of capillaries, which enables the uptake of the lipids. My study on the GPIHBP1-deficient mouse samples showed a significant decrease of fatty acid uptake in BAT, heart and SKM, and an increase in the liver tissue. Experiments on ^{15}N-labelled antibodies and gold nanoparticle conjugated antibodies were also conducted to reveal the distribution of the GPIHBP1. Results from this work have been presented in 1 publication [242]. Another manuscript has been accepted by *Cell Metabolism*.

New protocols for correlative BSE and NanoSIMS analysis on these tissue samples were also developed. The characteristics of these two techniques make it possible to image large areas of tissue sections with high resolution to obtain more detailed information on the local distribution of the labelled molecules. In addition, three stages of fatty acids transport were observed by both BSE and NanoSIMS: (1) margination, (2) transport through endothelial cells, and (3) transport into the lipid droplets in adjacent parenchymal cells. Combining this data with fluorescence microscopy images, margination of the lipoproteins along the luminal side of the capillaries was proved to depend on the GPIHBP1-LPL complex.

In conclusion, this thesis has demonstrated the kind of data that can be obtained by applying NanoSIMS analysis of stable isotopes to three important biological mechanisms, including molecular interactions, subcellular metabolisms, and molecule tracking in tissues.

7.1 Suggested Future Work

The protocols for NanoSIMS analysis on three types of samples have been established and demonstrated in this thesis. There are several interesting areas worthy of further study in these different fields.

As noted in this thesis, understanding the interaction mechanisms between AMPs and cell membranes will help the development of anti-infective therapeutics, and overcome the growing problem of resistance to conventional antibiotics. In addition, a clear understanding of functional interactions between biopolymers and their native environments is critical for drug and biomaterial design. Hundreds of AMPs have been discovered in plants, insects and mammals, but only a few have been studied to expose the molecular mechanisms of action. Chapter 3 has demonstrated the capability of the NanoSIMS technique in providing an unambiguous chemical analysis of antimicrobial peptide-lipid interactions which could be widely applied for other classes of AMPs that have different mechanisms of action, such as cell penetrating peptides.

The effects of PYGL gene knock down and hypoxic conditions on the ability of specific organelles to interact with labelled molecules have been revealed with correlative BSE and NanoSIMS analysis. Cancer metabolism is a highly complicated system, and there are more interesting studies that can be carried out with this methodology on glutamine or glucose metabolisms in single cells. It might also be useful to analyse these kinds of metabolic pathways in tumours, and to quantify the incorporation of target molecules to specific types of cells in the tumour or adjacent healthy cells, with subcellular resolution to determine the specific locations where the pathways are most effective.

The discovery of a GPI-anchored protein (GPIHBP1) in 2007 improved our understanding of the lipolysis process. Margination and the transfer of labelled lipids to the lipid droplets have been successfully imaged by the NanoSIMS, but only a few images were captured of the critical stage in which the fatty acid is being transporting through the endothelial cells. More analysis need to be

carried out on this key mechanism to fully understand the transport through capillary endothelial cells, and the rate of fatty acid incorporation could be measured quantitatively, particularly with ^{2}D-labelling which has a low natural background. The combination of BSE imaging of very large areas to identify much smaller regions to analyse in the NanoSIMS could be automated to improve the data collection rate from areas showing key steps in a process or reaction. This topic is scientifically intriguing and is likely to be important for a complete understanding of human hypertriglyceridemia.

Various correlative analysis methods have been discussed in this thesis. To simplify the protocols to conduct correlative analysis, there are several important technical improvements that could be tried. Due to the fact that NanoSIMS and the complementary analysis technique need to be done in two instruments there are 3 advances that could be made in experimental methodology. (1) design of a sample holder which can fit into all the instruments would simplify the imaging process enormously; (2) a design of suitable flat substrates for this holder with markers or grids would also make it easier to find the same area in these techniques; (3) The image analysis process also could be speeded up significantly with software which allows registration of multiple images from different techniques and also provide the quantitative comparison of all the data of different types from the same position on the sample surface.

The limitations of the NanoSIMS analysis, such as lack of molecular information and limited lateral resolution, are still obvious. Correlating it with AFM and BSE has overcome some of these limitations, and has allowed useful application to different analytical areas. However, to understand other biological mechanisms may require experimental information of other kinds than those discussed in this thesis. The further development of multi-scale correlative imaging methods with other techniques would be very useful. Obtaining specific information on molecule location and concentration is difficult, but extremely useful for some studies. Techniques that might be interesting to try include Raman spectroscopy, matrix-assisted laser desorption mass spectrometry, time of flight secondary ion mass spectrometry and super resolution optical microscopy. These

techniques are able to provide molecular information with or without labelling from length scales from a whole body section to subcellular resolution. With these techniques, we will be able to (1) overcome the NanoSIMS limitation of lacking molecular information, and (2) study environmental or specific gene effects on metabolisms more quantitatively, and (3) enable correlation not only between structures and isotope ratios, but also between specific molecules and isotope ratios.

8 References

1. Schoenheimer, R. and D. Rittenberg, *Deuterium as an indicator in the study of intermediary metabolism.* Science, 1935. **82**(2120): p. 156-157.
2. Williams, P., *Secondary ion mass spectrometry.* Annual Review of Materials Science, 1985. **15**(1): p. 517-548.
3. Griffiths, J., *Secondary Ion Mass Spectrometry.* Analytical Chemistry, 2008. **80**(19): p. 7194-7197.
4. Boxer, S.G., M.L. Kraft, and P.K. Weber, *Advances in Imaging Secondary Ion Mass Spectrometry for Biological Samples.* Annual Review of Biophysics, 2009. **38**(1): p. 53-74.
5. Passarelli, M.K. and N. Winograd, *Lipid imaging with time-of-flight secondary ion mass spectrometry (ToF-SIMS).* Biochimica et Biophysica Acta - Molecular and Cell Biology of Lipids, 2011. **1811**(11): p. 976-990.
6. Wagner, M., *Single-Cell Ecophysiology of Microbes as Revealed by Raman Microspectroscopy or Secondary Ion Mass Spectrometry Imaging.* Annual Review of Microbiology, 2009. **63**(1): p. 411-429.
7. Fletcher, J.S., *Cellular imaging with secondary ion mass spectrometry.* Analyst, 2009. **134**(11): p. 2204-2215.
8. Ong, S.-E., et al., *Stable isotope labeling by amino acids in cell culture, SILAC, as a simple and accurate approach to expression proteomics.* Molecular & cellular proteomics, 2002. **1**(5): p. 376-386.
9. Radajewski, S., et al., *Stable-isotope probing as a tool in microbial ecology.* Nature, 2000. **403**(6770): p. 646-649.
10. Schoenheimer, R. and D. Rittenberg, *The application of isotopes to the study of intermediary metabolism.* Science, 1938. **87**(2254): p. 221-226.
11. Hu, V.W., et al., *3H-thymidine is a defective tool with which to measure rates of DNA synthesis.* The FASEB Journal, 2002. **16**(11): p. 1456-1457.
12. Lambert, B., et al., *Renal toxicity after radionuclide therapy.* Radiation research, 2004. **161**(5): p. 607-611.
13. Zhang, H., et al., *Identification and quantification of N-linked glycoproteins using hydrazide chemistry, stable isotope labeling and mass spectrometry.* Nature biotechnology, 2003. **21**(6): p. 660-666.
14. Radajewski, S., I.R. McDonald, and J.C. Murrell, *Stable-isotope probing of nucleic acids: a window to the function of uncultured microorganisms.* Current Opinion in Biotechnology, 2003. **14**(3): p. 296-302.
15. Keshishian, H., et al., *Quantitative, multiplexed assays for low abundance proteins in plasma by targeted mass spectrometry and stable isotope dilution.* Molecular & cellular proteomics, 2007. **6**(12): p. 2212-2229.
16. Keshishian, H., et al., *Quantification of cardiovascular biomarkers in patient plasma by targeted mass spectrometry and stable isotope dilution.* Molecular & cellular proteomics, 2009. **8**(10): p. 2339-2349.
17. Chikayama, E., et al., *Systematic NMR analysis of stable isotope labeled metabolite mixtures in plant and animal systems: coarse grained views of metabolic pathways.* PloS one, 2008. **3**(11): p. e3805.
18. Skrisovska, L., M. Schubert, and F.H.-T. Allain, *Recent advances in segmental isotope labeling of proteins: NMR applications to large proteins and glycoproteins.* Journal of biomolecular NMR, 2010. **46**(1): p. 51-65.
19. Ong, S.-E. and M. Mann, *A practical recipe for stable isotope labeling by amino acids in cell culture (SILAC).* Nature protocols, 2007. **1**(6): p. 2650-2660.

20. Everley, P.A., et al., *Quantitative cancer proteomics: stable isotope labeling with amino acids in cell culture (SILAC) as a tool for prostate cancer research.* Molecular & cellular proteomics, 2004. **3**(7): p. 729-735.
21. Harsha, H., H. Molina, and A. Pandey, *Quantitative proteomics using stable isotope labeling with amino acids in cell culture.* Nature protocols, 2008. **3**(3): p. 505-516.
22. Budge, S., et al., *Tracing carbon flow in an arctic marine food web using fatty acid-stable isotope analysis.* Oecologia, 2008. **157**(1): p. 117-129.
23. Hoefs, J., *Stable isotope geochemistry*2009: Springer.
24. Richards, M.P., et al., *Stable isotope evidence for increasing dietary breadth in the European mid-Upper Paleolithic.* Proceedings of the National Academy of Sciences, 2001. **98**(11): p. 6528-6532.
25. Hansson, S., et al., *The stable nitrogen isotope ratio as a marker of food-web interactions and fish migration.* Ecology, 1997. **78**(7): p. 2249-2257.
26. Wunder, M.B. and D.R. Norris, *Improved estimates of certainty in stable-isotope-based methods for tracking migratory animals.* Ecological Applications, 2008. **18**(2): p. 549-559.
27. Davis, L., *Basic methods in molecular biology*1986: Elsevier.
28. Steinhauser, M.L. and C.P. Lechene. *Quantitative imaging of subcellular metabolism with stable isotopes and multi-isotope imaging mass spectrometry*. in *Seminars in cell & developmental biology*. 2013. Elsevier.
29. Dettmer, K., P.A. Aronov, and B.D. Hammock, *Mass spectrometry ‐based metabolomics.* Mass spectrometry reviews, 2007. **26**(1): p. 51-78.
30. Gruhler, A., et al., *Stable isotope labeling of Arabidopsis thaliana cells and quantitative proteomics by mass spectrometry.* Molecular & cellular proteomics, 2005. **4**(11): p. 1697-1709.
31. Dollery, C., *Intracellular Drug Concentrations.* Clinical Pharmacology & Therapeutics, 2012.
32. Van Tendeloo, G., D. Van Dyck, and S.J. Pennycook, *Handbook of Nanoscopy: Vol. 1*2012: Wiley. com.
33. Haase, A., et al., *Application of laser postionization secondary neutral mass spectrometry/time-of-flight secondary ion mass spectrometry in nanotoxicology: visualization of nanosilver in human macrophages and cellular responses.* ACS nano, 2011. **5**(4): p. 3059-3068.
34. Thomson, J., *Rays of Positive Electricity and their Application to Chemical Analysis*, 1913, London: Longmans, Green, & Co.
35. Schroder, D.K., *Semiconductor material and device characterization*2006: John Wiley & Sons.
36. Gillen, G. and J. Bennett, *Cluster Secondary Ion Mass Spectrometry (SIMS) For Semiconductor and Metals Depth Profiling*, in *Cluster Secondary Ion Mass Spectrometry*2013, John Wiley & Sons, Inc. p. 247-268.
37. Strausser, Y. and G.E. McGuire, *Characterization in compound semiconductor processing*2009: Momentum Press.
38. Sigmon, T.W., *Quantitation of SIMS for Semiconductor Processing Technology*, in *Secondary Ion Mass Spectrometry SIMS II*, A. Benninghoven, et al., Editors. 1979, Springer Berlin Heidelberg. p. 80-84.
39. Benninghoven, A., *Surface analysis by secondary ion mass spectrometry (SIMS).* Surface Science, 1994. **299**: p. 246-260.
40. Vickerman, J., A. Brown, and N. Reed, *Secondary Ion Mass Spectrometry, Principles and Applications*, 1989, Oxford, Oxford University Press.
41. Vickerman, J.C. and I. Gilmore, *Surface analysis: the principal techniques*2009: Wiley Online Library.
42. Vickerman, J.C. and D. Briggs, *ToF-SIMS: Materials Analysis by Mass Spectrometry 2nd Edition*2013: IM publications.

43. Gilmore, I.S., *SIMS of organics—Advances in 2D and 3D imaging and future outlook.* Journal of Vacuum Science & Technology A, 2013. **31**(5): p. 050819.
44. *EAG SIMS Tutorials*. Available from: http://www.eaglabs.com/training/tutorials/sims_theory_tutorial/rsf.php.
45. Centre, P.P.R. [cited 2011 July]; Available from: http://pprco.tripod.com/SIMS/Theory.htm.
46. Gross, J.H., *Mass spectrometry: a textbook*2004: Springer Verlag.
47. Liebl, H., *Ion probe microanalysis.* Journal of Physics E: Scientific Instruments, 1975. **8**(10): p. 797.
48. Wilson, R.G., F.A. Stevie, and C.W. Magee, *Secondary ion mass spectrometry: a practical handbook for depth profiling and bulk impurity analysis*1989: Wiley New York.
49. Mallet, A. and S. Down, *Dictionary of mass spectrometry*2009: Wiley.
50. Guerquinkern, J., et al., *Progress in analytical imaging of the cell by dynamic secondary ion mass spectrometry (SIMS microscopy).* Biochimica et Biophysica Acta (BBA) - General Subjects, 2005. **1724**(3): p. 228-238.
51. Benninghoven, A. and W. Sichtermann, *Secondary ion mass spectrometery: A new analytical technique for biologically important compounds.* Organic Mass Spectrometry, 1977. **12**(9): p. 595-597.
52. Wanner, K. and H. Georg, *Mass spectrometry in medicinal chemistry: applications in drug discovery*2007: John Wiley & Sons.
53. Schueler, B.W., *Microscope imaging by time-of-flight secondary ion mass spectrometry.* Microscopy Microanalysis Microstructures, 1992. **3**: p. 119-119.
54. Chandra, S.S., *Subcellular Imaging of Cells and Tissues with Dynamic Secondary Ion Mass Spectrometry.* The Encyclopedia of Mass Spectrometry, 2010. **5**: p. 469-480.
55. Alford, T.L., L.C. Feldman, and J.W. Mayer, *Sputter Depth Profiles and Secondary Ion Mass Spectroscopy.* Fundamentals of Nanoscale Film Analysis, 2007: p. 59-83.
56. Winograd, N., *The magic of cluster SIMS.* Analytical Chemistry, 2005. **77**(7): p. 142-149.
57. Moon, D., et al., *GaAs delta‐doped layers in Si for evaluation of SIMS depth resolution GaAs.* Surface and Interface Analysis, 2000. **29**(6): p. 362-368.
58. Besmehn, A. and P. Hoppe, *A NanoSIMS study of Si-and Ca-Ti-isotopic compositions of presolar silicon carbide grains from supernovae.* Geochimica et Cosmochimica Acta, 2003. **67**(24): p. 4693-4703.
59. Ito, M. and S. Messenger, *Isotopic imaging of refractory inclusions in meteorites with the NanoSIMS 50L.* Applied Surface Science, 2008. **255**(4): p. 1446-1450.
60. Wacey, D., et al., *Use of NanoSIMS in the search for early life on Earth: ambient inclusion trails in a c. 3400 Ma sandstone.* Journal of the Geological Society, 2008. **165**(1): p. 43.
61. Becker, J.S., *Recent developments in isotope analysis by advanced mass spectrometric techniquesPlenary lecture.* Journal of Analytical Atomic Spectrometry, 2005. **20**(11): p. 1173-1184.
62. Messenger, S., *Identification of molecular-cloud material in interplanetary dust particles.* Nature, 2000. **404**(6781): p. 968-971.
63. Cupples, A.M. and G.K. Sims, *Identification of in situ 2, 4-dichlorophenoxyacetic acid-degrading soil microorganisms using DNA-stable isotope probing.* Soil Biology and Biochemistry, 2007. **39**(1): p. 232-238.
64. Neilson, R., et al., *Stable isotope natural abundances of soil, plants and soil invertebrates in an upland pasture.* Soil Biology and Biochemistry, 1998. **30**(13): p. 1773-1782.
65. Metzner, R., et al., *Tracing cationic nutrients from xylem into stem tissue of French bean by stable isotope tracers and cryo-secondary ion mass spectrometry.* Plant Physiology, 2010. **152**(2): p. 1030.
66. Kasemann, S.A., et al., *Biological and ecological insights into Ca isotopes in planktic foraminifers as a palaeotemperature proxy.* Earth and Planetary Science Letters, 2008. **271**(1-4): p. 292-302.

67. Cameca, *NanoSIMS 50/50L Instrumentation.* accessed in 2014.
68. Hoppe, P., S. Cohen, and A. Meibom, *NanoSIMS: Technical Aspects and Applications in Cosmochemistry and Biological Geochemistry.* Geostandards and Geoanalytical Research, 2013. **37**(2): p. 111-154.
69. Cameca, *NanoSIMS cell biology booklet.* 2009.
70. Wolfe-Simon, F., et al., *A bacterium that can grow by using arsenic instead of phosphorus.* Science, 2011. **332**(6034): p. 1163-1166.
71. Audinot, J.N., et al., *Imaging of arsenic traces in human hair by nano-SIMS 50.* Applied Surface Science, 2004. **231–232**(0): p. 490-496.
72. Kraft, M.L., *Phase Separation of Lipid Membranes Analyzed with High-Resolution Secondary Ion Mass Spectrometry.* Science, 2006. **313**(5795): p. 1948-1951.
73. Cameca, *NanoSIMS50 biology application booklet.* 2009.
74. Peteranderl, R. and C. Lechene, *Measure of carbon and nitrogen stable isotope ratios in cultured cells.* Journal of the American Society for Mass Spectrometry, 2004. **15**(4): p. 478-485.
75. Cameca, *NanoSIMS50 materials application booklet.* 2008.
76. Lechene, C., et al., *High-resolution quantitative imaging of mammalian and bacterial cells using stable isotope mass spectrometry.* Journal of Biology, 2006. **5**(20): p. 20.1-20.30.
77. Messenger, S., et al., *Samples of stars beyond the solar system: Silicate grains in interplanetary dust.* Science, 2003. **300**(5616): p. 105-108.
78. Mostefaoui, S. and P. Hoppe, *Discovery of abundant in situ silicate and spinel grains from red giant stars in a primtive meteorite.* The Astrophysical Journal Letters, 2004. **613**(2): p. L149.
79. Sandford, S.A., et al., *Organics captured from comet 81P/Wild 2 by the Stardust spacecraft.* Science, 2006. **314**(5806): p. 1720-1724.
80. Hashizume, K., et al., *Extreme oxygen isotope anomaly with a solar origin detected in meteoritic organics.* Nature Geoscience, 2011. **4**(3): p. 165-168.
81. *EAG Analytical Techniques*. [cited 2011 July]; Available from: http://www.eaglabs.com/techniques/analytical_techniques/.
82. Grovenor, C.R.M., et al., *Specimen preparation for NanoSIMS analysis of biological materials.* Applied Surface Science, 2006. **252**(19): p. 6917-6924.
83. Dykstra, M.J. and L.E. Reuss, *Biological electron microscopy: theory, techniques and troubleshooting*2003: Springer.
84. Lechene, C., et al., *High-resolution quantitative imaging of mammalian and bacterial cells using stable isotope mass spectrometry.* Journal of Biology, 2006. **5**(6): p. 20.
85. Lechene, C.P., et al., *Quantitative Imaging of Nitrogen Fixation by Individual Bacteria Within Animal Cells.* Science, 2007. **317**(5844): p. 1563-1566.
86. Senyo, S.E., et al., *Mammalian heart renewal by pre-existing cardiomyocytes.* Nature, 2012.
87. Steinhauser, M.L., et al., *Multi-isotope imaging mass spectrometry quantifies stem cell division and metabolism.* Nature, 2012. **481**(7382): p. 516-519.
88. Zhang, D.-S., et al., *Multi-isotope imaging mass spectrometry reveals slow protein turnover in hair-cell stereocilia.* Nature, 2012. **481**(7382): p. 520-524.
89. Chandra, S., *Challenges of biological sample preparation for SIMS imaging of elements and molecules at subcellular resolution.* Applied Surface Science, 2008. **255**(4): p. 1273-1284.
90. Cavalier, A., D. Spehner, and B.M. Humbel, *Handbook of Cryo-Preparation Methods for Electron Microscopy*2009: CRC Press.
91. Lozić, I., et al., *Changes in subtypes of Ca microdomains following partial injury to the central nervous system.* Metallomics, 2014. **6**(3): p. 455-464.
92. McDonald, K.L., et al., *Recent advances in high-pressure freezing*, in *Electron Microscopy*2007, Springer. p. 143-173.
93. Kuypers, M.M. and B.B. Jørgensen, *The future of single‐cell environmental microbiology.* Environmental Microbiology, 2007. **9**(1): p. 6-7.

94. Finzi-Hart, J.A., et al., *Fixation and fate of C and N in the cyanobacterium Trichodesmium using nanometer-scale secondary ion mass spectrometry.* Proceedings of the National Academy of Sciences, 2009. **106**(15): p. 6345-6350.
95. Popa, R., et al., *Carbon and nitrogen fixation and metabolite exchange in and between individual cells of Anabaena oscillarioides.* The ISME journal, 2007. **1**(4): p. 354-360.
96. Clode, P.L., et al., *In situ mapping of nutrient uptake in the rhizosphere using nanoscale secondary ion mass spectrometry.* Plant Physiology, 2009. **151**(4): p. 1751-1757.
97. Smart, K.E., et al., *NanoSIMS and EPMA analysis of nickel localisation in leaves of the hyperaccumulator plant Alyssum lesbiacum.* International Journal of Mass Spectrometry, 2007. **260**(2-3): p. 107-114.
98. Moore, K.L., et al., *NanoSIMS analysis of arsenic and selenium in cereal grain.* New Phytologist, 2010. **185**(2): p. 434-445.
99. Moore, K.L., et al., *High-resolution secondary ion mass spectrometry reveals the contrasting subcellular distribution of arsenic and silicon in rice roots.* Plant Physiology, 2011. **156**(2): p. 913-924.
100. Moore, K.L., et al., *Localisation of iron in wheat grain using high resolution secondary ion mass spectrometry.* Journal of Cereal Science, 2012. **55**(2): p. 183-187.
101. Moore, K.L., et al., *Combined NanoSIMS and synchrotron X‐ray fluorescence reveal distinct cellular and subcellular distribution patterns of trace elements in rice tissues.* New Phytologist, 2014. **201**(1): p. 104-115.
102. Kilburn, M.R., et al., *Application of nanoscale secondary ion mass spectrometry to plant cell research.* Plant Signaling and Behavior, 2010. **5**(6): p. 1-3.
103. Anderton, C.R., et al., *Correlated AFM and NanoSIMS imaging to probe cholesterol-induced changes in phase behavior and non-ideal mixing in ternary lipid membranes.* Biochimica et Biophysica Acta (BBA)-Biomembranes, 2011. **1808**(1): p. 307-315.
104. Wilson, R.L., et al., *Fluorinated colloidal gold immunolabels for imaging select proteins in parallel with lipids using high-resolution secondary ion mass spectrometry.* Bioconjugate chemistry, 2012. **23**(3): p. 450-460.
105. Frisz, J.F., et al., *Sphingolipid Domains in the Plasma Membranes of Fibroblasts Are Not Enriched with Cholesterol.* Journal of Biological Chemistry, 2013. **288**(23): p. 16855-16861.
106. Klitzing, H.A., P.K. Weber, and M.L. Kraft, *Secondary ion mass spectrometry imaging of biological membranes at high spatial resolution*, in *Nanoimaging*2013, Springer. p. 483-501.
107. Wedlock, L.E., et al., *Visualising gold inside tumour cells following treatment with an antitumour gold(I) complex.* Metallomics, 2011(9): p. 9.
108. Berners-Price, S., et al., *NanoSIMS multi-element imaging reveals internalisation and nucleolar targeting for a highly-charged polynuclear platinum compound.* Chem. Commun., 2013. **49**(62): p. 6944-6946.
109. Lau, K.H., et al., *Development of a new bimodal imaging methodology: a combination of fluorescence microscopy and high-resolution secondary ion mass spectrometry.* Journal of Microscopy, 2010. **240**(1): p. 21-31.
110. Weber, P. and J. Holt, *Virus and Bacterial Cell Chemical Analysis by NanoSIMS*, 2008, Lawrence Livermore National Laboratory (LLNL), Livermore, CA.
111. Karney, G.B., et al., *Characterizing the microstructure of Arctica islandica shells using NanoSIMS and EBSD.* Geochemistry, Geophysics, Geosystems, 2012. **13**(4).
112. Kraft, M.L., et al., *Quantitative analysis of supported membrane composition using the NanoSIMS.* Applied Surface Science, 2006. **252**(19): p. 6950-6956.
113. steinhauser, M.L., et al., *Quantifying cell division with D2O and multi-isotope imaging mass spectrometry (MIMS).* NanoSIMS Workshop, poster, 2013.
114. Steinhauser, M.L., et al., *Increasing analytical throughput of human samples with multi-isotope imaging mass spectrometry (MIMS).* NanoSIMS Workshop, poster, 2013.

115. Ploug, H., et al., *Carbon and nitrogen fluxes associated with the cyanobacterium Aphanizomenon sp. in the Baltic Sea.* The ISME journal, 2010. **4**(9): p. 1215-1223.
116. Ploug, H., et al., *Carbon, nitrogen and O2 fluxes associated with the cyanobacterium Nodularia spumigena in the Baltic Sea.* The ISME journal, 2011. **5**(9): p. 1549-1558.
117. Li, T., et al., *Simultaneous analysis of microbial identity and function using NanoSIMS.* Environmental Microbiology, 2008. **10**(3): p. 580-588.
118. Westin, L., et al., *Study of protein and RNA in dendritic spines using multiisotope imaging mass spectrometry (MIMS).* NanoSIMS Workshop, poster, 2013.
119. Rubakhin, S.S., et al., *Imaging mass spectrometry: fundamentals and applications to drug discovery.* Drug Discovery Today, 2005. **10**(12): p. 823-837.
120. Andersson, M., et al., *Imaging mass spectrometry of proteins and peptides: 3D volume reconstruction.* Nature methods, 2008. **5**(1): p. 101-108.
121. Sugiura, Y., et al., *Visualization of the cell-selective distribution of PUFA-containing phosphatidylcholines in mouse brain by imaging mass spectrometry.* Journal of lipid research, 2009. **50**(9): p. 1776-1788.
122. Passarelli, M.K. and A.G. Ewing, *Single-cell imaging mass spectrometry.* Current Opinion in Chemical Biology, 2013. **17**(5): p. 854-859.
123. Chaurand, P., et al., *From whole-body sections down to cellular level, multiscale imaging of phospholipids by MALDI mass spectrometry.* Molecular & cellular proteomics, 2011. **10**(2).
124. Gagnon, A.C., J.F. Adkins, and J. Erez, *Seawater transport during coral biomineralization.* Earth and Planetary Science Letters, 2012. **329**: p. 150-161.
125. Rust, M.J., M. Bates, and X. Zhuang, *Sub-diffraction-limit imaging by stochastic optical reconstruction microscopy (STORM).* Nature methods, 2006. **3**(10): p. 793-796.
126. Willig, K.I., et al., *STED microscopy reveals that synaptotagmin remains clustered after synaptic vesicle exocytosis.* Nature, 2006. **440**(7086): p. 935-939.
127. Gustafsson, M.G., *Nonlinear structured-illumination microscopy: wide-field fluorescence imaging with theoretically unlimited resolution.* Proceedings of the National Academy of Sciences of the United States of America, 2005. **102**(37): p. 13081-13086.
128. Behrens, S., et al., *Linking microbial phylogeny to metabolic activity at the single-cell level by using enhanced element labeling-catalyzed reporter deposition fluorescence in situ hybridization (EL-FISH) and NanoSIMS.* Applied and Environmental Microbiology, 2008. **74**(10): p. 3143.
129. Fike, D.A., et al., *Micron-scale mapping of sulfur cycling across the oxycline of a cyanobacterial mat: a paired nanoSIMS and CARD-FISH approach.* The ISME journal, 2008. **2**(7): p. 749-759.
130. Dekas, A.E. and V.J. Orphan, *Identification of diazotrophic microorganisms in marine sediment via fluorescence in situ hybridization coupled to nanoscale secondary ion mass spectrometry (FISH-NanoSIMS).* Methods in Enzymology: Research on Nitrification and Related Processes, Vol 486, Part A, 2011. **486**: p. 281-305.
131. Musat, N., et al., *Detecting metabolic activities in single cells, with emphasis on nanoSIMS.* FEMS microbiology reviews, 2012. **36**(2): p. 486-511.
132. Moore, K.L., et al., *High-Resolution Secondary Ion Mass Spectrometry Reveals the Contrasting Subcellular Distribution of Arsenic and Silicon in Rice Roots.* Plant Physiology, 2011. **156**(2): p. 913.
133. Anderton, C.R., et al., *Correlated AFM and NanoSIMS imaging to probe cholesterol-induced changes in phase behavior and non-ideal mixing in ternary lipid membranes.* Biochimica et Biophysica Acta (BBA)-Biomembranes, 2010. **1808**(1): p. 307-315.
134. Prinz, C., et al., *Structural effects in the analysis of supported lipid bilayers by time-of-flight secondary ion mass spectrometry.* Langmuir, 2007. **23**(15): p. 8035-8041.
135. Gallimarxer, C., *Supported Membrane Composition Analysis by Secondary Ion Mass Spectrometry with High Lateral Resolution.* Biophysical Journal, 2005. **88**(4): p. 2965-2975.

136. Bozzola, J.J. and L.D. Russell, *Electron microscopy: principles and techniques for biologists*1999: Jones & Bartlett Learning.
137. Frisz, J.F., et al., *Direct chemical evidence for sphingolipid domains in the plasma membranes of fibroblasts.* Proceedings of the National Academy of Sciences, 2013. **110**(8): p. E613-E622.
138. Department, O.M., *http://www-em.materials.ox.ac.uk/instruments/ionbeam/zeiss-nvision-40-fib-sem.html*
139. Lyubchenko, Y.L., *Preparation of DNA and nucleoprotein samples for AFM imaging.* Micron, 2011. **42**(2): p. 196-206.
140. Skarnes, R.C. and D.W. Watson, *Antimicrobial factors of normal tissues and fluids.* Microbiology and Molecular Biology Reviews, 1957. **21**(4): p. 273.
141. Brogden, K.A., *Antimicrobial peptides: pore formers or metabolic inhibitors in bacteria?* Nature Reviews Microbiology, 2005. **3**(3): p. 238-250.
142. Steiner, H., et al., *Sequence and specificity of two antibacterial proteins involved in insect immunity.* Nature, 1981. **292**: p. 246-8.
143. Gallo, R.L., *Antimicrobial peptides in human health and disease*2005: Horizon bioscience.
144. Zasloff, M., *Magainins, a class of antimicrobial peptides from Xenopus skin: isolation, characterization of two active forms, and partial cDNA sequence of a precursor.* Proceedings of the National Academy of Sciences, 1987. **84**(15): p. 5449.
145. Ganz, T., M.E. Selsted, and R.I. Lehrer, *Defensins.* European journal of haematology, 1990. **44**(1): p. 1-8.
146. Wang, G., *Antimicrobial Peptides: Discovery, Design, and Novel Therapeutic Strategies*2011: Cabi.
147. Izadpanah, A. and R. Gallo, *Antimicrobial peptides.* Journal of the American Academy of Dermatology, 2005. **52**(3): p. 381-390.
148. Karp, G., *Cell and molecular biology: concepts and experiments*2009: Wiley.
149. Fjell, C.D., et al., *Designing antimicrobial peptides: form follows function.* Nature Reviews Drug Discovery, 2012. **11**(1): p. 37-51.
150. Fantner, G.E., et al., *Kinetics of antimicrobial peptide activity measured on individual bacterial cells using high-speed atomic force microscopy.* Nature nanotechnology, 2010. **5**(4): p. 280-285.
151. Mingeot-Leclercq, M.-P., et al., *Atomic force microscopy of supported lipid bilayers.* Nature protocols, 2008. **3**(10): p. 1654-1659.
152. Richter, R.P., R. Bérat, and A.R. Brisson, *Formation of solid-supported lipid bilayers: an integrated view.* Langmuir, 2006. **22**(8): p. 3497-3505.
153. Francius, G., et al., *Nanoscale membrane activity of surfactins: Influence of geometry, charge and hydrophobicity.* Biochimica et Biophysica Acta (BBA) - Biomembranes, 2008. **1778**(10): p. 2058-2068.
154. Lin, W.-C., et al., *Lipid asymmetry in DLPC/DSPC-supported lipid bilayers: a combined AFM and fluorescence microscopy study.* Biophysical Journal, 2006. **90**(1): p. 228-237.
155. Blanchette, C.D., et al., *Galactosylceramide domain microstructure: impact of cholesterol and nucleation/growth conditions.* Biophysical Journal, 2006. **90**(12): p. 4466-4478.
156. Blanchette, C.D., et al., *Quantifying growth of symmetric and asymmetric lipid bilayer domains.* Langmuir, 2008. **24**(4): p. 1219-1224.
157. Cabin-Flaman, A., et al., *Combed single DNA molecules imaged by secondary ion mass spectrometry.* Analytical Chemistry, 2011. **83**(18): p. 6940-6947.
158. Bailey, R., et al., *Atomic Force Microscopy Measurements of the Mechanical Properties of Cell Walls on Living Bacterial Cells.* Bulletin of the American Physical Society, 2014.
159. Müller, D.J. and Y.F. Dufrene, *Atomic force microscopy as a multifunctional molecular toolbox in nanobiotechnology.* Nature nanotechnology, 2008. **3**(5): p. 261-269.
160. Weber, P., et al., *AFM and NanoSIMS analyses of Vaccinia virions.* Microscopy and Microanalysis, 2013. **19**(S2): p. 666-667.

161. Ryadnov, M.G., et al., *RE Coil: An Antimicrobial Peptide Regulator.* Angewandte Chemie International Edition, 2009. **48**(51): p. 9676-9679.
162. Rakowska, P.D., et al., *Multimodal nanoprobe development for biomolecular targeting.* poster, 2012.
163. Burger, W. and M.J. Burge, *Digital image processing: an algorithmic introduction using Java*2009: Springer.
164. Rakowska, P.D., et al., *Nanoscale imaging reveals laterally expanding antimicrobial pores in lipid bilayers.* Proceedings of the National Academy of Sciences, 2013. **110**(22): p. 8918-8923.
165. Lee, M.-T., et al., *Mechanism and kinetics of pore formation in membranes by water-soluble amphipathic peptides.* Proceedings of the National Academy of Sciences, 2008. **105**(13): p. 5087-5092.
166. Matsuzaki, K., et al., *An antimicrobial peptide, magainin 2, induced rapid flip-flop of phospholipids coupled with pore formation and peptide translocation.* Biochemistry, 1996. **35**(35): p. 11361-11368.
167. Yang, L., et al., *Barrel-stave model or toroidal model? A case study on melittin pores.* Biophysical Journal, 2001. **81**(3): p. 1475-1485.
168. Matsuzaki, K., S. Yoneyama, and K. Miyajima, *Pore formation and translocation of melittin.* Biophysical Journal, 1997. **73**(2): p. 831-838.
169. Schmitt, M.A., B. Weisblum, and S.H. Gellman, *Interplay among folding, sequence, and lipophilicity in the antibacterial and hemolytic activities of α/β-peptides.* Journal of the American Chemical Society, 2007. **129**(2): p. 417-428.
170. Law, R.H., et al., *The structural basis for membrane binding and pore formation by lymphocyte perforin.* Nature, 2010. **468**(7322): p. 447-451.
171. Yang, L., et al., *Crystallization of antimicrobial pores in membranes: magainin and protegrin.* Biophysical Journal, 2000. **79**(4): p. 2002-2009.
172. Yu, Y., et al., *Vesicle budding induced by a pore-forming peptide.* Journal of the American Chemical Society, 2009. **132**(1): p. 195-201.
173. O'Connor, C., J.U. Adams, and J. Fairman, *Essentials of Cell Biology.*
174. *All about Human Cells, Cell in Human*, 2012.
175. Arshadchaudry *Cell Culture*. 2006.
176. Wang, D. and S. Bodovitz, *Single cell analysis: the new frontier in 'omics'.* Trends in biotechnology, 2010. **28**(6): p. 281-290.
177. Di Carlo, D., H.T.K. Tse, and D.R. Gossett, *Introduction: why analyze single cells?*, in *Single-Cell Analysis*2012, Springer. p. 1-10.
178. Denkert, C., et al., *Mass spectrometry–based metabolic profiling reveals different metabolite patterns in invasive ovarian carcinomas and ovarian borderline tumors.* Cancer Research, 2006. **66**(22): p. 10795-10804.
179. Korfmacher, W.A., *Using mass spectrometry for drug metabolism studies*2010: CRC Press.
180. Lanni, E.J., S.S. Rubakhin, and J.V. Sweedler, *Mass spectrometry imaging and profiling of single cells.* Journal of Proteomics, 2012. **75**(16): p. 5036-5051.
181. Prideaux, B. and M. Stoeckli, *Mass spectrometry imaging for drug distribution studies.* Journal of Proteomics, 2012. **75**(16): p. 4999-5013.
182. Römer, W., et al., *Sub-cellular localisation of a 15N-labelled peptide vector using NanoSIMS imaging.* Applied Surface Science, 2006. **252**(19): p. 6925-6930.
183. Becker, R. and M. Sogard, *Visualization of subsurface structures in cells and tissues by backscattered electron imaging.* Scanning electron microscopy, 1978(2): p. 835-870.
184. Bloebaum, R., et al., *Determining mineral content variations in bone using backscattered electron imaging.* Bone, 1997. **20**(5): p. 485-490.
185. Muscariello, L., et al., *A critical overview of ESEM applications in the biological field.* Journal of cellular physiology, 2005. **205**(3): p. 328-334.

186. Helmstaedter, M., et al., *Connectomic reconstruction of the inner plexiform layer in the mouse retina.* Nature, 2013. **500**(7461): p. 168-174.
187. Lichtman, J.W. and W. Denk, *The big and the small: challenges of imaging the brain's circuits.* Science, 2011. **334**(6056): p. 618-623.
188. *World Health Organization*. [cited 2011 July, 21st]; Available from: http://www.who.int/cancer/en/.
189. *American Cancer Society*. [cited 2011 July, 1st]; Available from: http://www.cancer.org/Cancer/CancerBasics/TheHistoryofCancer/the-history-of-cancer-what-is-cancer.
190. *Cancer Study UK*. [cited 2011 July, 1st]; Available from: http://info.cancerresearchuk.org/cancerstats/incidence/all-cancers-combined/#Trends.
191. Ruddon, R.W., *Cancer biology*2007: Oxford University Press, USA.
192. Franks, L.M. and N.M. Teich, *Introduction to the cellular and molecular biology of cancer*1997: Oxford University Press, USA.
193. Hejmadi, M., *Introduction to cancer biology*2010.
194. Warburg, O.H., *Über den Stoffwechsel der Tumoren*1926: J. Springer.
195. Kroemer, G. and J. Pouyssegur, *Tumor cell metabolism: cancer's Achilles' heel.* Cancer Cell, 2008. **13**(6): p. 472-482.
196. DeBerardinis, R.J. and T. Cheng, *Q's next: the diverse functions of glutamine in metabolism, cell biology and cancer.* Oncogene, 2009. **29**(3): p. 313-324.
197. Medina, M.A., *Glutamine and Cancer.* Journal of Nutrition, 2001. **131**(9): p. 2539S-2542S.
198. Wise, D.R. and C.B. Thompson, *Glutamine addiction: a new therapeutic target in cancer.* Trends in Biochemical Sciences, 2010. **35**(8): p. 427-433.
199. Lu, W., H. Pelicano, and P. Huang, *Cancer Metabolism: Is Glutamine Sweeter than Glucose?* Cancer Cell, 2010. **18**(3): p. 199-200.
200. Dang, C.V., et al., *Therapeutic targeting of cancer cell metabolism.* Journal of Molecular Medicine, 2011. **89**(3): p. 205-212.
201. Vander Heiden, M.G., *Targeting cancer metabolism: a therapeutic window opens.* Nature Reviews Drug Discovery, 2011. **10**(9): p. 671-684.
202. Cairns, R.A., I.S. Harris, and T.W. Mak, *Regulation of cancer cell metabolism.* Nature Reviews Cancer, 2011. **11**(2): p. 85-95.
203. Lloyd, G.E., *Atomic number and crystallographic contrast images with the SEM: a review of backscattered electron techniques.* Mineralogical Magazine, 1987. **51**(359): p. 3-19.
204. Joy, D.C. and C.S. Joy, *Low voltage scanning electron microscopy.* Micron, 1996. **27**(3): p. 247-263.
205. WINTER, D., et al., *Tomography of insulating biological and geological materials using focused ion beam (FIB) sectioning and low‐kV BSE imaging.* Journal of Microscopy, 2009. **233**(3): p. 372-383.
206. Ziegler, J.F., M.D. Ziegler, and J.P. Biersack, *SRIM – The stopping and range of ions in matter (2010).* Nuclear Instruments and Methods in Physics Research Section B: Beam Interactions with Materials and Atoms, 2010. **268**(11–12): p. 1818-1823.
207. Mayer, J., et al., *TEM sample preparation and FIB-induced damage.* Mrs Bulletin, 2007. **32**(05): p. 400-407.
208. Donnet, D. and H. Roberts, *FIB applications for semiconductor device failure analysis*, in *Microscopy of Semiconducting Materials*2005, Springer. p. 403-408.
209. Stokes, D., F. Morrissey, and B. Lich. *A new approach to studying biological and soft materials using focused ion beam scanning electron microscopy (FIB SEM)*. in *Journal of Physics: Conference Series*. 2006. IOP Publishing.
210. Marko, M., et al., *Focused ion beam milling of vitreous water: prospects for an alternative to cryo‐ultramicrotomy of frozen‐hydrated biological samples.* Journal of Microscopy, 2006. **222**(1): p. 42-47.

211. Zhang, J., et al., *Creating new fluorescent probes for cell biology.* Nature Reviews Molecular Cell Biology, 2002. **3**(12): p. 906-918.
212. Fernández-Suárez, M. and A.Y. Ting, *Fluorescent probes for super-resolution imaging in living cells.* Nature Reviews Molecular Cell Biology, 2008. **9**(12): p. 929-943.
213. Puech, P.-H., et al., *A new technical approach to quantify cell–cell adhesion forces by AFM.* Ultramicroscopy, 2006. **106**(8): p. 637-644.
214. Engler, A.J., et al., *Surface probe measurements of the elasticity of sectioned tissue, thin gels and polyelectrolyte multilayer films: correlations between substrate stiffness and cell adhesion.* Surface Science, 2004. **570**(1): p. 142-154.
215. Brahimi-Horn, M.C., J. Chiche, and J. PouyssÈgur, *Hypoxia and cancer.* Journal of Molecular Medicine, 2007. **85**(12): p. 1301-1307.
216. Brown, J.M. and W.R. Wilson, *Exploiting tumour hypoxia in cancer treatment.* Nature Reviews Cancer, 2004. **4**(6): p. 437-447.
217. Harris, A.L., *Hypoxia key regulatory factor in tumour growth.* Nature Reviews Cancer, 2002. **2**(1): p. 38-47.
218. Favaro, E., et al., *Glucose utilization via glycogen phosphorylase sustains proliferation and prevents premature senescence in cancer cells.* Cell Metabolism, 2012.
219. Fahy, E., et al., *Update of the LIPID MAPS comprehensive classification system for lipids.* Journal of lipid research, 2009. **50**(Supplement): p. S9-S14.
220. Wenk, M.R. and G. Di Paolo, *Lipids*2012: Elsevier/Academic Press.
221. Beigneux, A.P., et al., *Glycosylphosphatidylinositol-anchored high-density lipoprotein-binding protein 1 plays a critical role in the lipolytic processing of chylomicrons.* Cell Metabolism, 2007. **5**(4): p. 279-291.
222. Young, S.G. and R. Zechner, *Biochemistry and pathophysiology of intravascular and intracellular lipolysis.* Genes & Development, 2013. **27**(5): p. 459-484.
223. Adeyo, O., et al., *Glycosylphosphatidylinositol‐anchored high‐density lipoprotein‐binding protein 1 and the intravascular processing of triglyceride‐rich lipoproteins.* Journal of Internal Medicine, 2012. **272**(6): p. 528-540.
224. Gin, P., et al., *Chylomicronemia mutations yield new insights into interactions between lipoprotein lipase and GPIHBP1.* Human molecular genetics, 2012. **21**(13): p. 2961-2972.
225. Gin, P., et al., *Binding preferences for GPIHBP1, a glycosylphosphatidylinositol-anchored protein of capillary endothelial cells.* Arteriosclerosis, thrombosis, and vascular biology, 2011. **31**(1): p. 176-182.
226. Olafsen, T., et al., *Unexpected expression pattern for glycosylphosphatidylinositol-anchored HDL-binding protein 1 (GPIHBP1) in mouse tissues revealed by positron emission tomography scanning.* Journal of Biological Chemistry, 2010. **285**(50): p. 39239-39248.
227. Becker, J.S., et al., *Bioimaging of Metals and Biomolecules in Mouse Heart by Laser Ablation Inductively Coupled Plasma Mass Spectrometry and Secondary Ion Mass Spectrometry.* Analytical Chemistry, 2010. **82**(22): p. 9528-9533.
228. Goodwin, R.J.A., et al., *Use of a Solvent-Free Dry Matrix Coating for Quantitative Matrix-Assisted Laser Desorption Ionization Imaging of 4-Bromophenyl-1,4-diazabicyclo(3.2.2)nonane-4-carboxylate in Rat Brain and Quantitative Analysis of the Drug from Laser Microdissected Tissue Regions.* Analytical Chemistry, 2010. **82**(9): p. 3868-3873.
229. Solé-Domènech, S., et al., *Localization of cholesterol, amyloid and glia in Alzheimer's disease transgenic mouse brain tissue using time-of-flight secondary ion mass spectrometry (ToF-SIMS) and immunofluorescence imaging.* Acta neuropathologica, 2013. **125**(1): p. 145-157.
230. Passarelli, M.K. and N. Winograd, *Lipid imaging with time-of-flight secondary ion mass spectrometry (ToF-SIMS).* Biochimica et Biophysica Acta (BBA)-Molecular and Cell Biology of Lipids, 2011. **1811**(11): p. 976-990.
231. Knott, G., et al., *Serial section scanning electron microscopy of adult brain tissue using focused ion beam milling.* The Journal of Neuroscience, 2008. **28**(12): p. 2959-2964.

232. UIC, *http://www.uic.edu/classes/bios/bios100/lectf03am/fats.htm, accessed in 2014*.
233. *Liver and Lipoproteins, http://www.elu.sgul.ac.uk/rehash/guest/scorm/294/package/content/liver_lipoprotein.html, accessed in 2014*.
234. Cannon, B. and J. Nedergaard, *Brown adipose tissue: function and physiological significance.* Physiological Reviews, 2004. **84**(1): p. 277-359.
235. Park, T.-S., et al., *Lipids in the heart: a source of fuel and a source of toxins.* Current opinion in lipidology, 2007. **18**(3): p. 277-282.
236. Scriver, C.R., *The metabolic & molecular bases of inherited disease*2001: McGraw-Hill.
237. Goldberg, I.J., *Lipoprotein lipase and lipolysis: central roles in lipoprotein metabolism and atherogenesis.* Journal of lipid research, 1996. **37**(4): p. 693-707.
238. Cryer, A., *The role of the endothelium in myocardial lipoprotein dynamics.* Molecular and cellular biochemistry, 1989. **88**(1-2): p. 7-15.
239. Davies, B.S., et al., *GPIHBP1 is responsible for the entry of lipoprotein lipase into capillaries.* Cell Metabolism, 2010. **12**(1): p. 42-52.
240. Scow, R.O., E.J. Blanchette-Mackie, and L.C. Smith, *Role of capillary endothelium in the clearance of chylomicrons. A model for lipid transport from blood by lateral diffusion in cell membranes.* Circulation research, 1976. **39**(2): p. 149-162.
241. Sheridan, S.D., et al., *Microporous membrane growth substrates for embryonic stem cell culture and differentiation.* Methods in cell biology, 2008. **86**: p. 29-57.
242. Jiang, H., et al., *Stable isotope imaging of biological samples with high resolution secondary ion mass spectrometry and complementary techniques.* Methods, 2014. **68**(2): p. 317-324.